HEAT TRANSFER STUDIES OF STRONTIUM RECOMBINATION LASERS

Trevor R. Pugsley

A Thesis Submitted for the Degree of PhD
at the
University of St Andrews

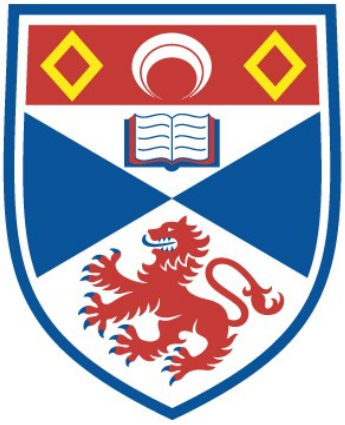

1995

Heat Transfer Studies of Strontium Recombination Lasers

Trevor R. Pugsley

A thesis submitted in application for the degree of
Doctor of Philosophy
in the
School of Physics and Astronomy
University of St. Andrews
19th September 1994.

DECLARATION

I, T. R. Pugsley, hereby certify that this thesis has been composed by me, is a record of the work done by me and that it has not been accepted in partial or complete fulfilment of any other degree or professional qualification.

The research, herein presented, was carried out in the Physical Science Laboratory of St. Salvator's College, in the University of St. Andrews, under the supervision of Dr. C. E. Little.

T. R. Pugsley,

Date. 19/9/94

CERTIFICATE

I certify that T. R. Pugsley has spent nine terms at research in the Physical Science Laboratory of St. Salvator's College, in the University of St. Andrews, under my supervision, that he has fulfilled the conditions of ordinance No. 16 (St. Andrews) and that he is qualified to submit the following thesis in application for the degree of Doctor of Philosophy.

C. E. Little

Research Supervisor

Date. 19/9/94

ACKNOWLEDGEMENTS

I would like to thank Dr. Chris Little for his supervision and guidance throughout this work and EEV Ltd. for their financial support. I am grateful to Prof. Arthur Maitland for remembering my interest when the project was first proposed and the pleasure and enthusiasm he brought to research.

Thanks must be given to Frits Akerboom, for his skill in making the glassware used, and his patience when it got broken, and to the Workshop Technicians for producing much of the metal work used in the construction of the laser systems.

For their helpful advice and discussions, I would like to thank: Dr. C. Pirrie (EEV), Dr. E. Livingstone (EEV), Dr. G. Clarke (EEV), Dr. C. Wetherup (EEV), Dr D. R. Jones, Dr. P. F. Hirst and Dr. N. Ridge. Thanks also go to Jason Bethel and Colin Whyte for their assistance while performing the beam profiling measurements, Clare Parnell for showing me the benefit of programming in Fortran and Dr Steve 'trains' Fairlie for allowing me to invade his office and jam his laser printer while completing this thesis.

Finally, I would like to thank Duncan Robertson for the warmth his valve amplifiers brought to my ears on many a cold winter's evening and the free saunas in the summer and Dr. J. C. G. Lesurf for our many interesting and productive conversations over coffee.

To my Parents

ABSTRACT

Thermal loading models have been developed in order to predict the optimum input powers of free-convection cooled strontium recombination lasers (SRLs) and forced-convection cooled SRLs. Gas temperature models have also been developed for circular bore and rectangular bore SRLs, to complement the thermal loading models, so that the performances of circular and rectangular bore SRLs can be compared. It has been shown, in theory, that rectangular bore tubes offer operation at lower gas temperatures than do circular bore tubes of the same cross-sectional area, with the same input power per unit length. Laser performance is, therefore, expected to be improved through the use of rectangular bores in the construction of SRLs.

The results of the thermal loading models are validated by experiments. The need to oven process alumina tubes in forming gas, prior to their use in the SRL, is demonstrated by an increase in output power from tubes processed using this technique. Enhanced radiative heat extraction, accompanied by an increase in average laser output power, is obtained from a free-convection cooled SRL by increasing the emissivity of the outer surface of the ceramic discharge tube. Three rectangular bore water-cooled SRLs, optimising at different input powers, have been constructed, operated and compared in performance to a free-convection cooled SRL, constructed using the *same* ceramic discharge tube.

An average output power of 2.3 W has been obtained from a 40 cm long rectangular bore beryllia discharge tube through the use of active water cooling. This represents an improvement of over 200% when compared to the performance of a free-convection cooled SRL utilizing the same ceramic discharge tube.

CONTENTS

1. Recombination principles and the strontium recombination laser

2. Thermal modelling of strontium recombination laser tubes

3. Results of gas temperature modelling for helium filled laser tubes

4. Strontium recombination laser scaling issues

5. Enhanced radiative cooling of SRL laser tubes: experiments

6. Enhanced convective cooling of SRL laser tubes: experiments

7. Summary, conclusions and suggestions for further work

APPENDICES

CHAPTER 1:

Recombination principles and the strontium recombination laser

1.1 Introduction: an overview of recombination lasers.

Recombination lasers form an important class of gas discharge lasers. They are usually produced as a result of transitions taking place within the excited states of metal atoms and ions (when in the presence of an inert buffer-gas), although recombination larer action has also been observed in a mixture of helium and hydrogen [1]. Recombination lasers are characterized by the production of a population inversion via the process of electron-ion recombination. In such lasers, the lasant is ionized (usually via electron-atom collisions), and the upper laser level is fed from higher-lying energy levels as a result of the recombination of the ions with slow electrons. The recombining electrons are usually cooled (slowed down sufficiently to permit recombination to proceed) via de-exciting collisions with other electrons and/or heavy bodies (our lasers, to be described later, use this method of electron cooling to cause the onset of recombination). The cooling of a plasma can, however, be enhanced by producing it in a small volume and then allowing it to expand into a larger volume [2]. When contolled expansion of the plasma (via the technique of plasma segmentation) is used to provide enhanced electron cooling, the term SPER (segmented-plasma-excitation recombination) is generally used to describe the laser [3]. An alternative charge-transfer mechanism for the creation of a population inversion in some so-called SPER lasers has, however, been proposed, casting some doubt as to whether they are true recombination lasers [4, 5, 6].

The recombination mechanism was first proposed in 1964 by Gudzenko and Shelepin as a possible excitation route for the production of stimulated emission in a hydrogen plasma [7]. In their paper, the authors considered the possibility of recombining protons and electrons producing a population inversion between atomic hydrogen levels, giving rise to radiation in the ultra-violet, visible and infra-red regions of the spectrum. Ten years later, Bohn showed, in theory, that recombination pumping offerred the potential for high gain in the VUV and XUV in hydrogen like species possessing charges in the range 2 to 8 [8]. The realisation of high small-signal gains in plasma recombination lasers is made possible because, under the right conditions, the excitation (produced over a broad spectrum of energies via electron ionization) is funneled to a single upper laser level, giving rise to good laser efficiencies of up to 0.15% in the case of the strontium recombination laser.

The utilization of plasma expansion and the subseqent electron cooling (which is generally believed to give rise to recombination pumping) in SPER lasers has resulted in the observation of stimulated emission at over seventy wavelengths [6, 9] from within the excited states of neutral and multiply charged metal vapours, with output powers ranging from milliwatts to watts [9, 10]. SPER lasers are capable of covering the spectrum from the infra-red (Ag^{+}), through the visible (Cd^{++}) and into the ultraviolet (In^{+++}) via isoelectronic scaling [9]. An interesing possiblility associated with the SPER laser is that of simultaneous generation at multiple frequencies (i. e., the production of a broad spectrum metal-vapour gas discharge laser). For example, a laser

could be produced which operates simultaneously in the blue, blue-green, green and yellow spectral regions through the use of metal segments of In, Zn, Cd and Sn [6].

Recombination-based population inversions can be produced in non-hydrogen like ions without the use of plasma expansion techniques by selecting those transitions which ocurr across the large gaps that are present in the spectra of many such ions (for example in Sr^+, Ca^+ and Ba^+) [11, 12]. Three-body recombination pumping leading to transitions between the energy levels of singly-ionised alkaline-earth metals appears, at present, to be the most promising with regard to producing recombination laser output at the multi-watt level, owing to their high gain.

Laser action in ionic strontium (Sr^+) metal vapour was first observed by Deech and Saunders [13] in 1968 on the infrared self-terminating transitions, $5p^2P^0_{3/2} \rightarrow 4d^2D_{5/2}$ and $5p^2P^0_{1/2} \rightarrow 4d^2D_{3/2}$ at 1.033 μm and 1.092 μm respectively. Note that these transitions were *not* produced via an electron-ion recombination scheme. The infrared Sr^+ laser pulse occurred at low helium or neon buffer gas pressures (3 torr), began on the leading edge of the discharge current pulse, 150 ns after its onset, and lasted for approximately 20 ns. The gain for these transitions was typically 300 dB m^{-1}.

In 1973 two new laser transitions were reported in a pulsed d.c. discharge struck through a mixture of strontium vapour and helium buffer gas [14]. These new transitions occurred in the violet region at

0.4162 μm and 0.4305 μm and, unlike in the case of Deech and Saunder's infrared Sr^+ laser, lasing took place after cessation of the discharge current pulse, in high pressures of helium buffer gas (35 torr). The gain for the 430.5 nm transition was approximately 30 dB m^{-1}. Lasing at 430.5 nm and 416.2 nm in a mixture of strontium and helium was attributed to a recombination mechanism in which the upper laser levels are pumped via the three-body recombination of doubly ionized strontium atoms with electrons to form Sr^+ in the discharge afterglow. Three-body recombination pumped lasing at 373.7 nm and 370.6 nm has also been reported in a high pressure mixture of calcium and helium [14]. The gains for these transitions (12 dB m^{-1} at 373.7 nm) were lower than the gains obtained from the strontium transitions, making the calcium based laser of less interest than the strontium based laser.

The recombination excitation mechanism proposed for the strontium and calcium systems was subsequently elucidated by Zhukov et al. in 1977 [15, 16]. Zhukov's work is described and discussed later, in Sections 1.3 to 1.7.

Strontium recombination lasers (SRLs) can be operated with either longitudinal or transverse discharges and the laser pulse can be characterised as 'short' or 'long', according to its duration [17]. The various types of strontium recombination laser and their operating characteristics are described and discussed in detail later in Sections 1.6 to 1.8.

Since the first reported observation of lasing at 430.5 nm, considerable interest has been concentrated on scaling strontium recombination lasers (and, to a lesser extent, calcium recombination lasers) to multi-watt average output powers. The highest average laser output power reported to date for an SRL is 3.9 W. This was achieved by Bukshpun et al. using a self-heated, water-cooled discharge tube of volume ~26 cm^3, at a record (for this system) pulse repetition frequency (PRF) of 29 kHz [18]. More typically, SRLs are capable of output powers in the range 300 mW - 3 W at PRFs of a few hundred Hz to several kHz (see Sections.1.6 to 1.8 and Chapter 4) [19].

This thesis will be concerned with the design and operation of longitudinally excited strontium recombination lasers operating in the 'short-pulse' mode. Particular attention will be focussed on the thermal management of the laser tubes, since this is crucial to obtaining high output powers (> 1W) from the laser system of interest (see Chapters 2, 3 and 4).

1.2 Applications of the strontium and calcium recombination lasers

Owing to the high peak output powers (~ kW) and the high average output powers (1 - 4 W) available from multi-kilohertz strontium and calcium recombiation lasers, these lasers are potentially an important source of violet/utra-violet radiation, with many applications. Several of the potential and currently realised applications of SRLs and CRLs are reviewed below.

The high pulse repetition frequencies of metal vapour lasers (> 15 kHz) make them attractive sources for use in laser projectors for large screen entertainment. In particular, the strontium recombination laser could be used to produce the blue component, if average output powers in the 5 - 10 W range could be achieved. The red and green components could be generated by the gold (628.3 nm) and copper (510.6 nm) vapour lasers respectively.

The strontium vapour laser's long pulse width of > 200 ns makes it an attractive alternative to traditional pump sources such as the nitrogen and copper vapour lasers with regard to the pumping of narrow linewidth pulsed dye lasers. The longer pulse width of the SRL enables high quality output from the dye, with monochromacy approaching that of CW-dye lasers. A practical dye laser pumped using the 430.5 nm output from an SRL is described in Reference [20]. The dye used was Coumarin 7 (with an absorption maximum at 442 nm) and resulted in an average output power of 15 mW at 524 nm with tunability in the range 499 - 557 nm.

The pumping of other lasers is also possible using the SRL and the CRL. For example, the 373.7 nm line emitted by the calcium recombination laser has been used to pump the 377.6 nm resonance line of thallium vapour mixed with He [21]. This has led to an average output power of 8 mW at a wavelength of 535 nm with PRFs in the range 5 to 6 kHz. The conversion efficiency was ~30 %. The strontium recombination laser has been used to pump an optical resonator containing dimer molecules of tellurium vapour [22]. This pumping scheme led to laser output at 14 wavelengths (between 623.9 and 663.3 nm) which extended down to the red-yellow region, the most intense of which occurred at 642, 641.66, 631.95, 632.46, and 624.45 nm. The ability to tune the frequency of the SRL [23] is of importancce in the pumping of dimers as it allows fine tuning onto the dimer's rotational lines.

The use of non-linear optics would appear to be a feasible means by which wavelength conversion of the 430.5 nm SRL transition could be achieved [24]. For example, a BBO crystal would be appropriate for second harmonic generation of the SRL output as the crystal remains transparent at 215 nm [25]

Other potentially important applications of the SRL include, phototherapy, the treatment of neonatal jaundice [26] and other disorders involving the blood (i. e., cancers) [27].

1.3 The three-body recombination process

In a dense plasma, three-body recombination of ionic species, X^{Z+}, proceeds via elastic collisions with slow electrons:

$$X^{Z+} + e^-_{slow} + e^-_{slow} \rightarrow X^{(Z-1)+*} + e^-_{fast}.$$

The second electron helps to conserve momentum during the interaction and carries away the energy liberated during the recombination process.

The rate of three-body recombination of multiply-charged ions with electrons is governed by the equation [15]:

$$\frac{d}{dt} N_{ion} = -\alpha n_e^2 N_{ion}, \qquad [1.3.1]$$

where N_{ion} is the ion concentration, n_e is the electron density and α is the recombination coefficient. When the source of ionization is removed, the decay of the ion density proceeds exponentially,

$$N_{ion}(t) = N_{ion}(0)\exp(-\alpha n_e^2 t), \qquad [1.3.2]$$

with a characteristic (recombination) time constant, τ_r, given by:

$$\tau_r = (\alpha n_e^2). \qquad [1.3.3]$$

The three-body recombination coefficient, α, is given by [15]:

$$\alpha = 1.8\text{x}10^{-8} Z^3 \ln(Z^2+1)^{0.5} T_e^{-4.5}, \qquad [1.3.4]$$

where Z is the ionic charge and T_e is the electron temperature. It follows that rapid recombination arises when the electron temperature is low, the ionic charge is high and the plasma density is high (the requirement for overall charge neutrality is met by $n_e \cong ZN_{ion}$). It should be noted that the electron density and electron temperature in the afterglow of a current pulse are related through recombination heating. A high plasma density ensures a high rate of recombination, which heats the secondary electrons involved in the recombination process. A high plasma density is obtained by ensuring that the peak electric current density is sufficiently high. This electric current must terminate, without ringing, in a time shorter than the characteristic recombination time if the fastest recombination of electrons and ions is to be achieved, i.e. the dependence given by Equation 1.3.2 is followed.

1.4 Conditions for achieving a population inversion in a recombining plasma

The probability per second, $A_{2\to1}$, that a radiative transition will occur between two energy levels 2 (upper) and 1 (lower), separated in energy by $\Delta E_{2\to1}$, is given by [28]:

$$A_{2\to1} = f_{12}\left(\frac{g_1}{g_2}\right)\frac{8\pi e^2 \Delta E^2{}_{2\to1}}{m_e h^2 c^3}, \qquad [1.4.1]$$

where f_{12} is the oscillator strength for the absorption transition, g_1 and g_2 are the statistical weights of the participating levels, e is the electron charge and m_e, its mass, h is Planck's constant and c is the speed of light. Optical transitions are therefore more likely to occur as the energy separation between the participating levels *increases*.

The transition rate for electron-atom collisional de-excitation from an upper level, 2, to a lower level, 1, $F_{2\to1}$, depends on the energy difference between the levels and the electron temperature and is governed by the equation [15]:

$$F_{2\to1} \propto f_{12}\left(\frac{g_1}{g_2}\right)\left(\Delta E_{2\to1} T_e^{\,0.5}\right)^{-1}, \qquad [1.4.2]$$

provided that $\Delta E_{2\to1} \gg kT_e$. Collisional de-excitation is therefore more likely to occur as the energy separation between the participating levels *decreases*. Using the principle of detailed balance, the rate of collisional excitation, $F_{1\to2}$, can be calculated from Equation 1.4.2 to be [15]:

$$F_{1\to2} \propto f_{12}\left(\Delta E_{2\to1} T_e^{\,0.5}\right)^{-1} \exp\left(\frac{-\Delta E_{2\to1}}{kT_e}\right). \qquad [1.4.3]$$

From Equations 1.4.2 and 1.4.3, the ratio of the collisional de-excitation rate to the collisional excitation rate is

$$\frac{F_{2\to1}}{F_{1\to2}} \propto \left(\frac{g_1}{g_2}\right)\exp\left(\frac{\Delta E_{2\to1}}{kT_e}\right), \qquad [1.4.4]$$

so that, if the condition

$$\left(\frac{\Delta E_{2\to 1}}{kT_e}\right) > 1, \qquad [1.4.5]$$

is satisfied (i.e. the electron temperature is low), the rate of collisional de-excitation between two energy levels can exceed the rate of collisional excitation.

Between closely spaced energy levels, collisional transitions dominate over radiative transitions and the population will therefore cascade downwards, through the excited states, when the electron temperature falls below the equilibrium value.

If the population distribution within a group of levels is governed by collisional transitions, rather than radiative transitions, the population of the levels can be assumed to follow a Maxwell-Boltzmann distribution at the electron temperature, T_e. Suppose a system consists of two *widely spaced groups*, each group being composed of a number of *closely spaced energy levels*, as depicted in Figure 1.1, then if E_j represents the energies associated with the levels which make up the upper group, 2, the population of these upper levels will be:

$$N_j = \frac{N_2 g_j \exp\left(-\Delta E_j / kT_e\right)}{\sum_j g_j \exp\left(-\Delta E_j / kT_e\right)}, \qquad [1.4.6]$$

where N_2 is the total population in the upper group of levels, and ΔE_j is the energy difference between the *j*th level of the upper group and the lowest level in the *same* group.

Zhukov et al. considered quasi-steady-state conditions, where the total pump rate to the levels in the upper group, W_2, from higher-lying groups, must be equal to the total de-excitation rate of the upper group (group 2) levels to the levels which collectively form the lower group (group 1). The de-excitation can proceed via radiative energy exchange or collisional energy exchange, so that the pump rate, W_2, is given by:

$$W_2 = \sum_j \left[N_j \left(A_{j\to 1} + n_e F_{j\to 1} \right) \right], \qquad [1.4.7]$$

where $A_{j\to 1}$ is the probability per second of optical transitions taking place between the *j*th level of the *upper* group, 2, and the levels of the *lower* group, 1, and $n_e F_{j\to 1}$ is the probability per second of electron-collisional transitions between the *j*th level of the *upper* group, 2, and the levels of the *lower* group, 1. Note that depopulation by excitation is not considered here and, because the energy difference between the lower and upper *groups* is large (radiative transitions dominate), the relative distribution between the *groups* will *not* be Maxwellian (until very high values of electron density are reached). From Equations 1.4.5,

1.4.6 and 1.4.7, the pump rate to the upper group of levels becomes:

$$W_2 = \sum_j \left[\frac{N_2 g_j \exp\left(-\Delta E_j / kT_e\right)}{\sum_j g_j \exp\left(-\Delta E_j / kT_e\right)} \left(A_{j\to 1} + n_e F_{j\to 1}\right) \right], \quad [1.4.8]$$

which simplifies to:

$$W_2 = \frac{N_2 \sum_j \left[g_j \left(A_{j\to 1} + n_e F_{j\to 1}\right) \exp\left(-\Delta E_j / kT_e\right) \right]}{\sum_j g_j \exp\left(-\Delta E_j / kT_e\right)}. \quad [1.4.9]$$

However, from Equations 1.4.5 and 1.4.6,

$$\frac{N_2}{\sum_j g_j \exp\left(-\Delta E_j / kT_e\right)} = \frac{N_j}{g_j \exp\left(-\Delta E_j / kT_e\right)}, \quad [1.4.10]$$

so that Equation 1.4.9 can be rewritten as:

$$N_j = \frac{W_2 g_j \exp\left(-\Delta E_j / kT_e\right)}{\sum_j \left[g_j \left(A_{j\to 1} + n_e F_{j\to 1}\right) \exp\left(-\Delta E_j / kT_e\right) \right]}. \quad [1.4.11]$$

Similarly, the population of the *i*th level in the *lower* group is given by:

$$N_i = \frac{W_1 g_i \exp\left(-\Delta E_i / kT_e\right)}{\sum_i \left[g_i \left(A_{i\to 0} + n_e F_{i\to 0}\right) \exp\left(-\Delta E_i / kT_e\right)\right]}, \qquad [1.4.12]$$

where the subscript $i \to 0$ is used to represent transitions from the *i*th level of the lower group, 1, to the ground state level, 0. Here the total pump rate, W_1, to the levels that collectively form the lower group, is composed of the pump rates from the next highest group (group 2) and higher-lying groups.

In order for a population inversion to exist, it is necessary, by definition, for the population in *one* of the upper group's levels to *exceed* the population in *one* of the lower group's levels. Hence, for a population inversion, the inequality

$$\frac{g_i N_j}{g_j N_i} > 1 \qquad [1.4.13]$$

must be satisfied, where the subscripts *j* and *i* denote *any* of the upper group and lower group levels respectively. Using Equations 1.4.11 and 1.4.12, the criterion for population inversion (Inequality 1.4.13) can be rewritten as:

$$\frac{W_2}{W_1} F \exp\left(\frac{\Delta E_i - \Delta E_j}{kT_e}\right) > 1, \qquad [1.4.14]$$

where F represents the factor by which the probability of the decay of the lower group levels is greater than the probability of decay of the upper group levels, i. e.,

$$F = \frac{\sum_i \left[g_i \left(A_{i\to 0} + n_e F_{i\to 0} \right) \exp\left(\frac{-\Delta E_i}{kT_e} \right) \right]}{\sum_i \left[g_j \left(A_{j\to 1} + n_e F_{j\to 1} \right) \exp\left(\frac{-\Delta E_j}{kT_e} \right) \right]}. \qquad [1.4.15]$$

Equation 1.4.14 can be rearranged to give the condition for population inversion as:

$$F > \frac{W_1}{W_2} \exp\left(\frac{\Delta E_j - \Delta E_i}{kT_e} \right). \qquad [1.4.16]$$

Zhukov et al. went on to consider the case in which the levels within a group are so close together ($\lim \Delta E_{i,j} \to 0$), compared to the spacing between the groups, that the two groups can be treated as two discrete levels. In this case, using Equations 1.4.15 and 1.4.16, the condition for population inversion becomes:

$$\frac{g_1 \left(A_{1\to 0} + n_e F_{1\to 0} \right)}{g_2 \left(A_{2\to 1} + n_e F_{2\to 1} \right)} > \frac{W_1}{W_2}. \qquad [1.4.17]$$

We consider two plasma regimes of importance, viz: low electron density and high electron density. For low electron densities, a population inversion can be established through optical transitions between levels, provided that $A_{1\to 0} > A_{2\to 1}$. This will in general be true if

the separation between the upper and lower levels is small compared to that between the lower level and ground level (Figure 1.2A). If, on the other hand, the electron density is high, as it is required to be for high rates of recombination, collisional processes will be dominant. Hence, for the energy level distribution shown in Figure 1.2A, where $n_e F_{2\to 1} > n_e F_{1\to 0}$, a high electron density will serve to destroy the population inversion. This distribution of energy levels is therefore unlikely to give rise to high gain and output powers if pumped by recombination.

If the electron density is high and the separation between the upper and lower laser levels is larger than that between the lower level and ground level (Figure 1.2B), rapid recombination can proceed and a population inversion which is determined by collisional de-excitation can be established, provided that collisional processes dominate over radiative decay. Then, if $\Delta E_{2\to 1} > \Delta E_{1\to 0}$ and $n_e F_{1\to 0} > n_e F_{2\to 1}$, the condition for a collisional de-excitation dominated population inversion, which can be written as

$$\frac{g_1 n_e F_{1\to 0}}{g_2 n_e F_{2\to 1}} > \frac{W_1}{W_2}, \qquad [1.4.18]$$

can be satisfied, assuming that $W_1 \approx W_2$, which is usually true under conditions of recombination non-equilibrium. Note that, if the electron temperature is too high for the condition $\Delta E_{1\to 0} > kT_e$ to be satisfied, the lower laser level can be collisionally populated, rather than cleared, and the population inversion will therefore be reduced. Consequently, it is undesirable for the lower laser level to be too close to the ground level.

Finally, Zhukov et al. considered the situation where the zeroth level is the ground state of a singly charged ion so that it is long lived (the recombination of singly charged ions is approximately 18 times slower than that of doubly charged ions) and densely populated. If the electron density is sufficiently high to ensure that transitions are predominantly due to electron impact then, from Equation 1.4.7, the population of the upper level is given by:

$$N_2 = \frac{W_2}{n_e F_{2\to 1}}. \qquad [1.4.19]$$

The population of the lower level (level 1) is determined by the pump rate from above, collisional excitation from the ground level and collisional de-excitation to the ground level. Hence, we have

$$W_1 + n_e N_0 F_{0\to 1} = n_e N_1 F_{1\to 0}, \qquad [1.4.20]$$

so that the population of the lower level can be written as:

$$N_1 = \frac{W_1 + n_e N_0 F_{0\to 1}}{n_e F_{1\to 0}}. \qquad [1.4.21]$$

Assuming that the pump energy reaching the upper level is transferred completely to the lower and ground levels, so that $W_1 = W_2 = W$, the condition for population inversion (Inequality 1.4.13) can be written as

$$\frac{g_2\left(W + n_e N_0 F_{0\to 1}\right) F_{2\to 1}}{g_1 W F_{1\to 0}} < 1, \qquad [1.4.22]$$

which becomes

$$\frac{g_2}{g_1}\frac{F_{2\to1}}{F_{1\to0}} + \frac{g_2}{g_1}\frac{n_e N_0 F_{0\to1} F_{2\to1}}{W F_{1\to0}} < 1. \qquad [1.4.23]$$

However, from Equations 1.4.2 and 1.4.3,

$$\frac{F_{0\to1}}{F_{1\to0}} = \mathrm{C}_1\left(\frac{g_1}{g_0}\right)\exp\left(\frac{-\Delta E_{1\to0}}{kT_e}\right) \qquad [1.4.24]$$

where C_1 is a constant. Equation 1.4.23 therefore becomes:

$$\frac{g_2}{g_1}\frac{F_{2\to1}}{F_{1\to0}} + \frac{g_2}{g_0}\mathrm{C}_1\frac{n_e N_0 F_{2\to1}}{W}\exp\left(\frac{-\Delta E_{1\to0}}{kT_e}\right) < 1. \qquad [1.4.25]$$

Substituting for $F_{2\to1}$, $F_{1\to0}$ and W, using Equations 1.4.2, 1.3.1 and 1.3.4, leads to the inequality

$$\mathrm{C}_2 + \mathrm{C}_3\frac{g_1}{g_0}\frac{n_e N_0}{\Delta E_{2\to1} {T_e}^{0.5}}\frac{{T_e}^{4.5}}{{n_e}^2 N_{\mathrm{ion}}}\exp\left(\frac{-\Delta E_{1\to0}}{kT_e}\right) < 1, \qquad [1.4.26]$$

which, since $N_{\mathrm{ion}} \equiv N^{++}$ and $N_0 \equiv N^{+}$, reduces to:

$$\mathrm{C}_2 + \mathrm{C}_4\frac{{T_e}^4}{n_e N^{++}} N^{+}\exp\left(\frac{-\Delta E_{1\to0}}{kT_e}\right) < 1. \qquad [1.4.27]$$

A population inversion, produced via the recombination mechanism, is therefore extremely sensitive to the electron temperature. If the lower level lies too close to the ground state, or the electron temperature is too

high, the lower level will be repopulated as a result of collisions between electrons and the ground level and the population inversion will diminish.

As a result of their work, Zhukov et al. were able to summarize the general requirements for the energy level distribution which supports a population inversion under conditions of collisional recombination as:-

1. The upper laser level should be one of the lowest in the higher group of closely spaced levels.

2. The lower laser level should be one of the highest in the lower group of closely spaced levels.

3. Transitions between levels within each group should be allowed.

4. The electron density should be sufficiently high to ensure that the probability of collisional transitions within groups exceeds the probability of optical transitions.

5. The electron temperature should be as low as possible.

As an aside to Requirement 4, note that a Boltzmann distribution will be established between the groups of excited levels and the ground state if the electron density is sufficiently high. It follows that there is a limit to the specific output power which can be extracted from a recombination laser. There will, however, be a threshold electron

density, below which the population will not invert as a result of radiative transitions dominating over collisional processes. These points demonstrate that the current density in a recombination laser is critical. If it is too high, or too low, laser output will be poor, or non-existent.

1.5 The evolution of the electron and gas temperatures during the creation and relaxation of a plasma

In the preceding Sections (1.3 and 1.4) we have seen that the electron temperature needs to be low to ensure strong recombination pumping of the upper laser level and a healthy population inversion. It is therefore interesting to follow the evolution of the electron temperature during the course of a current pulse and throughout the afterglow period of the discharge. Ignoring minor terms (i.e., plasma reheating due to incomplete termination of the applied field), the electron energy in an inert buffer gas will follow the rate equation:

$$\frac{\mathrm{d}}{\mathrm{d}t}\left(1.5kT_e n_e\right) = \sigma E^2 - 1.5\delta_{jk}\nu_{jk}k\left(T_e - T_g\right)n_e + \Delta E_r \alpha n_e{}^3 + E_m\left\langle\sigma\upsilon_e\right\rangle N_m n_e, \qquad [1.5.1]$$

where σ is the discharge medium's electrical conductivity, $\boldsymbol{E}$ is the electric field, E_m is the energy of metastable atoms, $\langle\sigma\upsilon_e\rangle$ is the rate of quenching of the metastable atoms by electrons, N_m is the concentration of metastable atoms, ΔE_r is the energy evolved during ion-electron recombination and T_g is the buffer gas temperature. The quantity $\delta_{jk}\,\nu_{jk}$ contained in the second term of Equation 1.5.1 is itself composed of two

terms:

$$\delta_{jk}\nu_{jk} = \delta_{ea}\nu_{ea} + \delta_{ei}\nu_{ei}. \qquad [1.5.2]$$

Here, the first term represents the collisional transfer of energy from the electrons, of mass M_e, to a concentration N_a of buffer gas *atoms*, of mass M_a, and is given by [16]:

$$\delta_{ea}\nu_{ea} = \frac{2M_e}{M_a}\sigma_{ea}N_a\left(\frac{8kT_e}{\pi M_e}\right)^{0.5}. \qquad [1.5.3]$$

The second term represents the collisional transfer of energy from the electrons to buffer gas *ions*, this being given by [16]:

$$\delta_{ei}\nu_{ei} = \frac{4e^4 N_i}{3(kT_e)^{1.5}}\frac{(2\pi M_e)^{0.5}}{M_i}\ln(Z^2+1)^{0.5}. \qquad [1.5.4]$$

Equation 1.5.1 cannot be solved analytically because of the complicated manner in which its right hand side depends on the electron temperature. Some simple conclusions can, however, be drawn, by inspecting Equations 1.5,1, 1.5.3 and 1.5.4.

Firstly, from consideration of Equation 1.5.1, it is apparent that the electron temperature will fall rapidly as the applied field reaches zero, whereupon the first term on the right hand side becomes zero. Immediately following removal of the field, the electron temperature will be very high (~80 kK [29]) and high-lying states will be strongly populated. At high T_e, the third (recombination will be negligible) and

fourth terms in Equation 1.5.1 will be unimportant, so that the second term in Equation 1.5.1 will dominate. This, second, term represents cooling of the electrons in the discharge afterglow via superelastic collisions with the buffer gas atoms and ions. It is clear that the electron temperature will fall towards the buffer gas temperature, but cannot drop below it. Hence, in order to attain the low afterglow electron temperature necessary for strong recombination pumping, the average buffer gas temperature should be kept as low as possible.

Equation 1.5.3 reveals that the electron cooling as a result of collisions with buffer gas *atoms* will be most effective when the mass of the atoms, M_a, is low, their concentration, N_a, high and the electron temperature high. We therefore require a light buffer gas and high operating pressures in order to obtain a rapid initial fall in electron temperature.

As the electron temperature falls, electron cooling as a result of electron-ion collisions begins to take over from electron-atom cooling, as seen from Equation 1.5.4. If helium is used as the buffer gas at a pressure of 10 torr, Zhukov et al. estimate that electron-ion collisions take over from electron-atom collisions as the dominant electron cooling process when the electron temperature has fallen to below 3000 K [16].

When the electron temperature has fallen sufficiently to permit recombination, the third term in Equation 1.5.1 becomes important. This term describes the *reheating* of the plasma electrons in the late afterglow as a result of electron-ion recombination. The more rapidly the

recombination proceeds, the more pronounced the plasma reheating will be. Recombination-heating therefore acts in such a manner as to regulate the recombination rate. Further, if the recombination rate of species is too high (i.e. there are too many ions in the discharge for the buffer gas to supply adequate cooling), the electron temperature will actually rise as a result of recombination heating. This will quench the recombination and prematurely terminate the population inversion. The fourth term in Equation 1.5.1, which represents plasma reheating due to super-elastic collisions with helium metastables, also becomes inportant in the late discharge afterglow. Hence, after an initially rapid decrease in the electron temperature, which follows removal of the applied field, to a point where recombination sets in, the electron temperature then settles into a lower rate of decline, due to plasma reheating [16, 29].

The fractional ionization of the buffer gas is low during the excitation pulse so that a small fraction of the input pulse energy is consumed in heating the buffer gas during excitation, raising its temperature [29]. This fractional increase in the buffer gas temperature during the current pulse is typically much lower than that of the electron temperature [29]. There is, additionally, a net transfer of energy to the buffer gas, from the plasma electrons, during the afterglow (due to elastic collisions between the electrons and buffer gas species), which raises the buffer gas temperature. The energy transferred to the buffer gas is ultimately removed by conduction through the container walls so that, in a high repetition rate system, the buffer gas temperature can be treated as one in approximate steady-state and an *average* gas temperature can be ascribed (see Chapter 3).

1.6 Strontium as the lasant in a recombination non-equilibrium laser

We have seen that non-equilibrium conditions are necessary to obtain a population inversion in a recombining plasma. The recombination non-equilibrium regime is characterized by the ion temperature, T_i, being *above* the equilibrium value at the electron temperature, T_e, so that a Boltzmann distribution cannot be established between the upper and lower laser levels. This generally occurs in the early afterglow of a pulsed electrical discharge, just as the current pulse ends, where the plasma density is high and the electron temperature is falling rapidly ($T_e < 4000$ K [29]). In contrast, the ionization non-equilibrium regime, during which cyclic systems such as copper-vapour and barium-vapour lasers oscillate, is characterized by the ion temperature, T_i, being *below* the equilibrium value at the electron temperature, T_e. An advantage of the recombination non-equilibrium regime over the ionization non-equilibrium regime is that, in the case of the former, the upper laser level is populated from above, rather than from below as in the latter case. Stray pumping of the lower laser level is therefore *less* likely to occur in recombination lasers than in ionization non-equilibrium (cyclic) lasers. Consequently, we can expect to obtain more efficient pumping of the upper laser level in recombination lasers than in cyclic lasers.

Zhukov et al. have shown that the energy level distribution of an ion needs to meet certain requirements (Section 1.4) in order for the population to be inverted as a result of recombination pumping. Latush

and Sem investigated several metals [14] to see if laser action could be observed on their ionic transitions. One of the most promising metals investigated to date is strontium. The partial energy level diagram for this system is shown in Figure 1.3. It can be seen, in this figure, that the $6^2S_{1/2}$ level is the lowest in a group of closely spaced levels, while the $5^2P_{1/2,3/2}$ doublet levels are the highest in the lower group of closely spaced levels. The separation between the $5^2P_{1/2,3/2}$ levels and the $4^2D_{3/2,5/2}$ metastable levels is small compared to that between the $6^2S_{1/2}$ and $5^2P_{1/2,3/2}$ levels. There appears to be a good correlation between the strontium ion level structure and Zhukov et al.'s criteria for recombination based creation of a population inversion. It follows that the 430.5 nm and 416.2 nm transitions are ideally located for recombination lasing to occur on these lines. Recombination lasing at 430.5 and 416.2 nm in a mixture of strontium and helium was first reported in 1973 by Latush and Sem [14]. Table 1.1 lists the spectral lines for the strontium system. This table, produced using the Massachusetts Institute of Technology Wavelength Tables, must be used with care. There appear to be some discrepancies over the origins of the lines, i.e., the *430 nm* line is listed as originating in the *Sr I* excited state levels rather than in the *Sr II* levels [29].

The $5^2P_{1/2,3/2}$ lower laser levels are radiatively cleared to the $4^2D_{3/2,5/2}$ metastable levels. These transitions give rise to the cyclic, (ionization non-equilibrium) infrared laser action at 1032.7 nm and 1091.4 nm, first reported by Deech and Saunders [13] in 1968. Stimulated emission can often be observed on both the violet and infrared lines with the same excitation pulse, so that stray pumping of

the lower recombination laser levels is often reduced through radiative decay by stimulated emission during the current pulse.

The Sr^+ metastable levels are collisionally cleared to the Sr^+ ground state, during the discharge afterglow [30], while the Sr^+ ground level is cleared to the strontium atom levels via three-body recombination. Because the recombination of singly ionized strontium is approximately 18 times slower than that of doubly ionized strontium, Tarte [30] believes that a de-excitation 'bottle-necking' occurs at the Sr^+ metastable levels (to which the lower laser levels clear). This places an upper limit on the duration of the population inversion in a conventional SRL. Tarte has suggested that greater laser output powers may be achievable through the introduction of 'impurities' (into the discharge) which enhance deactivation of the Sr^+ ground level (by, for example, collisional processes). This approach would be complicated because impurities have a tendency to lower the electron density produced during the discharge and to react with the strontium itself. In addition, any impurity which is introduced must not have a detrimental effect on the rate of electron cooling in the discharge afterglow. Zhukov et al. suggest that increasing the pulse repetition rate, so that Sr^+ is given insufficient time in which to recombine, will lead to an increase in laser efficiency [16], since Sr^{++} ions will then be produced by excitation from the Sr^+ ground state rather than from atomic levels. This would require the laser to be operated with inter-pulse periods shorter than the characteristic recombination time of Sr^+ ($< 20\mu s$). The operation of SRLs at PRFs higher than 5 kHz is complicated by thermal loading and gas temperature considerations (see Chapters 2 to 4).

1.7 Buffer gas requirements in the strontium recombination laser

The population inversion mechanism in recombination lasers is very sensitive to the electron temperature, which must be made as low as possible to achieve the strongest recombination pumping. The electrons must therefore be cooled as quickly as possible, on cessation of the current pulse. The principal process, governing the rate of electron cooling, is inelastic collisions between the electrons and buffer gas species. The fraction of energy transferred from the electrons to the buffer gas, during their interaction, must therefore be as high as possible, as should also be the collision frequency. A light buffer gas at high pressures is therefore required for good cooling (Equation 1.5.3).

In addition to being light, the buffer gas atoms must also possess a high ionization potential, compared to that of strontium. This ensures that the metal atoms are ionized preferentially to the buffer gas. Hydrogen is the lightest gas. However, its ionization energy of 13.6 eV is insufficiently high to ensure efficient Sr^{++} creation. Helium, the next lightest gas, has a first ionization energy of 24.6 eV, much higher than that of strontium or Sr^{+}:

$$Sr + 5.7eV \rightarrow Sr^{+} + e^{-},$$
$$Sr^{+} + 11eV \rightarrow Sr^{2+} + e^{-},$$
$$Sr + 16.7eV \rightarrow Sr^{2+} + 2e^{-}.$$

Helium is therefore the usual choice as buffer gas in the strontium recombination laser.

1.8 Modes of operation in the strontium recombination laser system

In order to produce the ions required for recombination to pump the upper laser levels, it is first necessary to vaporize the strontium. This has, to date, been accomplished in one of three ways. In *self-heated* lasers, an electrical current is passed over pieces of strontium which are placed at regular intervals along the discharge tube wall [31]. The discharge heats the tube walls, thereby vaporizing the strontium. An electrical discharge is used in most SRLs to produce the metal ions from its vapour. In *externally-heated* lasers, an oven is used to produce the required strontium vapour density. The oven is generally placed around a discharge tube which contains the strontium pieces, so that the vapour is generated within the laser tube [32]. An interesting hybrid of self and externally-heated laser schemes is the technique which involves producing the strontium vapour in an oven, outside the discharge tube, entraining it in helium buffer gas and pumping the gas mixture inside the self-heated discharge tube [19]. Here, the discharge tube wall must be maintained at a sufficiently high temperature to ensure that there is no re-condensation of the strontium vapour on entering the tube. An advantage of externally-heated devices over self-heated devices is that, in the case of the former, the experimenter has more independent control over the strontium vapour pressure and discharge conditions. It is necessary, for both types of vapour production, to ensure that the discharge does not overheat the laser tube. In the case of self-heated lasers, the discharge tube dimensions and method of cooling determine the power which must be put into it (see Chapter 3) in order to obtain the correct wall temperature for the strontium vapour density required.

Recently a self-heated SRL was reported in which both the strontium vapour and strontium ions were produced using a microwave discharge [33]. Laser oscillation has been demonstrated to be feasible using microwave pumping, but average output powers are low at present (i.e., the lasing is at threshold).

SRLs can be classified according to the way the electric field is oriented with respect to the optical axis of the laser. In a *longitudinal discharge* laser, electrodes are placed at the ends of the discharge tube so that the electrical current passes down the length of the tube, parallel to the optical axis [26]. A *transverse discharge* laser is one in which multiple pairs of electrodes are placed along the length of the discharge tube so that discharges are struck perpendicular to the optical axis [34]. Transverse discharge SRLs are operated at higher buffer gas pressures (to obtain matching of the laser tube to the excitation circuit) and electric fields, so that current densities tend to be higher than in longitudinal discharge SRLs [35]. Consequently, the pulse energy densities are higher in transverse discharge SRLs than in longitudinal discharge SRLs. Brandt, however, has pointed out that the operation of transverse devices at multi-kHz pulse repetition frequencies is difficult [36], possibly because of severe, non-uniform gas temperature gradients. On the other hand, narrow-bore (~1 cm) longitudinally excited SRLs are readily operated in the multi-kHz regime [37]. Figure 1.4 shows a 'family tree' for the strontium recombination laser, summarizing the most commonly used types.

The strontium recombination laser oscillates at the two wavelengths, 430.5 and 416.2 nm. Under typical operating conditions, the 430.5 nm transition is the dominant source of laser output power. This is believed to be due to competition at the common upper laser level [16], with the 430.5 nm transition dominating, though collisional coupling between the lower laser levels may also contribute to the latter's dominance [30]. Oscillation at 416.2 nm can be selected by inserting a prism into the laser cavity. This acts to suppress the stimulated emission at 430.5 nm by refracting its amplified spontaneous emission out of the cavity, whilst retaining cavity alignment for the 416.2 nm radiation [16, 30]. Laser action at 416.2 nm is generally considered to be of less interest than lasing on the 430.5 nm line. This is because the output power at the shorter wavelength is significantly lower than that which can be obtained at 430.5 nm [16, 30].

Two distinct temporal 'modes' of operation are possible in the SRL. These are: the 'short pulse mode' and the 'long pulse mode' [18]. The long (laser) pulse begins ~1 μs after cessation of the discharge current pulse and lasts for ~1 - 2 μs. In contrast, the short pulse occurs immediately on cessation of the current pulse and lasts for up to 1 μs. Optimization of a particular mode requires the use of quite different operating conditions [17]. The long laser pulse, which gives high output energies (250 μJ) at low peak powers (250 W), occurs for strontium vapour pressures in the range 0.2 - 0.4 torr (laser tube operating temperature, 660 - 670°C) and peak current densities of approximately 450 A cm^{-2}. The short pulse mode, delivering lower output energies (180 μJ) at higher peak powers (1 kW), optimizes at lower strontium

vapour pressures and peak current densities, these being 0.03 - 0.06 torr (operating temperature, 590 - 600°C) and 260 A cm^{-2} respectively. The two pulse modes are attributed to different strontium ion production processes. Since the short-pulse occurs directly on termination of the discharge pulse, it is believed to be due to the stepwise and direct production of Sr^{++} during the discharge:

$$Sr + e^- \rightarrow Sr^+ + 2e^-,$$
$$Sr^+ + e^- \rightarrow Sr^{2+} + 2e^-,$$
$$Sr + e^- \rightarrow Sr^{2+} + 3e^-.$$

Because the long pulse is delayed with respect to the short pulse, the ions giving rise to it are believed to be created later, in the discharge afterglow, by charge transfer collisions between heavy bodies [24]

$$Sr + He^+ \rightarrow Sr^{2+} + He + e^-,$$
$$Sr + He_2^+ \rightarrow Sr^{2+} + 2He + e^-.$$

Strontium recombination lasers are usually optimized for operation in the short pulse mode, owing to the higher peak powers which can be developed in this case, at elevated pulse recurrence frequencies.

1.9 Summary

The energy levels of singly ionized strontium are particularly suitable for the creation of a population inversion under recombination non-equilibrium conditions, provided that the electron density is sufficiently high ($n_e > 10^{14}$ cm^{-3} [16]). Suitable conditions are usually found in the immediate afterglow of a high current density (> 200 A cm^{-3}) pulsed electrical discharge.

Strontium vapour is produced by heating the metal to approximately 600°C. The strontium vapour number density is then of the order 3 x 10^{14} cm^{-3} [29]. Doubly charged strontium ions are obtained during the current pulse through direct and stepwise electron impact processes. On termination of the current pulse, the electrons cool rapidly, via collisions of the second kind with helium atoms and ions, to a temperature in the range 3000 - 5000 K. Here, rapid three-body recombination sets in and high-lying Sr^+ states become populated from relaxing higher states. The high-lying Sr^+ levels are closely spaced so that the population fluxes downwards, via collisions with super-cooled electrons, to the upper laser level, which is the lowest in the group of high-lying levels. A relatively large energy gap between the upper and lower laser levels, the latter of which is the highest in a group of closely spaced levels, prevents the establishment of a Boltzmann distribution between the populations of these levels, while allowing the lower laser level to be collisionally cleared. A population inversion is therefore set up between the upper and lower laser levels, which gives rise to laser oscillation primarily at 430.5 nm.

1.10 Figures for Chapter 1

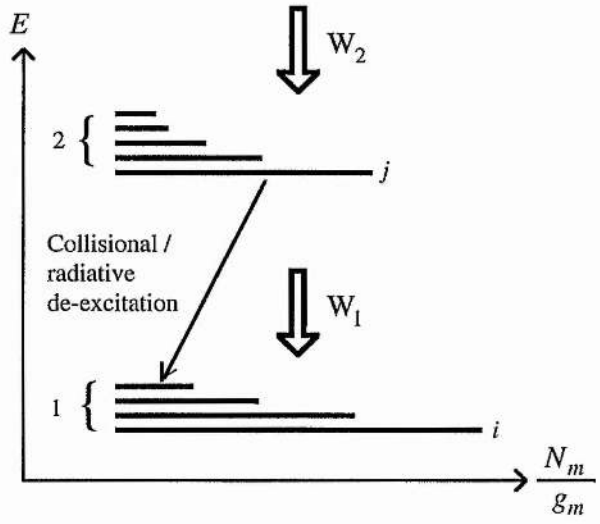

Figure 1.1 **Twin group energy level scheme explored by Zhukov et al. [3].**

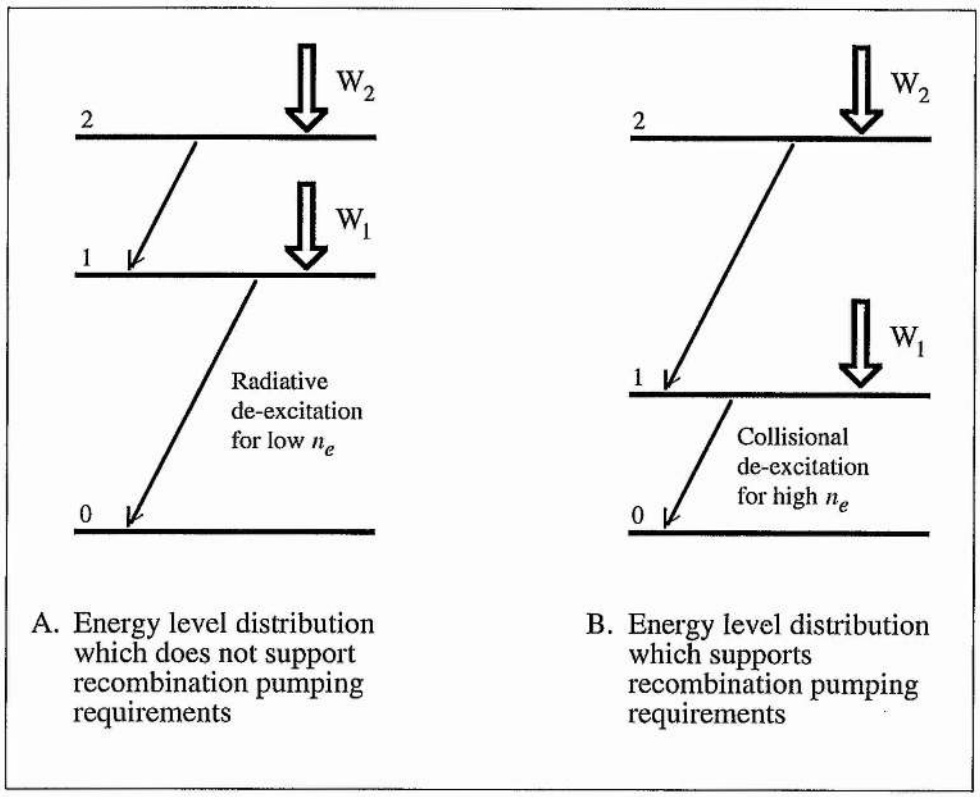

Figure 1.2 Possible energy level distributions considered by Zhukov et al. [3].

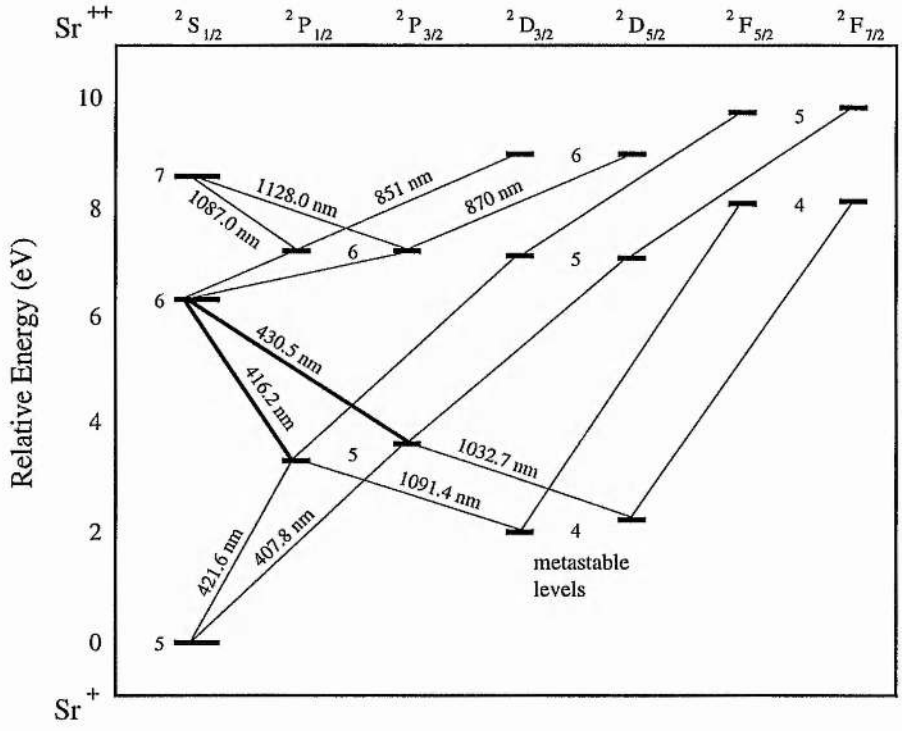

Figure 1.3 Partial energy level diagram for ionic strontium.

3366.333	Sr II	100	*4077.714*	Sr II	400r	4876.06	Sr I	6
3371.00	Sr	2	4080.1	bh Sr	2	4876.325	Sr	200
3376.35	Sr II	-	4087.344	Sr I	12h	4891.980	Sr I	40
3380.711	Sr II	150	4092.6	bh Sr	4	4962.263	Sr I	40
3390.67	Sr I	4	4102.3	bh Sr	2	4967.944	Sr I	20
3401.23	Sr II	3	4107.55	Sr II	1	4971.668	Sr I	2
3411.94	Sr I	4	4113.6	bh Sr	5	5156.066	Sr I	80
3412.8	bh Sr	4	4124.7	bh Sr	2	5165.46	Sr I	15
3418.36	Sr	1	4135.0	bh Sr	4	5212.980	Sr	10
3441.43	Sr	-	4140.35	Sr	5	5222.199	Sr	70
3445.2	bh Sr	12	**4161.7**	Sr I	30	5225.113	Sr	70
3452.30	Sr II	1	4167.2	bh Sr	5	5229.270	Sr	70
3456.52	Sr I	3	4189.1	bh Sr	4	5238.551	Sr	90
3464.457	Sr II	200	4202.522	Sr I	6	5256.903	Sr	90
3467.5	bh Sr	4	4211.2	bh Sr	3	5263.73	Sr II	2
3474.887	Sr II	80	*4215.524*	Sr II	300r	5329.823	Sr I	40
3491.62	Sr II	1	4233.2	bh Sr	2	5385.45	Sr II	2h
3499.672	Sr I	50	4240.493	Sr II	1	5450.842	Sr	30
3503.8	bh Sr	30	4253.5	Sr	2	5480.84	Sr	100h
3523.51	Sr	1	4281.0	bh Sr	5	5486.12	Sr	40
3525.4	bh Sr	8	4296.82	Sr	3	5504.17	Sr	60
3546.6	bh Sr	4	4302.7	bh Sr	4	5521.83	Sr	50
3548.083	Sr I	50	***4305.4***	Sr I	40	5534.807	Sr	20
3548.66	Sr I	2	4308.105	Sr I	20h	5540.052	Sr	20
3553.4	Sr I	4	4312.74	Sr II	7	5543.357	Sr I	30
3556.44	Sr	-	4313.182	Sr I	3h	5556.450	Sr	4
3559.087	Sr II	-	4324.3	bh Sr	3	5674.03	Sr	3
3577.243	Sr I	2	4326.445	Sr I	8	5693.13	Sr	4
3586.9	bh Sr	8	4337.664	Sr I	30h	5767.05	Sr	4
3593.214	Sr II	3	4337.89	Sr I	150	5816.78	Sr	5
3628.345	Sr I	10	4345.9	bh Sr	3	5970.10	Sr I	10
3629.144	Sr I	30	4361.710	Sr I	20	6092.85	Sr	4
3646.0	bh Sr	4	4367.6	bh Sr	2	6158.967	Sr	6
3653.270	Sr II	30	4399.6	bh Sr	6	6178.89	Sr	6
3653.928	Sr II	15	4406.12	Sr I	3	6248.52	Sr	4h
3671.5	bh Sr	4	4406.85	Sr	50h	6272.052	Sr	15
3677.56	Sr	-	4420.9	bh Sr	5	6295.65	Sr	8
3705.901	Sr II	30	4438.044	Sr I	25	6317.3	Sr	4wh
3717.30	Sr II	1	4442.10	bh Sr	3	6321.79	Sr I	4
3729.34	Sr	-	4451.804	Sr I	2	6345.749	Sr I	25
3762.00	Sr	1	4463.3	bh Sr	4	6363.939	Sr I	25
3769.99	Sr II	3	4480.507	Sr I	10h	6369.962	Sr	25
3774.22	Sr II	1	4484.5	bh Sr	3	6380.746	Sr I	30
3780.46	Sr I	30	4523.3	bh Sr	4	6386.501	Sr I	35
3807.38	Sr I	50	4531.348	Sr I	10	6388.239	Sr I	35
3822.4	bh Sr	4	4544.1	bh Sr	5	6408.473	Sr	50
3865.46	Sr I	50	4564.8	bh Sr	5	6446.676	Sr	8
3867.1	Sr I	2h	4585.5	bh Sr	3	6465.793	Sr	5
3897.1	bh Sr	8	4606.2	bh Sr	2	6503.995	Sr	35
3919.6	bh Sr	4	*4607.331*	Sr I	1000R	6509.20	Sr II	2h
3926.13	Sr I	4h	4652.4	bh Sr	3	6546.791	Sr I	25
3940.800	Sr I	20	4672.6	bh Sr	4	6550.255	Sr I	100
3950.81	Sr I	8h	4678.326	Sr I	20h	6643.540	Sr I	100
3962.61	Sr	10h	4692.7	bh Sr	5	6791.05	Sr I	200
3969.261	Sr I	30	4703.984	Sr I	2	6878.38	Sr I	500
3970.043	Sr I	20	4707.288	Sr I	10	6892.59	Sr I	100
3975.4	bh Sr	8	4712.8	bh Sr	2	7070.10	Sr I	1000
3997.7	bh Sr	4	4713.959	Sr I	3	7153.09	Sr I	15
4009.75	Sr	-	4722.278	Sr I	30	7167.24	Sr I	100hl
4020.1	bh Sr	2	4729.466	Sr I	4h	7232.27	Sr I	50hl
4030.377	Sr I	40	4741.922	Sr I	30	7233.2	bh Sr	3
4032.379	Sr I	20	4784.320	Sr I	30	7287.41	Sr I	10h
4033.191	Sr I	6	4787.2	bh Sr	2	7309.41	Sr I	200
4050.9	Sr	1h	4811.881	Sr I	40	7405.79	Sr	2
4056.67	Sr II	4	*4832.075*	Sr I	200	7438.42	Sr I	2
4058.0	bh Sr	3	4855.045	Sr I	20	7621.50	Sr I	100
4061.06	Sr I	8	4868.700	Sr I	20	7673.06	Sr I	200hs
4070.86	Sr I	3	*4872.493*	Sr I	25	7408.12	Sr I	3

Table 1.1 The spectral lines of strontium.

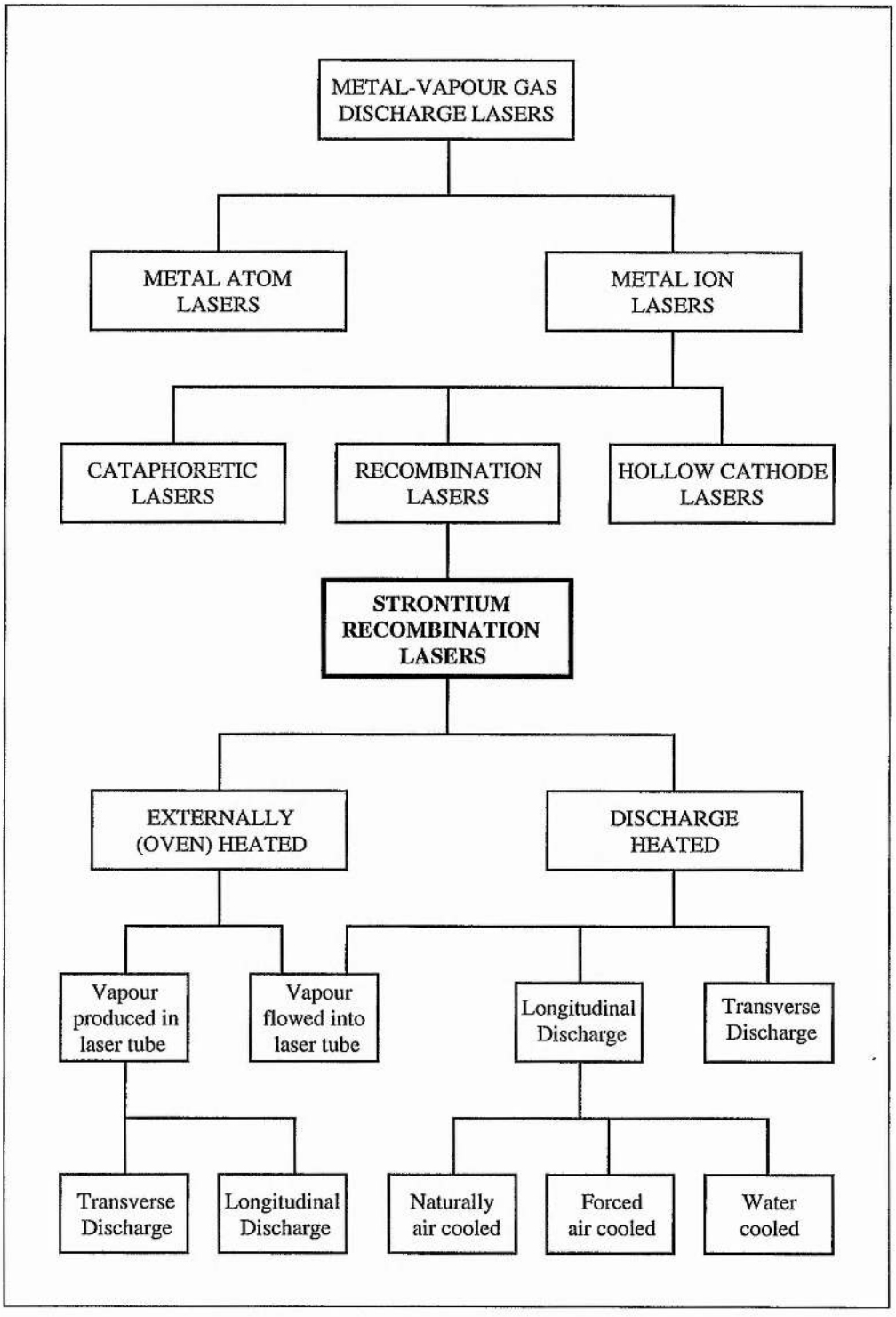

Figure 1.4 Strontium recombination laser family tree.

1.11 References

1. Schmieder, D. and Salamon, T. I.,
   Opt. Commun. **55**, No. 1 (1985), pp.49-54

2. Silfvast, W. T., Szeto, L. H. And Wood, O. R.,
   App. Phys. Lett. **31** (1977) p. 334

3. Silfvast, W. T., Szeto, L. H. And Wood, O. R.,
   App. Phys. Lett. **36** (1980) p. 615

4. Apollonov, V. V. and Sirotkin, A. A.,
   Sov. J. Quantum Electron. **19**, No.10 (1989), pp. 1319-1320

5. Green, J. M., Collins, G. J. and Webb, C. E.,
   J. Phys. B **6** (1973) p. 1545

6. Silfvast, W. T. and Wood II, O. R.,
   Optics Letters **7**, No.1 (1982), pp. 34-36

7 Gudzenko, L. I. and Shelepin, L. A.,
   Sov. Phys. JETP **18**, No. 4 (1964), pp. 998-1000

8. Bohn, W. L.,
   App. Phys. Lett. **24**, No. 1 (1974) pp. 15-17

9. Silfvast, W. T., Szeto, L. H. And Wood, O. R.,
   App. Phys. Lett. **39**, No. 3 (1981) pp. 212-214

10. Apollonov, V. V. and Sirotkin, A. A.,
    Sov. J. Quantum Electron. **19**, No.8 (1989), pp. 1029-1030

11. Gordiets, B. F., Gudzenko, L. I. and Shelepin, L. A.,
    Sov. Phys. JETP **28**, No. 3 (1969) pp. 489-493

12. Zhukov, V. V., Latush, E. L., Mikhalevskii, V. S.and Sem, M. F., *Sov. J. Quantum Electron.* **7**, No.6 (1977), pp. 704-708

13. Deech, J. S. and Sanders, J. H., *IEEE J. Quantum Electron.* **QE-4** (1968), p. 474

14. Latush, E. L. and Sem, M. F., *Sov. J. Quantum Electron.* **3**, No. 3 (1973), pp. 216-219

15. Zhukov, V. V., Latush, E. L., Mikhalevskii, V. S.and Sem, M. F., *Sov. J. Quantum Electron.* **7**, No.6 (1977), pp. 704-708

16. Zhukov, V. V., Kucherov, V. S., Latush, E. L.and Sem, M. F., *Sov. J. Quantum Electron.* **7**, No.6 (1977), pp. 708-714

17. Butler, M. S. and Piper, J. A., *Appl. Phys. Lett.* **45**, No. 7 (1984), pp. 707-709

18. Bukshpun, L. M., Latush E. L. and Sem, M. F., *Sov. J. Quantum Electron.* **18**, No. 9 (1988), pp. 1098-1100

19. Loveland, D. G., Orchard, D. A., Zerrouk, A. F. and Webb, C. E., *Meas. Sci. Technol.* **2** (1991), pp. 1083-1087

20. Zinchenko, S. P., Latush, E. L., Sem, M. F. and Tikidzhi-Kambur'yan, *Sov. J. Quantum Electron.* **22**, No. 9 (1992), pp. 798-799

21. Atamas S. N., Koptev, Y. V. and Latush, E. L., *Sov. J. Quantum Electron.* **15**, No.2 (1984), pp. 161-162

22. Atamas S. N., Koptev, Y. V. and Latush, E. L., *Sov. J. Quantum Electron.* **15**, No.2 (1985), pp. 288-289

23. Bukshpun, L. M. Zhukov, V. V., Latush, E.L. and Sem, M. F., *Sov.J . Quantum Electron.*, **11**, No.6 (198), pp. 804-805

24. Latush E. L,. and Sem, M. F.,
Opt. Spectrosc. **72**, No.5 (1992), pp. 672-680

25. OiKang, F., ZuKang, L., Bizheng, W. and Zhi, H.,
Acta. Opt. Sin. **12**, No. 5 (1992), pp. 402-405

26. Little, C. E. and Piper, J. A.,
IEEE J. Quantum Electron. **QE-26**, No. 5 (1990), pp. 903-910

27. Edelson, R. L.,
Sci. American. **256**, No. 2 (1988)

28. Bates, D. R. and Damgaard, A.,
Phil. Trans. Royal Soc. **A-242** (1950), pp. 101-119

29. Carman, R. J.,
IEEE J. Quantum Electron. **QE-26**, No. 9 (1990), pp. 1588-1608

30. Tarte, B. J.,
Ph.D. Thesis, Macquarie University, 1991

31. McLucas, C. W. and McIntosh, A. I.,
J. Phys. D: Appl. Phys. **18** (1986), pp. 1189-1195

32. Butler, M. S. and Piper, J. A.,
IEEE J. Quantum Electron. **QE-21**, No. 1 (1985), pp. 1563-1566

33. Bethel, J and Little, C. E.,
CLEO Technical digest, 1994

34. Butler, M. S. and Piper, J. A.,
Appl. Phys. Lett. **42**, No. 12 (1983), pp. 1008-1010

35. Brandt M. ,
Appl. Phys. Lett. **42**, No. 2 (1983), pp. 127-129

36. Brandt M.,
IEEE J. Quantum Electron. **QE-20**, No. 9 (1984), pp. 1006-1007

37. McLucas, C. W. and Mcintosh, A. I.,
J. Phys. D: Appl. Phys. **20**, (1987) pp. 591-596

38. Butler, M. S,
Ph.D. Thesis, Macquarie University, 1986

CHAPTER 2:

Thermal modelling of strontium recombination laser tubes

2.1 Introduction

In the strontium recombination laser (SRL), the discharge channel wall must be heated to ~600°C [1] in order to obtain the correct strontium vapour pressure (~0.05 torr) for operation in the short pulse mode (see Chapters 1 and 4 for more details). This can be accomplished by using an oven placed around the laser tube (externally-heated SRLs) or by using the 'waste' heat generated when an electric current is passed through the laser tube (self-heated SRLs).

This thesis will deal with the design and operation of longitudinally excited, self-heated SRLs. A crucial factor which must be considered during the design and subsequent operation of such a laser system is thermal management of the laser tube: i.e. it is important to know how much electrical power must be deposited into a given laser tube in order to maintain the discharge channel wall at the temperature required to produce the optimum metal vapour pressure (600°C for the SRL). This optimum average input power ultimately limits the maximum laser output power (through the laser efficiency) and further influences laser performance by establishing laser gas temperatures, which affect laser kinetics (see Chapters 1, 3 and 4). Thermal loading models are presented below which can be used to model laser systems for the cases of (i) steady-state free-convection cooling (laser tube surrounded by static air) and (ii) steady-state forced-convection water-cooling (laser tube enveloped by a fused silica annular jacket, through which water is forced to flow at high speed). Use of the steady-state approximation to model a pulsed laser system thermally is justified below.

2.2 The construction of longitudinal discharge, self-heated strontium recombination laser tubes

The simplest strontium recombination laser tube consists of a vitreous silica cylinder (thermal conductivity 1.4 W m^{-1} K^{-1} at 20°C) [2]), along which small (2 - 3 mm^2) strontium pieces are placed at regular intervals (3 - 5 cm). A disadvantage of this simple arrangement is that the hot strontium vapour is highly reactive towards quartz [3]. Laser tubes constructed in this manner require some time to passivate [4], and their lifetime between strontium reloads is short. It is therefore more common to use a high temperature ceramic vessel to contain the strontium vapour and electrical discharge. The discharge tube (henceforth used as a generic term to refer to the vessel which directly contains the electrical discharge and the laser medium) is typically made of either alumina (Al_2O_3) or beryllia (BeO), though other discharge tube materials, such as sapphire, can been used in this arrangement. Beryllia has a higher thermal conductivity (62 W m^{-1} K^{-1} at 600°C as shown in Figure 2.1 for Beramic 995 (CBL) [5], than alumina (~10 W m^{-1} K^{-1}) and has a very good resistance to strontium vapour attack. Beryllia is, however, expensive compared to alumina due to toxicity issues during manufacture (the powder from which the solid is formed presents a danger to the respiratory system). The ceramic discharge tube is enclosed in a quartz envelope which can be (i) placed in air so that it is free-convection cooled, (ii) placed in air and blasted with fans so that it is forced-convection-air cooled [6] or (iii) forced-convection water cooled by surrounding it with another quartz jacket so

that an annulus is formed through which water can be forced to flow at high speeds (>1 m s^{-1}).

The cross-sectional structure of a free-convection air cooled ceramic based laser tube is shown in Figure 2.2. The cross-sectional structure of a forced-convection water cooled ceramic based laser tube is shown in Figure 2.3. Both types of laser tube possess a helium layer separating the ceramic discharge tube from its quartz envelope. The rate of heat transfer through helium is discussed below and thermal loading models for the systems represented in Figures 2.2 and 2.3 are subsequently developed in Sections 2.5 and 2.6 respectively.

2.3 The dependence of heat transfer on helium temperature

The thermal conductivity of gaseous helium as a function of the gas temperature, T, can be expressed as [7]:

$$\lambda_{He}(T) = \lambda_0 T^{0.73}, \qquad [2.3.1]$$

with $\lambda_0 = 0.0024$ and the helium temperature in Kelvin. The variation of the thermal conductivity of helium with temperature is shown below in Figure 2.4 over the temperature range 0°C to 700°C.

The steady state heat conduction equation for a cylindrical geometry, in which the thermal conductivity of the conducting medium, λ, is taken as constant, can be written as:

$$\frac{dQ}{dt} = -\lambda A(r)\frac{dT}{dr}, \qquad [2.3.2]$$

where dQ/dt is the rate of heat flow across an element of radius, dr, with surface area, A, owing to a temperature difference, dT, being imposed across the radial element. Separating the variables and integrating leads to the equation for the rate of heat flow from a hollow cylinder in terms of its length, L, inner and outer radii, R_1 and R_2, and respective boundary temperatures, T_1 and T_2:

$$\frac{dQ}{dt} = \frac{2\pi L\lambda}{\ln(R_2/R_1)}(T_1 - T_2). \qquad [2.3.3]$$

If the heat conduction takes place through helium, Equation 2.3.1 must be combined with Equation 2.3.2 (to take account of the temperature dependence), so that the heat conduction equation becomes:

$$\frac{dQ}{dt} = -\lambda_0 T^{0.73} A(r)\frac{dT}{dr}. \qquad [2.3.4]$$

This can be integrated:

$$\int_{R_1}^{R_2} -\frac{dQ/dt}{2\pi L\lambda_0}\frac{dr}{r} = \int_{T_1}^{T_2} T^{0.73} dT, \qquad [3.3.5]$$

to give:

$$-\frac{dQ/dt}{2\pi L\lambda_0}[\ln r]_{R_1}^{R_2} = \left[\frac{T^{1.73}}{1.73}\right]_{T_1}^{T_2}. \qquad [2.3.6]$$

The equation describing the rate of heat flow radially out of a hollow cylinder of helium is therefore:

$$\frac{dQ}{dt} = \frac{2\pi L\lambda_0}{1.73}\left[\frac{T_1^{1.73} - T_2^{1.73}}{\ln(R_2/R_1)}\right]. \qquad [2.3.7]$$

Note that Equation 2.3.7 (incorporating the variation of helium thermal conductivity with temperature) is equivalent to Equation 2.3.3 (constant thermal conductivity) if the thermal conductivity in the latter is replaced by the average thermal conductivity of the gas, λ_{av}:

$$\begin{aligned}\lambda_{Av} &= \frac{\int_{T_1}^{T_2}\lambda_0 T^{0.73}dT}{\int_{T_1}^{T_2}dT} \\ &= \frac{\lambda_0}{1.73(T_2 - T_1)}(T_2^{1.73} - T_1^{1.73}).\end{aligned} \qquad [2.3.8]$$

2.4 Justification for using the steady-state approximation to model a pulse periodic thermal problem

SRLs usually operate in the sealed-off pulsed mode (as do ours, to be described later). This means that energy is delivered to the active volume in the form of a train of pulses. The helium buffer gas temperature will consequently exhibit a time dependency.

Consider a volume (the volume of a laser's discharge channel) containing m moles of gaseous helium, which is subjected to an input energy pulse. The increase in gas temperature, ΔT, accompanying the

energy pulse is related to the input pulse energy, ΔE, through the gas molar heat capacity at constant volume, $c_{V,m}$, according to:

$$\Delta E = mc_{V,m}\Delta T. \qquad [2.4.1]$$

The equation of state for an ideal gas, such as helium, which is used in the SRL as buffer gas, is:

$$pV = m\mathrm{R}T. \qquad [2.4.2]$$

Hence, eliminating the amount of gas, m, from Equation 2.4.1 gives,

$$\Delta E = \frac{pV}{\mathrm{R}T}c_{V,m}\Delta T. \qquad [2.4.3]$$

Now, the kinetic theory prediction of the molar heat capacity at constant volume for an ideal gas is,

$$c_{V,m} = \frac{3}{2}\mathrm{R}, \qquad [2.4.4]$$

so that Equation 2.4.3 can be rewritten as:

$$\Delta E = \frac{3pV}{2T}\Delta T. \qquad [2.4.5]$$

The fractional change in gas temperature, expressed in terms of the energy added to a system under isovolumetric conditions, is therefore

given by:

$$\frac{\Delta T}{T} = \frac{2\Delta E}{3pV}. \qquad [2.4.6]$$

As the temperature of a fixed amount of gas at constant volume increases so does its pressure. Here the pressure, p, exerted by the gas is the pressure to which the gas relaxes during the inter-pulse period (i.e., the external reservoir pressure).

Notice that the above discussion assumes that *all* of the input energy is used to raise the *internal energy* of the gas. However, in practical laser systems, the discharge channel volume will not account for the *whole sealed-off* volume (due to the finite volume of the laser heads). Hence, in practice, the input pulse energy will not be used *entirely* to raise the internal energy of the discharge channel gas, as some will be used to perform work when the gas contained in the discharge channel expands (to equalize the gas pressure in the entire laser tube's sealed-off volume). This will result in the true fractional change in gas temperature being somewhat lower than that obtained using Equation 2.4.6. However, for the purposes of this discussion, a simplification which leads to an *overestimate* of the gas temperature rise accompanying an input energy pulse is justified.

Taking 5 $\mu J\ cm^{-3}$ as a typical value for the specific laser pulse energy of an SRL, operating with a typical efficiency of 0.1%, if the helium buffer gas pressure is 50 kPa, the fractional change in gas temperature due to an input energy pulse will be less than 0.07. An

increase in gas temperature of 7% is sufficiently low to enable us to treat the laser as operating under steady-state conditions of temperature.

It is interesting to seek the specific input energy at which the gas temperature changes by say 50% during a pulse, as a means of evaluating the limits under which the laser can be treated as a steady-state system. At a pressure of 50 kPa, from Equation 3.4.6, this would occur for a specific input energy of 0.0375 J cm^{-3}. On the basis of a laser efficiency of 0.1%, the expected specific laser pulse energy would then be 37.5 μJ cm^{-3}. In practice such a laser would have to be operated at low (sub 1 kHz) PRFs to avoid overheating the discharge channel wall or the gas (see Chapter 4). It should be noted that the preceding example is based on a hypothetical laser. No *longitudinal-discharge* SRL has yet been built which is capable of delivering this sort of specific laser pulse energy under these pressure conditions.

The fractional change in gas temperature is related to the input power density, P_V, and PRF, f, through the expression:

$$\frac{\Delta T}{T} = \frac{2P_V}{3pf}. \qquad [2.4.7]$$

Equation 2.4.7 shows us that if the fractional change in gas temperature is to be kept low during a pulse, the repetition rate must be increased with the input power density, P_V. The minimum PRF, at a pressure of 50 kPa, which must be used to keep the change in temperature during a pulse below 10% of the starting value, is shown in Figure 2.5 as a function of input power density.

Input energy pulses will raise the gas temperature of a cold SRL to a level after which the temperatures associated with the system show no significant short term or long term time dependences. However, attempting to raise the specific output pulse energy of a given laser tube by increasing the specific input energy and lowering the PRF will result in an increase in the fractional change in gas temperature, so that the steady-state approximation may not be valid.

Our lasers, to be described, all operate at low specific input energies (<5 mJ cm^{-3}) and high PRFs (above 1 kHz), so that the fractional change in gas temperature during an input pulse is expected to be less than 10%. The steady state approximation is therefore applicable in our laser systems and, indeed, to all longitudinally excited SRLs cited in the literature at this time.

2.5 A steady-state thermal loading model for free-convection cooled cylindrical laser tubes

The overall steady-state heat transfer equation, due to conduction and convection, for a multiple-layered cylinder with innermost surface temperature, T_i, bounded by a convecting fluid at a bulk temperature, T_b, can be written as [8]:

$$\left(\frac{dQ}{dt}\right)_{\lambda+\alpha} = UA(T_i - T_b), \qquad [2.5.1]$$

where U, the overall heat transfer coefficient for the system, shown schematically in Figure 2.2, is given by Equation 2.5.2 below [9], and A is the outermost surface area of the cylinder, with which the convecting fluid is in contact.

$$U = \left[\frac{r_4 \ln(r_2/r_1)}{\lambda_{\text{tube}}} + \frac{r_4 \ln(r_3/r_2)}{\lambda_{\text{helium}}} + \frac{r_4 \ln(r_4/r_3)}{\lambda_{\text{quartz}}} + \frac{1}{\alpha_{\text{air}}} \right]^{-1}. \qquad [2.5.2]$$

The parameters λ_x are the coefficients of thermal conductivity and α_{air} is the coefficient of convective heat transfer for air given by:

$$\alpha_{\text{air}} = \frac{N_{\text{NU}} \lambda_{\text{air}}}{D}. \qquad [3.5.3]$$

The Nusselt number, N_{NU}, for a free convecting fluid, surrounding a horizontal cylinder of diameter D, is given by [10]:

$$N_{\text{NU}} = 0.53 \left(N_{\text{GR}} N_{\text{PR}} \right)^{0.25}, \qquad [2.5.4]$$

provided that $10^4 < (N_{\text{GR}} N_{\text{PR}}) < 10^9$, where N_{GR} is the Grashof number. The Prandtl number, N_{PR}, is well tabulated and the Grashof number can be calculated using the expression [11]:

$$N_{\text{GR}} = \frac{D^3 \rho^2 g \beta (T_s - T_b)}{\mu^2}, \qquad [2.5.5]$$

where: ρ is the density of air, g is the acceleration due to gravity, β is the thermal coefficient of volume expansion of air, T_s is the temperature of

the air at the surface of the quartz jacket, T_b is the bulk air temperature and μ is the coefficient of dynamic viscosity of air. Conventionally, ρ and μ are evaluated at the *mean* air film temperature, T_m, while β is evaluated at the *bulk* fluid temperature:

$$T_m = \frac{T_s + T_b}{2}, \qquad [2.5.6]$$

$$\beta = \frac{1}{T_b(\mathrm{K})}. \qquad [2.5.7]$$

Equation 2.5.1 cannot be solved directly to obtain the rate of conducted and convected heat flow from the laser tube, as the heat transfer coefficient for the air film surrounding the quartz jacket depends on the undetermined temperature of the air in contact with the quartz jacket. However, since the system is in steady state, Equation 2.3.8, below must be satisfied along with Equation 2.5.1:

$$\alpha_{air}(T_s - T_b) = U(T_i - T_b). \qquad [2.5.8]$$

An iterative procedure can therefore be followed by first making an estimate of the surface air temperature (so as to obtain an approximate value for the overall heat transfer coefficient) and then using Equation 2.5.8 to generate a better estimate of T_s. This new value for the surface air temperature can then be used in Equation 2.5.2 to recalculate U, whence a more accurate value for the rate of heat flow from the laser tube, due to conduction and convection, can be obtained.

The physical properties of air which it is necessary to know in order to perform the calculations are given in Table 2.1, below.

During the calculations, account must be taken of the fact that the thermal conductivity of helium varies with temperature, as discussed earlier in Section 2.3. It therefore follows that the average helium thermal conductivity, λ_{Av} (Equation 2.3.8), should be used as λ_{helium} in Equation 2.5.2.

$$\lambda_{Av} = \frac{0.0024}{1.73(T_2 - T_1)}(T_2^{1.73} - T_1^{1.73}). \qquad [2.5.11]$$

However, the temperatures of the helium layer boundaries, T_1 and T_2, are unknown, prior to modelling the system, so that values must be assumed before the calculations can commence. The optimum temperature of the inner wall of the SRL discharge tube is ~600°C and the bulk temperature of the air will usually be in the range 20 - 30°C. The helium layer has the lowest thermal conductivity of the heat conducting layers so that, for the purposes of this exercise, the inner wall temperature and the ambient room temperature will be sufficiently close to the actual temperatures of the helium boundaries to be used. An iteration could be performed, in conjunction with the main one, to determine the helium layer temperatures accurately. In this model, however, this is not deemed to be necessary since the effect of free convection is far more significant than conduction through the helium layer, and radiation from the laser is shown (in Chapter 5) to be by far the most effective process by which heat is removed from the laser tube. Hence, if T_1, approximately equal to the tube inner wall temperature, is

873 K and T_2, approximately equal to the bulk air temperature, is 303 K, then the average thermal conductivity of the helium layer can be taken to be 0.25 W m^{-1} K^{-1}.

An estimate of the amount of heat extracted from the discharge tube via radiation in the infrared can be obtained using the Stefan-Boltzmann law for grey bodies:

$$\left(\frac{dQ}{dt}\right)_{\sigma} = \sigma \varepsilon A_{\sigma} T^4. \qquad [2.5.9]$$

Quartz has a transmittance cut off (transmittance, 50%) at ~4.3 μm [2]. Wien's displacement law,

$$\lambda_{max} T = 2.9 \text{x} 10^{-3}, \qquad [2.5.10]$$

can be used to estimate the wavelength at which the radiation from the discharge tube has its intensity maximum. If T, the temperature of the discharge tube's outer surface, is taken as ~800 K, the radiation intensity maximum occurs at ~3.5 μm. The transmittance of quartz (at 1 mm thickness) is ~85% at 3.5 μm [2]. We assume, in our models, that all the power radiated by the discharge tube passes directly through the quartz.

2.6 A steady-state thermal loading model for forced-convection water-cooled cylindrical laser tubes

The overall steady-state heat transfer equation, due to conduction and convection, for a multiple-layered cylinder with innermost surface temperature, T_i, bounded by a forced convecting fluid of bulk temperature, T_f, (like our water-cooled laser assembly) can be written as:

$$\left(\frac{dQ}{dt}\right)_{\lambda+\alpha} = UA(T_i - T_f), \qquad [2.6.1]$$

where U, the overall heat transfer coefficient, for a forced-convection water-cooled laser system, such as is shown in schematic cross-section in Figure 2.3, is given by Equation 2.6.2 below and A is the outermost surface area of the fused silica cylinder, with which the convecting fluid is in contact.

$$U = \left[\frac{R_4 \ln(R_2/R_1)}{\lambda_{\text{tube}}} + \frac{R_4 \ln(R_3/R_2)}{\lambda_{\text{helium}}} + \frac{R_4 \ln(R_4/R_3)}{\lambda_{\text{quartz}}} + \frac{1}{\alpha_{\text{water}}}\right]^{-1}. \qquad [2.6.2]$$

The parameters λ_x are the coefficients of thermal conductivity and α_{water} is the coefficient of convective heat transfer for water, which is given by the expression [12]:

$$\alpha_{\text{water}} = \frac{N_{\text{NU}}\lambda_{\text{water}}}{D_E}, \qquad [2.6.3]$$

where D_E , the equivalent diameter [13] of the water flow annulus, is given by:

$$D_E = 2(R_5 - R_4). \qquad [2.6.4]$$

Provided that the difference between the temperatures of the pipe surface and the bulk fluid is no more than 5°C, the Nusselt number, N_{NU}, for a forced convecting fluid, flowing through a horizontal circular annulus, is given empirically by the expression [14]:

$$N_{NU} = 0.023 N_{RE}^{0.8} N_{PR}^{0.4}. \qquad [2.6.5]$$

The Prandtl number, N_{PR}, is well tabulated [15] and the Reynolds number, N_{RE}, can be obtained using the expression [16]:

$$N_{RE} = \frac{uD_E}{\nu}, \qquad [2.6.6]$$

where u is the speed of fluid flow through the annulus and ν is the kinematic viscosity of the convecting fluid. Using Equations 2.6.3, 2.6.4, 2.6.5 and 2.6.6, the coefficient of convective heat transfer for water can be written as:

$$\alpha_{water} = \frac{0.02 \lambda_{water} u^{0.8} N_{PR}^{0.4}}{\nu^{0.8} (R_5 - R_4)^{0.2}}. \qquad [2.6.7]$$

The physical properties of water required as input data by this forced-convection heat transfer model are presented below in Table 2.2.

In order to gain information about the relative importance of the four terms in Equation 2.6.2, in regard to predicting the behaviour of a water-cooled SRL, it is convenient to recast the overall steady-state heat transfer equation for the system in the form:

$$\left(\frac{dQ}{dt}\right)_{\lambda+\alpha} = \frac{2\pi L(T_i - T_f)}{\xi + \chi + \eta + \kappa}, \qquad [2.6.8]$$

where:

$$\xi = \frac{\ln(R_2/R_1)}{\lambda_{tube}}, \qquad [2.6.9]$$

$$\chi = \frac{\ln(R_3/R_2)}{\lambda_{helium}}, \qquad [2.6.10]$$

$$\eta = \frac{\ln(R_4/R_3)}{\lambda_{quartz}}, \qquad [2.6.11]$$

$$\kappa = \frac{\nu^{0.8}(R_5 - R_4)^{0.2}}{0.02 R_4 \lambda_{water} u^{0.8} N_{PR}{}^{0.4}}. \qquad [2.6.12]$$

Notice that the term due to convection, κ, (Equation 2.6.12) will be small for the following cases: small R_5 - R_4 (water layer thickness), large R_4 and high rates of fluid flow. The thermal conductivity, Prandtl number and kinematic viscosity for water vary with the water's temperature. The factor $(0.02\lambda_{water}\nu^{-0.8}N_{PR}{}^{0.4})^{-1}$ in Equation 2.6.12 is plotted as a function of water temperature in Figure 2.6, using the data given in Table 2.2.

Before continuing with the discussion of the implications of Equations 2.6.8 through to 2.6.12 it is useful to consider the longitudinal water temperature gradient which will occur across the ends of the water jacket as a result of heat being conducted into the water jacket. Any increase in fluid temperature will be accompanied by a change in discharge tube wall temperature, leading to a change in strontium vapour density. A longitudinal temperature gradient will therefore result in a non-uniform longitudinal strontium vapour density, which must be minimized if efficient lasing is to be achieved. Furthermore, if the temperature gradient is of sufficient severity, some of the laser volume will be overheated, reducing the active gain length of the laser. An equation describing the evolution of the water temperature with distance along the water jacket is required.

Consider a fluid entering a cylindrical annular region at some temperature, T_o, and moving longitudinally through it with speed, u. If heat is entering the annulus, through the innermost wall, at a total rate q, which is uniformly distributed over the innermost surface of the annulus, a rate of heat entry per unit fluid mass, q_m, can be defined. The temperature, T_d, of the fluid, at a given distance along the tube from its point of entry, will be a function of position and time:

$$T_d = T(x,t). \qquad [2.6.13]$$

Assuming that all of the heat entering the annulus is carried away by the fluid and that there is negligible frictional heating of the fluid, the rate of increase in the fluid's temperature will be related to the rate of

heat entry per unit fluid mass, q_m, through the specific heat capacity of the fluid, c, as follows:

$$\frac{dT}{dt} = \frac{q_m}{c}. \qquad [2.6.14]$$

The total derivative of the fluid temperature with respect to time is given by:

$$\frac{dT}{dt} = \frac{dT}{dx}\frac{\partial x}{\partial t} + \frac{\partial T}{\partial t}, \qquad [2.6.15]$$

which can be written as:

$$\frac{dT}{dt} = u\frac{\partial T}{\partial x} + \frac{\partial T}{\partial t}. \qquad [2.6.16]$$

If a sufficient time has elapsed since any changes were made to the system (i.e., changing the input power or fluid flow rate), the partial derivative of temperature with respect to time will be zero, so that using Equation 2.6.14, Equation 2.6.16 can be rewritten as:

$$\frac{q_m}{c} = u\frac{\partial T}{\partial x}. \qquad [2.6.17]$$

This can be integrated over some distance, d, from the point of fluid entry,

$$\int_{T_0}^{T_d} \partial T = \int_0^d \frac{q_m}{cu}\partial x, \qquad [3.6.18]$$

to give the following expression for the evolution of the fluid temperature with longitudinal distance along the cylindrical annulus:

$$T_d = T_0 + \frac{q_m}{cu} d. \qquad [2.6.19]$$

The rate of heat entry, per unit fluid mass, can now be expressed in terms of the linear input power density, P_L, such that Equation 2.6.19 becomes:

$$T_d = T_0 + \frac{P_L}{\rho c F} d, \qquad [2.6.20]$$

where ρ is the density of the fluid and F is the volumetric flow rate of the fluid. The change in water temperature per unit length, ΔT_L, is therefore given by:

$$\Delta T_L = \frac{P_L}{\rho c F}. \qquad [2.6.21]$$

If the fluid flow rate is expressed in *litres/minute*, the above formula becomes:

$$\Delta T_L = \frac{P_L}{70 F}. \qquad [2.6.22]$$

Figures 2.7 and 2.8 show the flow rates which are necessary to keep the change in water temperature per unit length between 1 and 10°C m^{-1} as a function of linear input power density. These graphs enable the laser designer to select the flow rate necessary to cool a given laser tube such

that the longitudinal water temperature variation is satisfactorily low (<10°C from end to end). In practice, the design of the water jacket and water couplings and the water supply which is available will place an upper limit on the attainable water flow rate (see later). The evolution of the inner discharge tube wall temperature as a function of distance along the tube (in the direction of water flow) in terms of the fluid flow rate can be obtained from the expression:

$$T_i(d) = T_0 + P_L\left(\frac{(\xi+\chi+\eta+\kappa)}{2\pi} + \frac{d}{\rho c F}\right). \qquad [2.6.23]$$

Returning now to the discussion of Equations 2.6.9 to 2.6.12, it can be seen, for the water-cooled laser tube as specified in Figure 2.9, that the most significant term in Equation 2.6.8 is that due to conduction through the helium layer (Equation 2.6.12). The convection term can therefore be assumed negligible in the model, for helium layers of practical thickness (>1 mm), while retaining good accuracy, provided that the flow annulus is narrow (1 - 2 mm as defined by R_5 and R_4) and the fluid flow rate is of the order of 1 m s^{-1}, which it must be in order to keep the temperature gradient across the ends of the water jacket acceptable (<10°C). *Fast-flow water cooling, through a narrow annulus of large surface area, simply fixes the surface temperature of the fused silica with which the water is in contact.*

Note that beryllia is specified for the discharge tube material in a water-cooled laser tube. This is because beryllia is more resistant to thermal shock than alumina and has the higher thermal conductivity (see Section 2.2).

2.7 Extensions to the thermal loading model for forced-convection water-cooled cylindrical laser tubes

We have seen, in Section 2.6, that the helium layer is the most 'influential' layer in terms of the heat transfer out of a water-cooled SRL. Two factors which affect the character of the helium layer are (i) its thermal conductivity and (ii) its thickness. A more detailed discussion of these factors and how they should be incorporated into our thermal loading model is presented below.

2.7.1 Inclusion of the variation of helium thermal conductivity with temperature in the forced-convection thermal loading model

The thermal conductivity of helium is a function of its temperature (Section 2.3) and, prior to modelling the system, this temperature is an unknown quantity which depends on the amount of heat which can be extracted. However, the amount of heat which can be extracted from a water-cooled laser tube depends on the helium layer's thermal conductivity. Further, if the outer surface of the beryllia is at a temperature T_1 and the quartz bounding the helium layer is at a temperature T_2, the thermal conductivity of the helium will vary with position in the layer. As the helium layer has the most significant impact on the heat removal from the laser tube, the variation of thermal conductivity with temperature, and hence position, must be incorporated into the thermal loading model if it is to be accurate.

The thermal conductivity variation across the helium layer can be incorporated into the thermal loading model by calculating the average thermal conductivity over the helium layer as shown in Section 2.3. The average thermal conductivity of the helium is then used in Equation 2.6.2 in place of the fixed λ used previously. The problem of unknown helium boundary conditions can be solved by adopting an iterative procedure in order to perform the modelling (see Section 2.8).

2.7.2. Inclusion of thermal expansion of the discharge tube in the forced-convection thermal loading model

The helium layer thickness is crucial to the thermal management model for a water-cooled laser tube, particularly when it is made small to enhance the heat removal capability of the water cooling. The outer radius of the ceramic discharge tube and the inner radius of the quartz water jacket define the helium layer thickness. However, during laser operation, the thickness of the helium layer will depend on the discharge tube's outer surface temperature due to thermal expansion of the ceramic. The quartz tube's expansion will be negligible, by comparison. Due to the strong influence of the helium layer on the rate of heat extracted from a water-cooled laser tube, the reduction in the helium layer thickness, accompanying laser operation, must be taken into account when designing a laser tube, particularly when the helium layer thickness is to be small (1 mm or less).

The variation of the radius of a beryllia cylinder with temperature is given by:

$$\frac{\mathrm{d}R}{\mathrm{d}T} = \alpha R_0, \qquad [2.7.1]$$

where α is the linear expansivity of beryllia (7.6×10^{-6} K^{-1} [5]) and R_0 is the tube radius at some specified temperature, T_0. The outer radius of the beryllia at optimum laser operation, R_1, is therefore given by:

$$R_1 = \left[1 + \alpha\left(T_1 - T_0\right)\right]R_0, \qquad [2.7.2]$$

where T_1 is the operating temperature of the outer surface of the tube and R_0 is the tube's outer radius at room temperature, T_0. The change in inner radius of a beryllia tube has negligible effect on the thermal management of the laser tube due to beryllia's high thermal conductivity with respect to that of helium.

The true outer radius of the discharge tube can be incorporated into the thermal loading model by using Equation 2.7.2 to calculate the new helium value for R_1 under optimum laser operating conditions and using this value in Equation 2.6.2. The problem of unknown T_1 can be solved by iteration (see Section 2.8).

2.8 Performing the thermal modelling calculations for a water-cooled laser tube using a computer

Incorporating the dependence of the helium layer thermal conductivity and discharge tube outer radius on the operating temperature into the thermal loading model presented in Section 2.6, necessitates the use of an iterative procedure, as both calculations require the use of initially unknown temperatures.

A computer program (Water-Cooled Laser Designer 1) has been written to calculate the rate of heat removal from a cylindrical water-cooled beryllia laser tube as a function of the user-specified system parameters, listed in Figure 2.10. This computer program neglects the water cooling term as it has earlier been shown to be negligible for practical helium layer thicknesses (>1 mm, Section 2.6). A simplified flow diagram illustrating how the program operates is shown in Figure 2.11. This program makes an initial estimate of the temperature distribution within the composite cylindrical arrangement, based on the specified boundary conditions. A loop is used which iterates until two consecutive rates of heat removal due to conduction and convection agree to within 1 W. The program also estimates the rate of heat radiated from the outer surface of the ceramic discharge tube to give the total rate of heat transfer from a given laser tube geometry. The quantities output by the program are given in Figure 2.12 and a sample printout for the program is shown in Figure 2.13. The code for the computer program is listed in Appendix A.

2.9 Summary

In this chapter, thermal loading models have been developed to calculate the optimum input powers for (i) free-convection cooled SRLs and (ii) forced convection-cooled SRLs. These models are based on the steady-state transfer of heat out of the laser tube through the processes of conduction, convection and radiation. Use of the steady-state approximation to model the SRL system has been justified, since it has been shown that the fractional change in gas temperature accompanying a typical input energy pulse is normally less than 10%. The thermal loading model for water-cooled SRLs has been developed into a computer program.

2.10 Figures and tables for Chapter 2

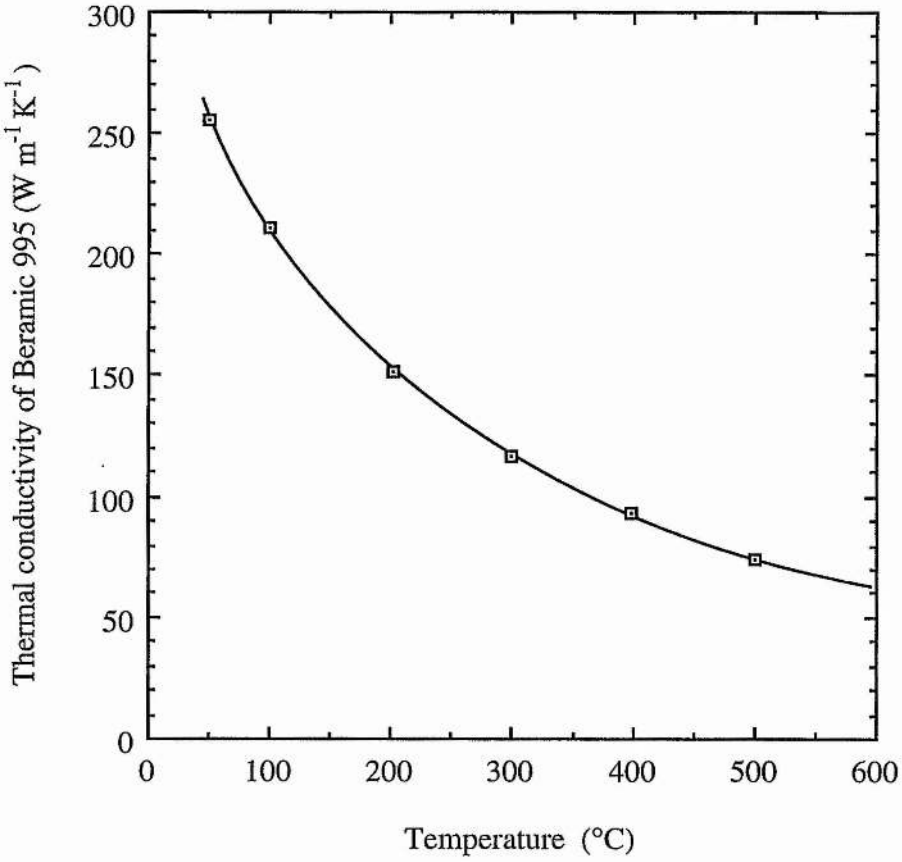

Figure 2.1 The thermal conductivity of Beramic 995 (CBL beryllia) as a function of temperature.

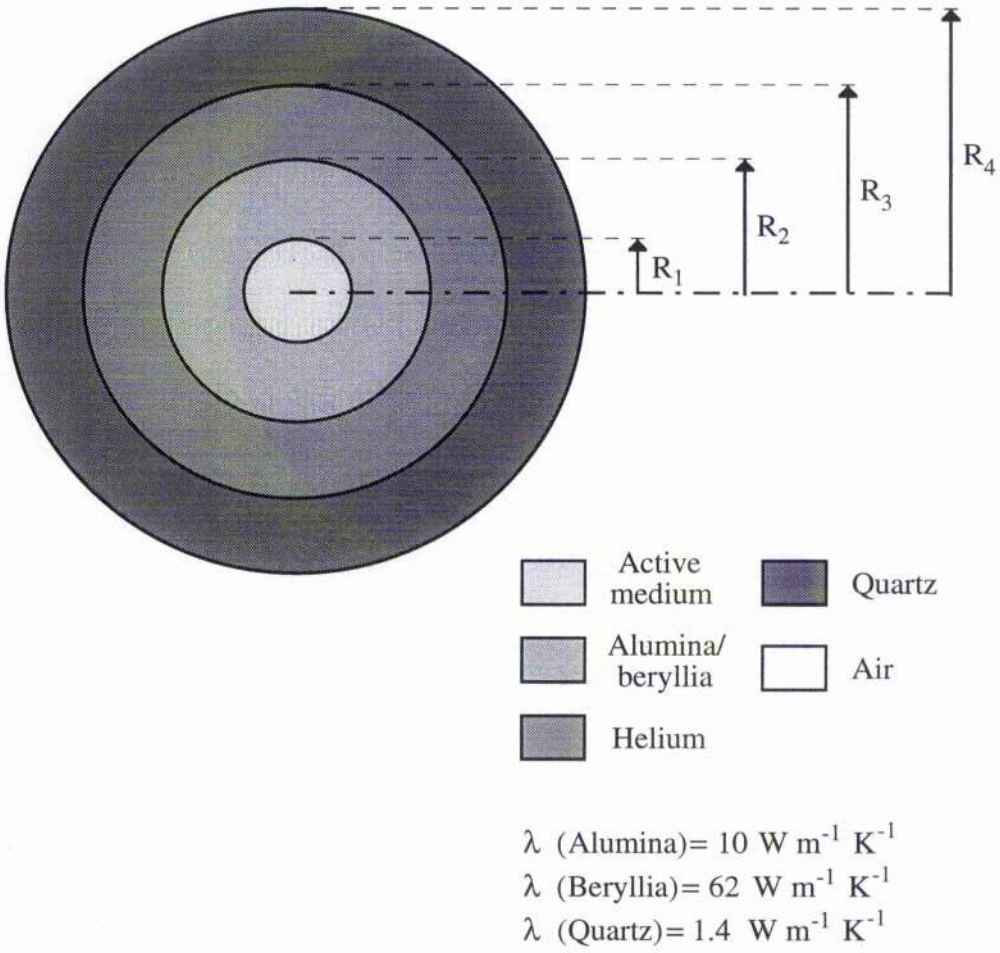

Figure 2.2 Schematic section through an air-cooled laser tube.

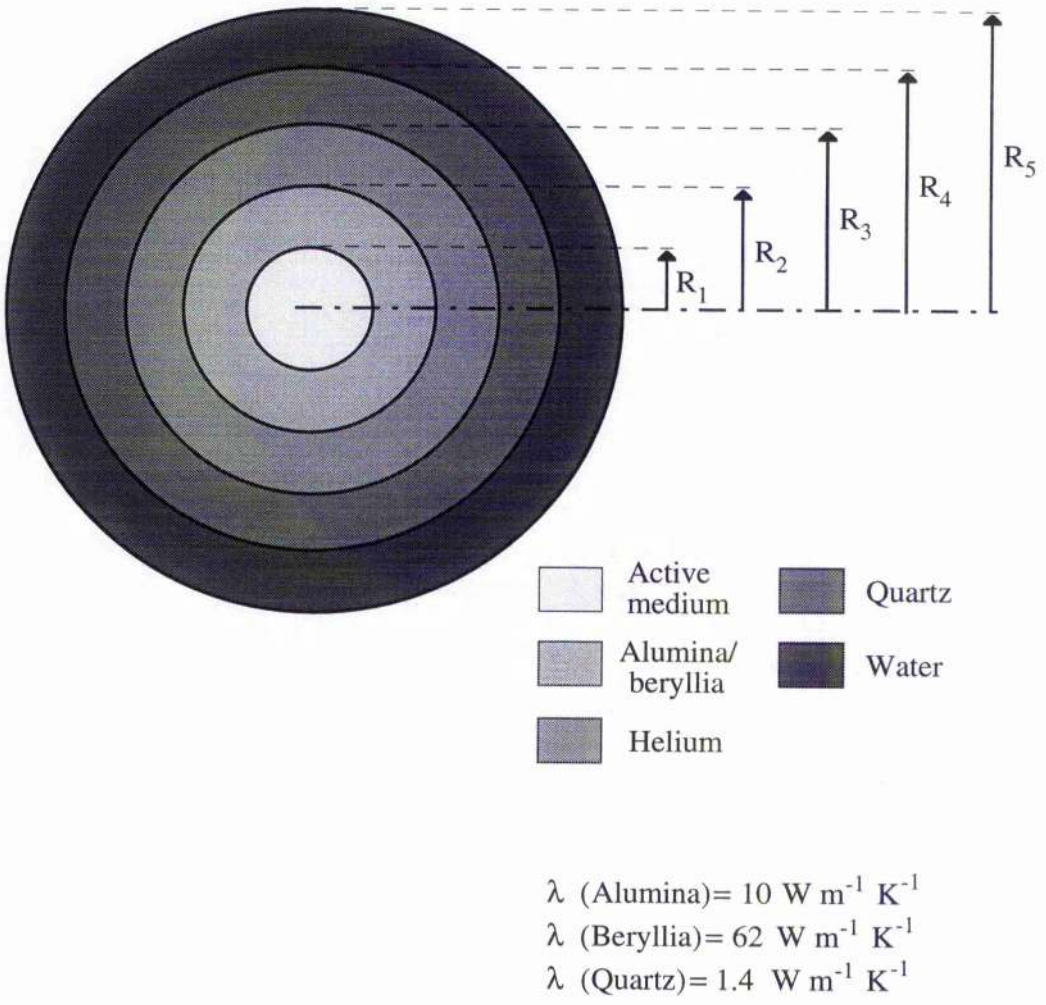

Figure 2.3 Schematic section through a water-cooled laser tube.

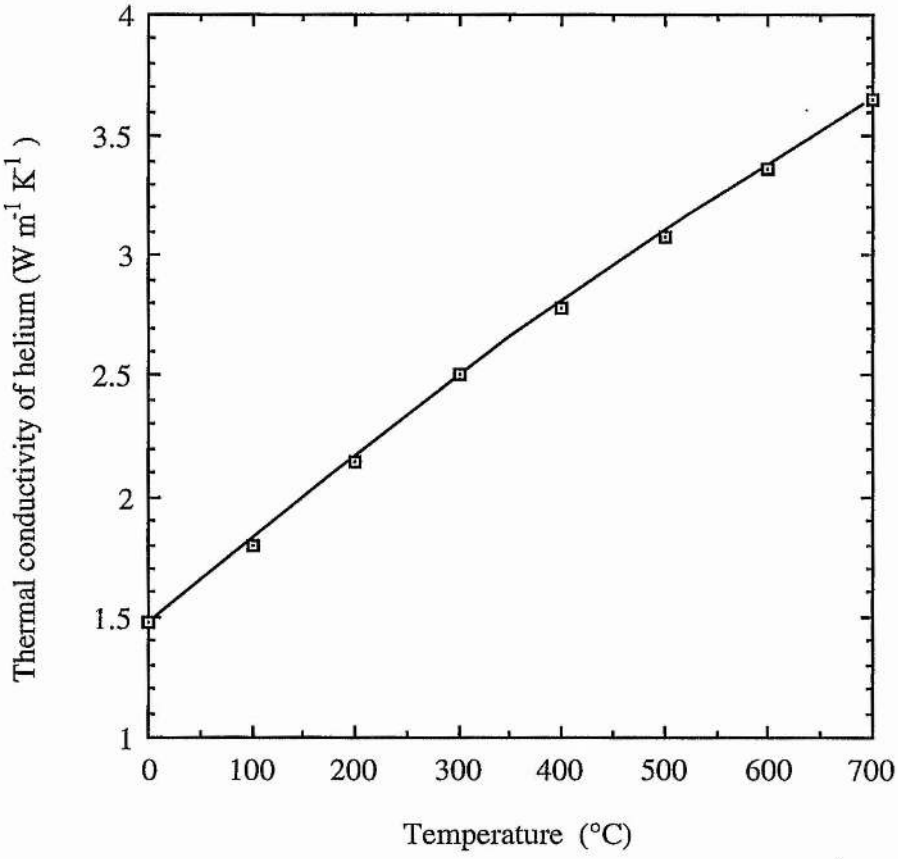

Figure 2.4 The thermal conductivity of helium as a function of temperature.

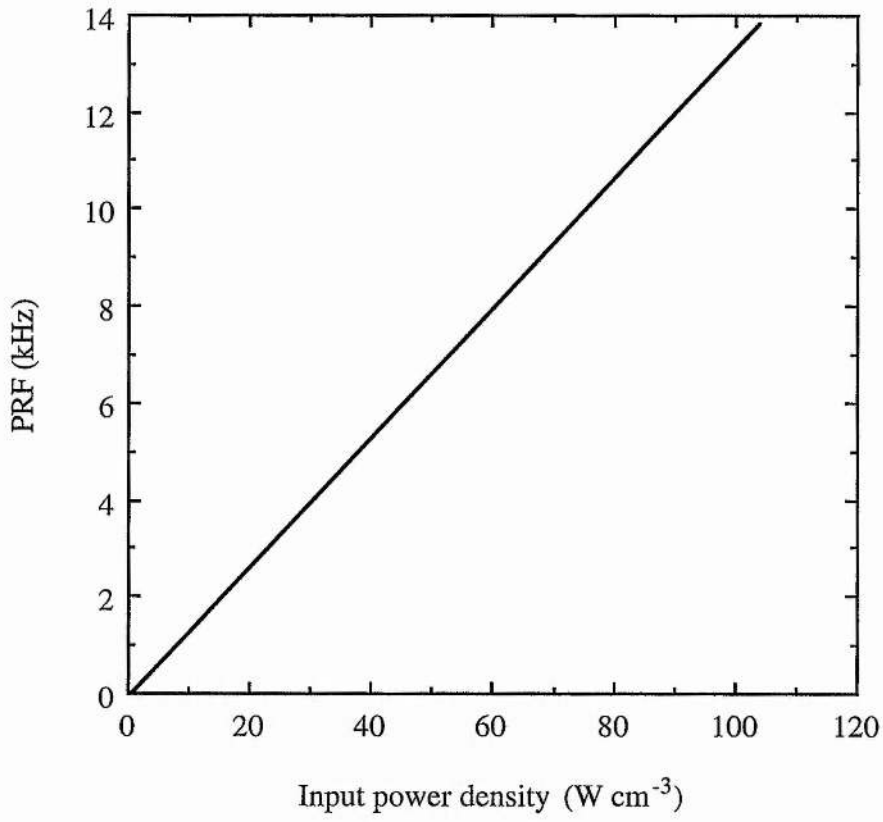

Figure 2.5 **The minimum repetition rate which must be used in order to keep the fractional change in gas temperature below 10% as a function of input power density.**

T °C	λ $W\,m^{-1}\,K^{-1}$	ρ $kg\,m^{-3}$	μ $kg\,m^{-1}\,s^{-1}$	β K^{-1}	N_{PR}
0	0.0244	1.293	17.2×10^{-6}	0.00366	0.707
20	0.0259	1.205	18.1×10^{-6}	0.00341	0.703
40	0.0276	1.128	19.1×10^{-6}	0.00319	0.699
60	0.0290	1.060	20.1×10^{-6}	0.00300	0.696
80	0.0305	1.000	21.1×10^{-6}	0.00283	0.692
100	0.0321	0.946	21.9×10^{-6}	0.00268	0.688
120	0.0334	0.898	22.8×10^{-6}	0.00254	0.686
140	0.0349	0.854	23.7×10^{-6}	0.00242	0.684
160	0.0364	0.815	24.5×10^{-6}	0.00231	0.682
180	0.0378	0.779	25.3×10^{-6}	0.00221	0.681
200	0.0393	0.746	26.0×10^{-6}	0.00211	0.680
225	0.0410	0.710	26.7×10^{-6}	0.00201	0.678
250	0.0427	0.674	27.4×10^{-6}	0.00191	0.677
275	0.0444	0.645	28.6×10^{-6}	0.00182	0.675
300	0.0460	0.615	29.7×10^{-6}	0.00175	0.674
325	0.0476	0.591	30.6×10^{-6}	0.00167	0.675

Table 2.1 Physical properties of air.

T (°C)	λ $W\,m^{-1}\,K^{-1}$	ν $m^2\,s^{-1}$	N_{PR}
0	0.566	1.791×10^{-6}	13.37
4.44	0.575	1.551×10^{-6}	11.36
10	0.585	1.311×10^{-6}	9.41
15.55	0.595	1.123×10^{-6}	7.88
21.1	0.604	0.983×10^{-6}	6.78
26.67	0.614	0.862×10^{-6}	5.81
32.2	0.623	0.769×10^{-6}	5.13
37.78	0.630	0.686×10^{-6}	4.52
43.33	0.637	0.622×10^{-6}	4.04
48.9	0.644	0.568×10^{-6}	3.65
54.44	0.649	0.521×10^{-6}	3.30
60	0.654	0.480×10^{-6}	3.01

Table 2.2 Physical properties of water.

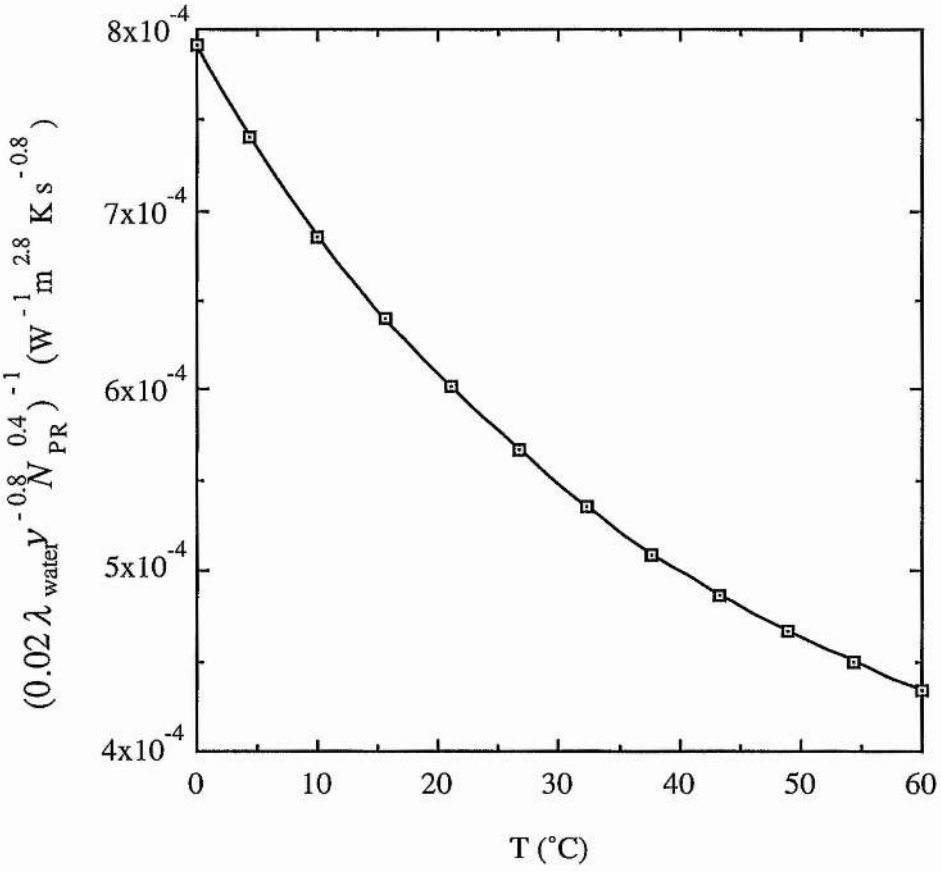

Figure 2.6 **The quantity $(0.02\lambda_{water}\nu^{-0.8}N_{PR}^{0.4})^{-1}$ plotted as a function of temperature for water.**

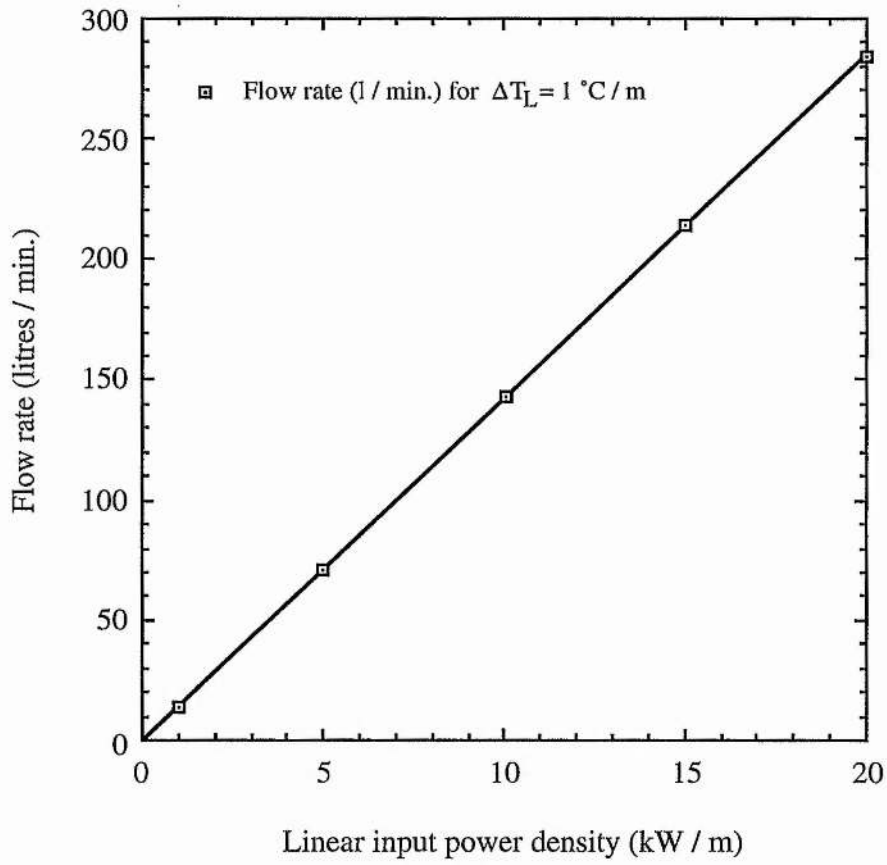

Figure 2.7 Graph of the water flow rate required to keep the longitudinal water temperature gradient at 1°C m^{-1} against linear input power density.

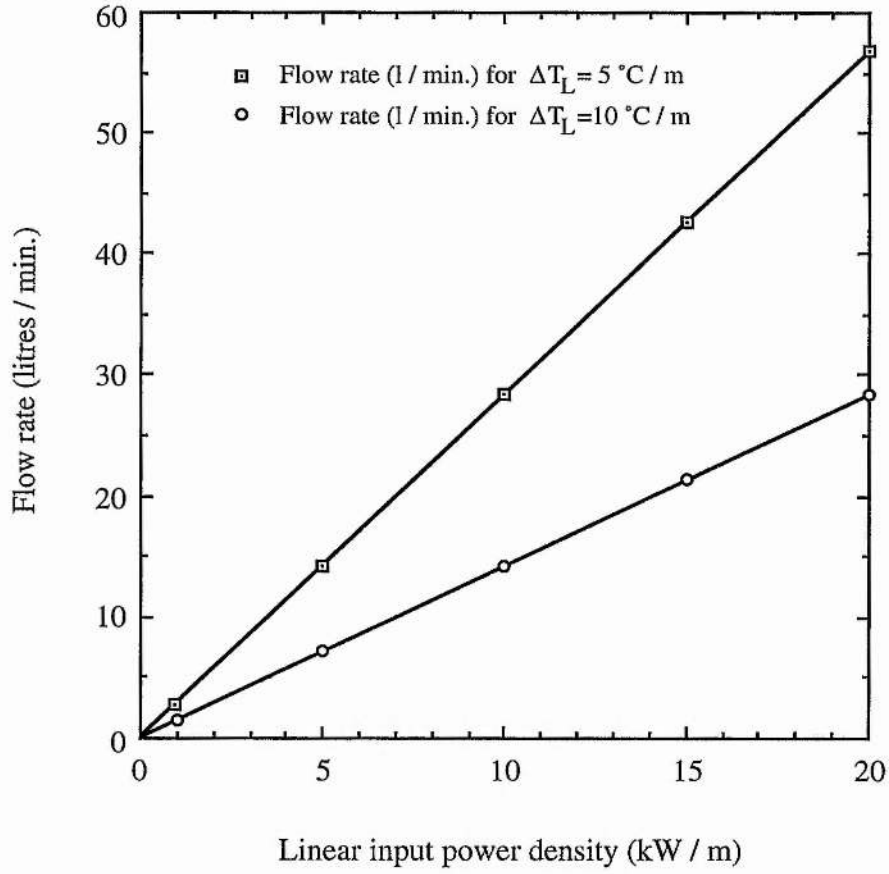

Figure 2.8 **Graph of the water flow rate required to keep the longitudinal water temperature gradient at 5°C m^{-1} and 10°C m^{-1} against linear input power density.**

Tube id = 15 mm	T_{Wall} = 600°C
Tube od = 20 mm	T_{Water} = 15°C
X_{Quartz} = 1.5 mm	$\lambda_{Beryllia}$ = 62 W m^{-1} K^{-1}
X_{Water} = 1.5 mm	λ_{Helium} = 0.25 W m^{-1} K^{-1}
Water speed = 1 m s^{-1}	λ_{Quartz} = 1.4 W m^{-1} K^{-1}
Tube emissivity = 0.5	(X_i = thickness of 'i')

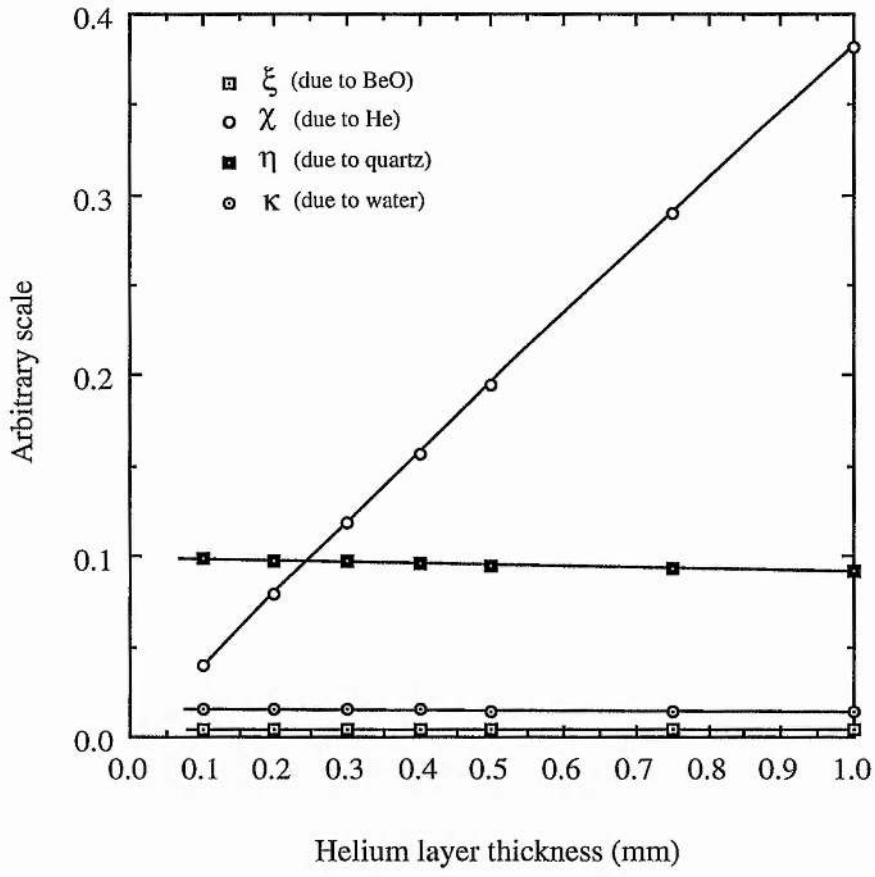

Figure 2.9 **A comparison of the heat transfer terms involved in water cooling. The helium layer thickness is varied by altering the diameters of the outer lying quartz tubes.**

Figure 2.10 Definitions of user inputs for Water-Cooled Laser Designer 1.

Tube id = The inner diameter of the discharge tube, measured at room temperature in millimetres.

Tube od = The outer diameter of the discharge tube, measured at room temperature in millimetres.

Quartz thickness = The difference between the inner and outer radii of the quartz tube separating the water from the helium layer, measured at room temperature in millimetres.

Tube length = The length of discharge tube in metres.

Tube emissivity = An estimate of the emissivity of the outer surface of the discharge tube (~0.5 normally).

Twall = The optimum operating temperature of the innermost surface of the discharge tube in °C.

Tfluid = The temperature of the water entering the cooling jacket in °C.

Helium thickness = The difference between the inner radius of the quartz tube which separates the water from the helium layer and the outer radius of the discharge tube, measured at room temperature in millimetres.

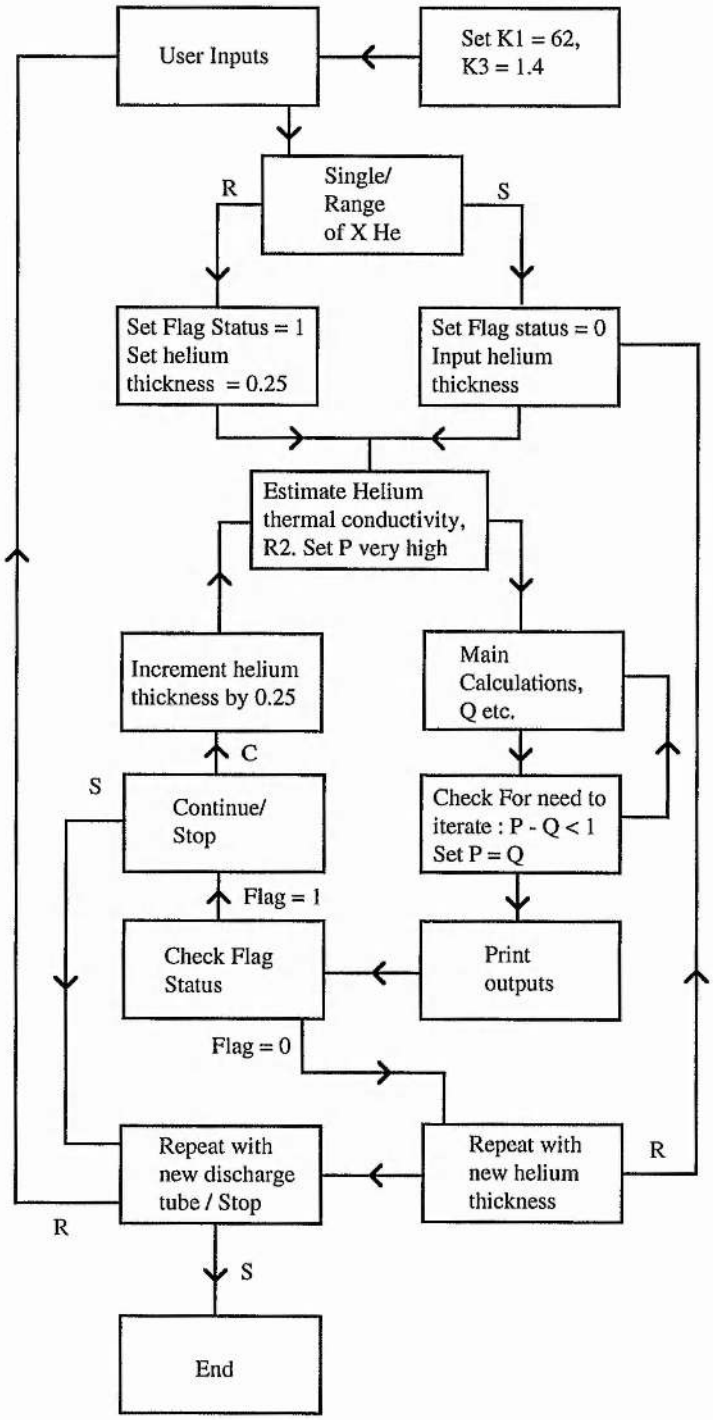

Figure 2.11 Flow diagram for Water-Cooled Laser Designer 1.

Figure 2.12 List of outputs from Water-Cooled Laser Designer 1.

Q/L tot = The power per unit length which must be supplied to the specified laser tube in order to attain the required discharge channel wall temperature, Twall.

Q cond+conv = The rate of heat removal from the specified laser tube through the combined processes of conduction and forced convection.

Q rad = The rate of heat removal from the specified laser tube through the process of radiation.

Q tot = The power which must be supplied to the specified laser tube in order to attain the required discharge channel wall temperature, Twall.

Nominal helium thickness = The difference between the inner radius of the quartz tube separating the water from the helium layer and the outer radius of the discharge tube, measured at room temperature.

Actual helium temperature = The calculated difference between the inner radius of the quartz tube separating the water from the helium layer and the outer radius of the discharge tube when the laser tube is operating at the specified Twall.

ΔT tube = The difference between the inner and outer surface temperatures of the discharge tube when the laser tube is operating at the specified Twall.

ΔT helium = The difference between the inner and outer surface temperatures of the helium layer when the laser tube is operating at the specified Twall.

ΔT quartz = The difference between the inner and outer surface temperatures of the quartz tube (which separates the helium layer from the water) when the laser tube is operating at the specified Twall.

Water flow rate = The volume of cooling water, in litres, which flows through the cooling jacket in one minute.

```
>          Thermal modelling program for helium filled,
               water-cooled beryllia laser tubes

                          Version 11.2

                          T. R. Pugsley
                       Copyright 1992,1994

 Enter tube id in mm, Tube od in mm, Quartz thickness in mm,
 Tube length in metres, Tube emissivity, Twall (°C) , Tfluid (°C)

?8,31,1.5,0.4,0.5,600,10

 To try a single helium layer thickness type S,
 for an 0.25 mm incremented range of Helium thicknesses type R
?s

 Enter desired helium thickness in mm
?3

 Q/L tot = 6327 W/m, Q cond+conv = 1942 W, Q rad = 589 W, Q tot = 2531 W
 at a nominal He thickness of 3 mm, actual He thickness of 2.93 mm.
 ΔT tube = 16.9 °C, ΔT helium = 530 °C, ΔT quartz = 43 °C

 For a water temp gradient of < 10 °C/m, the water flow rate must be > 9 litres/min

 Type D to try a different helium thickness, S to stop
?s
 Would you like to design for a different discharge tube? (type Y/N)
?n
 Design session terminated
>
```

Figure 2.13 A sample printout for Water-Cooled Laser Designer 1.

2.11 References

1. Butler, M. S. and Piper, J. A.,
Appl. Phys. Lett. **45**, (1984), pp. 707-709

2. Multilab Data Book

3. McLucas, C. W. and Mcintosh, A. I.,
J. Phys. D: Appl. Phys. **20** (1987) pp. 591-596

4. Butler, M. S. and Piper, J. A.,
IEEE J. Quantum Electron. **QE21**, No. 10, (1985), pp. 1563-1566

5. Consolidated Beryllia Ltd. (CBL),
P.O. Box 5,
Marble Hall Road,
Milford Haven.

6. Bethel, J. W. and Little, C. E.,
Opt. Commun. **84** , No. 5-6, (1991), pp. 317-322

7. Bukshpun, L. M. , Latush, E. L. and Sem, M. F.,
Sov. J. Quantum Electron. **18**, (1988), pp. 1098-1103

8. Chapman, A.J.,
Heat Transfer, p. 68
Macmillan (New York), 1974

9. Chapman, A.J.,
Heat Transfer, p. 69
Macmillan (New York), 1974

10. Chapman, A.J.,
Heat Transfer, p. 382
Macmillan (New York), 1974

11. Chapman, A. J.,
Heat Transfer, p. 368
Macmillan (New York), 1974

12. Chapman, A. J.,
Heat Transfer, p. 280
Macmillan (New York), 1974

13. Chapman, A. J.,
Heat Transfer, p. 343
Macmillan (New York), 1974

14. Chapman, A. J.,
Heat Transfer, p. 341
Macmillan (New York), 1974

15. Chapman, A. J.,
Heat Transfer, p. 586
Macmillan (New York), 1974

16. Chapman, A. J.,
Heat Transfer, p. 344
Macmillan (New York), 1974

CHAPTER 3:

Results of gas temperature modelling for helium-filled laser tubes

3.1 Gas temperature modelling: an introduction

Once the required input power for a given laser tube has been calculated, attention must be given to the temperature of the gas mixture making up the active volume. In the following sections *gas temperature* and *average gas temperature* refer to those temperatures of the buffer gas, the partial pressure of the lasing component being very low in comparison to the buffer gas pressure (p_{Sr} = 0.05 torr, p_{He} >100 torr).

The average gas temperature is an important quantity with regard to laser performance. It must be limited to achieve successful SRL operation since there is an average gas temperature (2300 K) above which lasing cannot be obtained [1]. This maximum average gas temperature arises because the population inversion in an SRL is extremely temperature dependent (see Chapters 1 and 4). The radial gas temperature profile in a laser tube is important because the concentration of the buffer gas will follow the reciprocal of its temperature, provided that the degree of ionization is negligible. This leads to spatial non-uniformities of the species densities and consequently to gain variations across the laser tube which affect its total average output power (see Chapter 4).

Modelling laser gas temperatures enables the laser designer to determine how the gas temperatures (and hence laser output power) are affected by input power and volume scaling (which are dealt with in detail in Chapter 4). It is also a useful exercise as it allows different tube geometries to be studied with respect to their effectiveness at

minimizing the gas temperature during and after the discharge. The most commonly used discharge tubes possess cylindrical bores. Recently [2], interest has been shown in discharge channels of rectangular cross-section (24mm by 8 mm) as it is believed that these will exhibit lower gas temperature maxima than a cylindrical bore tube of the same cross-sectional area (corresponding to a bore diameter of 15.5 mm), for the same input power density [3].

In the following sections three gas temperature models are developed and discussed. These are for the cases of (i) radial heat transfer out of an infinitely long cylindrical discharge channel, (ii) one-dimensional transverse heat transfer from an infinitely long rectangular bore discharge tube and (iii) two-dimensional transverse heat transfer from an infinitely long rectangular bore discharge tube. In the modelling that follows it is assumed, as was done by Kushner and Warner for the case of the copper-vapour laser [4], that there is uniform deposition of heat throughout the discharge channel volume. This is a reasonable assumption as experiments performed by Bukshpun et al. have shown the power absorbed by the strontium laser tube medium to be uniformly distributed throughout its volume [1]. The system is treated as one in steady-state since it has previously been shown (Section 2.4) that steady-state conditions prevail under typical laser operating conditions (i.e., for specific input pulse energies of <5 mJ cm^{-3}, corresponding to a fractional change in gas temperature of less than 10%).

3.2 The gas temperature in a helium-filled laser tube of cylindrical bore

Poisson's equation, describing the steady-state conduction of heat, through an arbitrary volume, within which heat is generated uniformly at a rate q^* per unit volume, is:

$$\lambda \nabla^2 T + q^* = 0. \qquad [3.2.1]$$

Since the volume to be considered here is the active volume of a laser tube with a cylindrical bore, the gradient is recast in cylindrical co-ordinates. The laser tube is treated as being of infinite length, so that only the radial conduction of heat is considered. Poisson's equation for the system therefore becomes:

$$\frac{\mathrm{d}^2 T}{\mathrm{d}r^2} + \frac{1}{r}\frac{\mathrm{d}T}{\mathrm{d}r} + \frac{q^*}{\lambda} = 0, \qquad [3.2.2]$$

which can be rewritten in the form:

$$\frac{\mathrm{d}}{\mathrm{d}r}\left(r\frac{\mathrm{d}T}{\mathrm{d}r}\right) + \frac{rq^*}{\lambda} = 0. \qquad [3.2.3]$$

Helium's thermal conductivity is a function of its temperature, as discussed in Section 2.3:

$$\lambda(T) = \lambda_0 T^{0.73}. \qquad [3.2.4]$$

To incorporate the variation of the gas thermal conductivity, Equation 3.2.3 must be rewritten as:

$$\frac{\mathrm{d}}{\mathrm{d}r}\left(r\frac{\mathrm{d}T}{\mathrm{d}r}\right)+\frac{rq^*}{\lambda_0 T^{0.73}}=0. \qquad [3.2.5]$$

The boundary conditions for the system are as follows:

(i) at $r = 0$ a point of inflection must exist due to symmetry, so that $\mathrm{d}T / \mathrm{d}r = 0$ and

(ii) at $r = \mathrm{R}$, the tube radius, T is equal to the discharge channel wall temperature, T_w.

Integrating Equation 3.2.5 once with respect to r yields:

$$r\frac{\mathrm{d}T}{\mathrm{d}r}+\frac{r^2q^*}{2\lambda_0 T^{0.73}}+\mathrm{C}_1=0. \qquad [3.2.6]$$

Application of the first boundary condition reveals that $\mathrm{C}_1 = 0$, so that we can separate the variables and integrate:

$$\int T^{0.73}\mathrm{d}T=-\int\frac{rq^*}{2\lambda_0}\,\mathrm{d}r. \qquad [3.2.7]$$

This leads to

$$\frac{T^{1.73}}{1.73}+\frac{r^2q^*}{4\lambda_0}=\mathrm{C}_2. \qquad [3.2.8]$$

The second boundary condition gives:

$$C_2 = \frac{T_w^{1.73}}{1.73} + \frac{R^2 q^*}{4\lambda_0}, \qquad [3.2.9]$$

so that the equation describing the radial gas temperature profile is:

$$T(r) = \left(T_w^{1.73} + \frac{1.73 q^*}{4\lambda_0}(R^2 - r^2) \right)^{\left(\frac{1}{1.73}\right)}. \qquad [3.2.10]$$

The average gas temperature is given by the expression (derived in Appendix B):

$$\langle T_g \rangle = \frac{4\lambda_0}{2.73 q^* R^2}\left(T(0)^{2.73} - T_w^{2.73} \right), \qquad [3.2.11]$$

where the axis gas temperature, $T(0)$, follows from Equation 3.2.10, as:

$$T(0) = \left(T_w^{1.73} + \frac{1.73 q^*}{4\lambda_0} R^2 \right)^{\left(\frac{1}{1.73}\right)}. \qquad [3.2.12]$$

A BASIC program (Gas Temperature Determinator A) has been written to calculate the radial gas temperatures and the average gas temperature. Figure 3.1 shows a flow diagram for this program and Figure 3.2 a sample printout. The program's code is listed in Appendix C. Figure 3.3 displays the expected radial temperature profile for a helium-filled discharge channel of 15.5 mm diameter, with a wall temperature of 600°C for a range of input power densities.

3.3 The gas temperature in a helium filled discharge channel of rectangular cross-section

Heat conduction within a discharge tube of rectangular bore is a multidimensional heat conduction problem. Poisson's equation, describing the steady-state conduction of heat, through a volume with a rectangular cross-section, within which heat is generated uniformly at a rate q^* per unit volume, is:

$$\frac{\partial^2 T}{\partial x^2}+\frac{\partial^2 T}{\partial y^2}+\frac{\partial^2 T}{\partial z^2}+\frac{q^*}{\lambda}=0. \qquad [3.3.1]$$

Here, the discharge channel will be treated as being of infinite length, so that conduction in the z-direction is negligible. The dependence of helium's thermal conductivity on the gas temperature must be included, so that Poisson's equation for the system becomes:

$$\frac{\partial^2 T}{\partial x^2}+\frac{\partial^2 T}{\partial y^2}+\frac{q^*}{\lambda_0 T^{0.73}}=0. \qquad [3.3.2]$$

Equation 3.3.2 is a *non-linear* differential equation, so that the principle of superposition of solutions, which is normally applied to multidimensional heat conduction problems involving *linear* differential equations, cannot be applied here in order to solve for the gas temperature. Two methods which can be used to obtain approximate solutions to Equation 3.3.2 are described below.

3.3.1 1-Dimensional approximation to the problem of heat conduction through a rectangular volume

If a discharge channel of rectangular cross-section approaches infinite height, heat conduction in the y-direction becomes negligible and, following the method used to treat the cylindrical case, the temperature distribution in the x-direction is given by:

$$T(x)=\left(T_w{}^{1.73}+\frac{1.73q^*}{2\lambda_0}\left[\left(\frac{W}{2}\right)^2-x^2\right]\right)^{\left(\frac{1}{1.73}\right)} \qquad [3.3.3]$$

where W, is the width of the discharge tube's bore. A BASIC computer program (Gas Temperature Determinator B) has been written to calculate the gas temperature in the limit of no heat transfer in the y-direction, as a function of position in the x-direction. Equation 3.3.3 is non-integrable, so that the average gas temperature cannot be obtained algebraically. A second program (Average Gas Temperature Determinator) has, therefore, been written to integrate Equation 3.3.3 numerically with respect to x and thus obtain the approximate average gas temperature. The codes for these programs are listed in Appendix D. Figure 3.4 shows a flow diagram for Gas Temperature Determinator B and Figure 3.5 gives a sample printout for this program. Figure 3.6 shows a flow diagram for the Average Gas Temperature Determinator and Figure 3.7 gives a sample printout for this program. The method used by the Average Gas Temperature Determinator to perform the numerical integration of Equation 3.3.3 is described in Appendix D.

Use of the programs Gas Temperature Determinator B and Average Gas Temperature Determinator will only lead to estimates of the temperature distribution and average gas temperature for practical rectangular bore SRL discharge tubes. Clearly, as the aspect ratio of the discharge channel becomes greater, the results will become more accurate. The laser designer must decide whether results so obtained are sufficiently accurate to be of use (see Section 3.3.3).

3.3.2 2-Dimensional approximation to the problem of heat conduction through a rectangular volume

It is possible to solve the multidimensional problem of heat transfer in a rectangular volume of variable thermal conductivity more accurately than in the 1-dimensional treatment given previously, by resorting to numerical analysis. Generality is lost, however, as it is then necessary to treat each aspect ratio individually. The use of the *finite difference approximation* as a tool for solving the multidimensional Poisson's equation is described below.

Suppose $T = T(x, y)$ is an unknown function, describing the temperature distribution within a rectangular volume of infinite length. This function must satisfy Poisson's equation at all points (x, y). Approximations to the second derivatives can be obtained by performing forward and backward expansions of $T = T(x, y)$ using Taylor's theorem of the mean and adding the forward expansion to the backward expansion.

The forward expansion of the function $T = T(x, y)$, at the point $(x+\delta x, y)$ around the point (x, y), is:

$$T(x+\delta x, y) = T(x, y) + \delta x\left(\frac{\partial T}{\partial x}\right)_{x,y} + \frac{\delta x^2}{2!}\left(\frac{\partial^2 T}{\partial x^2}\right)_{x,y} + \frac{\delta x^3}{3!}\left(\frac{\partial^3 T}{\partial x^3}\right)_{x,y} + \ldots\ldots, \quad [3.3.4]$$

where terms of the order of δx^4 and higher are neglected. The backward expansion of the function $T = T(x, y)$, at the point $(x-\delta x, y)$ around the point (x, y), is, similarly:

$$T(x-\delta x, y) = T(x, y) - \delta x\left(\frac{\partial T}{\partial x}\right)_{x,y} + \frac{\delta x^2}{2!}\left(\frac{\partial^2 T}{\partial x^2}\right)_{x,y} - \frac{\delta x^3}{3!}\left(\frac{\partial^3 T}{\partial x^3}\right)_{x,y} + \ldots\ldots \quad [3.3.5]$$

Adding Equations 3.3.4 and 3.3.5 yields:

$$T(x+\delta x, y) + T(x-\delta x, y) \approx 2T(x, y) + \delta x^2\left(\frac{\partial^2 T}{\partial x^2}\right)_{x,y}, \quad [3.3.6]$$

so that the second derivative can be approximated by:

$$\left(\frac{\partial^2 T}{\partial x^2}\right)_{x,y} \approx \frac{1}{\delta x^2}\left[T(x+\delta x, y) + T(x-\delta x, y) - 2T(x, y)\right]. \quad [3.3.7]$$

Similarly, the second derivative of $T = T(x, y)$ with respect to y can be approximated by:

$$\left(\frac{\partial^2 T}{\partial y^2}\right)_{x,y} \approx \frac{1}{\delta y^2}\left[T(x, y+\delta y) + T(x, y-\delta y) - 2T(x, y)\right]. \quad [3.3.8]$$

If $\delta x = \delta y = \delta$, from Equations 3.3.2, 3.3.7 and 3.3.8, the gas temperature at a point P(x, y) must satisfy the central difference relation:

$$T(x+\delta, y) + T(x-\delta, y) + T(x, y+\delta) + T(x, y-\delta) - 4T(x, y) + \frac{\delta^2 q^*}{\lambda_0 T(x, y)^{0.73}} = 0, \quad [3.3.9]$$

so that the gas temperature at any point, P(x, y), is known in terms of the gas temperatures at the four neighbouring points.

The rectangular bore laser tube of interest [2, 5], has a bore cross-section 8 mm x 24 mm. This can be divided up into 192 (1 mm x 1 mm) squares, although, due to symmetry, only 48 squares need to be considered. The temperatures at the corners of these squares are to be determined, though the wall temperature is known. Equation 3.3.9 was used to construct the 48 non-linear simultaneous equations, listed below, which describe the gas temperature at the 48 points at which it is unknown. λ_0 and q^* are expressed in terms of millimetres.

$$\text{P}(1, 1): \quad \lambda_{1,1}\,(2T_w + T_{2,1} + T_{1,2} - 4T_{1,1}) + q^* = 0 \quad [3.3.10]$$

$$\text{P}(2, 1): \quad \lambda_{2,1}\,(T_{1,1} + T_{3,1} + T_w + T_{2,2} - 4T_{2,1}) + q^* = 0 \quad [3.3.11]$$

$$\text{P}(3, 1): \quad \lambda_{3,1}\,(T_{2,1} + T_{4,1} + T_w + T_{3,2} - 4T_{3,1}) + q^* = 0 \quad [3.3.12]$$

$$P(4,1): \quad \lambda_{4,1}(2T_{3,1} + T_w + T_{4,2} - 4T_{4,1}) + q^* = 0 \qquad [3.3.13]$$

$$P(1,2): \quad \lambda_{1,2}(T_w + T_{2,2} + T_{1,1} + T_{1,3} - 4T_{1,2}) + q^* = 0 \qquad [3.3.14]$$

$$P(2,2): \quad \lambda_{2,2}(T_{1,2} + T_{3,2} + T_{2,1} + T_{2,3} - 4T_{2,2}) + q^* = 0 \qquad [3.3.15]$$

$$P(3,2): \quad \lambda_{3,2}(T_{2,2} + T_{4,2} + T_{3,1} + T_{3,3} - 4T_{3,2}) + q^* = 0 \qquad [3.3.16]$$

$$P(4,2): \quad \lambda_{4,2}(2T_{3,2} + T_{4,1} + T_{4,3} + 4T_{4,2}) + q^* = 0 \qquad [3.3.17]$$

$$P(1,3): \quad \lambda_{1,3}(T_w + T_{2,3} + T_{1,2} + T_{1,4} - 4T_{1,3}) + q^* = 0 \qquad [3.3.18]$$

$$P(2,3): \quad \lambda_{2,3}(T_{1,3} + T_{3,3} + T_{2,2} + T_{2,4} - 4T_{2,3}) + q^* = 0 \qquad [3.3.19]$$

$$P(3,3): \quad \lambda_{3,3}(T_{2,3} + T_{4,3} + T_{3,2} + T_{3,4} - 4T_{3,3}) + q^* = 0 \qquad [3.3.20]$$

$$P(4,3): \quad \lambda_{4,3}(2T_{3,3} + T_{4,1} + T_{4,3} + 4T_{4,3}) + q^* = 0 \qquad [3.3.21]$$

$$P(1,4): \quad \lambda_{1,4}(T_w + T_{2,4} + T_{1,3} + T_{1,5} - 4T_{1,4}) + q^* = 0 \qquad [3.3.22]$$

$$P(2,4): \quad \lambda_{2,4}(T_{1,4} + T_{3,4} + T_{2,3} + T_{2,5} - 4T_{2,4}) + q^* = 0 \qquad [3.3.23]$$

$$P(3,4): \quad \lambda_{3,4}(T_{2,4} + T_{4,4} + T_{3,3} + T_{3,5} - 4T_{3,4}) + q^* = 0 \qquad [3.3.24]$$

$$P(4,4) \quad \lambda_{4,4}(2T_{3,4} + T_{4,3} + T_{4,5} - 4T_{4,4}) + q^* = 0 \qquad [3.3.25]$$

$$P(1,5): \quad \lambda_{1,5}(T_w + T_{2,5} + T_{1,4} + T_{1,6} - 4T_{1,5}) + q^* = 0 \qquad [3.3.26]$$

$$P(2,5): \quad \lambda_{2,5}(T_{1,5} + T_{3,5} + T_{2,4} + T_{2,6} - 4T_{2,5}) + q^* = 0 \qquad [3.3.27]$$

$$P(3,5): \quad \lambda_{3,5}(T_{2,5} + T_{4,5} + T_{3,4} + T_{3,6} - 4T_{3,5}) + q^* = 0 \qquad [3.3.28]$$

$$P(4,5): \quad \lambda_{4,5}(2T_{3,5} + T_{4,4} + T_{4,6} - 4T_{4,5}) + q^* = 0 \qquad [3.3.29]$$

$$P(1,6): \quad \lambda_{1,6}(T_w + T_{2,6} + T_{1,5} + T_{1,7} - 4T_{1,6}) + q^* = 0 \qquad [3.3.30]$$

$$P(2,6): \quad \lambda_{2,6}(T_{1,6} + T_{3,6} + T_{2,5} + T_{2,7} - 4T_{2,6}) + q^* = 0 \qquad [3.3.31]$$

$$P(3,6): \quad \lambda_{3,6}(T_{2,6} + T_{4,6} + T_{3,5} + T_{3,7} - 4T_{3,6}) + q^* = 0 \qquad [3.3.32]$$

$$P(4,6): \quad \lambda_{4,6}(2T_{3,6} + T_{4,5} + T_{4,7} - 4T_{4,6}) + q^* = 0 \qquad [3.3.33]$$

$$P(1,7): \quad \lambda_{1,7}(T_w + T_{2,7} + T_{1,6} + T_{1,7} - 4T_{1,8}) + q^* = 0 \qquad [3.3.34]$$

$$P(2,7): \quad \lambda_{2,7}(T_{1,7} + T_{3,7} + T_{2,6} + T_{2,8} - 4T_{2,7}) + q^* = 0 \qquad [3.3.35]$$

$$P(3,7): \quad \lambda_{3,7}(T_{2,7} + T_{4,7} + T_{3,6} + T_{3,8} - 4T_{3,7}) + q^* = 0 \qquad [3.3.36]$$

$$P(4,7): \quad \lambda_{4,7}(2T_{3,7} + T_{4,6} + T_{4,8} - 4T_{4,7}) + q^* = 0 \qquad [3.3.37]$$

$$P(1,8): \quad \lambda_{1,8}(T_w + T_{2,8} + T_{1,7} + T_{1,9} - 4T_{1,9}) + q^* = 0 \qquad [3.3.38]$$

$$P(2,8): \quad \lambda_{2,8}(T_{1,8} + T_{3,8} + T_{2,7} + T_{2,9} - 4T_{2,8}) + q^* = 0 \qquad [3.3.39]$$

$$P(3,8): \quad \lambda_{3,8}(T_{2,8} + T_{4,8} + T_{3,7} + T_{3,9} - 4T_{3,8}) + q^* = 0 \qquad [3.3.40]$$

$$P(4,8): \quad \lambda_{4,8}(2T_{3,8} + T_{4,7} + T_{4,9} - 4T_{4,8}) + q^* = 0 \qquad [3.3.41]$$

$$P(1,9): \quad \lambda_{1,9}(T_w + T_{2,9} + T_{1,8} + T_{1,10} - 4T_{1,9}) + q^* = 0 \qquad [3.3.42]$$

$$P(2,9): \quad \lambda_{2,9}(T_{1,9} + T_{3,9} + T_{2,8} + T_{2,10} - 4T_{2,9}) + q^* = 0 \qquad [3.3.43]$$

$$P(3,9): \quad \lambda_{3,9}(T_{2,9} + T_{4,9} + T_{3,8} + T_{3,10} - 4T_{3,9}) + q^* = 0 \qquad [3.3.44]$$

$$P(4,9): \quad \lambda_{4,9}(2T_{3,9} + T_{4,8} + T_{4,10} + 4T_{4,9}) + q^* = 0 \qquad [3.3.45]$$

$$P(1,10): \quad \lambda_{1,10}(T_w + T_{2,10} + T_{1,9} + T_{1,11} - 4T_{1,10}) + q^* = 0 \qquad [3.3.46]$$

$$P(2,10): \quad \lambda_{2,10}(T_{1,10} + T_{3,10} + T_{2,9} + T_{2,11} - 4T_{2,10}) + q^* = 0 \qquad [3.3.47]$$

$$P(3,10): \quad \lambda_{3,10}(T_{2,10} + T_{4,10} + T_{3,9} + T_{3,11} - 4T_{3,10}) + q^* = 0 \qquad [3.3.48]$$

$$P(4,10): \quad \lambda_{4,10}(2T_{3,10} + T_{4,9} + T_{4,11} + 4T_{4,10}) + q^* = 0 \qquad [3.3.49]$$

$$P(1,11): \quad \lambda_{1,11}(T_w + T_{2,11} + T_{1,10} + T_{1,12} - 4T_{1,11}) + q^* = 0 \qquad [3.3.50]$$

$$P(2,11): \quad \lambda_{2,11}(T_{1,11} + T_{3,11} + T_{2,10} + T_{2,12} - 4T_{2,11}) + q^* = 0 \qquad [3.3.51]$$

$$P(3,11): \quad \lambda_{3,11}(T_{2,11} + T_{4,11} + T_{3,10} + T_{3,12} - 4T_{3,11}) + q^* = 0 \qquad [3.3.52]$$

$$P(4,11): \quad \lambda_{4,11}(2T_{3,11} + T_{4,10} + T_{4,12} - 4T_{4,11}) + q^* = 0 \qquad [3.3.53]$$

$$P(1,12): \quad \lambda_{1,12}(T_w + T_{2,12} + 2T_{1,11} - 4T_{1,12}) + q^* = 0 \qquad [3.3.54]$$

$$P(2,12): \quad \lambda_{2,12}(T_{1,12} + T_{3,12} + 2T_{2,11} - 4T_{2,12}) + q^* = 0 \qquad [3.3.55]$$

$$P(3,12): \quad \lambda_{3,12}(T_{2,12} + T_{4,12} + 2T_{3,11} - 4T_{3,12}) + q^* = 0 \qquad [3.3.56]$$

$$P(4,12): \quad \lambda_{4,12}(2T_{3,12} + 2T_{4,11} - 4T_{4,12}) + q^* = 0 \qquad [3.3.57]$$

where,

$$\lambda_{i,j} = \lambda_0 T_{i,j}^{0.73}. \qquad [3.3.58]$$

Note that the finite difference approximation neglectes terms of the order of δx^4 and higher, so that the accuracy of the method will increase as the incremental displacement is reduced, while the calculation will become more complex as more equations need to be solved.

A computer program (Gas Temperature Determinator C) has been compiled to solve the 48 non-linear difference equations generated for the laser tube of aspect ratio 3 : 1. This program is described in Appendix D. The average gas temperature can be obtained from the gas temperature data by linear approximation of the temperatures at the centres of each of the 192 squares followed by a summation of the centre temperatures and division of the sum by the cross-sectional area of the tube. Figures 3.8 to 3.12 inclusive show the gas temperature profiles obtained using Gas Temperature Determinator C for the discharge tube of rectangular bore 24 mm by 8 mm, with a wall temperature of 600°C, at the linear input power densities of 2.5, 5, 10, 15 and 20 kW m^{-1}.

3.3.3 Comparison of the 1-dimensional approximation with the 2-dimensional approximation.

The values obtained for the axis gas temperature and average gas temperature in the rectangular bore laser tube (of bore dimensions 8 mm by 24 mm) using the 1-dimensional approximation and the 2-dimensional approximation to the solution of Poisson's equation are shown in Figures 3.13 and 3.14, respectively.

For the laser tube with aspect ratio 3 : 1, the 1-dimensional approximation to the solution of the heat transfer equation overestimates the average gas temperatures, in comparison with the two dimensional approximation, by 25% for a linear input power density of 20 kW m^{-1}.

3.4 Summary

High buffer gas temperatures in the SRL lead to a low population inversion. In order to quantify the predicted superiority [3] of rectangular bore tubes over circular bore laser tubes (as far as low gas temperatures are concerned), gas temperature models for these types of tubes have been developed. In particular, we have considered the cases of: (i) radial heat transfer to the walls of an infinitely long cylindrical discharge channel and (ii) transverse heat transfer to the walls of an infinitely long rectangular discharge channel. In each case, it has been assumed that the discharge power is deposited uniformly throughout the discharge channel volume.

The conduction of heat out of a rectangular bore SRL discharge tube is a multidimensional problem with no analytic solution (since the thermal conductivity of helium is a non-linear function of temperature). Approximate solutions to Poisson's equation have therefore been sought in the case of the rectangular bore discharge tube. The simplest approach adopted was to model the problem as one of 1-dimensional transverse heat conduction (by considering only the narrowest dimension as a route for heat transfer). 2-dimensional heat transfer was modelled using the method of finite differences. In the case of a discharge channel aspect ratio of 3 : 1, modelling by 1-dimensional approximation leads to a laser gas temperature which is 25% higher than that obtained by using the 2-dimensional approximation. The results obtained from the two methods are, however, expected to converge as the discharge channel aspect ratio is made higher.

At a linear input power density of 20 kW m^{-1}, the axis-gas temperature of 2200 K obtained for the case of our rectangular bore tube by two-dimensional modelling compares very favourably with the axis-gas temperature of 3400 K expected in a circular bore tube of the same cross-sectional area. A more detailed discussion of the relative gas temperature performances of the circular and rectangular bore tubes, and their significance, is presented in Chapter 4, where output power scaling issues are dealt with.

3.5 Figures for Chapter 3

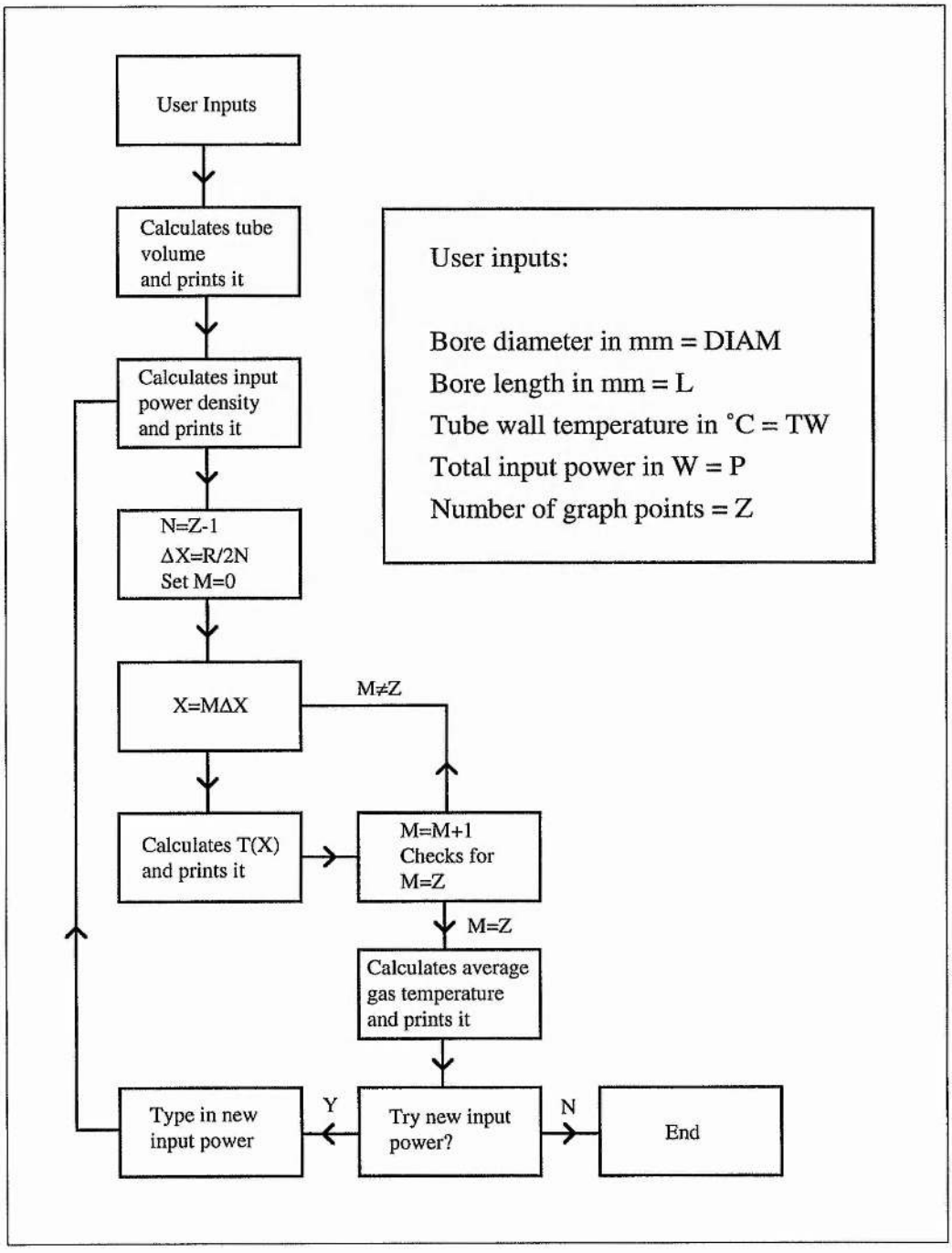

Figure 3.1 Flow diagram for Gas Temperature Determinator A.

```
>  This program calculates the steady-state gas (He) temperature
     in a discharge heated cylindrical bore laser tube as a
      function of the radial distance from the tube's axis.

                          Version 2

                Copyright T. R. Pugsley 1992, 1994

 Enter bore diameter (mm), bore length (mm),
 tube wall temperature in °C, total input power in W
 and the number of graph points desired.

?15.5,400,600,2994,11

 Gas volume = 75.5 cm^3
 Power density = 39.67 W/cm^3

 T(± 0) = 2084 K (1811 °C).
 T(± 0.775) = 2075 K (1802 °C).
 T(± 1.55) = 2047 K (1774 °C).
 T(± 2.325) = 1999 K (1726 °C).
 T(± 3.1) = 1930 K (1657 °C).
 T(± 3.875) = 1839 K (1566 °C).
 T(± 4.65) = 1724 K (1451 °C).
 T(± 5.425) = 1579 K (1306 °C).
 T(± 6.2) = 1399 K (1126 °C).
 T(± 6.975) = 1173 K (900 °C).
 T(± 7.75) = 873 K (600 °C).

 Average gas temperature = 1539 K.

 Would you like to try a different input power (y/n)?
?n
Calculation terminated
>
```

Figure 3.2 Sample print out for Gas Temperature Determinator A.

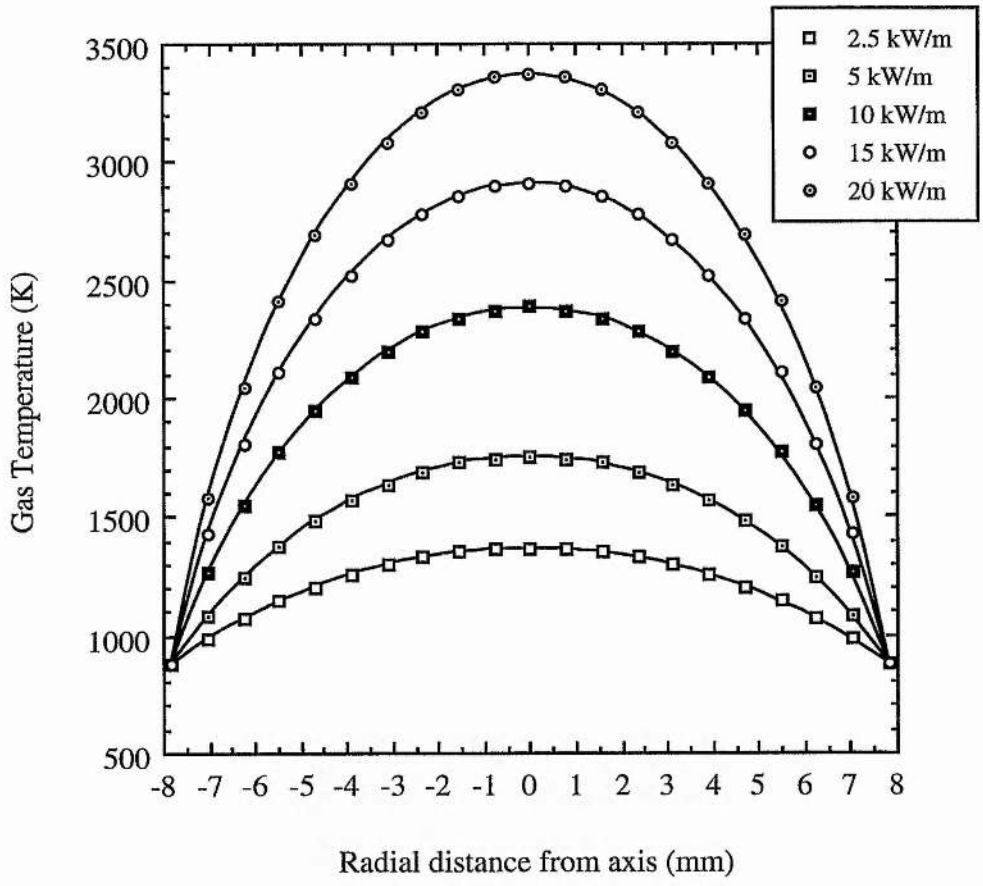

Figure 3.3 **The radial gas temperature profiles obtained using 'Gas Temperature Determinator A' for a discharge channel of diameter 15.5 mm with a wall temperature of 600°C at various linear input power densities.**

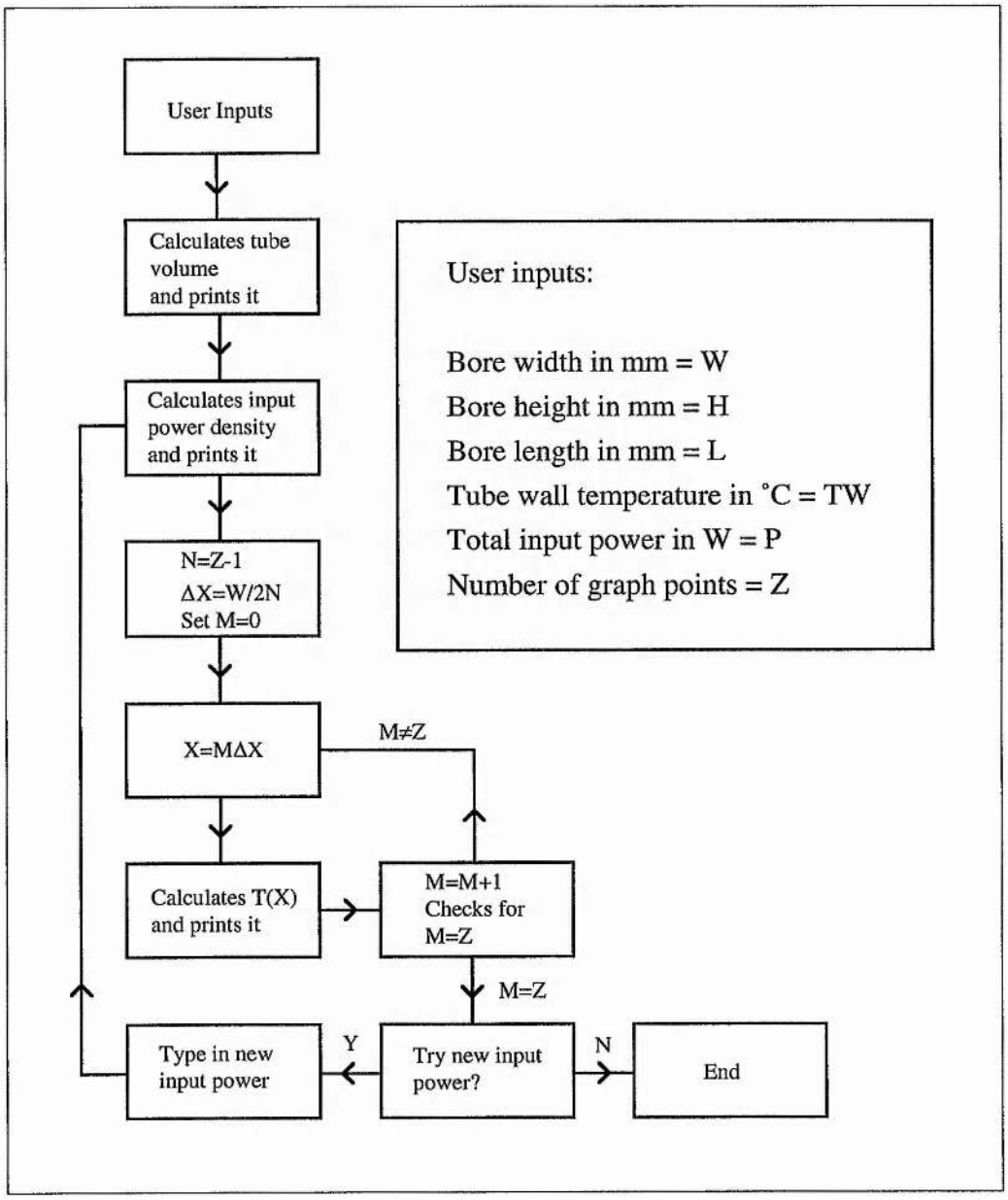

Figure 3.4 Flow diagram for Gas Temperature Determinator B.

```
>  This program calculates the steady-state gas (He) temperature
     in a discharge heated rectangular bore laser tube as a
        function of the distance from the tube's x=0 axis.

                          Version 2

                Copyright T. R. Pugsley 1992, 1994

 Enter bore width (mm), bore height (mm), bore length (mm),
 tube wall temperature in °C, total input power in W
 and the number of graph points desired.

?8,24,400,600,2994,11

 Gas volume = 76.8 cm^3
 Power density = 38.98 W/cm^3

 T(± 0) = 1595 K (1322 °C).
 T(± 0.4) = 1589 K (1316 °C).
 T(± 0.8) = 1571 K (1298 °C).
 T(± 1.2) = 1540 K (1267 °C).
 T(± 1.6) = 1497 K (1224 °C).
 T(± 2) = 1440 K (1167 °C).
 T(± 2.4) = 1368 K (1095 °C).
 T(± 2.8) = 1279 K (1006 °C).
 T(± 3.2) = 1171 K (898 °C).
 T(± 3.6) = 1038 K (765 °C).
 T(± 4) = 873 K (600 °C).

 Would you like to try a different input power (y/n)?
?n
Calculation terminated
>
```

Figure 3.5 Sample print out for Gas Temperature Determinator B.

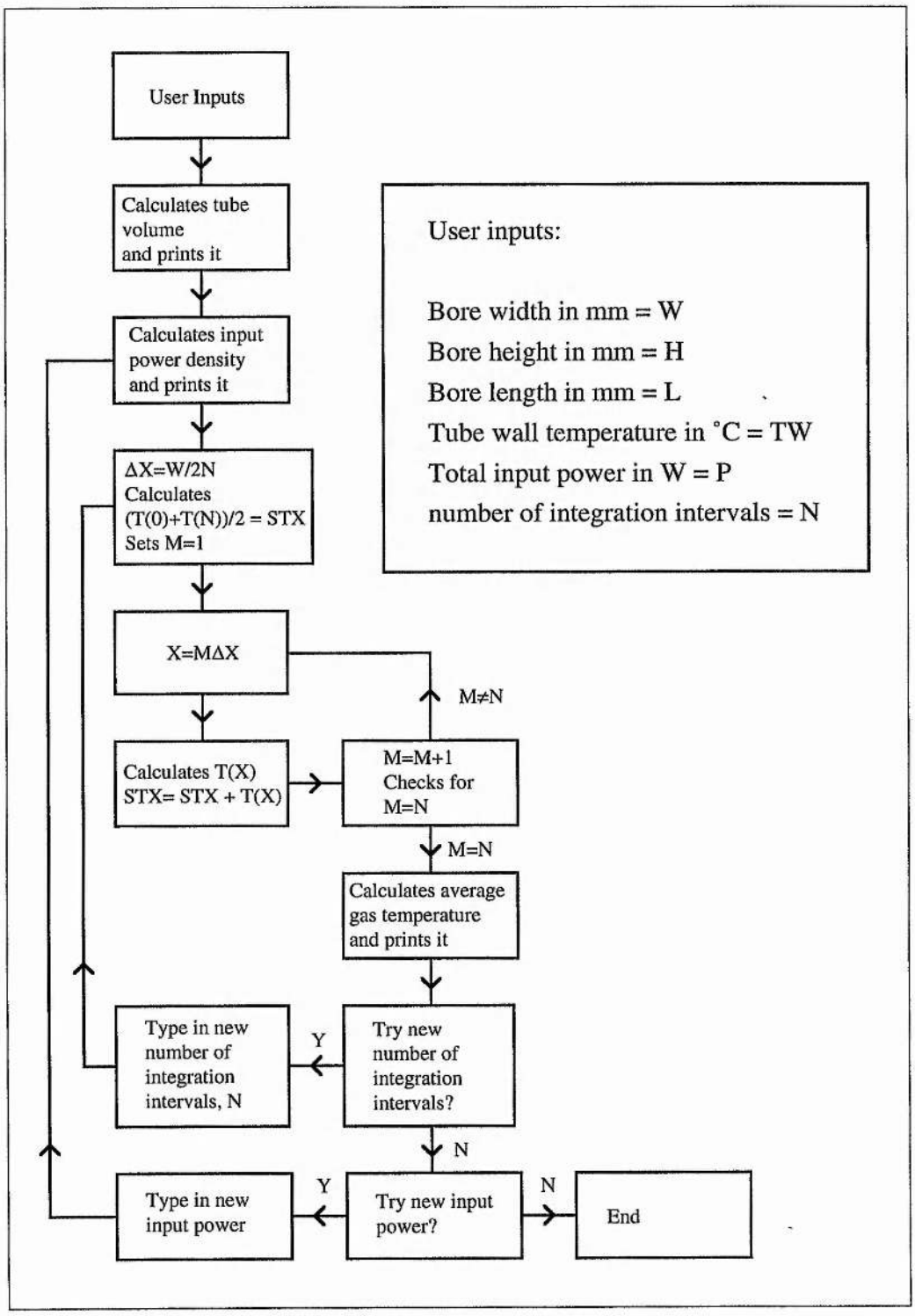

Figure 3.6 Flow diagram for Average Gas Temperature Determinator.

```
>   This program calculates the average steady-state gas (He)
 temperature in a discharge heated rectangular bore laser tube.

                        Version 2

              Copyright T. R. Pugsley 1992, 1994

 Enter bore width (mm), bore height (mm), bore length (mm),
 tube wall temperature in °C, total input power in W
 and the number of integration intervals.

?8,24,400,600,2994,50

Volume = 76.8 cm^3
Power density = 38.98 W/cm^3

.....................................................

 Average gas temperature = 1374 K (1101 °C)

 Would you like to try a new number of integration intervals (y/n)?
?n
 Would you like to try a different input power (y/n)?
?n
Calculation terminated
>
```

Figure 3.7 Sample print out for Average Gas Temperature Determinator.

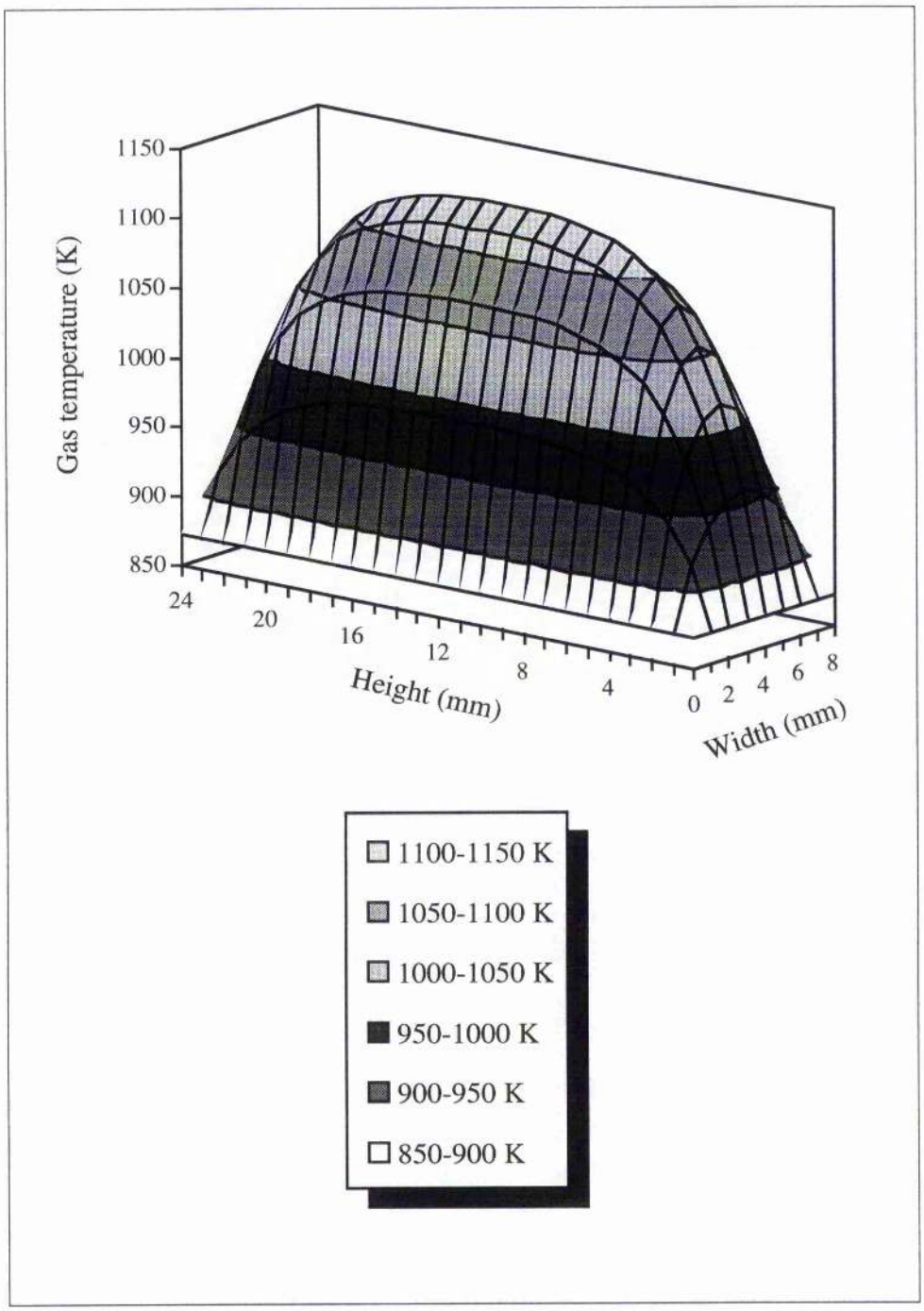

Figure 3.8 **Gas temperature profile for the rectangular discharge channel of bore 24 mm by 8 mm with a wall temperature of 600°C at a linear input power density of 2.5 kW m^{-1}.**

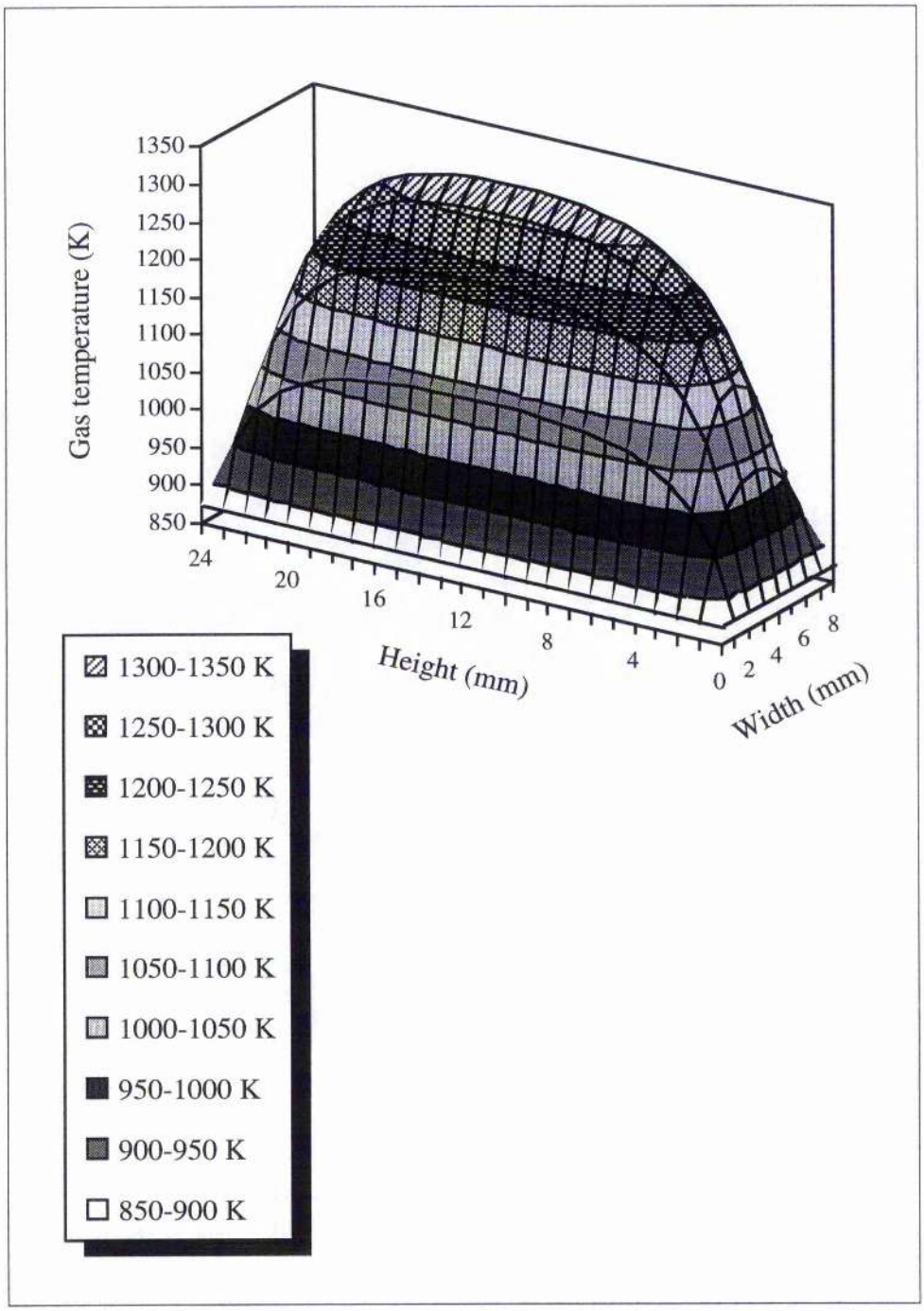

Figure 3.9 **Gas temperature profile for the rectangular discharge channel of bore 24 mm by 8 mm with a wall temperature of 600°C at a linear input power density of 5 kW m^{-1}.**

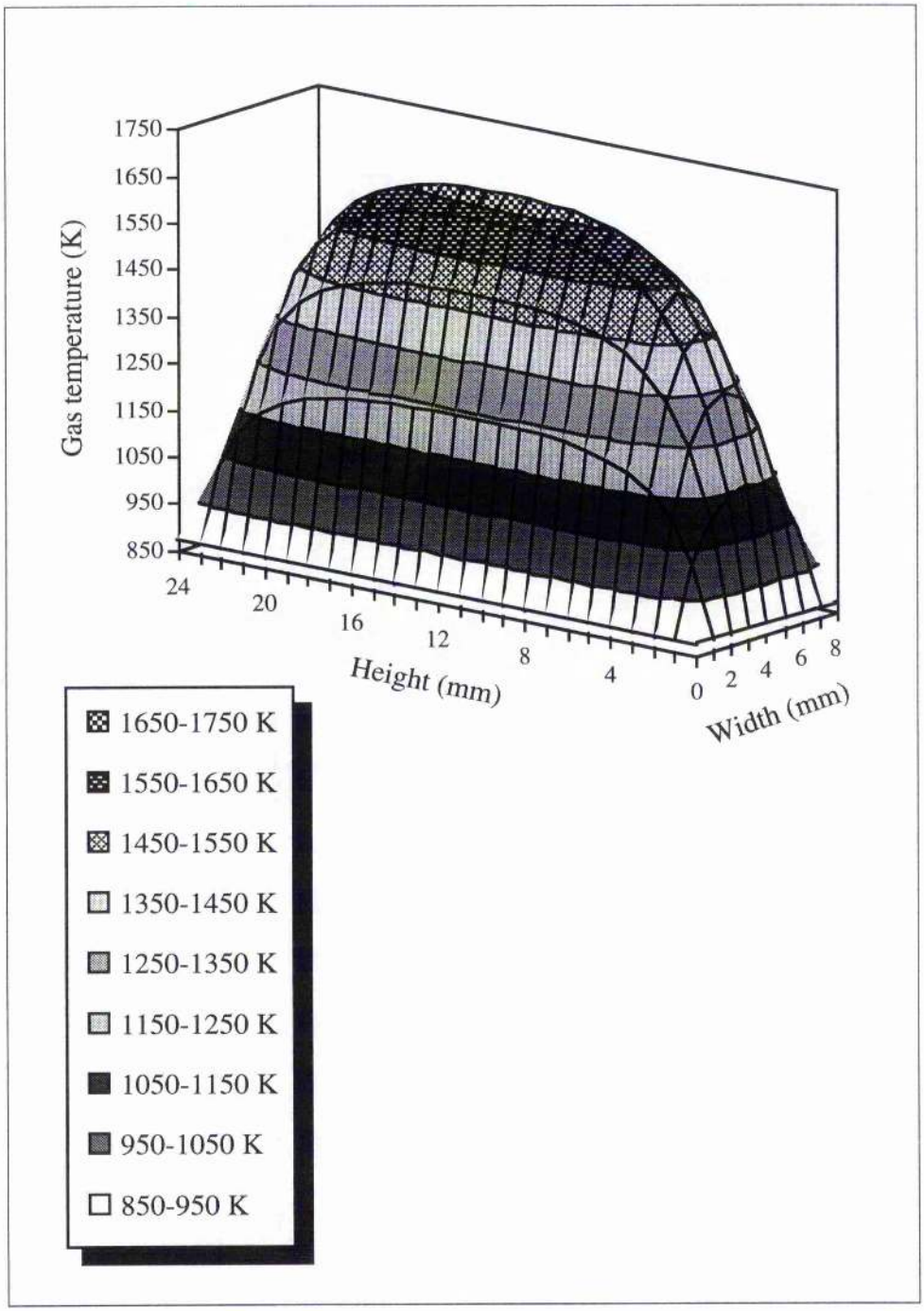

Figure 3.10 **Gas temperature profile for the rectangular discharge channel of bore 24 mm by 8 mm with a wall temperature of 600°C at a linear input power density of 10 kW m^{-1}.**

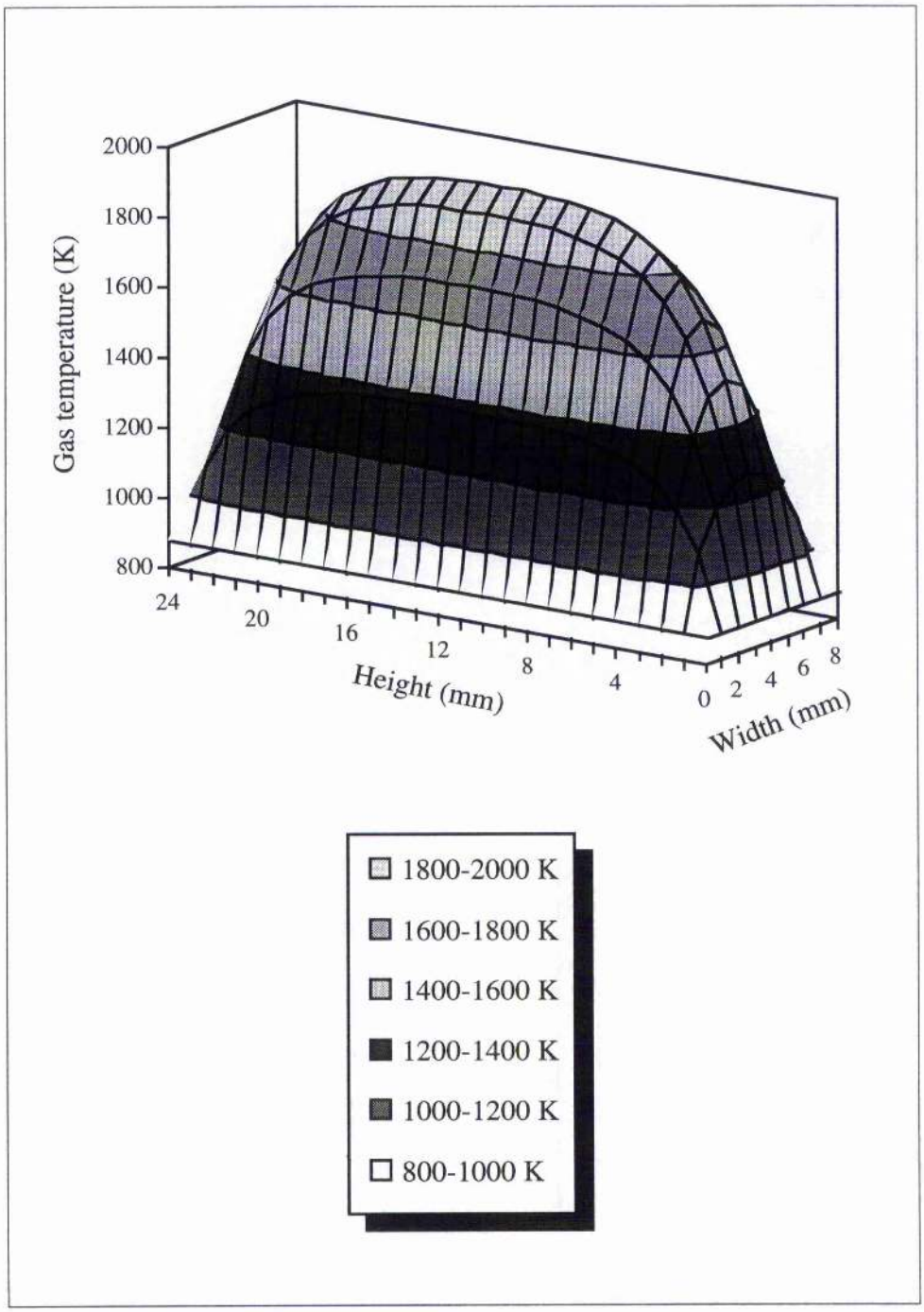

Figure 3.11 **Gas temperature profile for the rectangular discharge channel of bore 24 mm by 8 mm with a wall temperature of 600°C at a linear input power density of 15 kW m^{-1}.**

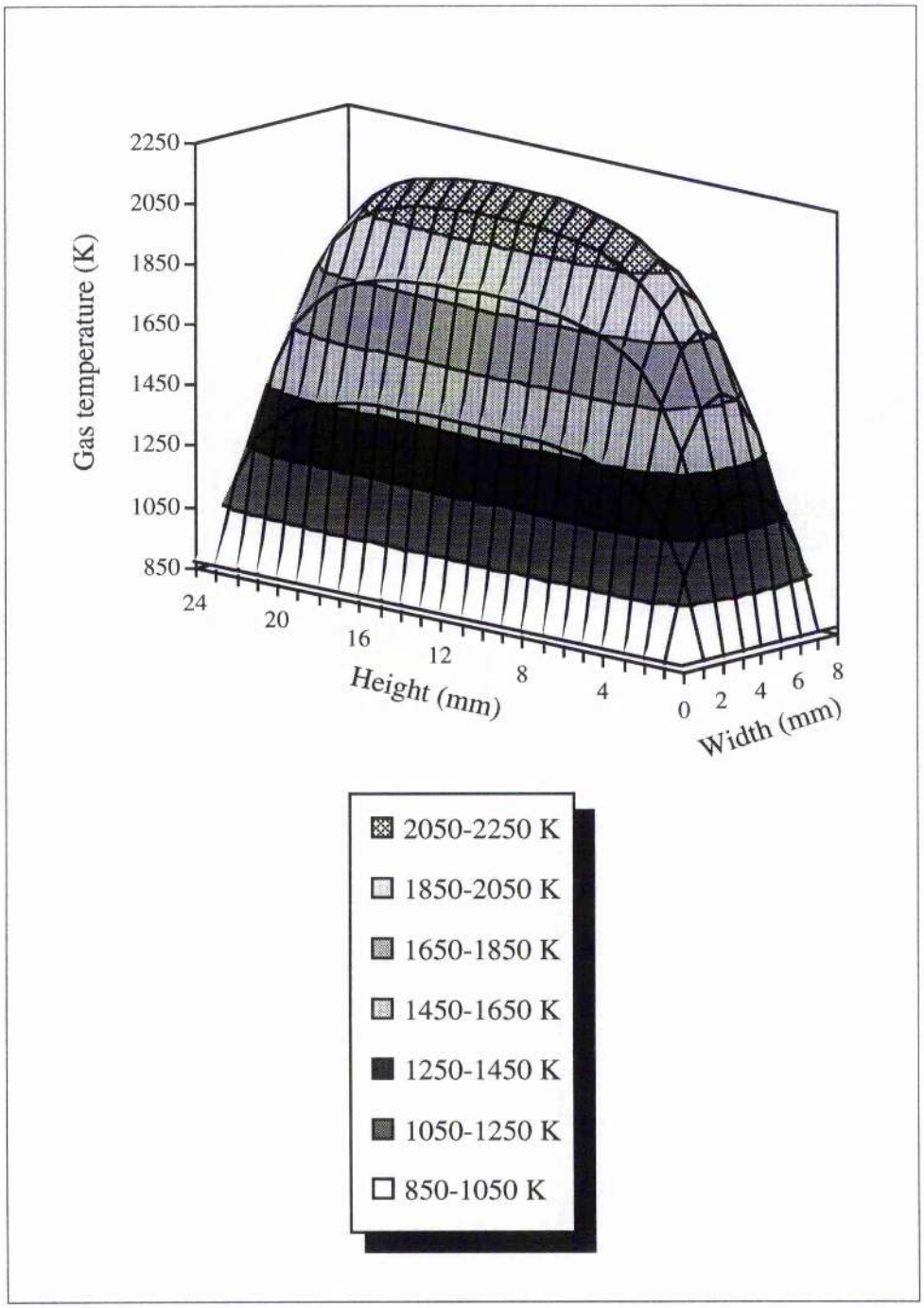

Figure 3.12 **Gas temperature profile for the rectangular discharge channel of bore 24 mm by 8 mm with a wall temperature of 600°C at a linear input power density of 20 kW m^{-1}.**

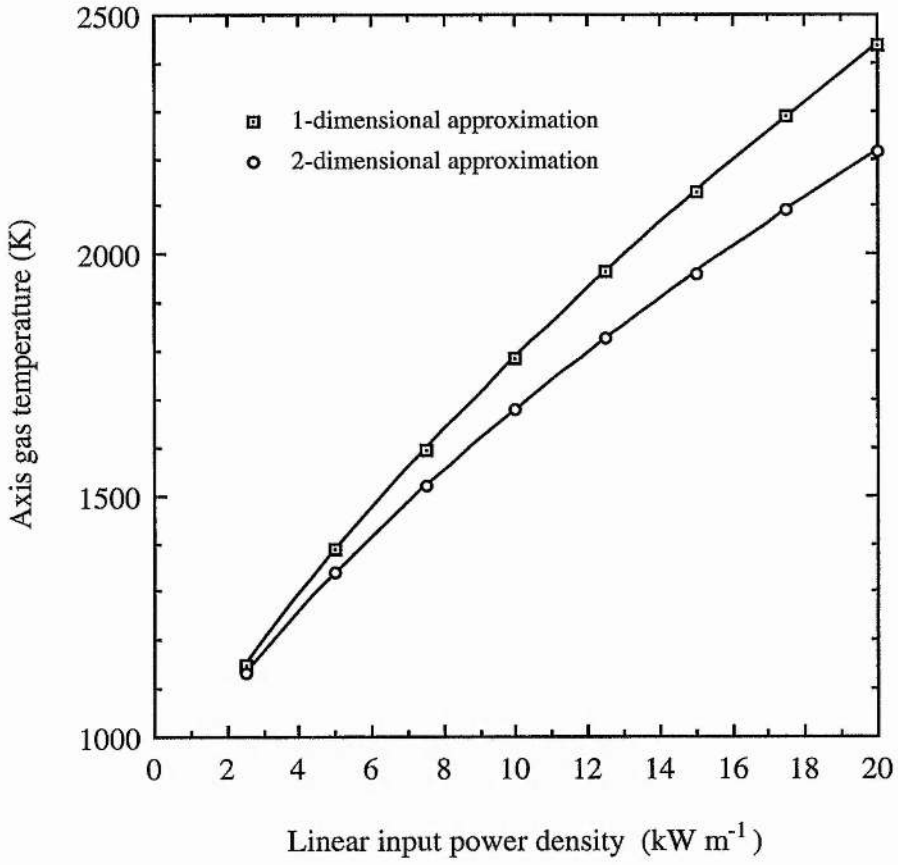

Figure 3.13 Graph of axis gas temperature against linear input power density for a rectangular bore discharge tube of cross-section 8 mm by 24 mm.

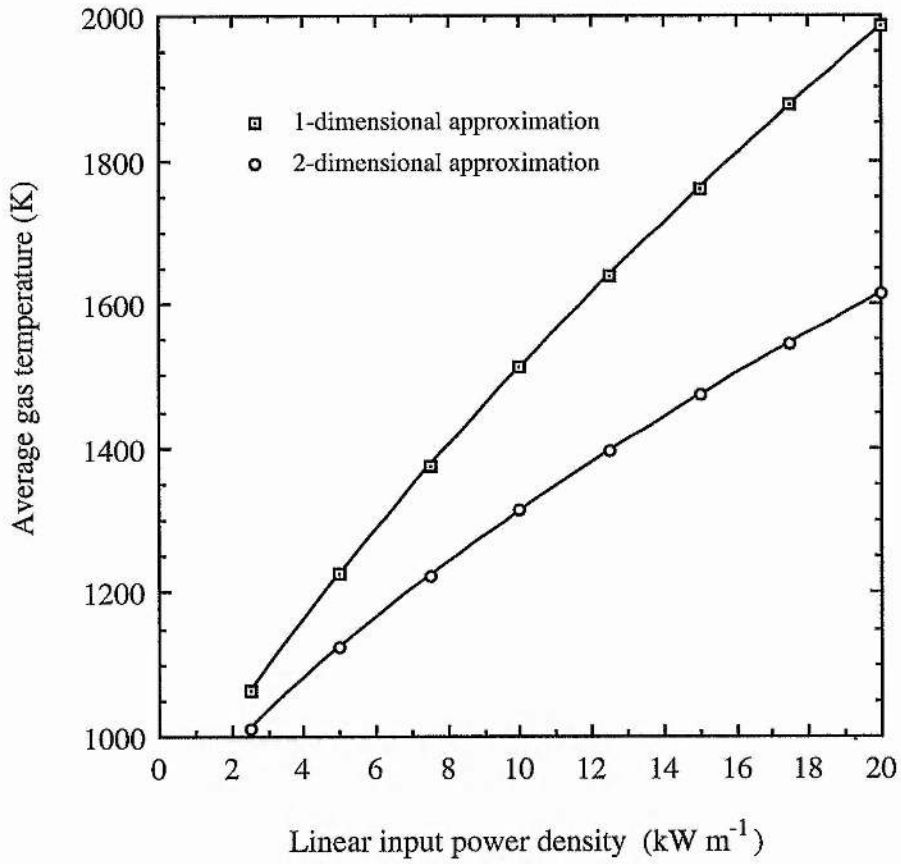

Figure 3.14 Graph of average gas temperature against linear input power density for a rectangular bore discharge tube of cross-section 8 mm by 24 mm.

3.5 References

1. Bukshpun, L. M. , Latush, E. L. and Sem, M. F.,
Sov. J. Quantum Electron. **18**, No. 9 (1988), pp.1098-1100

2. Hentschel, R. M., Carman, R. J. and Piper, J. A.,
CLEO, 1992

3. Little, C. E. and Piper, J. A.,
Opt. Commun. **68**, No. 4 (1988), pp. 282-286

4. Kushner, M. J. and Warner, B. E.,
J. Appl. Phys. **54**, No. 6 (1983), pp. 2970-2982

5. Little, C. E. and Piper, J. A.,
IEEE J. Quantum Electron. **QE-26**, No. 5 (1990), pp. 903-910

CHAPTER 4:

Strontium Recombination Laser Scaling Issues

4.1 Intoduction

Scaling the strontium recombination laser to higher average output powers involves raising the average input power. Raising the average input power means that more heat has to be removed from the laser tube to maintain the discharge channel wall at the temperature (~600°C) required to produce the optimum ratio of strontium vapour number density to helium buffer gas number density. Because the vapour pressure of strontium is strongly temperature dependent (see Section 4.4) [1], the SRL is very sensitive to input power, with laser output power falling if the discharge channel wall is 'overheated' (see Sections 4.2).

In addition to overheating due to non-optimum discharge channel wall temperature, the laser medium (gas) can become overheated if too high a *linear input power density* is required to achieve the optimum discharge channel wall temperature (see Section 4.3). Laser gas overheating is characterized by weak, annular lasing, at low specific output energies or, in severe cases, by the absence of oscillation on the laser lines, under otherwise optimum conditions. For successful power scaling to be achieved it is important to minimize the effects of gas temperature so that laser overheating is dominated by the discharge channel wall temperature becoming non-optimum.

There are numerous ways in which the SRL system can be scaled to higher input powers, while maintaining the discharge channel wall temperature at the optimum value and the gas temperature below its

limit. These are discussed and compared below. This chapter concludes with a laser design procedure which allows power scaling of the SRL system to be achieved.

4.2 The dependence of laser output power on discharge channel wall temperature

As the electrical input power to a *given* self-heated SRL is increased, the average laser output power rises to a maximum. Further increase in the input power results in the laser 'overheating' and laser output power falls. This may be explained as follows:- the afterglow electrons, produced predominantly through the double ionization of strontium atoms during the discharge pulse, are normally cooled via superelastic collision with light helium atoms and ions (see Chapter 2). An optimum ratio of strontium vapour number density to helium number density therefore exists for efficient electron cooling and a high rate of recombination pumping to the Sr^{+*} upper laser level. This optimum ratio occurs when the discharge channel wall temperature is approximately 600°C, though the precise optimum tube wall temperature will, of course, vary with buffer gas pressure (see Section 4.4). The electron cooling is therefore degraded when the wall temperature is increased above the optimum as light helium ions are effectively replaced by heavy strontium [2] (which is less efficient than helium at cooling the afterglow electrons due to its higher atomic mass).

In short, if the SRL discharge channel wall temperature is too high for the buffer gas pressure being used, too much strontium vapour will be produced. The ratio of strontium atoms to helium atoms/ions then becomes unfavourable with regard to efficient cooling of the electron gas. This results in the gain of the active medium diminishing, so that laser output power falls.

The effect of having too much strontium vapour in the laser tube has been demonstrated by Little and Piper [3]. On overheating the laser tube, Little and Piper found that the laser gain was reduced, while the ASE remained roughly constant. Thus, it would appear that overheating the tube affects the lower laser population, but leaves the upper laser level population unharmed. This observation is consistent with the above explanation for the fall in output power, when the input power is increased above optimum. The replacement of helium ions with strontium slows the *late* afterglow cooling of the electrons (see Chapter 1). The electron temperature is therefore unable to fall to a sufficiently low value for the lower laser level to be cleared effectively and the population inversion decreases.

4.3 Gas temperature limit to input power scaling

Ideally, gas temperatures in the active volume of an SRL should be as low as possible, in order to prevent plasma overheating. As the average gas temperature increases, the rate of afterglow electron cooling diminishes and the minimum afterglow electron temperature rises (since it can only relax to the average buffer gas temperature). The upper laser level pump rate therefore decreases with increasing gas temperature, as does the rate of lower laser level clearing (see Chapter 1). At high gas temperatures there is also an increased probability that thermal repopulation of the lower laser level will occur. The population inversion in an SRL consequently suffers as a result of rising gas temperatures. The radial profile of the gas temperature should be as flat as possible to avoid strong concentration gradients of the species, which can lead to a drop in the laser output power on the tube axis and annular lasing in severe cases.

The radial gas temperature profile, axis gas temperature and average gas temperature in a cylindrical bore laser tube depend on the linear input power density, P_L. This can be seen clearly by recasting Equations 3.2.10, 3.2.12 and 3.2.11 as follows:

$$T(r)=\left(T_w{}^{1.73}+\frac{1.73P_L}{4\pi\lambda_0}\left[1-\left(\frac{r^2}{R^2}\right)\right]\right)^{\left(\frac{1}{1.73}\right)} \qquad [4.3.1]$$

$$T(0)=\left(T_w{}^{1.73}+\frac{1.73P_L}{4\pi\lambda_0}\right)^{\left(\frac{1}{1.73}\right)} \qquad [4.3.2]$$

$$\langle T_g \rangle = \frac{4\pi\lambda_0}{2.73 P_L}\left(T(0)^{2.73} - T_w{}^{2.73}\right) \qquad [4.3.3]$$

by using the relationship:

$$q^* R^2 = P_V R^2 = P_L/\pi, \qquad [4.3.4]$$

where P_V is the average electrical input power deposited in the discharge channel per unit volume.

The curve in Figure 4.1 shows the variation of the average gas temperature with linear input power density, at a constant wall temperature of 600°C (873 K), and satisfies the quadratic equation:

$$P_L/\pi = P_V R^2 = 1.0553\text{x}10^{-3}\langle T_g \rangle^2 + 1.0971\langle T_g \rangle - 1793. \qquad [4.3.5]$$

Due to thermal repopulation of the lower laser level, a maximum average gas temperature exists, above which the SRL population inversion and hence lasing in the tube ceases. Taking this temperature to be 2300 K, as calculated by Bukshpun et al. [4], we obtain, from Equation 4.3.5, an upper bound on the acceptable linear input power density for an SRL:

$$P_{L,max}/\pi = 6313. \qquad [4.3.6]$$

The maximum linear power density, $P_{L,max}$, which should be put into a *cylindrical* bore SRL is therefore 20 kW m^{-1}. Any attempt to deposit

more than 20 kW m^{-1} of power into a cylindrical bore SRL will result in the buffer gas becoming overheated and lasing will be quenched. In practice, SRL gain will start falling before this upper limit is reached and Bukshpun et al. [4] estimate that a linear input power density of 13 kW m^{-1} is about the optimum value (which theoretically gives the maximum average output power) for his laser tube and operating conditions, above and below which average laser output power falls.

Equation 4.3.5 also reveals that there is a maximum PRF for a given tube radius, above which gas overheating will occur. This maximum recommended operating PRF, f_{max}, depends on the specific laser input energy, $E_{V,in}$, and is given by the expression:

$$E_{V,in} f_{max} R^2 = 6313. \qquad [4.3.7]$$

Let us take a typical specific laser output energy, E_V, of 5 μJ cm^{-3} produced at a (typical) conversion efficiency of 0.1% and assume that these remain constant as the radius and length of the active volume are varied. We then obtain a relationship between the laser tube's inner diameter, D, and the maximum PRF at which the laser can be operated, without incurring overheating of the active volume,

$$f_{max} = \frac{50.5}{D^2}, \qquad [4.3.8]$$

where f_{max} is in kilohertz and D is expressed in centimetres. The maximum recommended operating PRF is shown as a function of tube diameter in Figures 4.2, 4.3 and 4.4.

4.4 Buffer gas pressure scaling

Increasing the buffer gas pressure raises the helium atom concentration. A greater concentration of strontium vapour can then be introduced into the laser tube while still maintaining efficient electron cooling in the discharge afterglow (see Section 4.2). Hence, increasing the buffer gas pressure in a given SRL should lead to an increase in the available *specific output energy*. However, as shown in Figure 4.5, the tube wall temperature must be increased in order to obtain an increase in the strontium vapour pressure. Figure 4.5 shows that a 50°C variation in temperature, centred on 600°C, will cause the vapour pressure of strontium to change by a factor of 10. Relatively large changes in strontium vapour pressure can therefore be accomplished with relatively small changes in input power. It follows that, any increase in specific output energy, accompanying an increase in buffer gas pressure, will be obtained at roughly constant input power. The input pulse energy must therefore be increased with pressure, to ionize the additional strontium completely, while the average input power is held approximately constant. The PRF will therefore have to be lowered, as the buffer gas pressure is raised.

Since the laser tube conductivity decreases with increasing buffer gas pressure (because the electron-buffer gas atom collision frequency increases), the tube voltage must be increased with the pressure in order to maintain the current density (in practice, the optimum current density increases with pressure), while the capacitance must be reduced to obtain good matching between the laser's discharge circuit and its active

volume. If the current pulse does not terminate rapidly the electrons will not be cooled rapidly and any ringing at the end of the current pulse will reheat the electrons.

It should be noted that endlessly increasing the buffer gas pressure will not necessarily lead to an ever increasing output power. This is because it becomes increasingly difficult to maintain a stable discharge and good matching between the discharge circuit and laser tube at the higher pressures. High pressure operation is further complicated by the need for a power supply and switching element which are capable of supplying and handling the required voltages (tens of kV) and currents (hundreds of amps).

It has been noted in the literature that increasing the buffer gas pressure increases the specific output energy and efficiency of the SRL [5, 7, 8]. The need to lower the PRF, as the buffer gas pressure is increased, has also been noticed in the SRL [2] and in the analogous calcium recombination laser (CRL) system [9]. The observation that average output power does not seem to increase in line with the increase in specific output energy [9] could be due to the slower diffusion of strontium atoms back to the tube axis at higher pressures to reverse the effects of ambipolar diffusion of strontium ions to the walls during the excitation pulse. At present the highest pressure at which SRL operation has been observed is 4 atm [10], with the pulse energy increasing linearly up to 3 atm. The specific laser output energy of 13.8 $\mu J\ cm^{-3}$, observed from this laser at 4 atm, is currently the maximum achieved in a longitudinally excited SRL.

4.5 Water-cooling versus free-convection cooling

The dominant heat transfer term in water-cooled SRL systems is due to conduction through the laser tube's helium layer, which depends critically on the thickness of the helium layer (see Chapter 2). In free-convection cooled SRLs the dominant heat transfer process is radiation from the outer surface of the discharge tube (see Chapters 2 and 5).

The helium layer thickness in a water-cooled laser tube can be adjusted independently of the discharge tube's outer radius so that the designer of water-cooled laser tubes can control the required input power largely independently of the discharge tube's dimensions. Experiments involving the use of water cooling to increase the optimum input power to a given SRL discharge tube are discussed in Chapter 6. In contrast to water-cooled laser tubes, because the radiative energy loss from a surface depends on its surface area (Equation 2.5.9), the required input power to a free-convection cooled laser depends critically on the discharge tube's outer radius (which limits its inner radius) and its emissivity. The optimum electrical input power to a free-convection cooled, self-heated SRL is therefore fixed by the dimensions of the chosen discharge tube. The rate of heat removal from a given discharge tube can, however, be enhanced by increasing the emissivity of the tube's outer surface [11]. Experiments involving this technique for increasing the optimum input power to a given SRL discharge tube are discussed in Chapter 5.

The advantages of utilizing water cooling to define a laser's input power over air cooling can be summarized as follows:-

1. By the use of water cooling, the input power per unit discharge channel cross-sectional area can be increased over that required when the discharge tube is air cooled.

2. A range of lasers, optimizing at different input powers, can be constructed through the use of water cooling using a single discharge tube, by varying the helium layer thickness.

4.6 Changing the helium layer thickness: PRF scaling

The use of water-cooling allows the laser designer to cover a range of optimum input powers using a single discharge tube by varying the helium layer thickness (i.e., by constructing different water-cooled jackets for the discharge tube). The variation in the required linear input power density with helium layer thickness is shown in Figure 4.6 for the laser tube dimensions and conditions specified in Table 4.1 (overleaf).

In order to obtain the optimum discharge channel wall temperature, the input power to a laser tube must be increased as the helium layer thickness is reduced, with the fractional increase in input power becoming higher as the helium layer is made narrower. If the discharge volume is unchanged while the thickness of the helium layer is reduced, the input pulse energy should be kept roughly constant (close to the

'optimum' value for the chosen discharge tube at low input powers), with the additional input power being obtained by raising the PRF.

User input	Value
Discharge tube inner diameter	8 mm
Discharge tube outer diameter	31 mm
Discharge tube length	400 mm
Quartz thickness	1.5 mm
Discharge tube emissivity	0.5
Discharge channel wall temperature	600°C
Water temperature	10°C

Table 4.1

Very high specific output powers can be obtained through the operation of small bore, water-cooled laser tubes with small helium layer thicknesses at high PRFs. A disadvantage of increasing the power loading of an SRL by reducing the helium layer thickness and increasing the PRF is that any increase in output power is obtained by virtue of an increase in the linear input power density. This method of scaling laser output power therefore raises the gas temperature, which will be

detrimental to laser pulse energy performance. The design of high specific input power water-cooled lasers must include consideration of the input power per unit length, so that gas temperatures are moderated. Care in the design must also be exercised to ensure that the water flow rate is sufficiently high for it to be efficient (see Chapter 2).

We have seen that high input powers can be deposited in a given water-cooled discharge tube by using narrow helium layer thicknesses. There may, however, be a limit as to how narrow the helium layer can be made, while retaining satisfactory operation. The quartz tube, which along with the outer diameter of the discharge tube defines the helium layer, must be of uniform internal diameter in order to obtain uniform heat extraction from the water jacket. If small (1 mm) helium layer thicknesses are used, any irregularity in the internal diameter of the quartz tube will have a large effect on the rate at which heat is removed from the discharge tube. This may cause hot/cold regions along the discharge channel wall which will result in longitudinal inhomogeneities in the strontium vapour number density. Small helium layer thicknesses will also lead to problems associated with locating the discharge tube axially within the water jacket (see Chapter 6). These factors make the use of small helium layers (<1mm) less attractive than larger ones.

In a water-cooled laser, the helium layer can be widened, while depositing the same specific input power in the discharge channel (which is unchanged), by increasing the outer diameter of the discharge tube. This is illustrated in Figure 4.7 under the conditions specified in Table 4.2 (overleaf).

User input	Value
Discharge tube inner diameter	8 mm
Discharge tube outer diameter	30 mm to 100 mm
Discharge tube length	400 mm
Linear input power density	13.4 (± 0.1) kW m^{-1}
Quartz thickness	1.5 mm
Discharge tube emissivity	0.5
Discharge channel wall temperature	600°C
Water temperature	10°C

Table 4.2.

A disadvantage of increasing the outer diameter of the discharge tube is that the laser assembly becomes larger and more expensive. However, the discharge tube simultaneously becomes stronger, so that its resistance to thermal shock fractures is increased and its useful lifetime may be extended.

4.7 Volume scaling: an introduction

Assuming that the optimum specific input *energy* and conversion efficiency of the SRL system are independent of the discharge tube dimensions, more energy will become available for extraction as the volume of the discharge channel is increased (provided that the buffer gas pressure is not reduced). The average output power of an SRL should therefore increase with the tube volume, provided that the permissible rate of energy deposition does not decrease with tube volume, in such a manner as to offset the increase in energy which becomes available for extraction.

The active volume of a laser can be increased by enlarging the discharge channel cross-sectional area and/or lengthening the discharge tube. The consequences of changing these parameters are discussed below.

4.7.1 Volume scaling through changing discharge channel diameter

Changing the diameter of a cylindrical discharge channel does not automatically imply that there will be a change in the normalized radial gas temperature profile (that is, T_g plotted against r / R) or the average gas temperature (see Equations 4.3.1 through to 4.3.3). When using water-cooling, if the helium layer is made wider while the discharge channel diameter is increased, so that the linear input power density remains constant, there will be no change in gas temperature. This

approach will not, however, be expected to increase the average output power of the laser. Scaling the volume of a laser by increasing the discharge channel diameter and leaving the helium layer thickness the same will affect the gas temperatures. This is because the required linear input power density, for optimum tube wall temperature at a given buffer gas pressure, depends on the discharge channel diameter, as illustrated below.

Consider a hypothetical water-cooled beryllia discharge tube. Suppose that the inner radius of this tube is varied, while all other radii are adjusted such that the beryllia thickness is kept at a constant 5 mm and the helium layer thickness is maintained at a constant 3 mm. Using the forced convection model, described in Chapter 2, and setting the remaining user inputs to the values listed below in Table 4.3 (overleaf), leads to a linear relationship between the input power per unit length and the discharge tube's inner diameter. This is shown in Figure 4.8.

With this tube geometry the gas-temperature-limited (when the gas temperature reaches 2300 K) bore diameter is 90 mm. As the optimum input power per unit length increases in proportion with the tube's internal diameter, while the volume increases as the square of the tube radius, the average *specific* input power required for optimum tube wall temperature decreases with increasing tube internal diameter as shown in Figure 4.9.

User input	Value
Quartz thickness	1.5 mm
Discharge tube length	400 mm
Helium layer thickness	3 mm
Discharge tube emissivity	0.5
Discharge channel wall temperature	600°C
Water temperature	10°C

Table 4.3

In order to maintain the optimum discharge channel wall temperature and the specific input pulse energy as the discharge channel diameter is increased, the operating PRF must be reduced, in line with the falling required specific input power. Figure 4.10 shows the approximate relationship between PRF and discharge channel diameter, D , to be:

$$f \propto D^{-1.5} \qquad [4.6]$$

In producing Figure 4.10 it has been assumed that the maximum attainable specific output *energy* and laser efficiency shall be independent of discharge tube volume. In practice, as diameter is

increased, this may not be the case (see below), because the gas temperature has been shown to rise (under conditions of optimum discharge channel wall temperature) with increasing radius. It must be stressed that the above consideration of radius scaling is not presented as a rule of scaling. It has been included in order to descibe what might be *expected* to occur if radius scaling were undertaken.

In summary, scaling the laser's active volume by increasing the bore diameter *may be expected* to increase the average laser output power of the SRL system. The average laser output power will not, however, be expected to scale as the volume, but linearly with the tube diameter. Note that a similar trend is expected for simultaneously scaling the inner and outer diameters of free-convection cooled lasers because radiation is the main process by which heat is extracted from such systems (see Chapters 2 and 5).

It has been noted, in the literature, that large-bore tubes need to be operated at lower PRFs than narrow bore tubes [4, 9, 12, 13]. During the above discussion this has been seen to be due to the requirement that the tube wall temperature be maintained at 600°C as the diameter and input power are raised, if the specific output energy and efficiency are independent of the active volume.

Although the optimum specific output pulse energy and efficiency of low PRF (1 Hz), externally heated SRLs appear to be relatively independent of their bore diameter [8], the average output power of self-heated multihertz SRLs does not, in practice, appear to scale with tube

radius as the above discussion might suggest [2]. This could be due to the difference in time scales between fast ambipolar diffusion of strontium ions outwards during a current pulse and slow free diffusion of strontium atoms back to the tube axis after the current pulse becoming important in large bore tubes, so that the PRF must be reduced more than the thermal loading approach would suggest. Both Butler and Piper [8] and Little and Piper [2] have observed effects attributable to diffusion, which could limit the optimum operating PRF to less than 1 kHz in large (>25 mm) bore tubes (i.e. 200 Hz limit in Butler and Piper's 40 mm internal diameter tube). Also, because gas temperature profiles become more pronounced in large bore tubes (due to the necessary increase in linear input power density), the radial concentration gradients of strontium and helium species will become more severe as the laser tube bore is enlarged. The increase in gas temperatures accompanying diameter scaling also reduces the rate of cooling of the afterglow electrons and therefore diminishes the population inversion (see Chapter 1). It has been noticed that intensifying the heat removal from SRLs through the use of active cooling(increasing the gas temperature), leads to a reduction in the specific laser output energies [4, 14]. Hence, the gain in large bore laser tubes may be inhibited on the tube axis (where densities are low and gas temperatures are high) due to gas temperature effects and the specific output energy may be lower than in small bore tubes. The effective available specific output power is therefore expected to decrease as the bore is increased. Attempts at scaling the SRL to higher average output powers by increasing the tube diameter have generally been unsuccessful since the average laser output power shows little increase on scaling the discharge channel diameter.

4.7.2 Volume scaling through changing discharge tube geometry

The average gas temperature per unit input power, per unit volume, can be reduced below that expected in a cylindrical bore laser tube by the use of a rectangular bore. This is illustrated in Figures 4.11 and 4.12. In these figures the on-axis gas temperature and the average gas temperature in a rectangular bore tube of cross-section 8 mm by 24 mm are compared to those in a cylindrical bore tube, of the same cross-sectional area (radius = 7.82 mm), over a range of linear input power densities.

The average gas temperature in the rectangular bore tube laser of interest is 1600 K for a linear input power density of 20 kW m^{-1}. This value compares very favourably with the average gas temperature of 2300 K expected at 20 kW m^{-1} in a cylindrical discharge channel of the same cross-sectional area. Thus, from gas temperature considerations, it would seem that more power per unit length can be deposited in a rectangular bore tube than in a circular bore tube of the same cross-sectional area, before the onset of gas temperature limitations.

4.7.3 Volume scaling through changing the discharge tube length

The total input power required to maintain the tube wall temperature at 600°C increases linearly with discharge tube length (Equations 2.5.1 and 2.6.1), while having no effect on gas temperatures (Equations 4.3.1 to 4.3.3). The average laser output power should

therefore increase linearly with laser tube volume, if the volume is scaled by increasing the discharge tube length (assuming that the specific output energy is independent of tube length).

If length scaling is adopted as a means of increasing the average output power of an SRL, the average input power should be raised by increasing the tube voltage such that the input pulse energy rises in proportion with the tube length. The laser tube's cross-section should be designed to obtain the desired tube wall temperature (~600°C) by the use of a linear input power density somewhat lower than 20 kW m^{-1} (if a cylindrical bore is opted for). Once the input power per unit length has been decided upon the PRF is set by the expected maximum specific output energy and the cross-sectional area required to attain the desired 600°C wall temperature for the length of tube chosen. Increasing the tube voltage has no effect on the interpulse period, so that effects due to radial diffusion can be discounted if the longer tube fails to work. Length scaling has been used to produce 3 W of average output power from a 90 cm long tube with a 15 mm bore [10]. Length scaling has therefore been demonstrated to be a reliable means by which the SRL can be scaled to higher output powers.

Length scaling is not without its problems. In order to keep the electric field high enough to achieve efficient excitation, the discharge tube voltage must be increased with its length. Charging voltages of 30 kV per metre are typical in SRLs at buffer gas pressures of ~0.5 atm (see Chapters 5 and 6). This places a great demand on the switching element, which must be capable of supplying peak currents of the order

of 100's A. Length scaling is therefore limited by the capabilities of the available laser power supply and switching set-up. Furthermore, at high buffer gas pressures where high specific output energies are obtained, it becomes increasingly difficult to maintain a stable, uniform discharge over long distances. These problems can be reduced by running a number of short, individually excited SRLs in series [10]. This technique for boosting the length of a laser does, however, increase the complexity and component count of the system.

4.8 Summary and water-cooled laser design recipe

The main conclusions drawn from the discussions in this chapter can be summarized as follows:-

1. In a cylindrical bore laser tube, gas temperatures depend only on the linear input power density and discharge channel wall temperature.

2. Any scaling method which increases the linear input power density deposited in a laser tube will elevate the radial gas temperatures and the average gas temperature.

3. The normalized radial gas temperatures and average gas temperature in any two cylindrical bore laser tubes with identical discharge channel wall temperatures and linear input power densities will be the same, regardless of the bore diameter.

4. Due to thermal (collisional) repopulation of the lower laser level from below, the maximum linear input power density at which SRLs can operate is approximately 20 kW m^{-1}.

5. The SRL should be operated at the highest buffer gas pressure at which the laser power supply is capable of delivering a sufficiently high peak current which is both stable and well matched into the load.

6. The use of a rectangular bore laser tube will result in gas temperatures being lower compared with those expected in a cylindrical bore tube of the same cross-sectional area at the same linear input power density.

7. The best scaling method to use, from a consideration of gas temperatures, is length scaling, because this approach can lead to an increase in the total required average input power without affecting the linear input power density and gas temperature.

8. The average input power which must be deposited in a given discharge tube in order to obtain a given discharge channel wall temperature can be increased over that required when the tube is free-convection cooled by the use of water cooling, though gas temperatures will consequently be elevated.

9. A range of lasers optimizing at increasing average input powers can be developed using a single water-cooled discharge tube by reducing the helium layer thickness and increasing the pulse repetition rate.

10. By using water cooling and reducing the helium layer thickness, higher powers can be deposited in laser tubes at increasing specific power densities by using higher PRFs. By increasing the discharge channel diameter of a water-cooled laser tube higher powers need to be deposited at decreasing specific power densities and lower PRFs (see Figure 4.13).

11. Because average SRL output power does not appear to scale with discharge channel radius, the use of short, fat discharge tubes would seem to be less attractive than the use of long, thin tubes.

The general trends expected to accompany implementation of the most commonly used methods of input/output power scaling are summarized in Table 4.4.

Water cooling enables the laser designer to set the input power to a laser tube independently of the discharge tube dimensions (up to a limit). It is therefore the preferred cooling method for potential high average output power (>1 W) SRLs. A procedure for the design of self-heated, longitudinally excited water-cooled strontium recombination lasers is presented below.

1. Select the discharge tube length. It is preferable to make the discharge channel as long as practical because the total input power can then be made large, while keeping the gas temperatures low. The available power supply must be capable of providing a sufficiently high voltage to drive hundreds of amps of peak current through the chosen discharge channel length at pressures of hundreds of torr.

2. Decide upon the linear input power density to be aimed at. This should be kept below 20 kW m^{-1} in order to avoid overheating the buffer gas. This, along with Step 1, determines the total input power which must be put into the discharge channel.

3. Select the discharge channel diameter. It is good policy to make this small (~1cm) as it reduces diffusion times and allows for the possibility of high repetition rate operation.

4. Select the outer diameter of the discharge tube. It is good policy to make this dimension large, to give the laser tube strength, and a large helium layer can then be used to extract the deposited input power.

5. Using the thermal loading model developed for forced convection cooling in Chapter 2, calculate the helium layer thickness which is required to give the desired total input power for a 600°C discharge channel wall temperature in the chosen discharge tube.

6 Using the formula developed in Chapter 2 (Equation 2.6.21), estimate the volumetric water flow rate, F (litres per minute), which is required to keep the longitudinal water temperature gradient, ΔT_L, sufficiently low (say below 10°C m^{-1}) at the chosen linear input power density, P_L:

$$\Delta T_L = \frac{P_L}{70F} \qquad [4.8.1]$$

7. Estimate the required pulse energy, E_p, and operating PRF, f, using the relations:

$$E_p = \frac{1}{2}CV^2 \approx 5 \text{ (mJ cm}^{-3}\text{) x Volume (cm}^{-3}\text{)} \qquad [4.8.2]$$

$$f = \frac{\text{Input Power}}{E_p} \qquad [4.8.3]$$

Water-Cooled Laser Designer 2 can be used to aid the designer of *cylindrical* bore water-cooled SRLs. This program incorporates the features of Water-Cooled Laser Designer 1 and, in addition, estimates the PRF and calculates the average gas temperature. The code for Water-Cooled Laser Designer 2 is listed in Appendix E and a sample printout for the program is shown in Figure 4.14.

4.9 Figures for Chapter 4

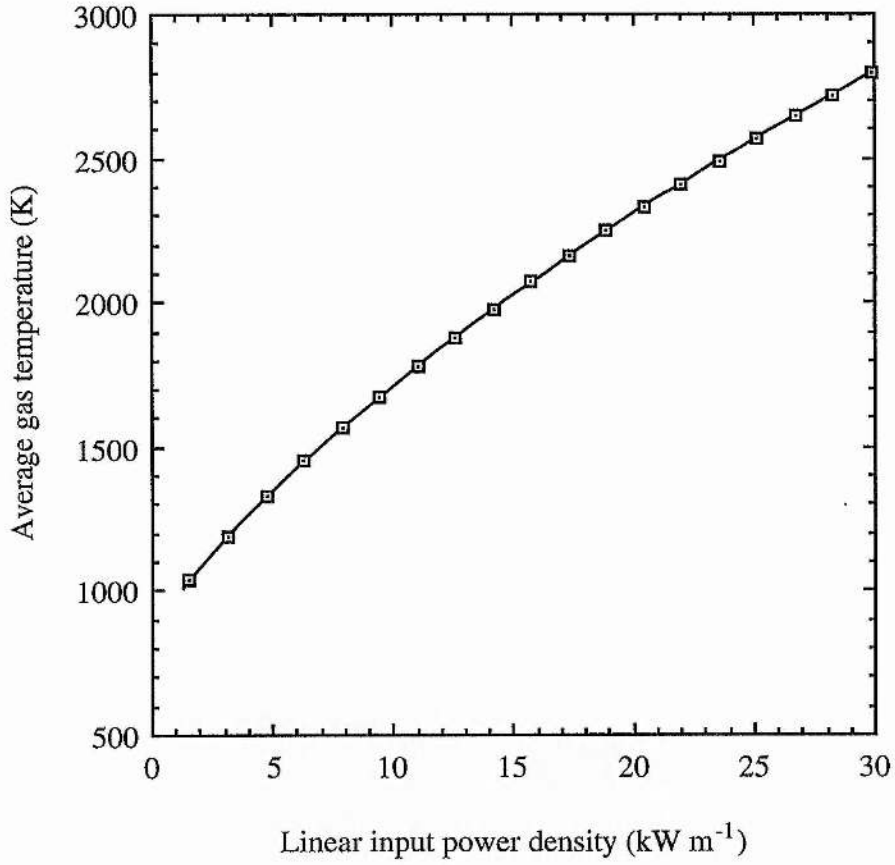

Figure 4.1 **The average gas temperature in a cylindrical bore laser tube as a function of linear input power density for a discharge channel wall temperature of 600°C.**

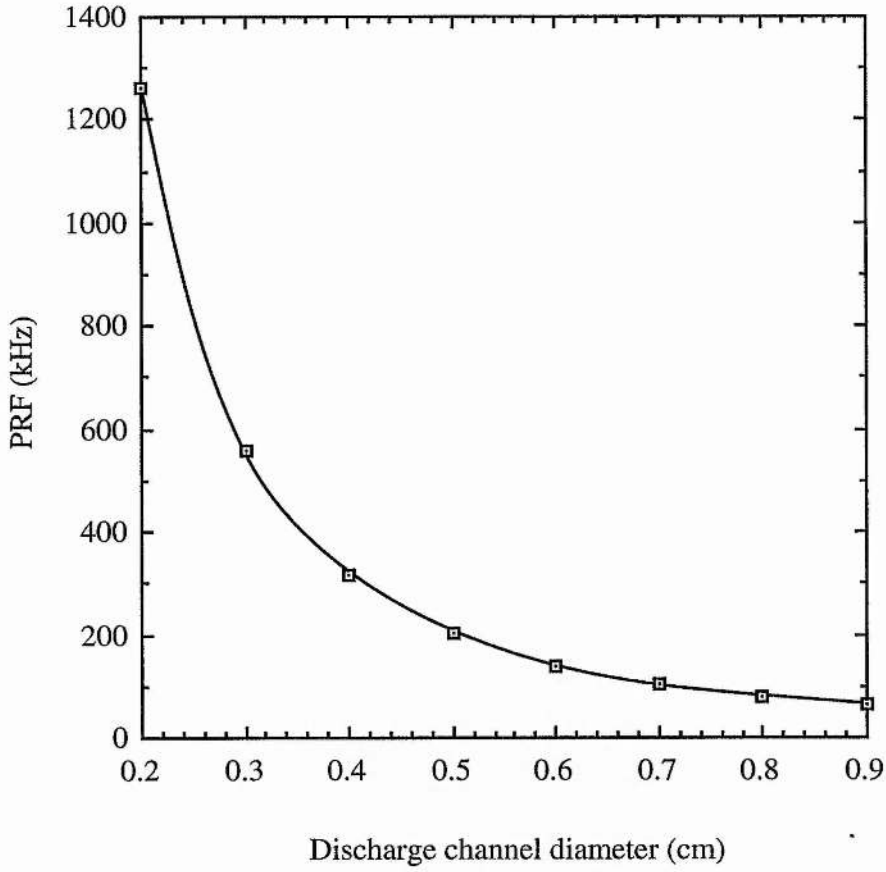

Figure 4.2 The maximum recommended operating PRF for an SRL as a function of the discharge channel diameter.

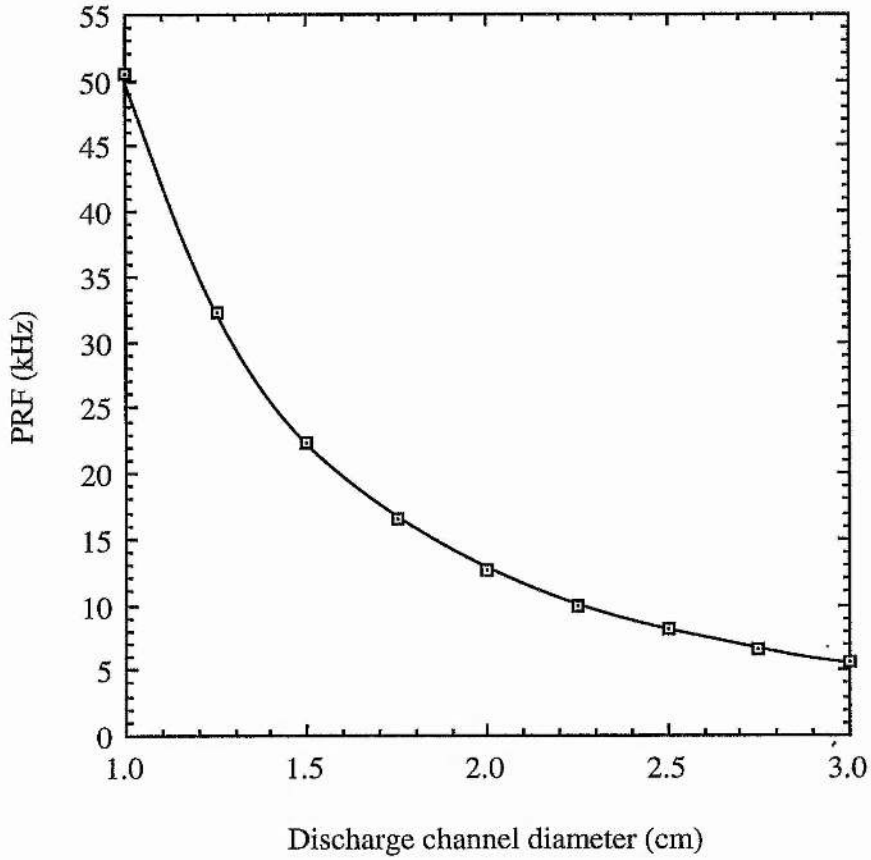

Figure 4.5 The maximum recommended operating PRF for an SRL as a function of the discharge channel diameter.

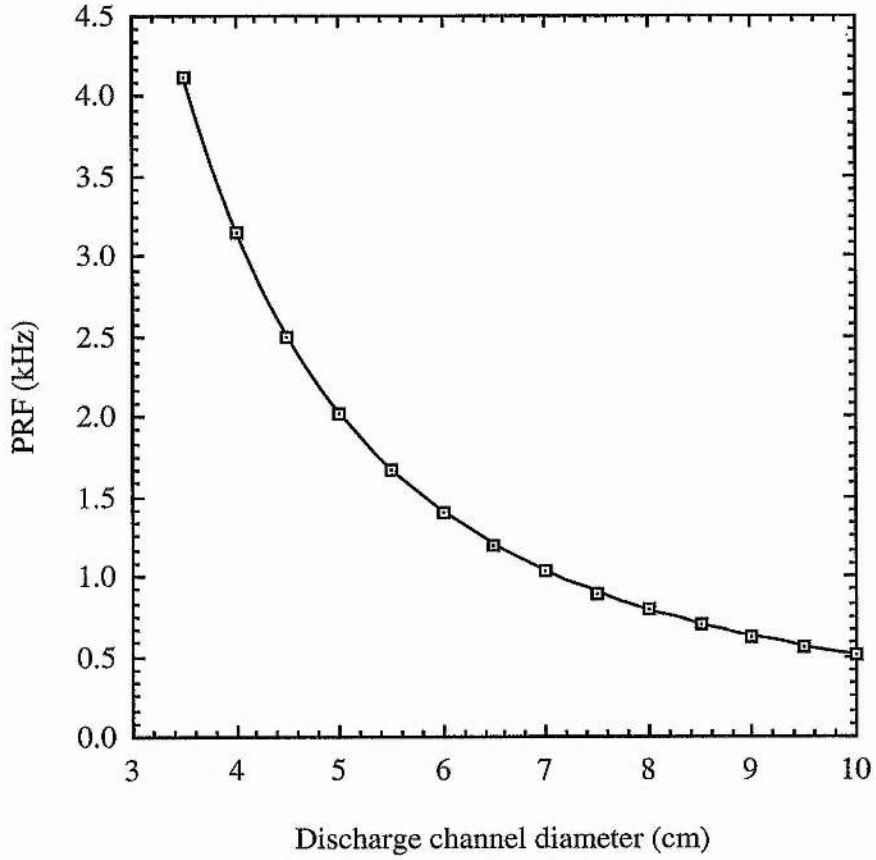

Figure 4.4 The maximum recommended operating PRF for an SRL as a function of the discharge channel diameter.

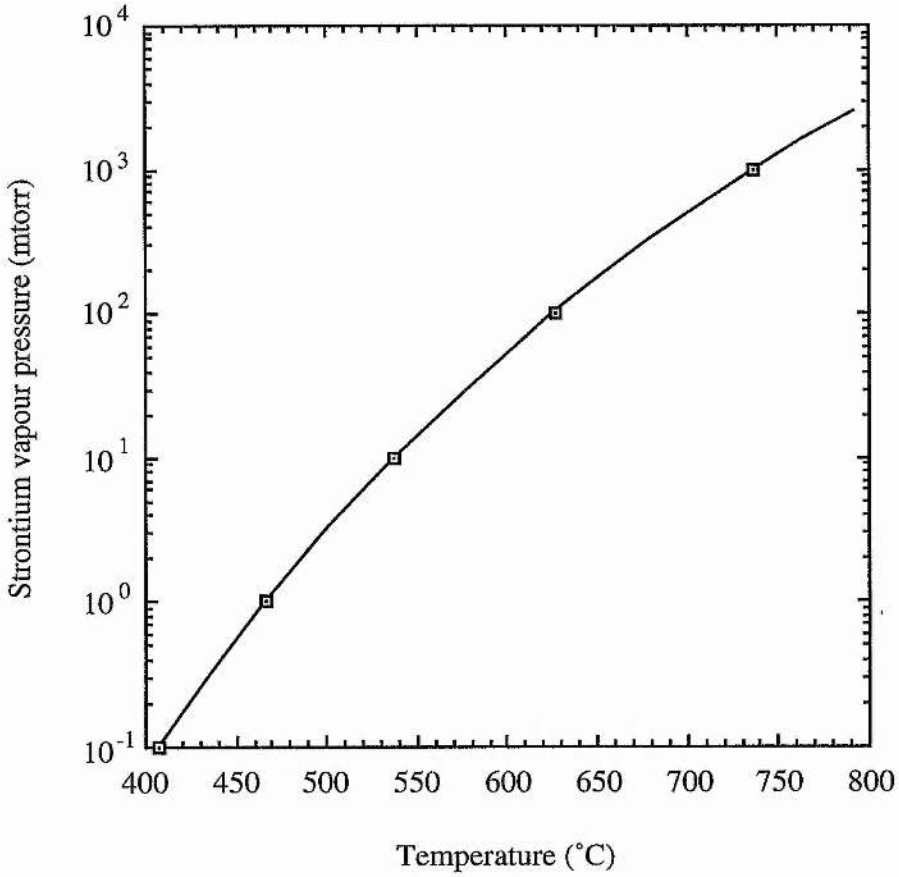

Figure 4.5 **The vapour pressure of strontium as a function of temperature.**

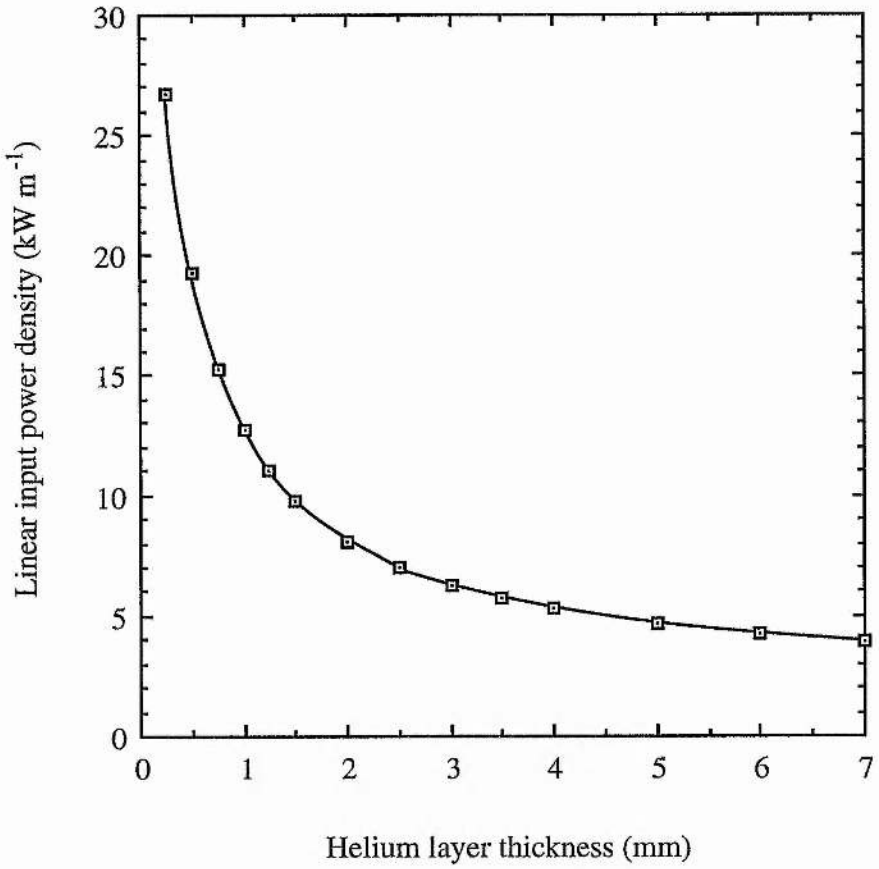

Figure 4.6 **Graph of required linear input power density for optimum tube wall temperature as a function of helium layer thickness under the conditions specified in Table 4.1.**

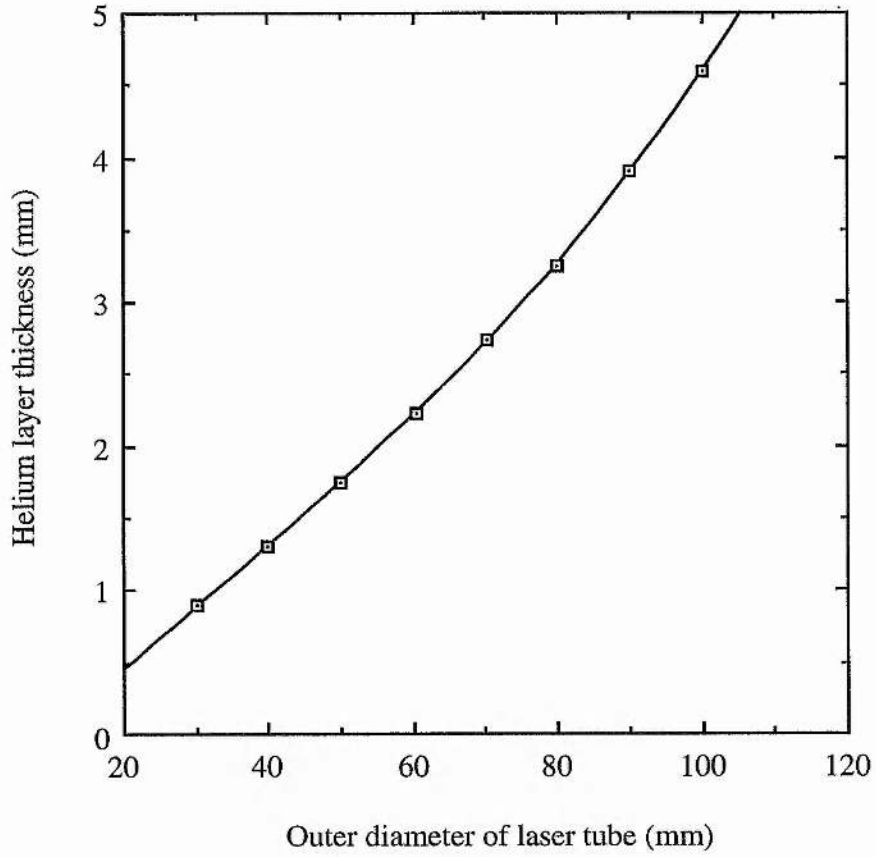

Figure 4.7 Graph of required helium layer thickness for optimum tube wall temperature as a function of discharge tube outer diameter under the conditions specified Table 4.2.

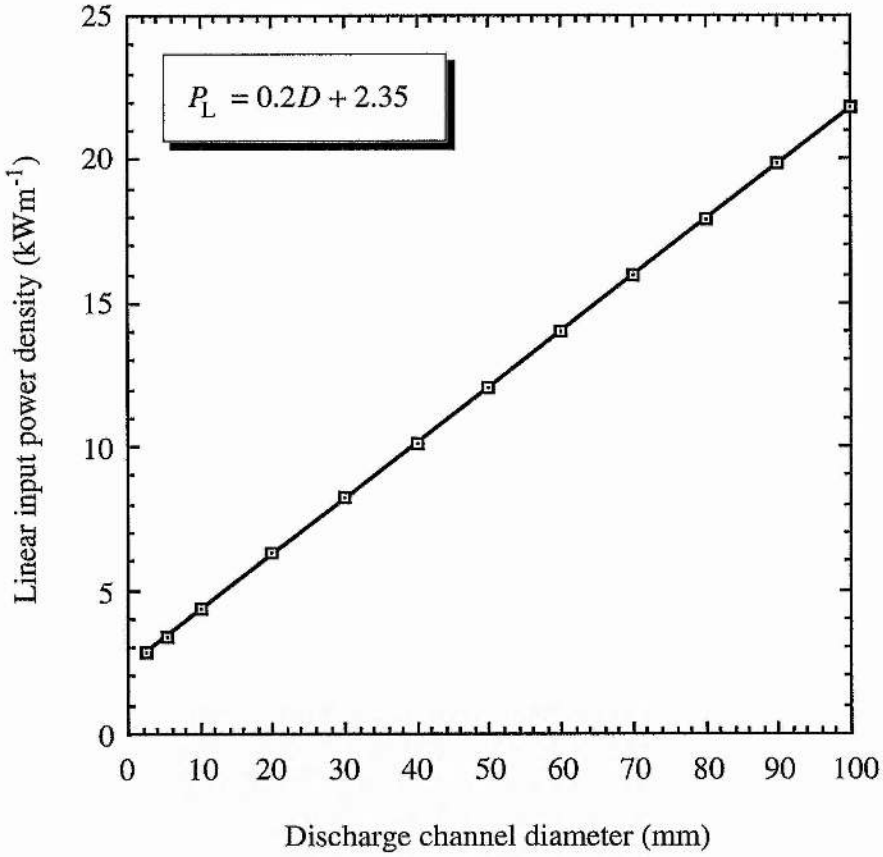

Figure 4.8 **Graph of required linear input power density for optimum tube wall temperature as a function of dicharge channel diameter when the discharge tube is 5 mm thick, the helium layer 3 mm thick and the other conditions as specified in Table 4.3.**

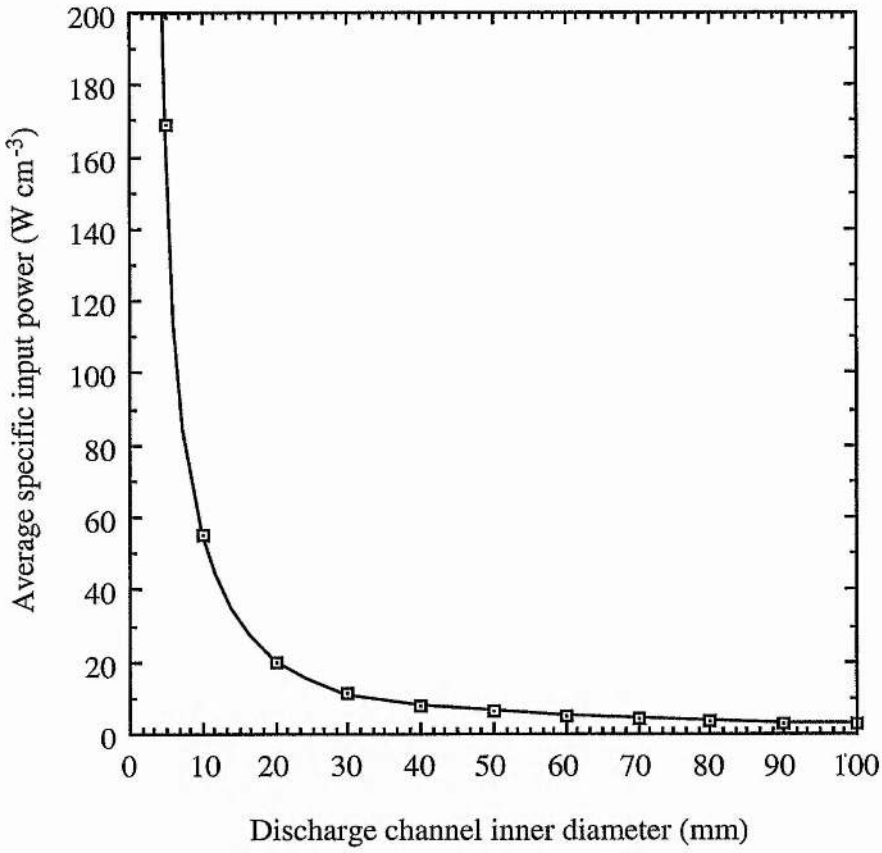

Figure 4.9 **The variation in the optimum average specific input power with discharge channel diameter for a 5 mm thick discharge tube and a 3 mm thick helium layer, under the conditions specified in Table 4.3.**

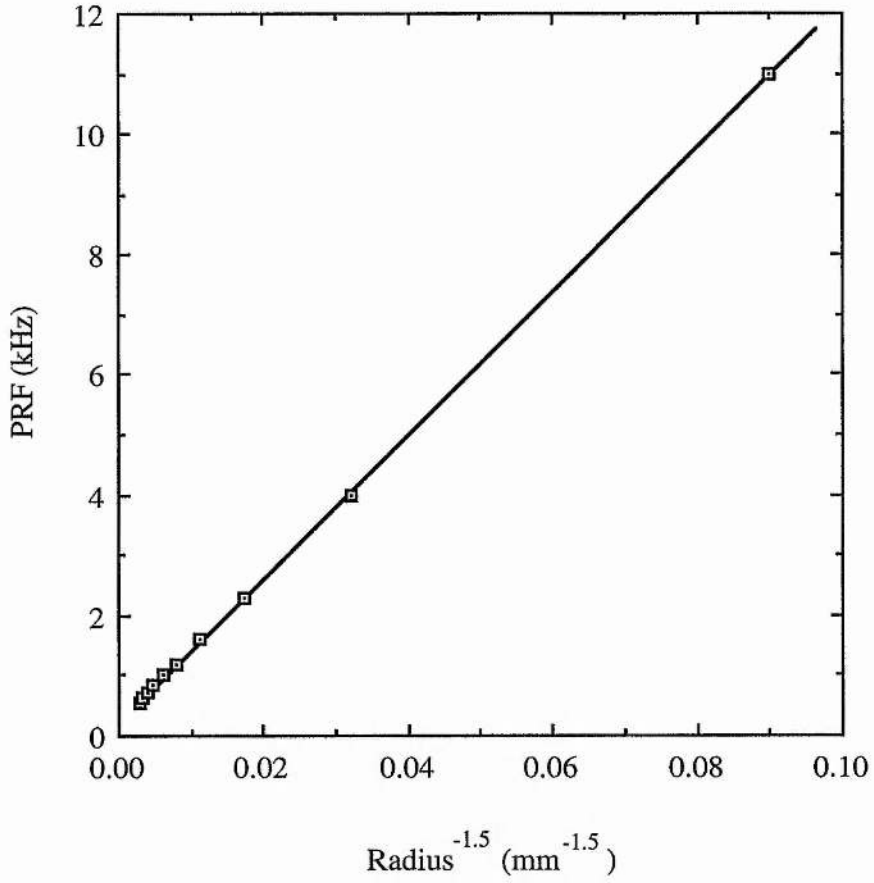

Figure 4.10 The variation in the optimum PRF with discharge channel radius$^{-1.5}$ for a 5 mm thick discharge tube and a 3mm thick helium layer, under the conditions specified in Table 4.3, assuming that the specific input energy and laser efficiency are independent of discharge tube bore.

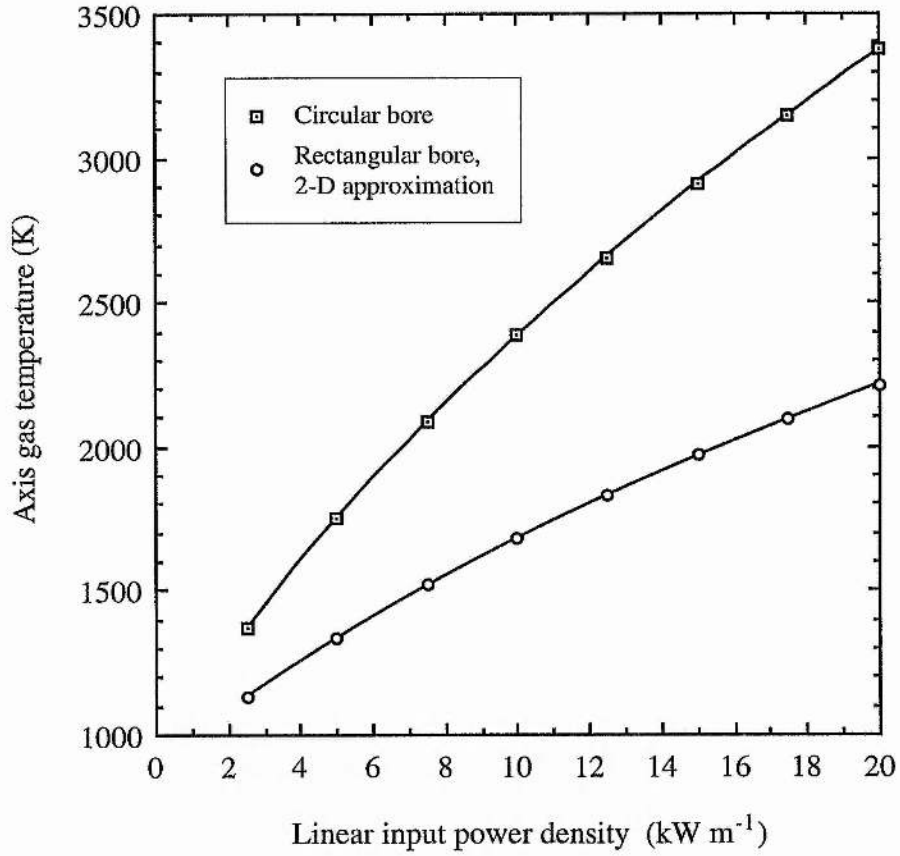

Figures 4.11 On-axis gas temperature against linear input power density for different discharge channel geometries.

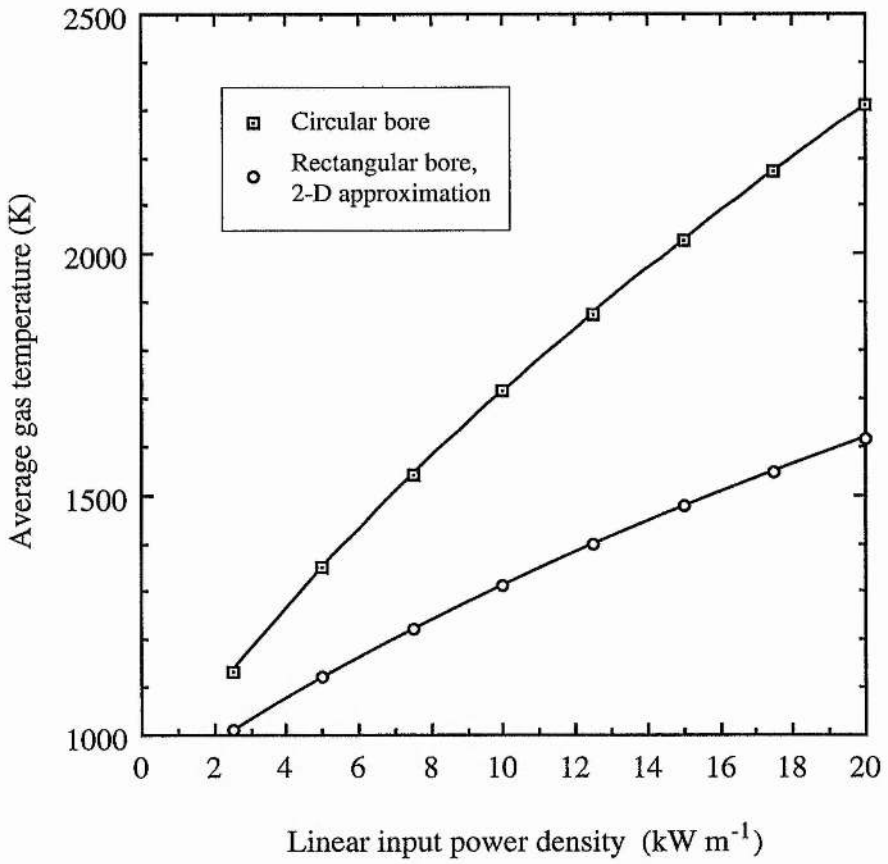

Figures 4.12 Average gas temperature against linear input power density for different discharge channel geometries.

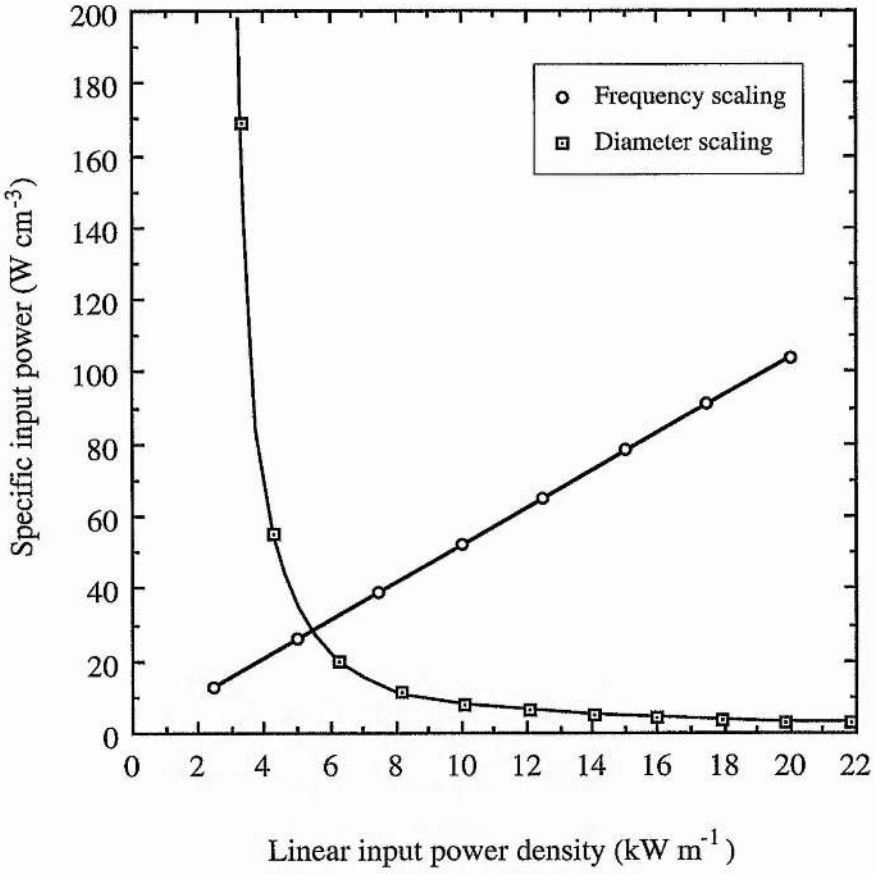

Figures 4.13 Graph of specific input power against linear input power density for helium layer thickness scaling and discharge channel diameter scaling (note that PRF is related to the specific input power, while gas temperature is related to the linear input power density).

Scaling method / Quantity affected	Increasing buffer gas pressure	Changing to water cooling/ decreasing helium layer thickness	Increasing discharge channel radius	Increasing discharge channel length
Total input power	Unchanged	Increased	Increased	Increased
Total input pulse energy	Increased	Unchanged	Increased	Increased
Specific input power	Unchanged	Increased	Decreased	Unchanged
Specific input pulse energy	Increased	Unchanged	Unchanged	Unchanged
Gas temperature	Unchanged	Increased	Increased	Unchanged
Storage capacitance	Should be decreased	Should not be changed	Should be increased	Should not be changed
Storage capacitor voltage	Should be increased	Should not be changed	Should not be changed	Should be increased
Pulse repetition frequency	Should not be changed	Should be increased	Should be decreased	Should not be changed

Table 4.4 Summary of scaling methods.

```
>      Thermal modelling program for helium filled,
       cylindrical water-cooled beryllia laser tubes

                    Version 11.4

                  T. R. Pugsley
              Copyright 1992,1994

 Enter tube id in mm, Tube od in mm, Quartz thickness in mm,
 Tube length in metres, Tube emissivity, Twall (°C) , Tfluid (°C)

?8,31,1.5,0.4,0.5,600,10

 To try a single helium layer thickness type S,
  for an 0.25 mm incremented range of Helium thicknesses type R
?s

 Enter desired helium thickness in mm
?3

 Q cond+conv = 1942 W, Q rad = 589 W, Q tot = 2531 W
 at a nominal He thickness of 3 mm, actual He thickness of 2.93 mm.
 ΔT tube = 16.9 °C, ΔT helium = 530 °C, ΔT quartz = 43 °C

 Volume = 20.1 cm^3, P/V = 125.87 W/cm^3, P/L = 6.327 kW/m, PRF = 25.17 kHz
 Axis gas temperature = 1935 K (1662 °C), Average gas temperature = 1454 K (1181 °C).

 For a water temp gradient of < 10 °C/m, the water flow rate must be > 9 litres/min

 Type D to try a different helium thickness, S to stop
?s
 Would you like to design for a different discharge tube? (type Y/N)
?n
 Design session terminated
>
```

Figure 4.14 A sample printout from Water-Cooled Laser Designer 2.

4.10 References

1. Honig, R. E. and Kramer, D. A.,
   RCA Review, (June 1969) pp. 285-305

2. Koptev, Y. V., Latush, E. L. and Sem, M. F.,
   Opt. Spectrosc. **72**, No. 5 (1992), pp. 681-684

3. Little, C. E. and Piper, J. A.,
   IEEE J. Quantum Electron. **QE-26**, No. 5 (1990), pp. 903-910

4. Bukshpun L. M., Latush, E. L. and Sem, M. F.,
   Sov. J. Quantum Electron. **18**, No. 9 (1988), pp. 1098-1100

5. Zhukov, V. V., Kucherov, V. S., Latush, E. L.and Sem, M. F.,
   Sov. J. Quantum Electron. **7**, No. 6 (1977), pp. 708-714

6. Butler, M. S.,
   Ph. D. Thesis, Macquarie University, 1986

7. Zhukov, V. V., Latush, E. L., Mikhalevskii, V. S.and Sem, M. F.,
   Sov. J. Quantum Electron. **7**, No. 6 (1977), pp. 704-708

8. Butler, M. S. and Piper, J. A.,
   IEEE J. Quant. Electron. **21**, No. 10 (1985), pp. 1563-1566

9. Little, C. E. and Piper, J. A.,
   Opt. Commun. **68**, No. 4 (1988) pp. 282-286

10. Latush,. E. L., Sem, M. F., Bukshpun L. M., Koptev, Y. V. and Atamus, S. N.,
    Opt. Spectrosc. **72**, No. 5 (1992), pp. 672-680

11. Bukshpun, L. M. , Latush, E. L. and Sem, M. F.,
    Teplofiz. Vys. Temp. **24** (1986), pp. 402-405

12. Lucas, C. W. and McIntosh, A. I.,
J. Phys. D: Appl. Phys. **19** (1986), pp. 1189-1195

13. Lucas, C. W. and McIntosh, A. I.,
J. Phys. D: Appl. Phys. **20** (1987), pp. 591-596

14. Bethel, J. W. and Little, C. E.,
Opt. Commun. **84** , No. 5-6 (1991), pp. 317-322

CHAPTER 5:

Enhancing the radiative heat extraction from SRLs: experiments

5.1 Introduction: intensifying the heat removal from free-convection cooled SRLs by increasing radiative transfer

In this chapter, the construction and operation of free-convection cooled strontium recombination lasers is described. The results of experiments performed in order to investigate the effect of enhancing the radiative extraction of heat from the outer surface of the SRL discharge tube are reported. The need to process alumina discharge tubes prior to their use in the SRL (if high output powers are to be obtained) is demonstrated.

The design of an SRL must begin with a calculation of the amount of electrical input power which will be needed in order to bring the discharge channel wall up to the correct operating temperature (~600°C). In Chapter 2, a thermal loading model was developed to estimate the rate of heat extraction from a free-convection cooled laser tube, of cross-section as shown earlier in Figure 2.2. The total heat extracted from such a laser tube is composed of components due to conduction, convection and radiation. Applying our model to a free-convection cooled laser tube, utilising an alumina discharge tube, with specifications and operating conditions as given in Table 5.1, reveals, in this case, that the approximate rate of heat removal due to conduction and convection totals 355 W. Using our model, radiation from the outer surface of the ceramic discharge tube amounts to approximately 530 W (taking the outer surface temperature to be 600°C). The total power which must be deposited in this laser tube, in order to attain the optimum SRL operating temperature, is therefore approximately 880 W.

Discharge tube inner diameter	13 mm
Discharge tube outer diameter	17 mm
Discharge tube length	600 mm
Helium layer thickness	1 mm
Quartz thickness	1.25 mm
Discharge tube emissivity	0.5
Discharge channel wall temperature	600°C
Bulk air temperature	30°C

Table 5.1

Approximately 60% of the total power deposited in a free-convection cooled laser is removed via radiation. There is, therefore, real scope for intensifying the heat transfer capacity of a discharge tube by increasing its outer diameter and/or increasing the emissivity of its outer surface. The effect of increasing the discharge tube emissivity on the theoretical optimum average input power for the previously described laser is shown in Figure 5.1.

If the discharge tube's emissivity could be increased from 0.5 to 0.9, we would expect to be able to increase the optimum average input power by ~46% and thereby obtain a commensurate increase in the average laser output power (provided no deleterious effects are caused by the additional gas heating). The effect of enhanced radiative extraction on the performance of the calcium recombination laser system has previously been reported, but no mention was made as to how the tube was blackened [1]. Bethel and Little have recently demonstrated an increase in the average output power of an SRL by fan-cooling the laser tube, to increase its rate of convection-cooling [2]. We now extend our investigations to study the effect of enhanced radiative heat extraction in the SRL system, in order to obtain a comparison between the performance of fan-assisted and enhanced emissivity high power SRLs.

5.2 A free-convection cooled SRL

A diagram of the longitudinally excited free-convection cooled laser, used to investigate the effect of increasing discharge tube emissivity, is shown in Figure 5.2. The active medium was confined in an alumina cylinder of 13 mm inner diameter, 17 mm outer diameter and 600 mm length. Helium layer and quartz wall thicknesses were 1 mm and 1.25 mm respectively. Zirconia felt strips, 1 cm wide, were wrapped around the discharge tube, 2 cm from both of its ends, in order to locate the tube concentrically within its quartz envelope and to prevent against the discharge running down the outside of the discharge tube during operation. Each of the two electrodes was formed by punching tens of

holes in a sheet of molybdenum, which was then rolled into a cylinder and pressed into the laser head, such that it projected up to the end of the discharge tube when the laser was assembled. The laser, of construction as described above, with tube emissivity taken as 0.5 - 0.6, shall henceforth be referred to as ACL 1 (Air-Cooled Laser 1). The laser in which the discharge tube was treated (blackened) in order to increase its emissivity (see Section 5.7), was otherwise identical to ACL 1 and shall henceforth be referred to as ACL 2.

Pulsed excitation of the active medium was achieved by switching the energy stored in a laser head mounted capacitor into the laser tube. The power supply used (built within the Department of Physics at St. Andrews) was capable of producing voltages of up to 20 kV. The storage capacitor was resonantly charged, using the circuit shown in Figure 5.3, in order to double the available charging voltage. The charging inductor, L_c, enables voltage doubling (by transiently allowing the capacitor voltage to ring up to twice the supply voltage) [3] and, in conjunction with the capacitance, C_s, determines the charging time of the storage capacitor, limiting the operating frequency, f_R, for voltage doubling to:

$$f_R = \frac{1}{\pi\sqrt{L_c C_s}} \qquad [5.2]$$

The charging diode prevents current reversal, which would otherwise act to discharge the capacitor and allow its voltage to fall to that of the power supply.

The laser switching element used was an EEV CX1535 pentode thyratron, shown symbolically in Figure 5.4, along with the external components required to obtain satisfactory thyratron operation when using our thyratron control unit (of EEV origin). The CX1535 thyratron is capable of holding off anode to cathode voltages of up to 20 kV. High frequency switching, up to 100 kHz, is guaranteed by the incorporation of the third grid, which is strapped to the cathode via a 10 Ω resistor. The purpose of this third grid, G3, is to shield the second (control) grid, G2, from the anode, thereby reducing the inter-electrode capacitance which would otherwise limit the switching speed. The first grid, G1, is supplied with a positive dc voltage in order to build up the space charge around the cathode. A resistor is connected between G1 and its dc supply to limit the grid current to about 90 mA. G2 is held at a negative potential relative to the cathode to prevent the cathode space charge from diffusing up to the anode and to aid recovery (current termination) after switching. A positive pulse, superposed on the negative G2-bias, enables breakdown and conduction from the anode to the cathode.

5.3 The preparation of the discharge tubes prior to their loading with strontium

Metal ion lasers are particularly susceptible to discharge impurities. This is because the introduction of easily ionizable species into the discharge lowers the electron temperature and therefore reduces the metal ion concentration that can be sustained during lasing. Prior to loading with strontium, the 99.7 % pure Alsint (Multilab Ltd.) discharge

tubes were discharge processed to reduce impurities. This was done by wrapping insulation around the quartz jacket and discharge baking the alumina (at red heat) for several hours, under a slow flow of helium. When the laser could be run sealed-off at optimum operating temperature (as determined by the input power), for more than one hour, with no change in discharge current, it was deemed 'clean' enough for the strontium to be loaded.

5.4 The preparation of strontium and its loading into the discharge tube

Strontium, being low down Group 2 in the Periodic Table of the Elements, is a soft, reactive metal. It readily combines with oxygen to form a white oxide (SrO) and reacts vigorously with water, forming an alkaline solution of strontium hydroxide and hydrogen gas.

Due to the metal's high reactivity, it is usually stored under oil. If absorbed into the body, there is a danger that strontium will displace the less reactive calcium from the bones. Strontium must therefore be handled with care. Gloves should be worn to prevent contact with the skin and a face mask used to avoid inhaling any air-borne particles.

Strontium (99.9% purity) rod (~1 cm diameter) was cut into 1 mm thick discs using a hacksaw. These discs were then compressed in a vice (to prevent the loaded strontium from aperturing the laser beam) and scraped clean under petroleum spirits to remove any oil and surface

oxidation. The discs were finally cut into 2 mm by 5 mm pellets. Under a slow flow of helium, these pellets were placed at 5 cm intervals down the length of the discharge tube, using a 1.5 m long loading rod of semi-circular cross-section. Note that if the strontium pieces are placed too close together, there is a danger that the discharge will jump between the metal pieces, along the tube wall, rather than pass down the axis of the discharge channel, preventing laser oscillation and possibly causing local overheating and tube breakage.

During loading, the strontium pieces were soaked in petroleum spirits to reduce their rate of oxidation (though some degree of oxidation still took place and the pellet's surface often appeared dull as it was being loaded into the discharge tube). A defect of this pellet preparation and loading procedure is that petroleum spirits inevitably ends up in the discharge tube as a contaminant (see Section 5.9.3 for an alternative loading procedure). In order to prevent the pellets from vibrating and aperturing the discharge channel during laser operation, they were melted onto the discharge channel wall by 'overheating' the tube. It was also often necessary to overheat the laser the first time it was operated in order to initiate the production of strontium vapour. Presumably this was due to the presence of a surface film which had to be broken through in order to expose the strontium metal.

5.5 The characterization of air cooled laser 1 (ACL 1)

ACL 1 was operated in the self-heated, sealed-off mode, at helium buffer gas pressures in the range 100 - 400 mbar. Excitation of the active medium was achieved by switching a resonantly charged 1.8 - 3.6 nF capacitor into the laser tube, giving laser current pulses of 100 - 300 A peak and 150 - 250 ns (FWHM) duration, at PRFs in the range 2.5 - 7 kHz. The (non-optimized) optical cavity, 1.2 m in length, was formed by a 2 m radius-of-curvature high reflector and a 6 m radius-of-curvature output coupler of reflectivity ~30% at 430.5 nm. Storage capacitor voltages, laser currents and PRFs were measured using the measurement cursors of a Tektronix 2445B oscilloscope. The potential difference across the storage capacitor was monitored on the oscilloscope using a Tektronix P6015 high voltage probe and the laser current was sensed using a Stangenes current transformer (0.1 volts output per Ampere) placed around the laser current return. At each buffer gas pressure investigated, the storage capacitor voltage was varied in order to change the average laser input power, while the PRF was held constant. The average laser input power, P_{IN}, based on the energy stored in the storage capacitor, was obtained using the formula:

$$P_{IN} = 0.5CV^2 f, \qquad [5.5]$$

where C is the storage capacitance, V is the potential difference across the capacitor before discharge and f is the operating PRF. Average laser output power was measured using a Photon Control Ltd. thermopile calorimeter (Model 25) and analogue power meter.

5.6 Discussion of the characterization results for ACL 1

Figure 5.5 shows a series of characterization graphs obtained for ACL 1 at buffer gas pressures in the range 100 - 300 mbar. Each point on the curves pertains to the conditions for *maximum* output power at the PRF and operating pressure specified. The storage capacitance used to obtain the graphs in Figure 5.5 measured 2.65 nF when cold, falling to approximately 2.35 nF under conditions of peak laser output. This capacitance was found to give the maximum average output power under the conditions investigated.

At each pressure investigated there exists an optimum storage capacitor voltage and PRF for maximum average laser output power. This reflects the need for an optimum peak current density (see Chapter 1) of approximately ~150 A cm^{-3}, to accompany the optimum average input power. As the PRF is increased (laser tube current decreased), under conditions of constant buffer gas pressure, the *calculated* optimum input power for maximum output power appears to increase slightly. This effect may be due to non-optimum laser current density, changes in matching of the discharge circuit to the laser tube, or a change in storage capacitance with pulse repetition rate (i.e., a change in dielectric constant with operating frequency).

Figure 5.6 shows the dependence of the average laser output power on the buffer gas pressure. The average laser output power shows a monotonic increase with buffer gas pressure, reaching 310 mW at 300 mbar. If the storage capacitance is kept constant, the rate of increase

in output power with pressure does, however, reduce as the pressure is increased, because the maximum obtainable peak current density falls and the current fall time rises.

300 mbar is the highest pressure at which output is reported for ACL 1 (of 600 mm active length) because the power supply began current limiting at the high voltages necessary to produce high output powers at pressures above 300 mbar. This made recording output powers above 300 mbar difficult and unreliable, since each time the power supply cut out, the laser would cool down and it could not be guaranteed that it had reached optimum temperature by the time the power supply cut out again.

The conversion efficiency and specific output pulse energy of ACL 1 both increase with buffer gas pressure, as shown in Figures 5.7 and 5.8 respectively. The maximum obtained efficiency, of 0.022% at 300 mbar, and specific output pulse energy, of 1.1 $\mu J\ cm^{-3}$ at 300 mbar, are low (even though the specific input pulse energy was ~5 $mJ\ cm^{-3}$) compared to those values obtained by Latush et al. [4], but comparable with those obtained by McLucas and McIntosh [5] and Bethel and Little [2], from similarly dimensioned laser tubes.

5.7 The treatment of alumina discharge tubes to increase their radiative transfer of heat (emissivity)

In theory, the power radiated from the outer wall of an alumina discharge tube can be increased by coating the tube with a substance of emissivity greater than 0.5. Ideally, the substance used would possess a high temperature ($\geq 600^{\circ}C$) total emissivity of 1. In addition, the chosen substance must:-

1. have a sufficiently high electrical resistance so that it will not conduct the discharge along itself,

2. have a low vapour pressure at lasing temperatures so that it does not contaminate the discharge and

3. not undergo any reaction with the discharge tube and its contents, or change in emissivity during laser operation at 600°C.

Nickel oxide, copper oxide and manganese dioxide have been investigated as potential discharge tube coating materials. The first two mentioned oxides were black at room temperature, but changed colour (oxidation state) when heated in the discharge tube. The nickel oxide became yellow and the copper oxide turned red in places, so that their infrared emissivity became unknown. Manganese dioxide, on the other hand, has a high temperature (1000°C) emissivity of ~0.9 and appeared to be unchanged by discharge heating.

Various techniques were used to coat the discharge tube. These are listed and commented upon below:

1. A slurry of water and the metal oxide was prepared and brushed onto the discharge tube. The resultant coating was thick, but uneven and lumpy. The coating was frequently rubbed off during insertion of the discharge tube into its quartz jacket.

2. A suspension of metal oxide in methanol was produced and painted onto the discharge tube in long stokes. The resultant coating was smoother than that produced using Technique 1, but remained uneven.

3. An artist's diffuser (used to spray fixative onto canvas) was connected to a high pressure air line and used to spray a suspension of the metal oxide (in propanol) onto the discharge tube. This technique produced the best results, as a smooth, uniform coating could gradually be built up.

5.8 Comparison between the performance of a high emissivity and a normal discharge tube

The *same* discharge tube as had been used in ACL 1 was coated with manganese dioxide (using Technique 3, described in Section 5.7, above) and loaded into the free-convection cooled laser assembly used in the construction of ACL 1. The ACL 2 discharge tube was processed

and loaded with strontium, as described in Sections 5.3 and 5.4 respectively. ACL 2 was operated under identical conditions to ACL 1. Figures 5.9 and 5.10 display the average laser output power observed from ACL 1 and ACL 2, at the buffer gas pressures of 200 mbar (charging voltage, 18 kV) and 300 mbar (charging voltage, 18.5 kV), respectively. Table 5.2 summarizes and compares the performance of ACLs 1 and 2 at 200 and 300 mbar.

A 40% increase in average laser output power was obtained by increasing the emissivity of the discharge tube and raising the PRF by 14%. The observed 14% increase in optimum input power is in good agreement with the theoretical increase in permissible input power of ~20% which is expected to accompany an increase in the discharge tube's emissivity from 0.6 to 0.8.

The increase in specific laser output energy, which followed the increase in the discharge tube emissivity, was higher than might be expected, given the 14% increase in input power. This increase in laser efficiency may point to there having been a contaminant problem in ACL 1, questioning the validity of the above comparison between the performance of blackenned and normal discharge tubes. It is important to ensure that discharge contamination is minimized. Further experiments, reported later in Section 5.9, use an alternative strontium loading technique and a better processing proceedure to reduce the possibility of contamination.

5.9 Modifications made to the alumina based free-convection cooled SRL system and subsequent operation of the lasers

5.9.1 Modifications made to the electrodes

During the operation of ACLs 1 and 2, it was noticed that the laser current occasionally became unstable and jumped between two modes, as illustrated in Figures 5.11 and 5.12, which we will call the 'low current mode' and the 'high current mode'. Transitions from the low current mode to the high current mode were characterized by an increase in the peak laser current, a decrease in the laser current fall time and an increase in the rate of collapse of the laser tube voltage and were generally accompanied by an increase in the average laser output power. This effect has also been observed by others [6]. Observation of the electrodes during discharge instability showed that the high current mode occurred when the discharge originated predominantly from a single spot on the cathode, leading to enhanced thermionic emission, while the discharge attachment was diffuse during the low current mode.

Several electrode structures have been investigated in an attempt to improve the discharge stability and maintain the high current mode which accompanies single-point discharge attachment. The most successful electrode consisted of a molybdenum sheet, rolled into a cylinder and spot welded along the seam through a thin strip of nickel, with a single 2 mm diameter hole punched through it, approximately 1 cm from the end lying nearest the discharge tube. This cylinder was surrounded by a second, tight fitting, molybdenum cylinder which

extended beyond the first cylinder's end so that it could be pushed over the discharge tube with the inner cylinder (main electrode) butted up to the end of the discharge tube. The second cylinder, surrounding the electrode proper, served two purposes. Firstly, it prevented the discharge from arcing back through the hole to the laser head and secondly, because it fitted over the end of the discharge tube, it ensured that the discharge originated from the inner surface of the electrode. Our 'improved' electrode is shown in Figure 5.13.

5.9.2 Modifications made to the discharge tube processing technique

The lifetime of sealed-off copper vapour lasers has been extended by using discharge tubes baked in forming gas [7] (a mixture of nitrogen and hydrogen, where the hydrogen acts as a reducing agent to remove discharge tube impurities). It was thought that the operation of SRLs may also be improved by using discharge tubes processed in this manner. Alumina discharge tubes were sent to EEV Ltd. (Chelmsford) where they were baked for approximately 1 hour at a temperature of 1000°C under a slow flow of forming gas.

As a result of processing, the appearance of the alumina discharge tubes was changed. Prior to processing they were yellow, while after processing they appeared white. In order to see if there was any difference between the spectra produced by the processed and unprocessed tubes, helium discharges were run in the tubes while the

discharge end-light was monitored using an optical multichannel analyzer. The results of the analysis were inconclusive because the line intensities were sensitive to detector position, which could not be guaranteed to be identical for all the spectra taken. There were no obvious lines missing from the processed tube's spectra which were present in the unprocessed tube's spectra. The processed tube did, however, appear to contain more hydrogen than the unprocessed tube, presumably as a direct result of using forming gas in the processing procedure.

5.9.3 Modifications made to the strontium loading technique

The use of petroleum spirits during strontium pellet preparation (see Section 5.7) results in an unwanted contaminant being introduced into the discharge tube. An alternative pellet preparation and loading procedure to the one adopted for ACL 1 and ACL 2 is presented below.

Strontium metal which had *not* been in contact with oil was cut, scraped in air and quickly loaded into the laser tube (before substantial surface oxidation had time to occur). Even though the melting point of strontium oxide (2430°C [8]) is significantly above the discharge tube's normal operating temperature of 600°C, no problem was experienced in respect of obtaining vapour from the strontium pellets prepared in this manner. Indeed, they appeared to vaporize more easily than the pellets which had been subjected to oil and petroleum spirits (i.e., it was not necessary to overheat the laser in order to initiate vapour production).

5.9.4 Characterization of the 'improved' SRL

A free-convection cooled laser, ACL 3, geometrically identical to ACL 1, but incorporating the modifications discussed in Sections 5.9.1 to 5.9.3, was assembled and loaded with strontium. The optical cavity and excitation circuit for ACL 3 were identical to those used in ACL 1, with the exception that an ALE 300L switch-mode power supply was used to charge the storage capacitor in place of the 'in-house' power supply which had been used previously.

ACL 3 was operated at buffer gas pressures in the range 100 - 500 mbar at PRFs in the range 2.5 - 5 kHz using a 2.65 nF (nominal) storage capacitance, as had been found optimal for ACL 1. The input power to the laser was varied between 1.0 kW and 1.6 kW. Figure 5.14 shows the dependence of the average laser output power (maximum observed at that pressure) obtained for ACL 3 on the buffer gas pressure.

Output power reached a maximum of 850 mW at a pressure of 300 mbar with an input power of 1.41 kW (based on the power supply voltage and average current), which was delivered at a PRF of 3.37 kHz through a laser current pulse of 200 A peak (current density of 150 A cm^{-3}). This corresponds to a specific laser output energy of 3.2 $\mu J\ cm^{-3}$, delivered at a conversion efficiency of 0.06%. The optimum average input power for ACL 3 showed little dependence on the buffer gas pressure, rising from 1.27 kW at 100 mbar to 1.42 kW at 500 mbar. The optimum PRF decreased with pressure from 3.75 kHz at 100 mbar to 3.33 kHz at 500 mbar.

5.9.5 Comparison between the performance of ACL 3 and a blackened laser tube (ACL 4)

The discharge tube which had been used to construct ACL 3 was blackened with manganese dioxide (using Technique 3, described in Section 5.7) and operated under similar conditions to ACL 3. The maximum average output power observed from the laser with the blackened discharge tube (ACL 4) was 880 mW at 300 mbar with an input power of 1.63 kW, delivered via a peak laser current of 155 A. It was not possible to perform a full characterization of ACL 4 because this laser's output power fell to 420 mW at 300 mbar after only a few hours of operation. Three discharge tubes were blackened and used in the laser, with all exhibiting a similar collapse in output power. On removing the manganese dioxide coating, the tubes were found to have turned yellow, suggesting that they were reverting to their unprocessed state (see Section 5.9.2).

Figures 5.15 and 5.16 compare the performance of ACL 4 with that obtained from ACL 3 at 200 mbar (charging voltage, 19 kV) and 300 mbar (charging voltage, 17 kV) respectively. Note that the output power reported at 300 mbar was obtained under non-optimum discharge conditions (i.e., the tube voltage and hence laser current were lower than optimum, while the PRF was higher than optimum). Blackening the discharge tube permitted the average laser input power to be raised by ~15%. The increase in input power was accompanied by an increase in average laser output power of ~10%. Table 5.3 summarizes the operating conditions and compares the performance of ACL 3 and ACL 4.

5.10 Summary and conclusions

A free-convection cooled strontium recombination laser, based around an alumina discharge tube of 600 mm length, 13 mm i.d. and 17 mm o.d., enclosed by a quartz envelope of 19 mm i.d. and 21.5 mm o.d. has been thermally modelled (using the theory developed in Chapter 2), built and its laser output power characterized.

It has been noted that 'quiet' electrodes are necessary in order to produce a stable laser output. Preferrably the electrodes should stabilize in the 'high current' mode (see Section 5.9.1) since this leads to higher output powers (owing to the input power being deposited in a shorter time, at a higher electron density). This involves using a hole in the electrode to 'lock' the discharge to a single point.

Discharge impurities must be minimized in order to obtain the maximum performance from an SRL. By processing alumina discharge tubes for an hour, in a flow of forming gas at a temperature of 1000°C, and by ensuring that the strontium loaded into the tube had not been in contact with oil or petroleum spirits and that the discharge was stable in the 'high current' mode, the output power of a free-convection cooled SRL has been increased by ~175% (from 310 mW to 850 mW). The increase in output power was obtained through an increase in the specific laser output energy and conversion efficiency (see Section 5.9). Since completion of the experiments, mass spectrometers have become available and it may now be possible to elucidate the nature of the contaminants responsible for poor SRL output.

Calculations have shown that approximately 60% of the theoretical optimum input power (~900 W) for our laser assembly is radiated from the outer surface of the discharge tube. A method for enhancing the emissivity of the discharge tube has been devised. This involves spraying the discharge tube's outer surface with a suspension of manganese dioxide in propanol. Experiments have subsequently been performed in order to investigate the effect on the laser performance of increasing the radiative removal of heat from the discharge tube. It has been found that the manganese dioxide coating permits the average input power to our free-convection cooled SRL to be raised by ~15%, which is consistent with an increase in discharge tube emissivity from approximately 0.6 to 0.8. The average laser output power has thereby been increased by approximately 10%, although our method of increasing the emissivity appears, in the long term, to be incompatible with the use of tubes which have been 'cleaned' in forming gas, since output power falls by approximately 50% after only a few hours in operation.

The optimum average input power for ACLs 1 and 3, based on a calculation of the energy stored in the storage capacitors, appears to be 30% higher than our thermal loading model would suggest. The calculation does, however, neglect power wasted in the discharge circuit due to lead resistance, heating of the charging inductor and diode and during thyratron commutation, the latter of which can amount to as much as 15% [9] of the switched energy. We might, therefore, expect the input power to the laser tube, calculated in this manner, to be higher than our theoretical value.

5.11 Figures for Chapter 5

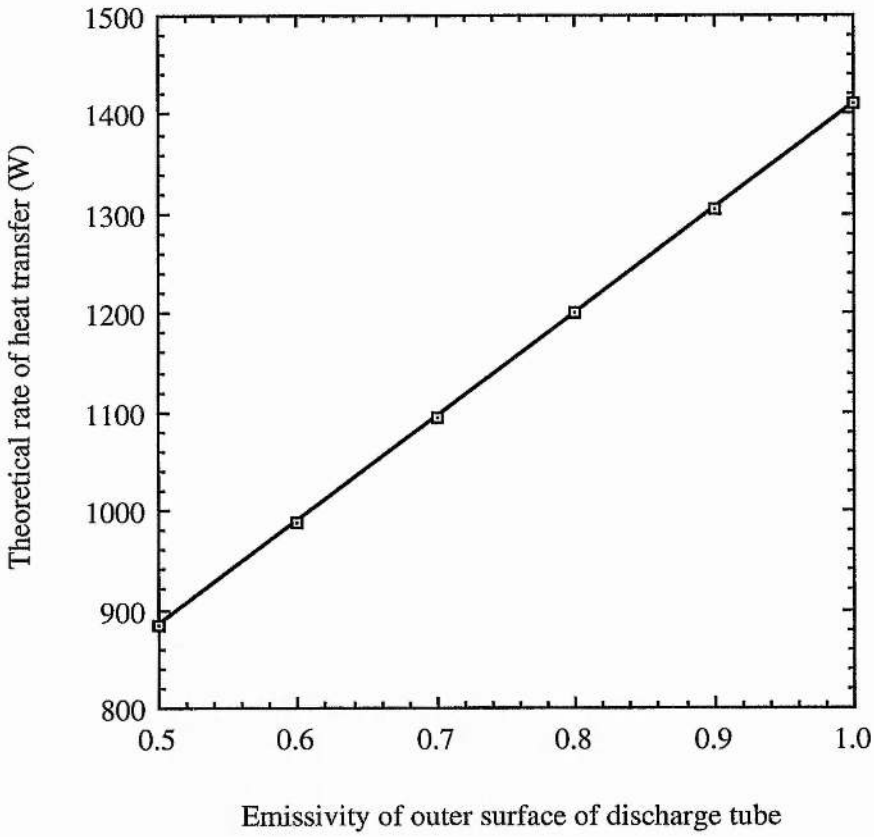

Figure 5.1 **Theoretical total rate of heat transfer from the laser tube specified in Table 5.1 as a function of the discharge tube emissivity.**

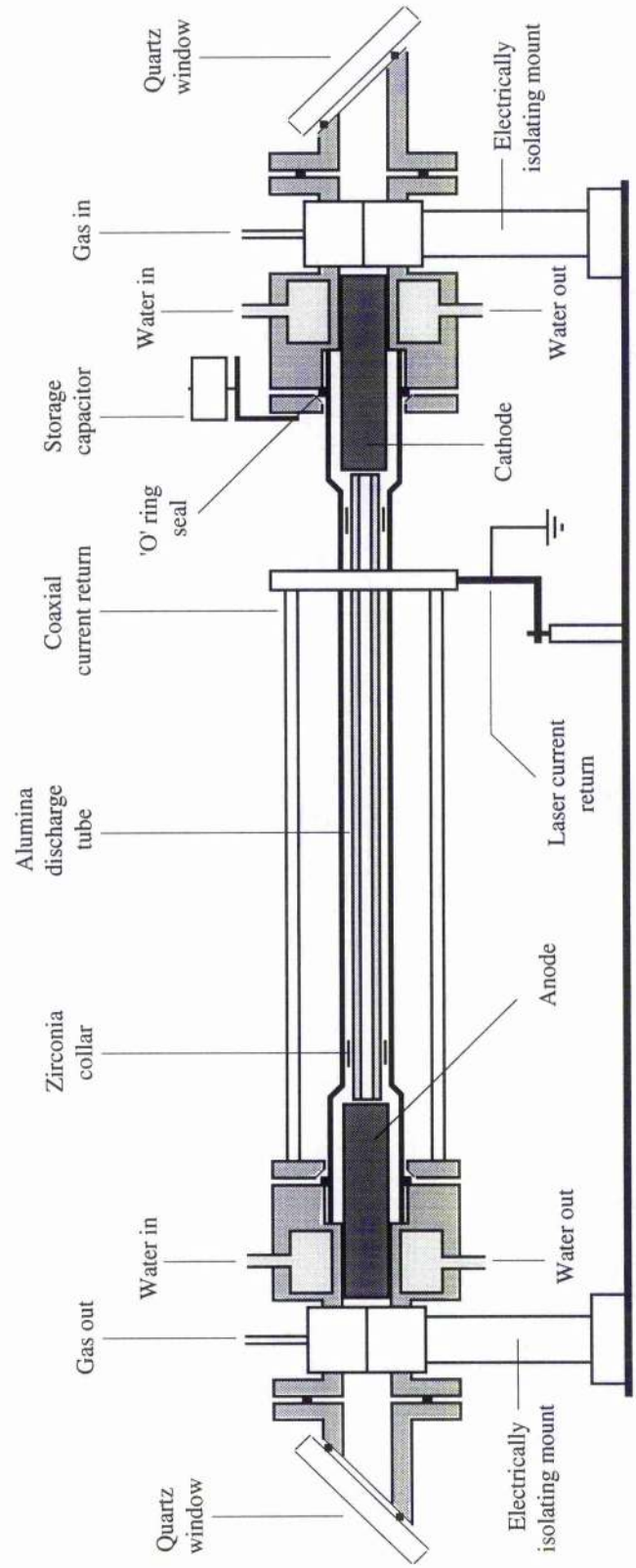

Figure 5.2 Diagram of an assembled alumina based free-convection cooled SRL.

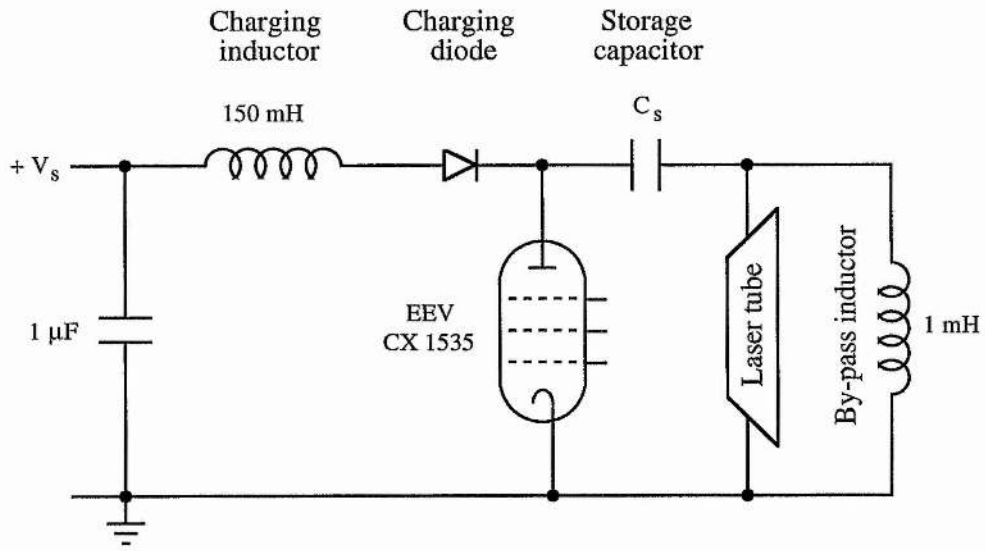

Figure 5.3 Laser excitation circuit.

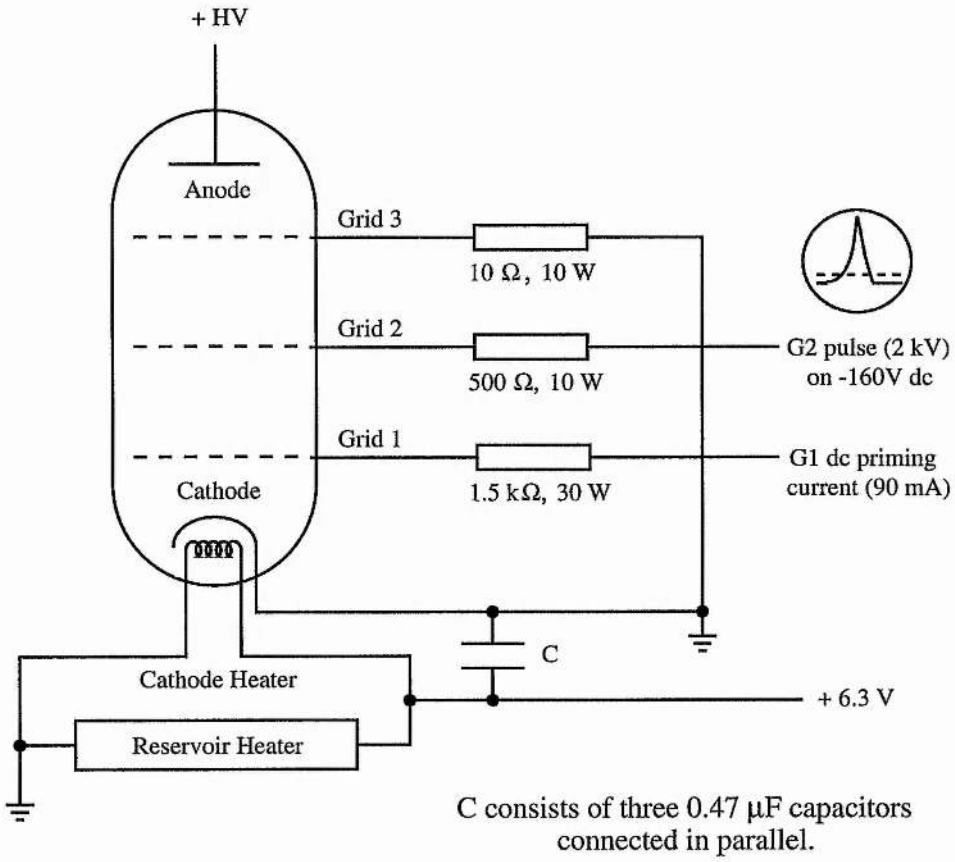

Figure 5.4 EEV CX1535 structure and external components.

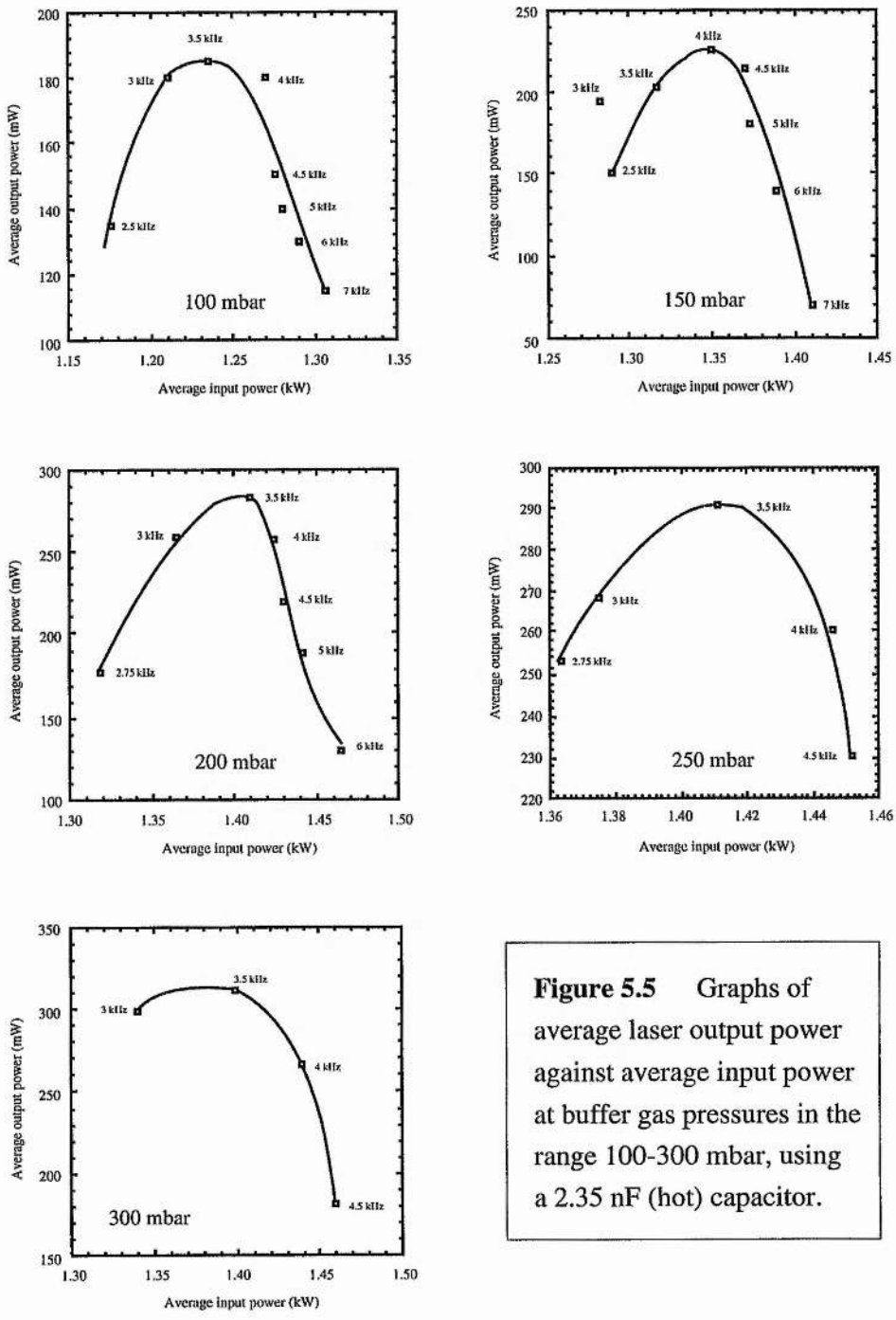

Figure 5.5 Graphs of average laser output power against average input power at buffer gas pressures in the range 100-300 mbar, using a 2.35 nF (hot) capacitor.

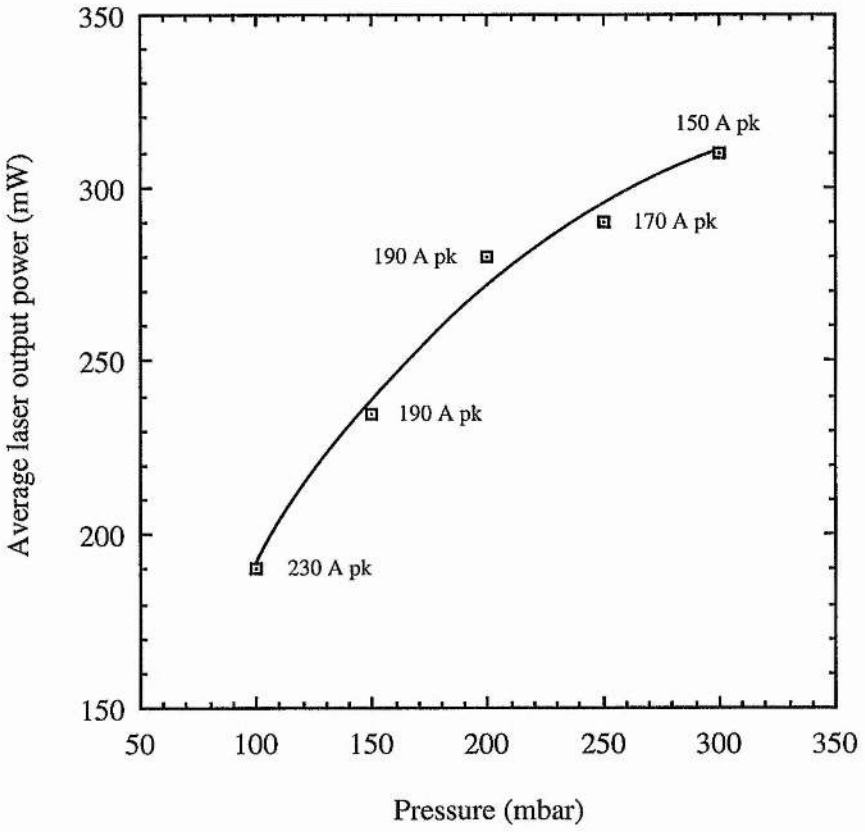

Figure 5.6 The dependence of the average laser output power for ACL 1 on the buffer gas pressure.

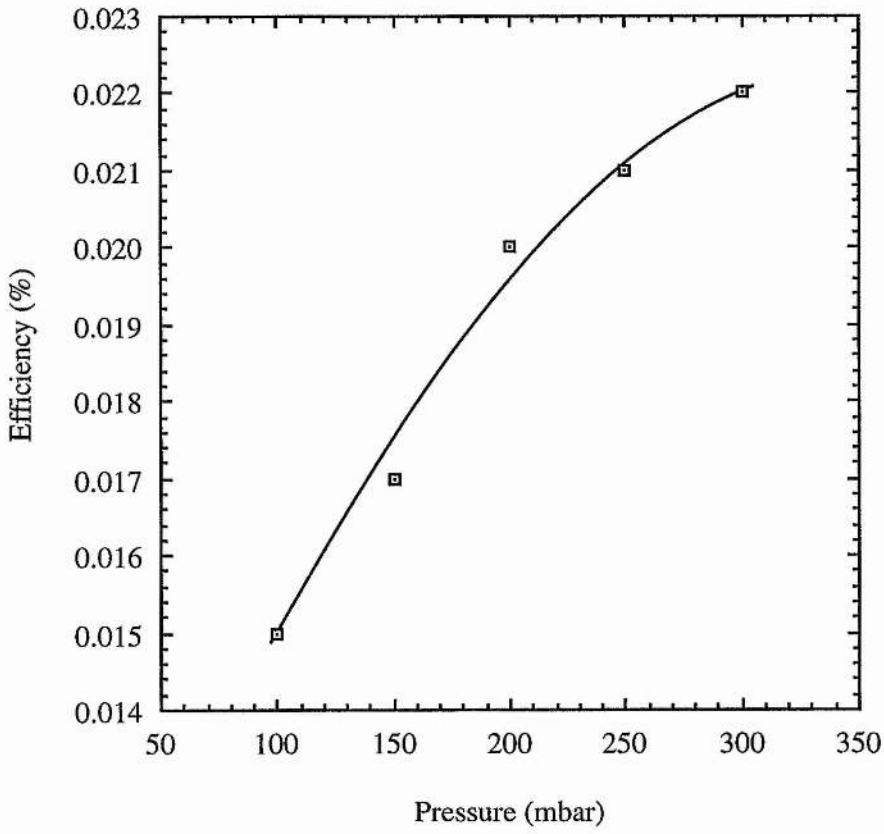

Figure 5.7 The dependence of the conversion efficiency for ACL 1 on the buffer gas pressure.

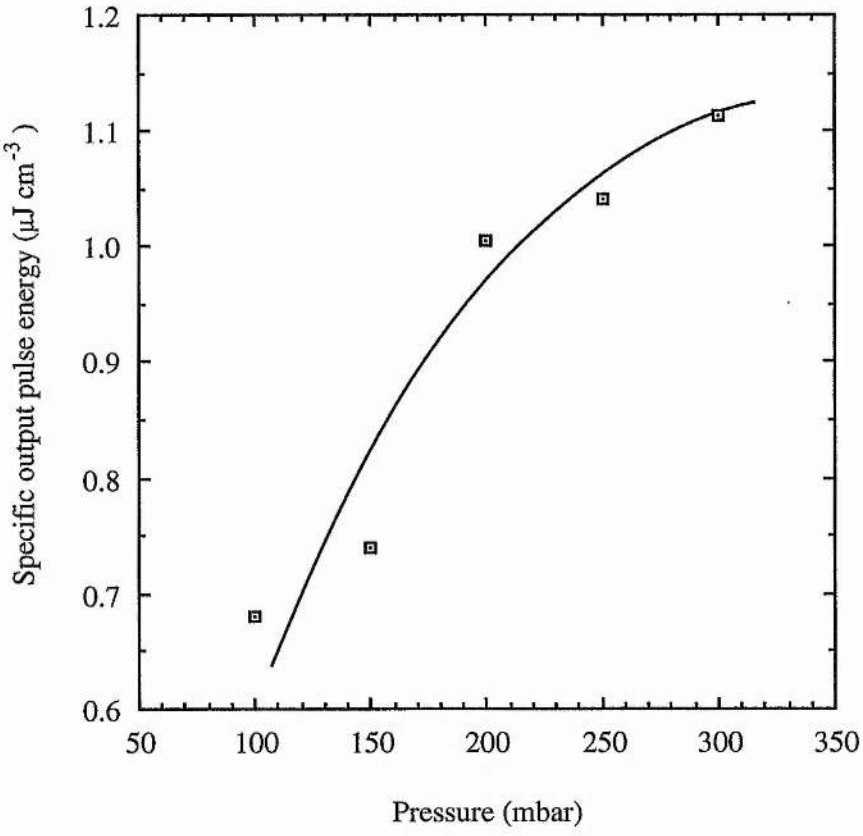

Figure 5.8 The dependence of the specific output pulse energy for ACL 1 on the buffer gas pressure.

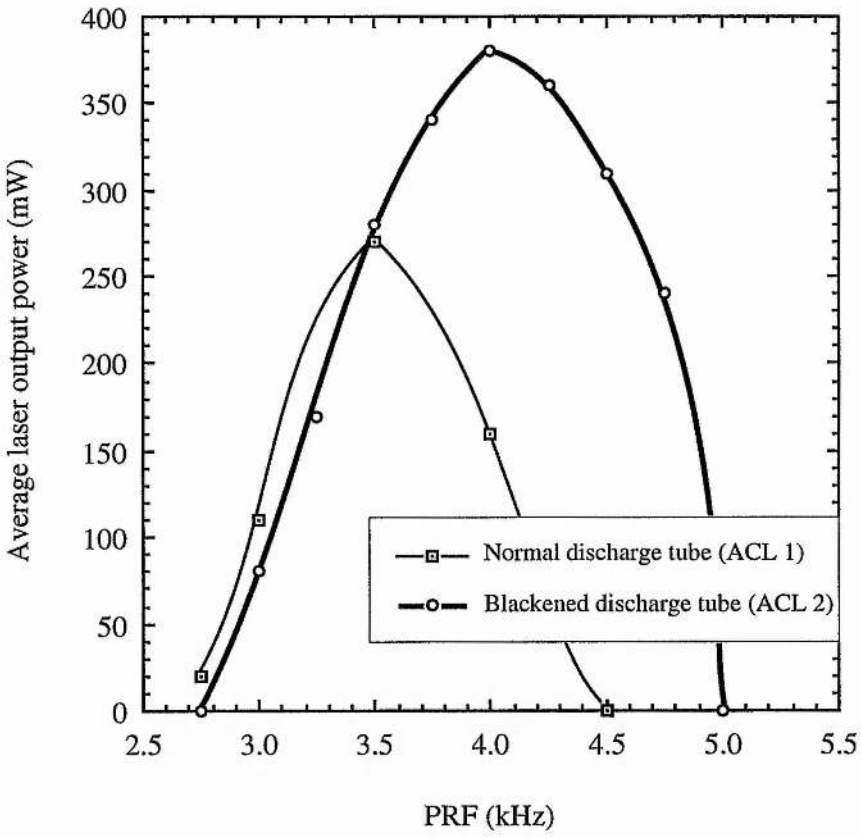

Figure 5.9 Average laser output power of ACL 1 and ACL 2 against PRF, at a storage capacitor voltage of 18 kV and a helium buffer gas pressure of 200 mbar.

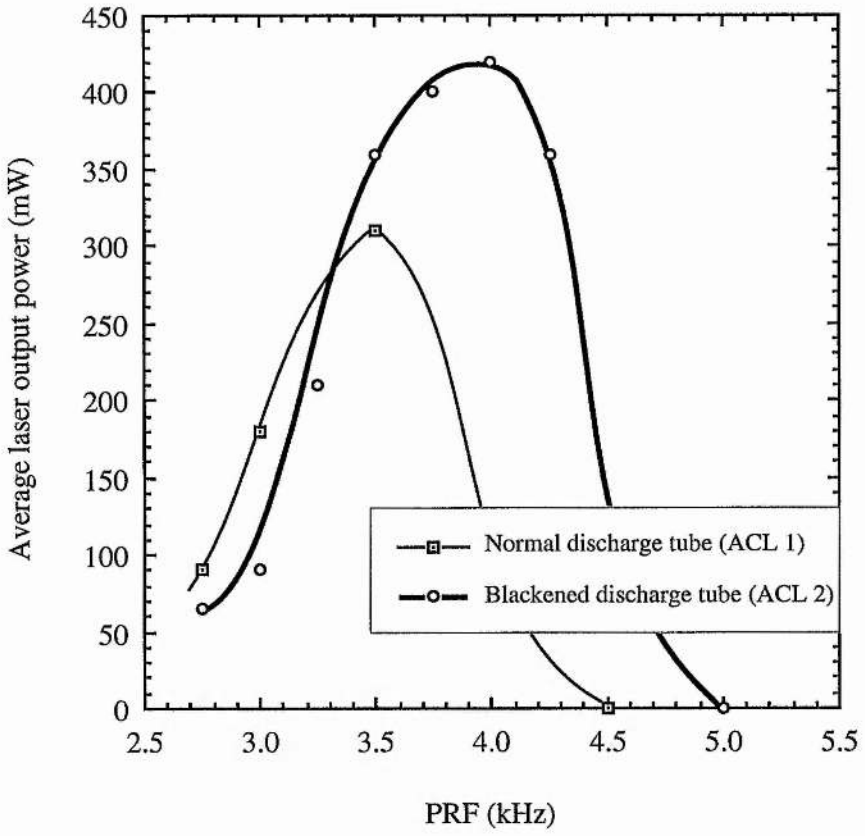

Figure 5.10 Average laser output power of ACL 1 and ACL 2 against PRF, at a storage capacitor voltage of 18.5 kV and a helium buffer gas pressure of 300 mbar.

Pressure (mbar)	200 mbar		300 mbar	
Nature of discharge tube	NORMAL (ACL 1)	BLACKENED (ACL 2)	NORMAL (ACL 1)	BLACKENED (ACL 2)
Average input power (kW)	1.33	1.52	1.41	1.61
Maximum average output power (mW)	270	380	310	420
Specific input pulse energy (mJ cm^{-3})	4.77		5.1	
Specific output pulse energy (μJ cm^{-3})	0.97	1.19	1.11	1.32
Conversion efficiency (%)	0.020	0.025	0.022	0.026
Increase in input power on blackening tube	14%		14%	
Increase in output power on blackening tube	40%		35%	

Table 5.2 Comparison of the operating conditions and laser performance of ACL 1 with those of ACL 2.

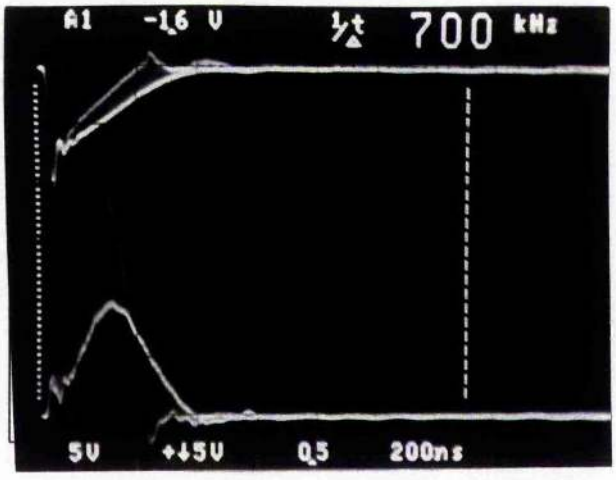

Figure 5.11 Oscillogram showing the 'low current mode'.

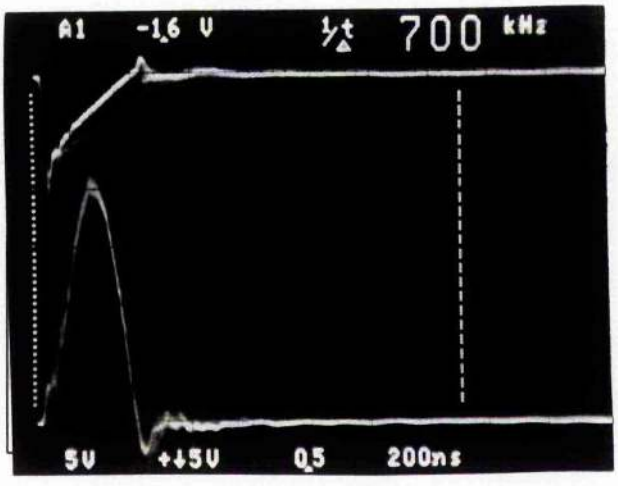

Figure 5.12 Oscillogram showing the 'high current mode'.

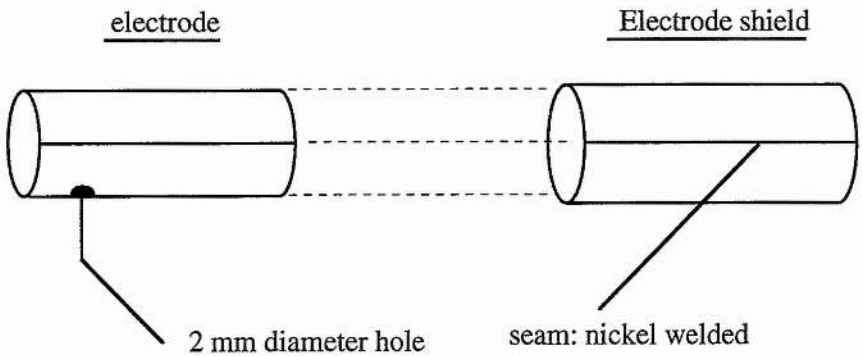

Figure 5.13 Exploded view of the 'improved' electrode

(assembly requires that the electrode be pushed into its shield)

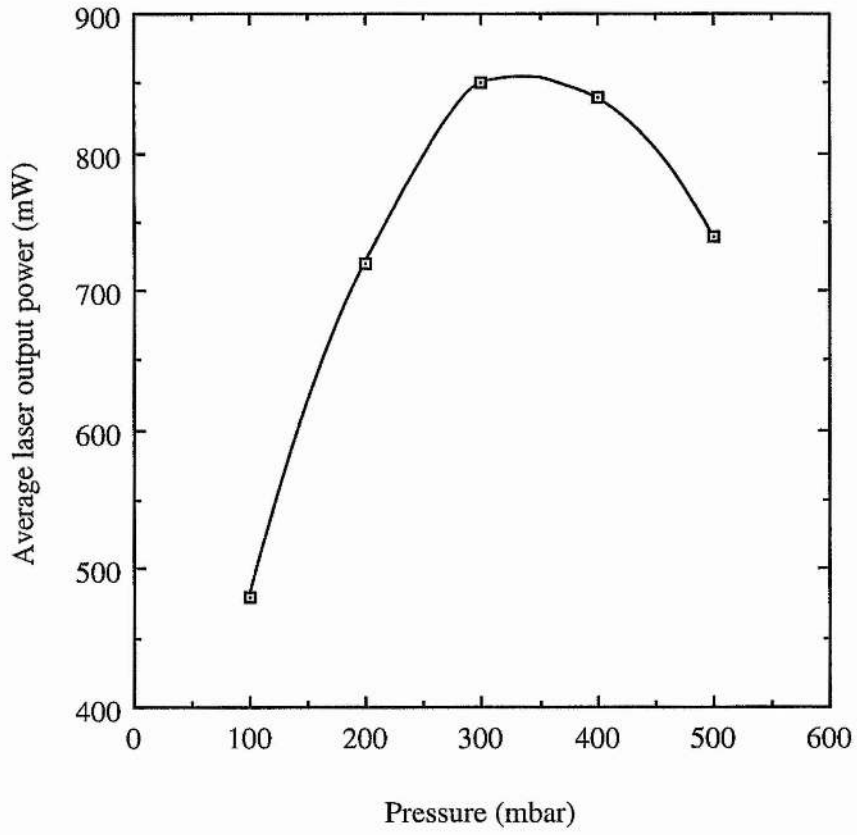

Figure 5.14 Average laser output power of ACL 3 as a function of buffer gas pressure using a 2.65 nF storage capacitor.

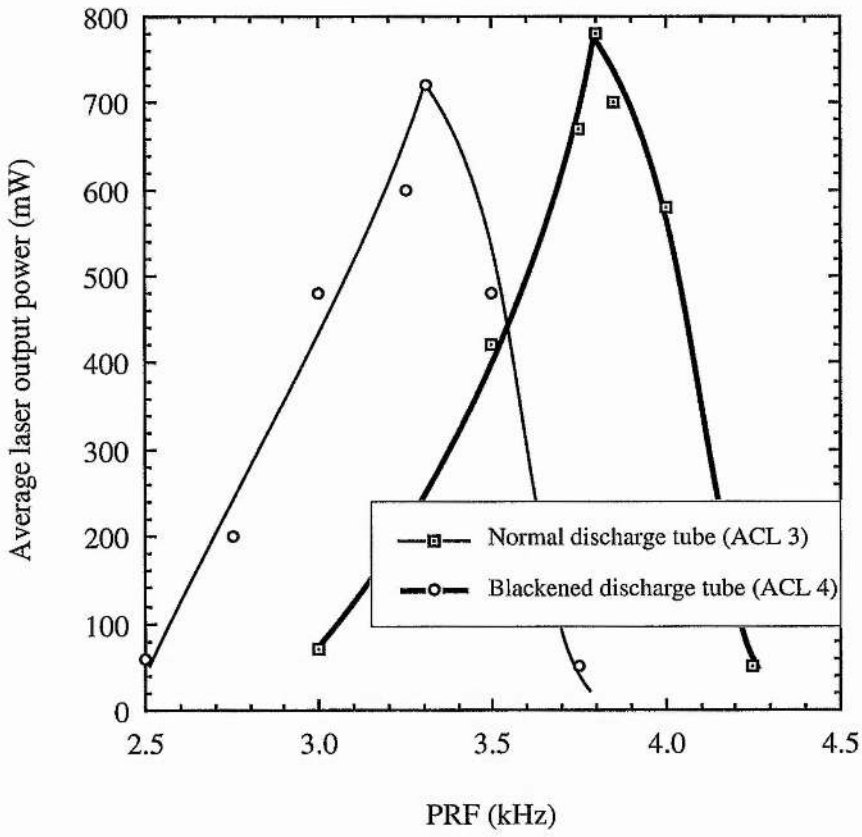

Figure 5.15 Average laser output power of ACL 3 and ACL 4 against PRF, at a storage capacitor voltage of 19 kV and a helium buffer gas pressure of 200 mbar.

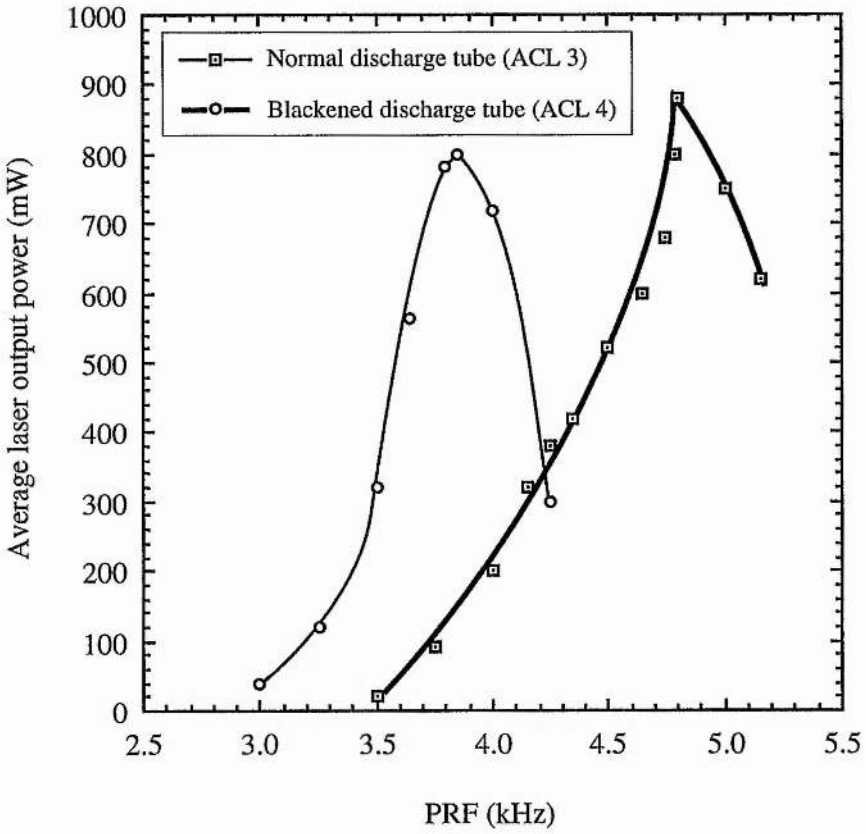

Figure 5.16 Average laser output power of ACL 3 and ACL 4 against PRF, at a storage capacitor voltage of 17 kV and a helium buffer gas pressure of 300 mbar.

Pressure (mbar)	200 mbar		300 mbar *	
Nature of discharge tube	NORMAL (ACL 3)	BLACKENED (ACL 4)	NORMAL (ACL 3)	BLACKENED (ACL 4)
Average input power (kW)	1.40	1.61	1.41	1.63
Average output power (mW)	720	780	800	880
Specific input pulse energy (mJ cm^{-3})	5.3		4.3	
Specific output pulse energy (μJ cm^{-3})	2.73	2.58	2.42	2.30
Conversion efficiency (%)	0.051	0.048	0.057	0.054
Increase in input power on blackening tube	15%		16%	
Increase in output power on blackening tube	8.3%		10%	

Table 5.3 Comparison of the operating conditions and laser performance of ACL 3 with those of ACL 4

(* non-optimum operating conditions).

5.12 References

1. Bukshpun, L. M. , Latush, E. L. and Sem, M. F.,
Templofiz. Vys. Temp. **24** (1986), pp. 402-405

2. Bethel, J. W. and Little, C. E.,
Opt. Commun. **84** (1991), pp. 317-322

3. Clarke, G. L.,
Ph.D. Thesis,
University of St. Andrews (1986)

4. Latush, E. L., Zhukov, V. V., Michalevskii, V. S. and Sem, M. F.,
Proc. Int. Conf. on Lasers 1981 (McLean: STS Press, 1982) pp. 1121-1127

5. McLucas, C. W. and McIntosh, A. I.,
J. Phys. D: Appl. Phys. **19** (1986), pp. 1189-1195

6. Bethel, J. W.,
Private communication

7. Livingstone, E.,
Private communication

8. Greenwood, N. N. and Earnshaw, A.,
Chemistry of the Elements
Pergaman, Oxford (1989)

9. Jones, D. R.,
Private communication

CHAPTER 6:

Enhanced convective cooling of SRL laser tubes: experiments

6.1 Introduction

In this chapter, we investigate scaling the average input power of the strontium recombination laser by water-cooling the laser tube. This permits input powers to the laser to be raised (above that required for a free-convection cooled laser using the same discharge tube), by reducing the helium layer thickness (see Chapter 2), while the discharge channel wall is maintained at the optimum operating temperature of 600°C.

The design and operation of three water cooled SRLs (WCL 1, WCL 2 and WCL 3) is described. The lasers all utilize the *same* discharge tube, formed by butting together two 20 cm long rectangular bore (8 mm by 24 mm) beryllia (BeO) sections of 31 mm outer diameter. The three water-cooled lasers were designed (using the forced convection thermal loading model presented in Chapter 2) for operation at different optimum input powers by incorporating different helium layer thicknesses into the laser tubes. This was accomplished by making three separate water jackets (see Section 6.6), with different inner diameters.

A free-convection (air) cooled laser (ACL 5), utilizing the same beryllia discharge tube as the water-cooled lasers (to give the same discharge channel volume), was designed and operated in order to compare the performance of the water-cooled lasers with an air-cooled laser, of similar active volume.

6.2 General notes pertaining to the construction and operation of the rectangular bore lasers

The beryllia discharge tube was supported within its quartz jacket, whether air-cooled or water-cooled, by three 1 cm wide Zircar AL30 AA (fibrous alumina) collars (one placed at the middle and one placed at each end of the discharge tube) which had been turned on the lathe to suit the outer diameter of the discharge tube (31 mm) and the inner diameter of the quartz jacket (variable).

In order to simplify interchanging between the air-cooling jacket and water-cooling jackets, adapters were made to interface between the different outer diameters of the jackets and our existing laser heads (which had been used to construct ACLs 1 to 4). An exploded view of the laser head and adapter assembly is shown in Figure 6.1.

The lasers were all excited by resonantly charging a laser-head mounted storage capacitor using a 10 kV d.c., 15 kW (1.5 A max.) power supply constructed by EEV Ltd. The switching element used was an EEV CX 1535 thyratron.

The average powers supplied to the lasers by the power supply were calculated from the power supply voltage and average current delivered. In Chapter 5, a discrepancy was noticed between the theoretical optimum laser input power (calculated using our thermal loading model) and the experimental optimum laser input power based on the power supplied by the power supply. This discrepancy was

attributed to energy being wasted as it was transferred from the power supply to the laser tube, particularly in the charging inductor and diode and during thyratron commutation.

In order to test our thermal loading models, while eliminating the losses mentioned above, the actual laser input powers were determined from measurements made of the laser tube voltage and laser current. The method used to obtain the actual laser input powers is described in detail in Appendix F.

6.3 A rectangular-bore free-convection cooled SRL

Applying the thermal loading model developed in Chapter 2, to a free-convection cooled rectangular bore, beryllia-based laser tube, with specifications and operating conditions as given in Table 6.1, reveals that the approximate rate of heat removal due to conduction and convection totals 360 W. Note that beryllia is such a good conductor of heat, compared with helium and quartz (see Chapter 2), that its thickness has a negligible effect on the total rate of heat transfer from the laser tube. The modelling can therefore be performed as if the discharge tube were of cylindrical bore, with the discharge channel diameter equal to 8 mm or 24 mm. Radiation from the outer surface of the discharge tube described in Table 6.1 amounts to approximately 640 W (using our model and taking the outer surface temperature of the beryllia to be 600°C). The total power which must be deposited in this laser tube

(ACL 5) in order to obtain the optimum SRL operating temperature, is therefore approximately 1 kW.

Discharge tube width	8 mm
Discharge tube height	24 mm
Discharge tube outer diameter	31 mm
Discharge tube length	400 mm
Helium layer thickness	2 mm
Quartz thickness	2 mm
Discharge tube emissivity	0.5
Discharge channel wall temperature	600°C
Bulk air temperature	30°C

Table 6.1

Notice that, while the theoretical optimum average input power and active volume for ACL 1 (see Chapter 5) and ACL 5 are both similar, the theoretical optimum linear input power density for the latter is ~1 kW m^{-1} higher than for the former. Hence, if a cylindrical bore beryllia discharge tube of the same length, outer diameter and active

volume were used in ACL 5 in place of the rectangular tube, the expected gas temperatures in this system would be higher than those in ACL 1 (see Chapters 3 and 4). However, the use of the rectangular bore tube, of aspect ratio 3 : 1 (which is more effective at removing the heat generated within it than a cylindrical bore tube of the same length and active volume, owing to its large surface area to volume ratio), results in the expected gas temperatures for ACL 5 being *lower* than those for ACL 1. These points are illustrated quantitatively in Table 6.2 below.

Quantity \ Laser	ACL 1	15.6 mm cylindrical bore tube	ACL 5
Discharge tube length (cm)	60	-	40
Active volume (cm^3)	79.6	76.5	76.8
Theoretical average input power (W)	880	-	1000
Theoretical linear input power density (kWm^{-1})	1.47	2.5	2.5
Expected axis gas temperature (K)	1181	1367	1131
Expected Average gas temperature (K)	1033	1133	1011

Table 6.2

By using a rectangular bore discharge tube, we have effectively increased the bore cross-sectional area, without (theoretical) detriment to the gas temperature. There should, therefore, be no fall in specific output pulse energy when comparing the performance of ACL 5 with that of ACL 1. Indeed, on the contrary, the reduced tube length of ACL 5 over that of ACL 1 may permit higher pressure operation (because the operating pressure for ACL 1 was limited by the power supply and thyratron voltage hold-off limit of 20 kV) and hence higher specific output pulse energies to be extracted from ACL 5 than were possible from ACL 1 .

6.4 The assembly and operation of ACL 5

ACL 5 was assembled as shown in Figure 6.2. Strontium rod (stored in air) was cut (in air) into 6 rectangular pellets measuring approximately 10 mm by 5 mm. These pellets were placed at approximately 6 cm intervals along the length of the discharge tube, using a 1 m long loading rod of semi-circular cross-section.

The electrodes, shown schematically in Figure 6.3, were machined from a stainless-steel rod. A stainless-steel disk, with a rectangular hole cut out of it to match the cross-section of the discharge channel, was welded to one end of the cylinder to prevent the discharge originating from the outer surface of the electrodes. In order to 'lock' the discharge to a single point on the electrode, a 3 mm hole was drilled through the

electrode and then welded up to prevent the discharge from projecting through the hole and striking to the outside of the electrode.

ACL 5 was operated in the self-heated, sealed-off mode, at helium buffer gas pressures in the range 200 - 500 mbar. Excitation of the active medium was achieved by switching a resonantly charged 2 - 4 nF capacitor into the laser tube at PRFs in the range 3 - 7 kHz. The (non-optimized) optical cavity, 1 m in length, was formed by a 2 m radius-of-curvature high reflector and a 6 m radius-of-curvature output coupler of reflectivity 35% at 430.5 nm.

6.5 The performance of ACL 5

6.5.1 Electrode performance

The operation of the electrodes below 300 mbar was disappointing. The discharge was erratic and the laser current pulse unstable, indicating that the hole in the electrodes was not effectively 'locking' the discharge. The discharge also spread onto the outer surface of the electrode. At higher buffer gas pressures the situation was somewhat better, with the discharge originating predominantly from inside the electrode and the current pulse stable to within 10% of its nominal value. It was, however, difficult to see whether the discharge was locked to the hole, as the discharge glow was too bright to be able to resolve detail when looking at the laser tube end light (even when neutral density filters were used). Satisfactory electrode operation appeared to

be very dependent on the PRF, with certain frequencies leading to a noisy discharge and poor laser output. Changes in PRF of 100 Hz were often sufficient to cause electrode instability. The discharge could be seen to flicker at the cathode (though the laser current monitored on the oscilloscope changed by less than 10%), with the laser beam cross-sectional area pulsating commensurately.

6.5.2 ACL 5 laser output power performance

The highest stable and repeatable average output power observed from ACL 5 was 760 mW. This was achieved at a peak laser current of 245 A in 350 mbar of helium with a PRF of 4.35 kHz. The average laser input power, based on the power supply voltage (7.75 kV) and average current, was 1.36 kW. The average input power obtained from measurements made on the laser tube voltage and current, using the method described in Appendix F was 1.1 kW.

6.6 The construction and operation of rectangular-bore forced-convection cooled SRLs

The three water-cooled lasers described in this chapter, used different helium layer thicknesses to achieve different optimum input powers. This was accomplished by using the thermal loading model presented in Chapter 2 to design three separate water jackets, each giving rise to a different helium layer thickness.

The three water jackets, of similar construction, were comprised of three concentric quartz tubes as shown in Figure 6.4. The water entered at the centre of the jacket, flowed to the jacket end and then returned to the other end before being removed at the tube's centre. This arrangement ensured that there were no dead flow regions adjacent to the discharge tube. The inner most flow annulus was kept narrow (~1mm) to ensure a high speed of flow from the available water supply and effective heat transfer from the quartz to the water (see Chapter 2). An assembled water-cooled laser is shown diagramatically in Figure 6.5.

The water jackets were supplied from a boosted water supply (~85 lb in^2), and the volumetric flow rate (litres $min.^{-1}$) was monitored with a gap meter. The inlet and outlet water temperatures were measured using platinum resistance thermometers.

The three water jackets were designed to give helium layer thicknesses of 7.5 mm, 3.5 mm and 1 mm when used with the rectangular bore beryllia discharge tube of external diameter 31 mm. The important dimensions, estimated discharge tube emissivity and approximate operating temperatures for the three laser systems, WCL 1, WCL 2 and WCL 3, are given in Table 6.3. The operating conditions expected for WCL 1, WCL 2 and WCL 3 at optimum discharge channel wall temperature are listed in Table 6.4.

Quantity \ Laser	WCL 1	WCL 2	WCL 3
Discharge tube width	8 mm	8 mm	8 mm
Discharge tube height	24 mm	24 mm	24 mm
Discharge tube outer diameter	31 mm	31 mm	31 mm
Discharge tube length	400 mm	400 mm	400 mm
Helium layer thickness	7.5 mm	3.5 mm	0.9 mm
Quartz thickness	2 mm	1.85 mm	2.55 mm
Inner diameter of water flow annulus	50 mm	41.7 mm	37.9 mm
Thickness of water flow annulus	1.5 mm	1.2 mm	0.95 mm
Discharge tube emissivity	0.5	0.5	0.5
Discharge channel wall temperature	600°C	600°C	600°C
Bulk water temperature	10°C	10°C	10°C

Table 6.3 Specifications for WCLs 1, 2 and 3

Quantity \ Laser	WCL 1	WCL 2	WCL 3
Theoretical rate of conduction and convection based on 8 mm ID (W)	901	1688	4675
Theoretical rate of radiation (W)	614	595	525
Theoretical optimum average input power based on 8 mm ID (kW)	1.5	2.3	5.2
Linear input power density based on 8 mm ID (kW m^{-1})	3.75	5.75	13
PRF required for a specific input pulse energy of 5 mJ cm^{-1} (kHz)	4	6	13.5
Obtainable volumetric water flow rate (litres min^{-1})	12	12	12
Water flow speed (m s^{-1})	0.82	1.23	1.82
Expected water temp. difference across ends of discharge tube (°C)	1.8	2.7	6.2
Expected axis gas temperature (K)	1240	1380	1850
Expected average gas temperature (K)	1070	1150	1410
Expected axis gas temperature in a cylindrical bore tube of same length, voume and average input power (K)	1575	1852	2708
Expected average gas temperature in a cylindrical bore tube of same length, volume and average input power (K)	1248	1406	1907

Table 6.4 Expected operating conditions for WCLs 1, 2 and 3

Water-cooled laser 1 used the same electrodes as ACL 5. These did not, however, perform well when used in WCL 2 and WCL 3 because the higher input powers caused the stainless-steel to sputter. New electrodes were therefore machined from a solid piece of molybdenum. A diagram of these molybdenum electrodes is shown in Figure 6.6.

Water-cooled laser 3, with the 0.9 mm helium layer thickness, proved difficult to assemble. The AL30 AA collars used to locate the beryllia discharge tube within the water jacket were very fragile. Further, because they powdered during handling, the collars became slack during insertion into the water jacket, resulting in the discharge tube lying off axis (within the water jacket). A non-uniformity in helium layer thickness as small as 0.1 mm has a large effect on the heat transfer from the discharge tube when the helium layer thickness is ~1 mm (see Chapter 2). Uniform heat transfer through helium layer thicknesses of 1 mm and less is difficult to achieve.

All of the water-cooled lasers were discharge processed for several hours, prior to loading with strontium. Strontium rod (stored in air) was cut (in air) into pellets (1 mm by 5 mm by 10 mm) which were placed along the discharge channel at ~6 cm intervals. Owing to the high input powers necessary to optimize the strontium vapour pressure in these lasers, difficulty was experienced in respect of melting the strontium to the discharge channel wall. The strontium pellets often moved before they had melted into place, most commonly settling in the electrodes.

6.7 The performance of the water-cooled SRLs

6.7.1 The performance of WCL 1

Figure 6.7 shows the average laser output power for WCL 1 as a function of buffer gas pressure using different storage capacitors, with the charging voltage and PRF optimized at each pressure used. The lowest storage capacitance used (2.65 nF) enabled laser output to be maintained to higher buffer gas pressures (output power peaked at 500 mbar) than the larger capacitors (3.2 and 3.7 nF). The highest stable and repeatable average laser output power of 1760 mW was obtained at 400 mbar using a 3.2 nF (nominal) storage capacitor.

Figure 6.8 shows the average laser output power for WCL 1 as a function of PRF, at buffer gas pressures of 300 mbar and 400 mbar, with the input power optimum at ~2.2 kW (based on power supply voltage and current). The actual optimum input power to WCL 1 (obtained from the laser tube voltage and laser current, shown in Figure 6.9) was calculated to be 1.65 kW.

Laser output power was sensitive to PRF, peaking at 6 kHz. At both 300 mbar and 400 mbar, the output power dropped when the PRF was increased from 6 kHz to 7 kHz (under conditions of constant input power), and then rose as the PRF was further increased to 8 kHz (still under conditions of constant input power).

The laser's output power showed a similar sensitivity to the PRF when the PRF was reduced at a fixed charging voltage (so that the input power was reduced with the PRF). This is illustrated in Figures 6.10, 6.11 and 6.12. These oscillograms display the laser pulse intensity as the PRF was reduced from 8 kHz to 7 kHz and then to 6 kHz, under conditions of constant charging voltage. They were taken within 10 seconds of changing the PRF, the PRF being further reduced as soon as a photograph had been taken (to maintain the Sr vapour density). The laser pulse intensity fell as the PRF was reduced from 8 kHz to 7 kHz and then rose as the PRF was further reduced from 7 kHz to 6 kHz.

We might expect the laser pulse intensity to decline steadily with decreasing PRF (at constant charging voltage) because the discharge channel wall temperature is decreasing, leading to a lower strontium vapour pressure. Our results do not show such a dependence. In order to ascertain the temporal dependence of the laser output power on the input power (strontium vapour pressure), the laser was first optimized for operation at 8 kHz. The input power was then reduced by 25%, by decreasing the PRF to 6 kHz, and the average laser output power was recorded at one minute intervals. After 4 minutes the PRF was returned to 8 kHz, so that the input power was once again optimum, and the output power was again recorded as a function of time. Figure 6.13 shows the temporal evolution of the average laser output power as the input power was varied at constant charging voltage. It can be seen that reducing the PRF from 8 kHz to 6 kHz resulted in an instantaneous increase in output power. Over the first minute of cooling, the output power changed by less than 10%. A further 3 minutes was required for

the strontium vapour pressure to fall significantly and cause the laser output power to drop to half of its initial value (at 8 kHz). The response time of the laser power meter, to changes in incident power of 1 W, was measured as ~6 seconds. Thus, on a minute time scale, SRL 1 output power is insensitive to decreases in input power of up to 25%. This means that the strontium vapour pressure does not change significantly in 1 minute as the input power is varied by up to 25%.

At 7 kHz, WCL 1 exhibited an output power minimum (turning point). This minimum could be observed by varying the PRF at constant input power, or by reducing the PRF at constant charging voltage in too short a time for the strontium vapour pressure to change significantly. This dependence of laser output power on PRF may be due to acoustic effects (see Appendix G) within the discharge channel (upsetting the helium density uniformity and therefore the electron cooling and population inversion) or discharge instability (causing the discharge to deviate from the tube axis, resulting in a non-uniform distribution of strontium vapour pressure by local wall heating). There was an unmistakable increase in acoustic output intensity (sound of the laser) at 7 kHz compared to that at 6 kHz or 8 kHz.

It is interesting to note, on studying the results reported by Hentschel and Piper [1] for a 60 cm long rectangular bore (24 mm by 8 mm) air-cooled SRL, that the laser output power exhibited minima of 400 mW at 100 torr (135 mbar) and 600 mW at 200 torr (270 mbar) when the PRF was set to 5 kHz. At 200 torr the output power rose, either side of 5 kHz, to 680 mW at 3 kHz and 700 mW at ~7 kHz. The ratio of

the frequencies at which output power turning points were observed in our and Hentschel's tubes is approximately equal to the reciprocal of the ratio of the discharge tube lengths, i.e.,

$$\frac{5}{7} \cong \frac{4}{6}.$$

This may be coincidental, but suggests the influence of acoustic standing waves in the helium, since (see Appendix F):

$$f_n \propto L^{-1},$$

where f_n is the frequency of the nth harmonic in a pipe of length L.

Because the strontium vapour pressure is insensitive to rapid changes in input power (performed over a time scale of less than 1 minute, so that the tube does not overheat), it is possible to obtain transient output powers in excess of those obtainable under steady-state conditions. By momentarily raising the PRF at optimum input power, output powers of over 2 W have been observed from WCL 1. Transient increases in output power have also been observed in other SRL systems [1]. Output powers obtained in such a manner should not really be used to evaluate the performance of SRLs, since the prolonged operation of self-heated lasers at elevated PRFs will result in the production of too much strontium vapour. Output power will ultimately fall as the ratio of strontium number density to helium number density becomes unfavourable (see Chapter 4) and the tube 'overheats'.

6.7.2 The performance of WCL 2

A maximum average laser output power of 2.3 W was observed from WCL 2 (the first time it was operated) at a PRF of 10 kHz, with an input power of 3.4 kW (based on power supply voltage and current). This level of output power was not observed again, although it was not a transient. The maximum stable and repeatable average output power of WCL 2 was typically 1.4 W, (lower than that obtained from WCL 1) at an input power of 3.3 kW (based on the power supply voltage and current). The actual optimum input power for WCL 2 (obtained from the laser tube voltage and laser current shown in Figure 6.14) was calculated to be 2.6 kW. The dependence of WCL 2 output power on the PRF, under conditions of constant input power at 300 mbar, with storage capacitances of 3.2 nF and 3.7 nF is shown in Figure 6.15. The optimum operating frequency for WCL 2 was 11.5 kHz. The discharge current in WCL 2 was often unstable, accompanied by the laser output power fluctuating between 1.2 W and 1.7 W. This instability was attributed to the many sharp edges on the moybdenum electrodes (remaining because the molybdenum had proved very hard to machine) which caused the discharge to move around on the electrodes.

After a few days operation, longitudinal cracks appeared in the beryllia discharge tube. These cracks began at the ends of the discharge tube, where the wall was thinnest (i.e., at the top and bottom of the tube), and gradually crept towards the tube's centre. The discharge began to track along the cracks, which filled with strontium, rather than passing down the axis of the tube. Laser output power fell.

6.7.3 The performance of WCL 3

Threshold laser oscillation (between two high reflectors) was observed from WCL 3 at a PRF of 15 kHz, with an input power of 7.4 kW. We were, however, unable to couple significant laser power out of the cavity, although some erratic bright 'flashes' of light were observed. After a few hours of operation the beryllia discharge tube cracked severely.

6.8 Discussion of the performances of the rectangular bore air-cooled and water-cooled lasers

Table 6.5, overleaf, summarizes the best stable and repeatable performances of ACL 5, WCL 1 and WCL 2. The use of water-cooling has enabled the input power to the 40 cm long rectangular bore beryllia discharge tube to be increased over the input power of 1.1 kW required by the rectangular bore air-cooled laser (ACL 5). The increase in permitted input power accompanying the use of water cooling has resulted in the output power extracted from the discharge channel being increased above the 760 mW value observed through the use of free-convection cooling. For the laser tube with the 7.5 mm thick helium layer (WCL 1), the maximum recorded stable average output power reached 1.8 W. This was achieved with a discharge tube input power of ~1.65 kW, so that the conversion efficiency was 0.11%. The specific laser output power of WCL 1 was 22.9 mW cm^{-3}, which is more than twice that obtained from ACL 5 (9.9 mW cm^{-3}). Higher specific output

powers can thus be obtained from water-cooled tubes than from air-cooled tubes. This is because the intensified heat transfer afforded by water cooling allows water-cooled laser tubes to be operated at higher PRFs than air-cooled tubes.

Quantity \ Laser	ACL 5	WCL 1	WCL 2
Buffer gas pressure (mbar)	350	400	300
Theoretical optimum average input power based on a bore of 8 mm (kW)	1	1.5	2.3
Average input power based on power supply voltage and current (kW)	1.36	2.22	3.27
Average input power based on laser tube voltage and current (kW)	1.1	1.65	2.6
PRF (kHz)	4.35	6	11.5
Maximum stable and repeatable average output power (mW)	760	1760	1420
Specific output power (mW cm^{-3})	9.9	22.9	18.5
Specific output energy ($\mu J\ cm^{-3}$)	2.3	3.8	1.61
Efficiency based on power supply voltage and current (%)	0.056	0.079	0.043
Efficiency based on laser tube voltage and current (%)	0.069	0.106	0.055

Table 6.5 The performances of ACL 5, WCL 1 and WCL 2.

Under optimum operating conditions (i.e., at a discharge tube input power of 2.6 kW, PRF of 11.5 kHz and a buffer gas pressure of ~300 mbar), the stable and repeatable average output power observed from WCL 2 (3.5 mm thick helium layer) was typically around 1.4 W. However, the first time that WCL 2 was operated, the average output power peaked at 2.3 W, corresponding to a specific output power of 30 mW cm^{-3}. Although this maximum observed output power from WCL 2 (2.3 W) was not obtained by transiently raising the input power above the optimum value of 2.6 kW, it could not be repeated on subsequent laser operation. A possible explanation for the decrease in output power noticed on subsequent laser operation is concerned with the appearence of cracks running longitudinally along the discharge tube. As the cracks filled with strontium, the discharge could be seen to track along these cracks, (conducted by the strontium) rather than pass down the axis of the tube. This effectively reduced the active length of the discharge tube as the strontium vapour distribution became non-uniform and the current density through the gas fell below optimum.

WCL 3 failed to give a significant output power. This may have been due to a number of reasons. As the optimum input power to a given discharge tube is raised, by making the helium layer narrower, the gas temperatures experienced at the optimum input power must also rise and because the PRF is raised, the interpulse period decreases. This rise in gas temperature is expected to reduce the population inversion, with lasing ceasing at some critical temperature (see Chapters 1, 3 and 4). Further, since the input power to the laser is raised by increasing the PRF, the increase in gas temperature coupled to the reduction in

interpulse period will cause increasing radial concentration gradients across the tube bore (the strontium swept away from the tube axis through ambipolar diffusion will have less time in which to diffuse back to the tube axis before the onset of the next current pulse). Use of the rectangular bore tube (rather than a circular bore tube of the same cross-sectional area) should lead to a reduction in these effects since they are determined by the smallest dimension of the bore. We expect the characteristic diffusion time for our lasers to be of the order of 1 ms [2] so that diffusion effects become important when the lasers are operated at kHz PRFs. However, the appearance of cracks in the discharge tube, coupled to increasing electrode instability encountered at the higher input powers, may also have been responsible for the poor performance of WCL 3. In order to ascertain whether the high linear input power density of 13 kW m^{-1} (i.e., the high theoretical average gas temperature of 1410 K) and the high operating PRF (15 - 20 kHz) of WCL 3 were responsible for its poor performance, electrode instability and thermal fracture of the discharge tube will have to be eliminated in future experiments.

The powers supplied to the lasers by the power supply (based on the power supply voltage and current), were ~40% higher than those predicted by our thermal loading models (Figure 6.16). This discrepancy is believed to be due to thyratron commutation loss and losses in the charging inductor and diode. Measurements made on the laser tube voltages and currents, revealed that the actual input power to the lasers agreed with the theoretical values to within ~10%.

6.9 Laser beam profiling experiments

Laser beam profiling was accomplished using a Thorlabs Model Det 2-Si high speed silicon photodiode detector. This has a usable sensitivity covering the spectral range 200 nm to 1100 nm (sensitivity peaks at 900 nm). The detector was mounted behind a 1 mm pin-hole and the assembly was scanned vertically and horizontally across the laser beam. The photodiode's output was monitored via the 1 MΩ input of an oscilloscope (to obtain a signal proportional to the average laser beam intensity through integration). Figure 6.17 shows the laser beam profile obtained for WCL 1 when operating at just below maximum output power (~1.6 W). The laser was operated at just below its optimum input power to avoid the possibility of small fluctuations in input power overheating the tube. The beam profile shows that the laser beam filled the discharge tube bore well. Gas temperatures within WCL 1 were deemed to be satifactorarily low since there was no drop in laser intensity on the discharge channel axis.

6.10 Laser gain measurement

The end-light collection scheme developed by Webb [3] was used to collect amplified spontaneous emission (ASE) from within a narrow cylindrical element of the laser tubes' active volume. Combined double pass and single pass ASE was collected by using a plane mirror placed at the opposite end of the laser tube to the end-light collecting optics [4, 5].

This mirror was covered in order to collect single pass ASE, so that the laser gain G (in % cm^{-1}) could be calculated from the formula [6]:

$$G\ (\%\ \mathrm{cm}^{-1}) = \frac{100}{L}\ln\left(\frac{I_2}{I_1}\right) \qquad [6.1]$$

where L is the length of the discharge tube, I_2 is the double pass ASE intensity and I_1 is the single pass ASE intensity.

Figure 6.18 shows a simplified diagram of the collimating and imaging system used to obtain the single and double pass ASE. In the limit of no diffraction, the first pin hole defines a cylindrical volume element within the active volume, from which light is collected. The first lens and second pin hole are used to adjust for diffraction effects at the first pin hole, so that only parallel rays of light originating from within a cylinder of diameter equal to that of the first pin hole are collected by the monochromator. If the solid angles for single pass ASE [3] (mirror covered) and double pass ASE (mirror uncovered) collection are to be the same, the optics must be arranged to accept parallel rays of light originating from the *mirror image* of the discharge tube also.

The monochromator grating was adjusted to pass only 430.5 nm radiation on to the photomultiplier tube (Thorn-EMI, type 990ZQBM). The optics were scanned horizontally and vertically across the bore of the discharge tube.

Figure 6.19 shows a 3-dimensional spatial gain profile obtained for ACL 5. The peak laser gain was ~4.3% cm^{-1}. Figure 6.20 shows a vertical

spatial gain profile obtained for WCL 1. The peak laser gain for WCL 1 was approximately 6.7% cm^{-1}. A complete 3-dimensional gain profile could not be obtained for WCL 1 owing to the movement of a strontium pellet into the cathode (while completing the measurements) giving rise to erratic ASE intensities. There was insufficient time available to strip the laser down, clean out the discharge tube and electrodes, reload it with strontium and repeat the experiment.

6.11 Summary

Three water-cooled strontium recombination lasers have been designed, built and operated. These lasers all utilized the *same* 40 cm long beryllia discharge tube of rectangular bore (24 mm by 8 mm). The thermal loading model developed in Chapter 2 for forced-convection cooling was used to design three separate water-cooled jackets, each giving rise to a different helium layer thickness, so that the three lasers would optimize at the input powers of ~1.5 kW, ~2.3 kW and ~5.2 kW.

An output power of 1.76 W was achieved from the laser (WCL 1) which incorporated the largest helium layer thickness (7.5 mm). A maximum output power of 2.3 W was achieved from the second water-cooled laser (WCL 2) with a 3.5 mm thick helium layer, although it could not be repeated when the laser was subsequently operated. The beryllia discharge tube cracked during use in WCL 2 and the discharge then appeared to track along the cracks, rather than pass down the centre of the discharge channel. Typical output powers from WCL 2, after the tube

had cracked were 1.4 W. Laser oscillation was observed between two high reflectors for the third water-cooled laser (WCL 3), but the tube failed to produce significant output power when an output coupler was used. The beryllia discharge tube cracked after a few hours of operation in WCL 3.

An air-cooled laser (ACL 5), based around the same 40 cm long, rectangular bore beryllia discharge tube, as used in the water-cooled lasers, gave an average output power of 750 mW.

Laser tube voltage and current measurements, revealed that the actual input power to the lasers agreed with the theoretical values to within ~10%. Our thermal loading models developed for free-convection cooled SRLs and forced-convection cooled SRLs therefore represent accurate means by which the optimum input power to air and water-cooled SRLs can be predicted.

6.12 Figures for Chapter 6

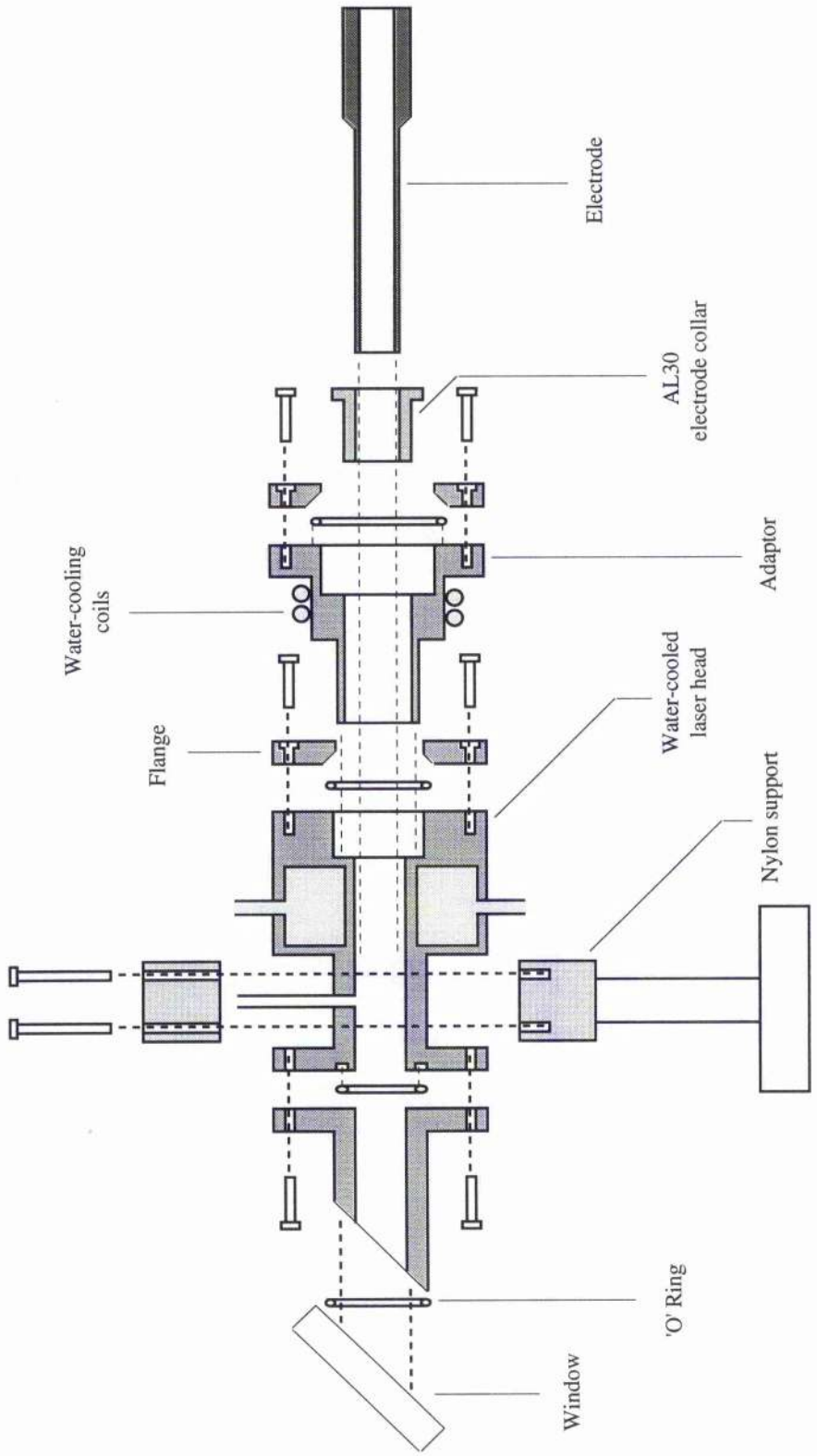

Figure 6.1. Exploded view of laser head assembly.

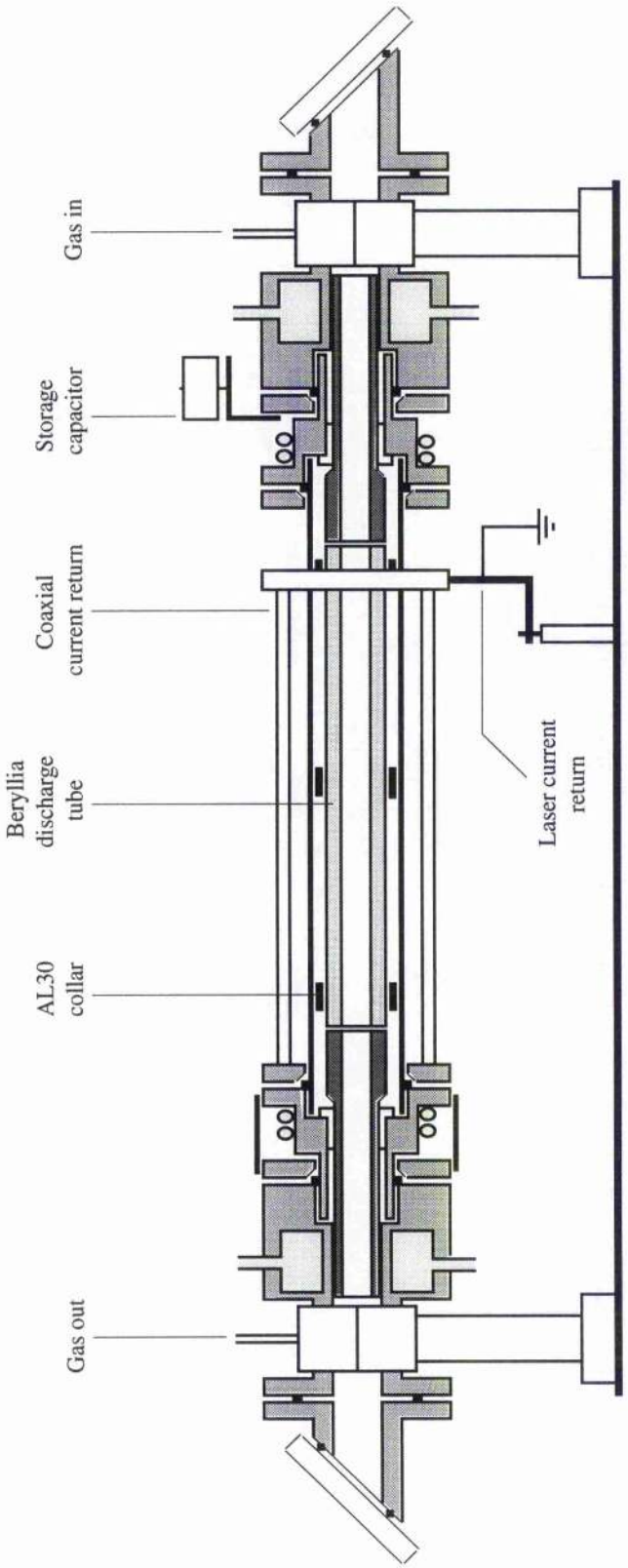

Figure 6.2 Diagram of an assembled beryllia based free-convection cooled SRL.

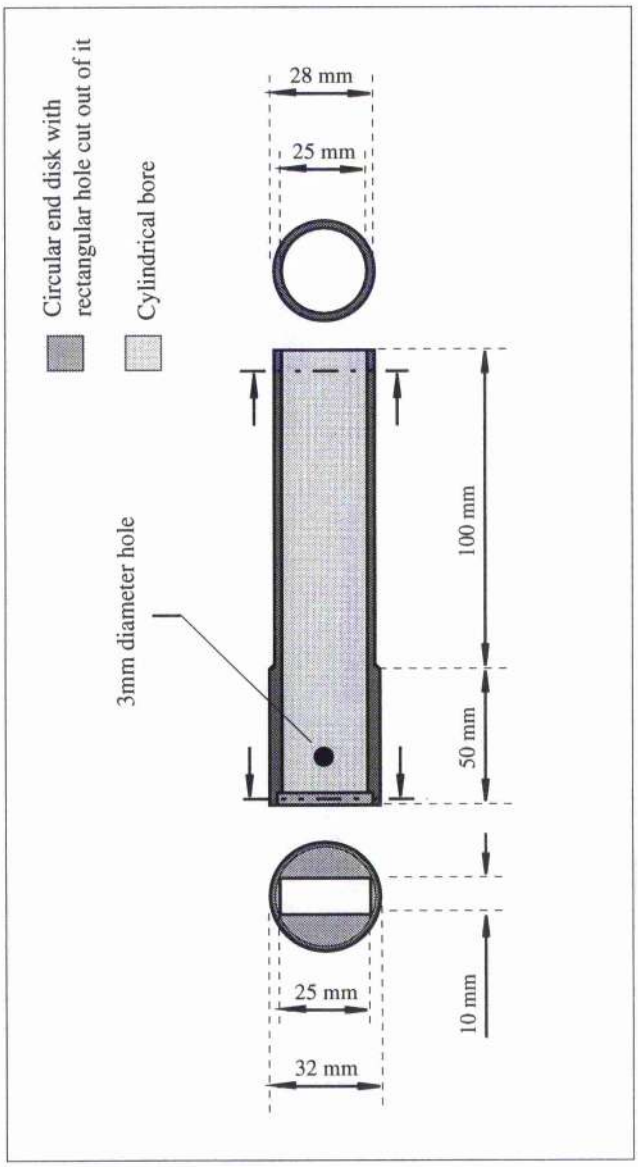

Figure 6.3 Stainless-steel electrode.

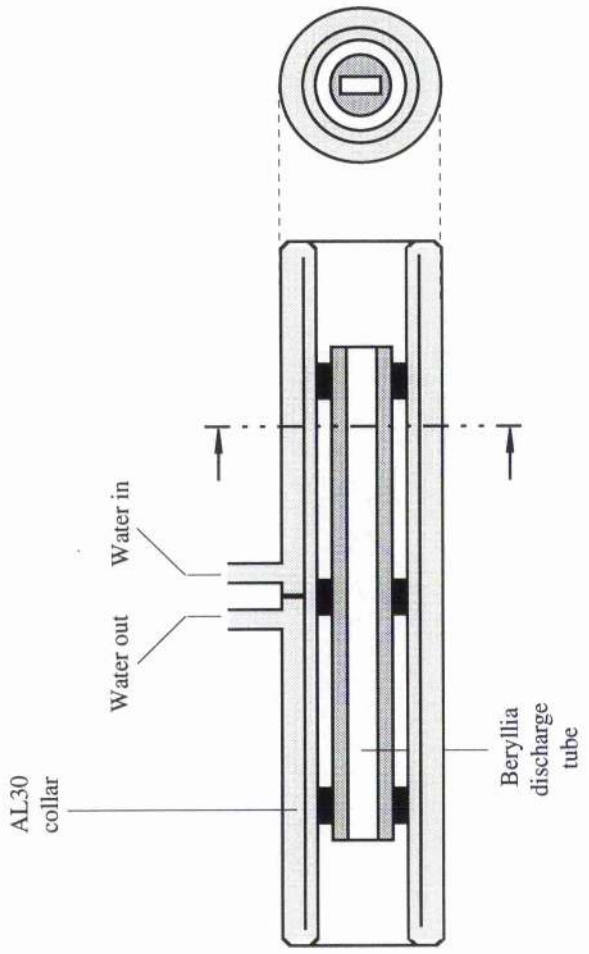

Figure 6.4 Diagram of water jacket surrounding beryllia discharge tube.

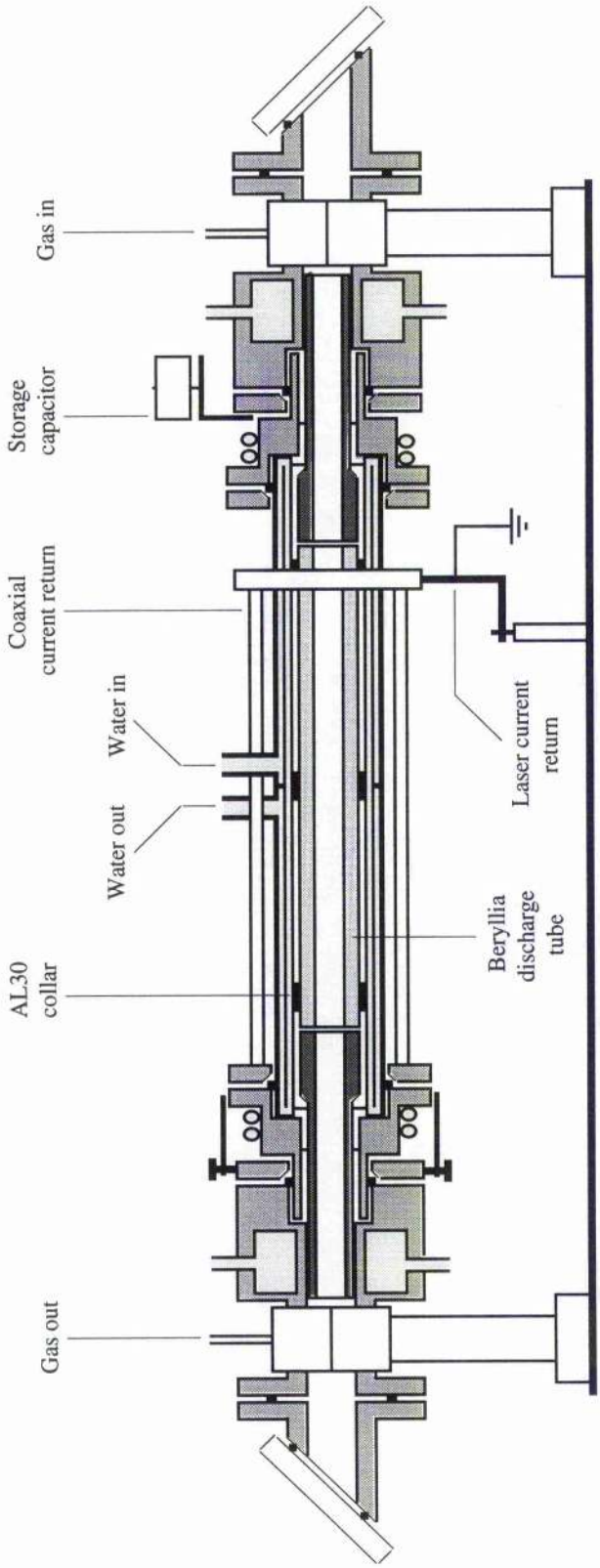

Figure 6.5 Diagram of an assembled forced-convection cooled SRL.

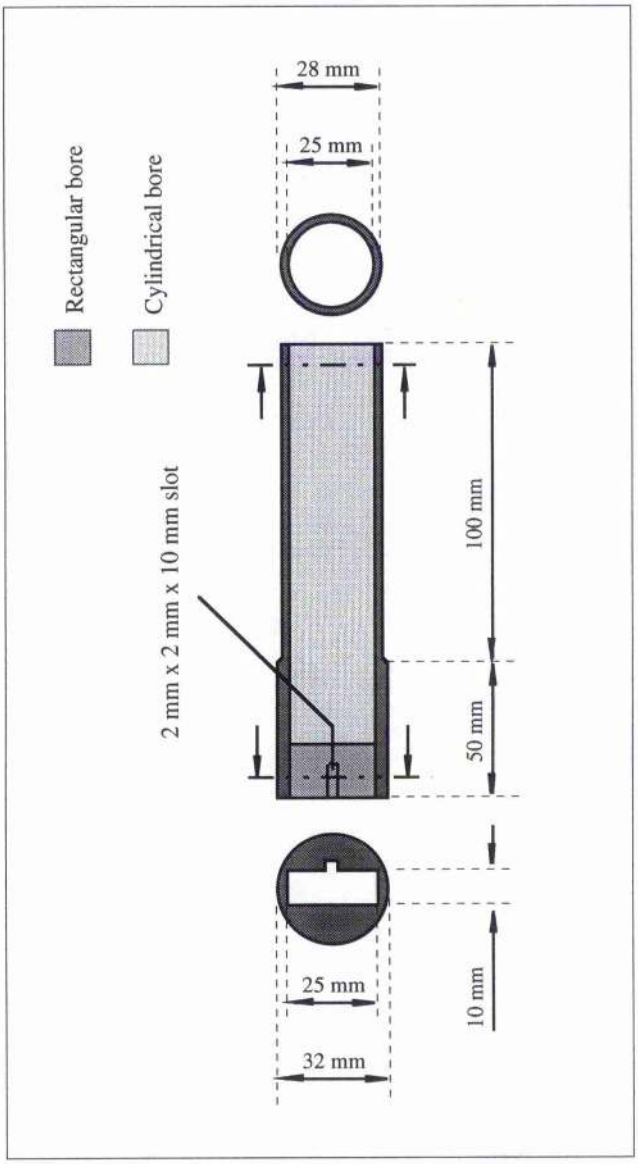

Figure 6.6 Machined molybdenum high-power electrode.

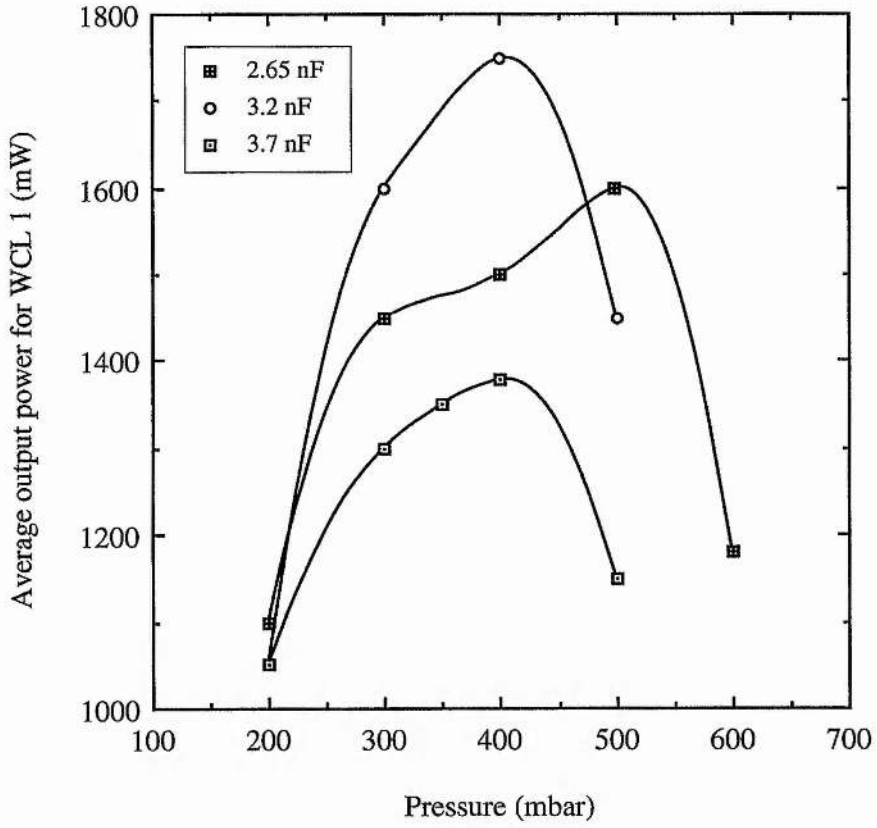

Figure 6.7 The average laser output power for WCL 1 as a function of buffer gas pressure using different storage capacitors with the charging voltage and PRF optimized for the pressure used.

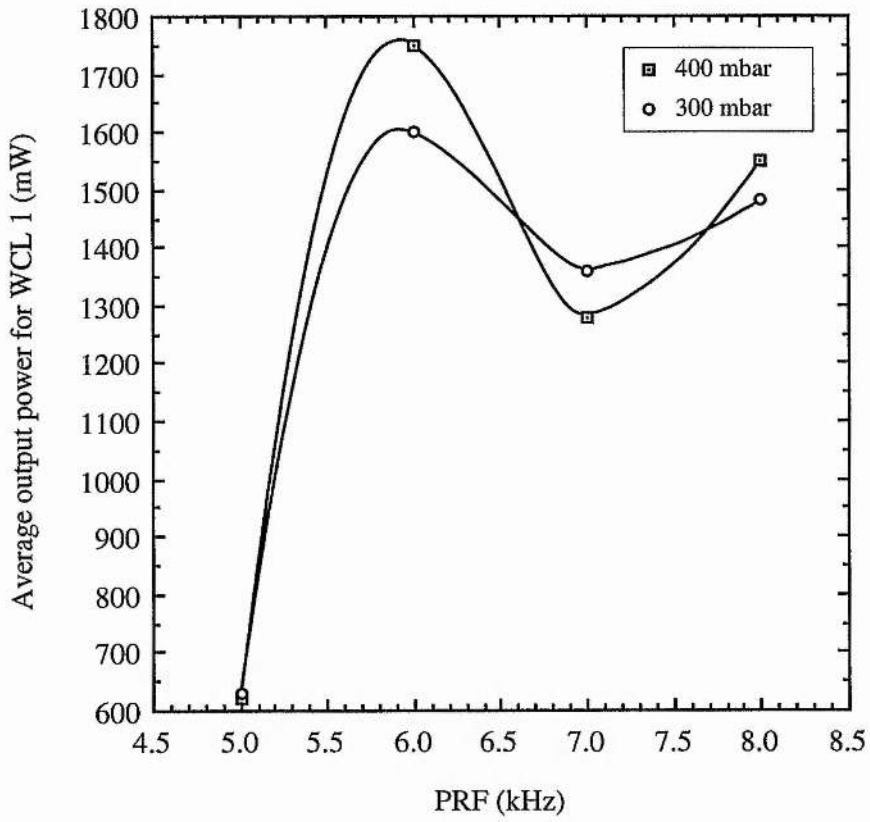

Figure 6.8 **The average laser output power for WCL 1 at buffer gas pressures of 300 mbar and 400 mbar with optimum input power as a function of PRF.**

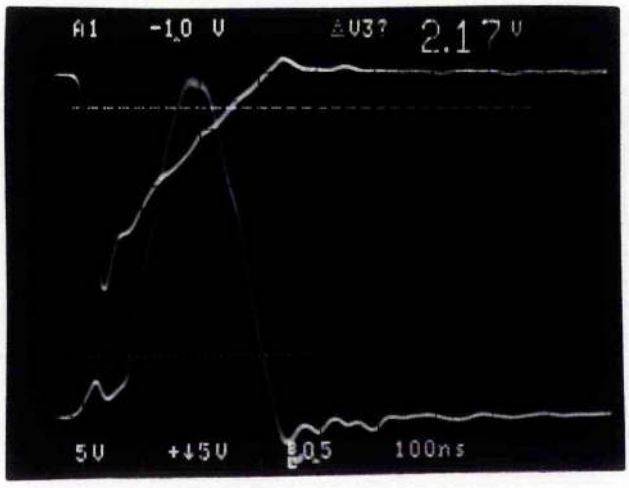

Figure 6.9 **The laser tube voltage and laser current from which the actual input power to WCL 1 was calculated.**

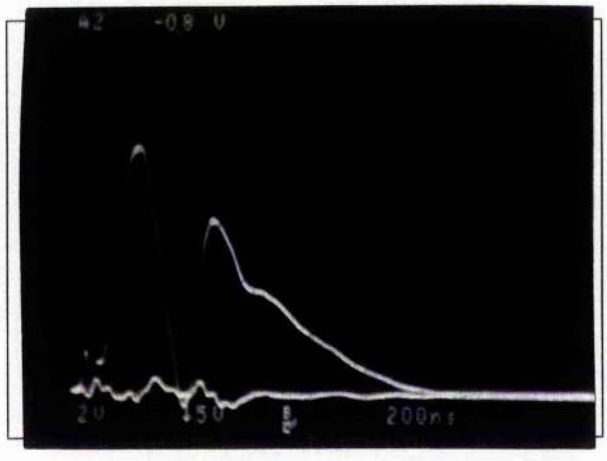

Figure 6.10 **Laser pulse intensity for WCL 1 at 8 kHz (input power optimum).**

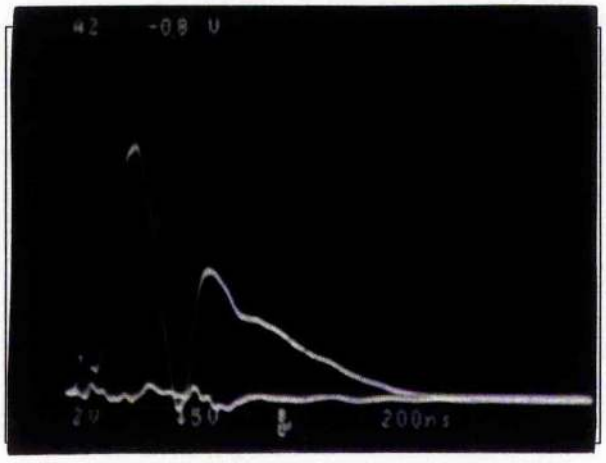

Figure 6.11 **Laser pulse intensity for WCL 1 at 7 kHz. The photograph was taken within 10 seconds of reducing the PRF from 8 kHz to 7 kHz.**

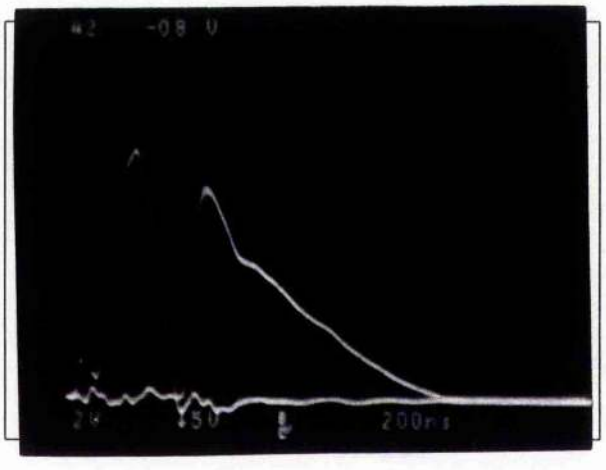

Figure 6.12 **Laser pulse intensity for WCL 1 at 6 kHz. The photograph was taken within 10 seconds of reducing the PRF from 7 kHz to 6 kHz.**

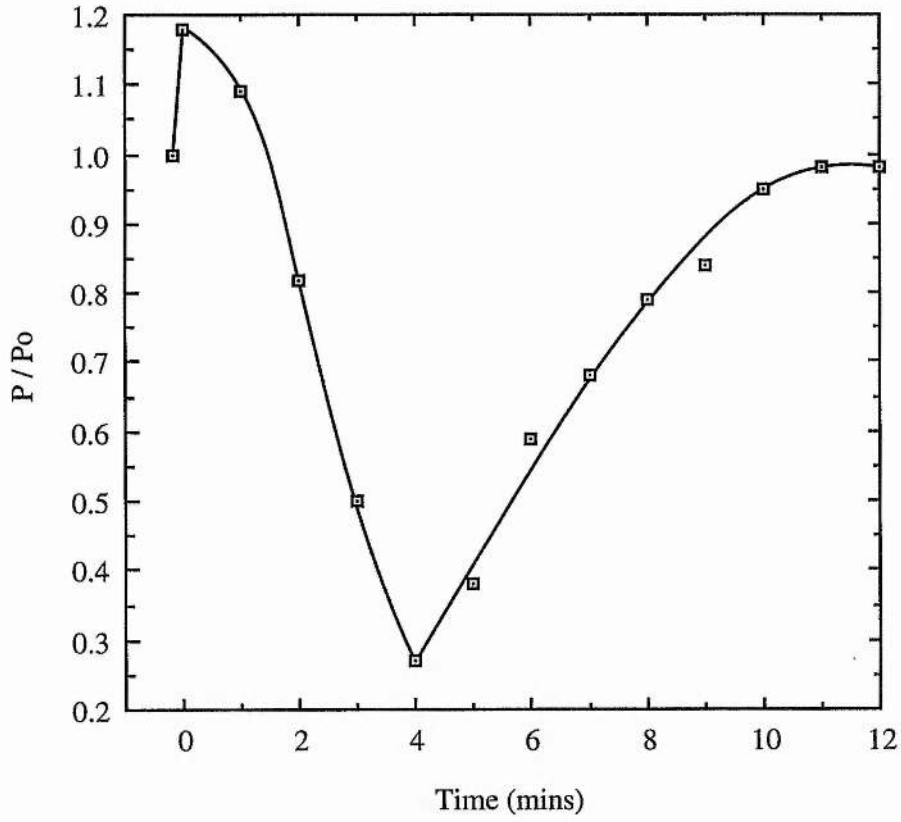

Figure 6.13 Normalized output power as a function of time for changing WCL 1 input power by varying the PRF at constant charging voltage. Po was the steady-state output power at 8 kHz. At t = 0 the PRF was reduced from 8 kHz to 6 kHz; at t = 4 the PRF was increased from 6 kHz to 8 kHz.

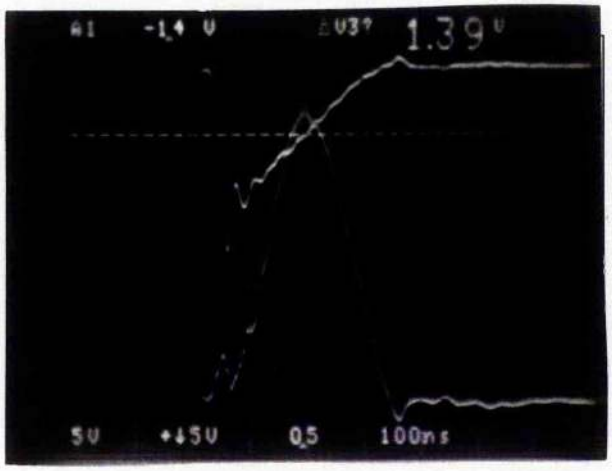

Figure 6.14 **The laser tube voltage and laser current from which the actual input power to WCL 2 was calculated.**

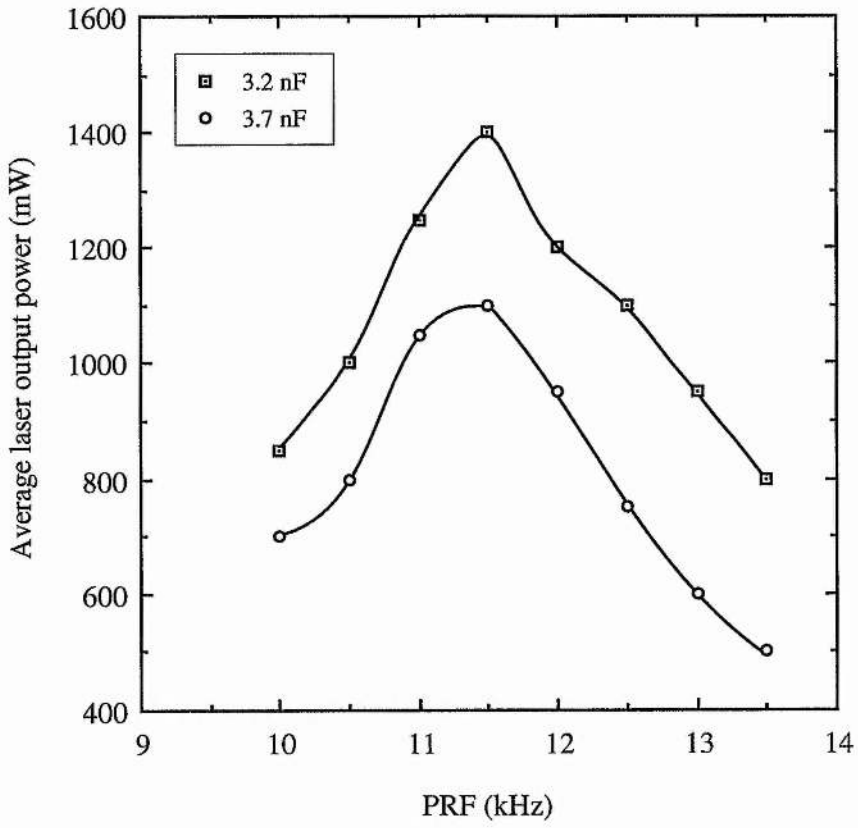

Figure 6.15 **Average laser output power of WCL 2 as a function of PRF under conditions of constant input power at a buffer gas pressure of 300 mbar.**

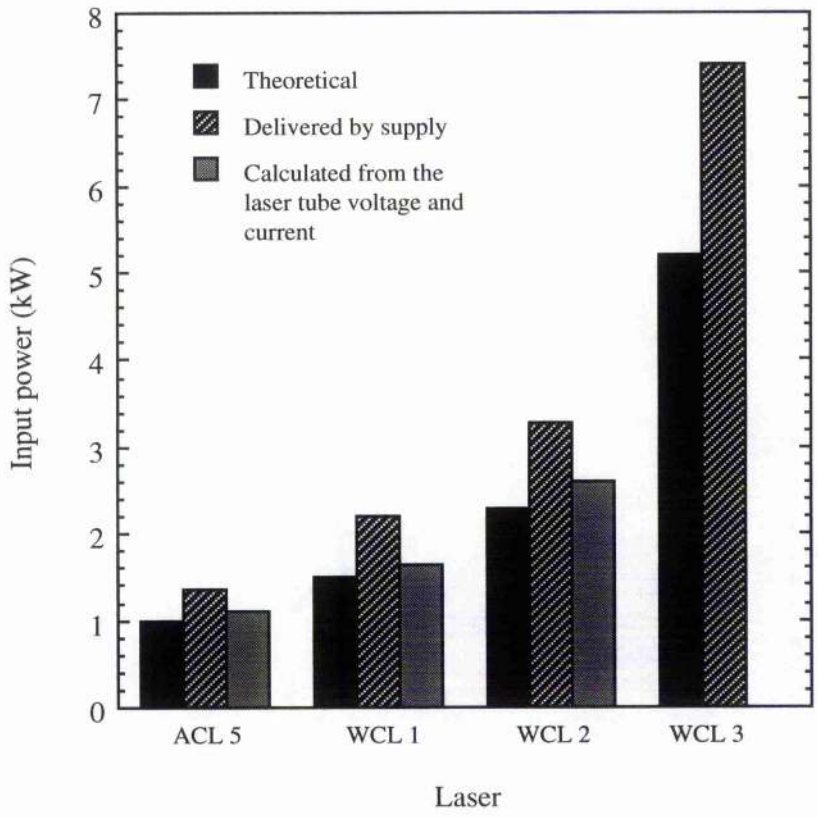

Figure 6.16 Comparison of the input powers for the rectangular bore strontium recombination lasers.

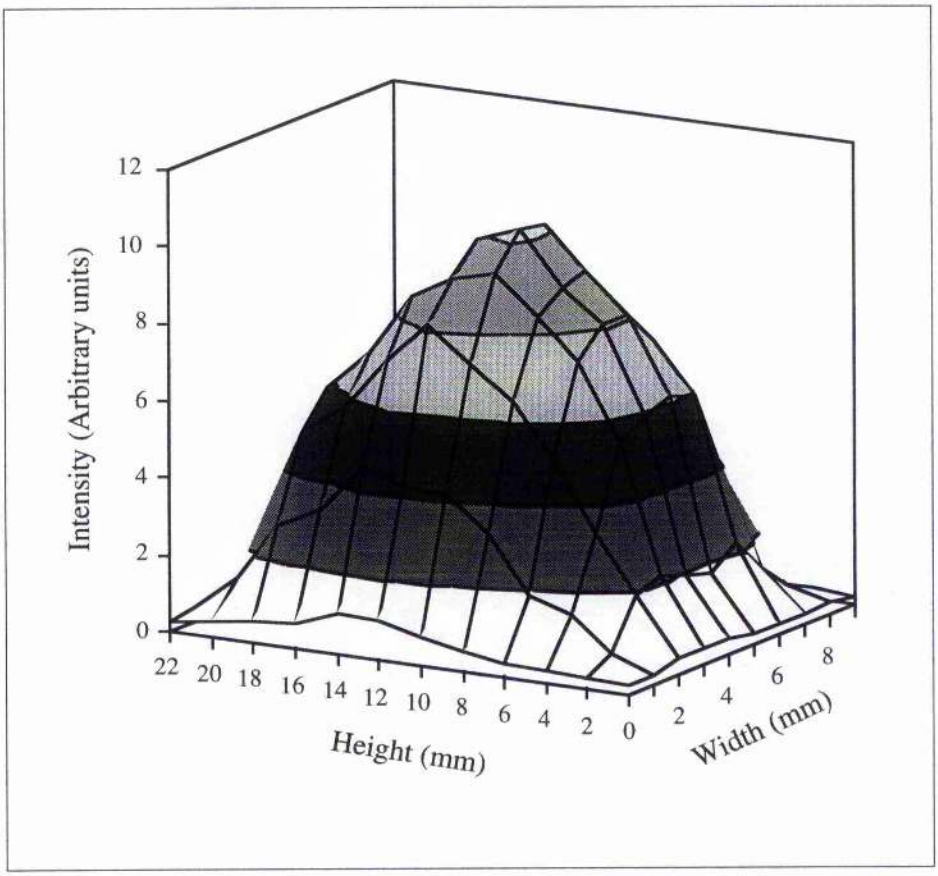

Figure 6.17 3-dimensional laser beam pofile for WCL 1.

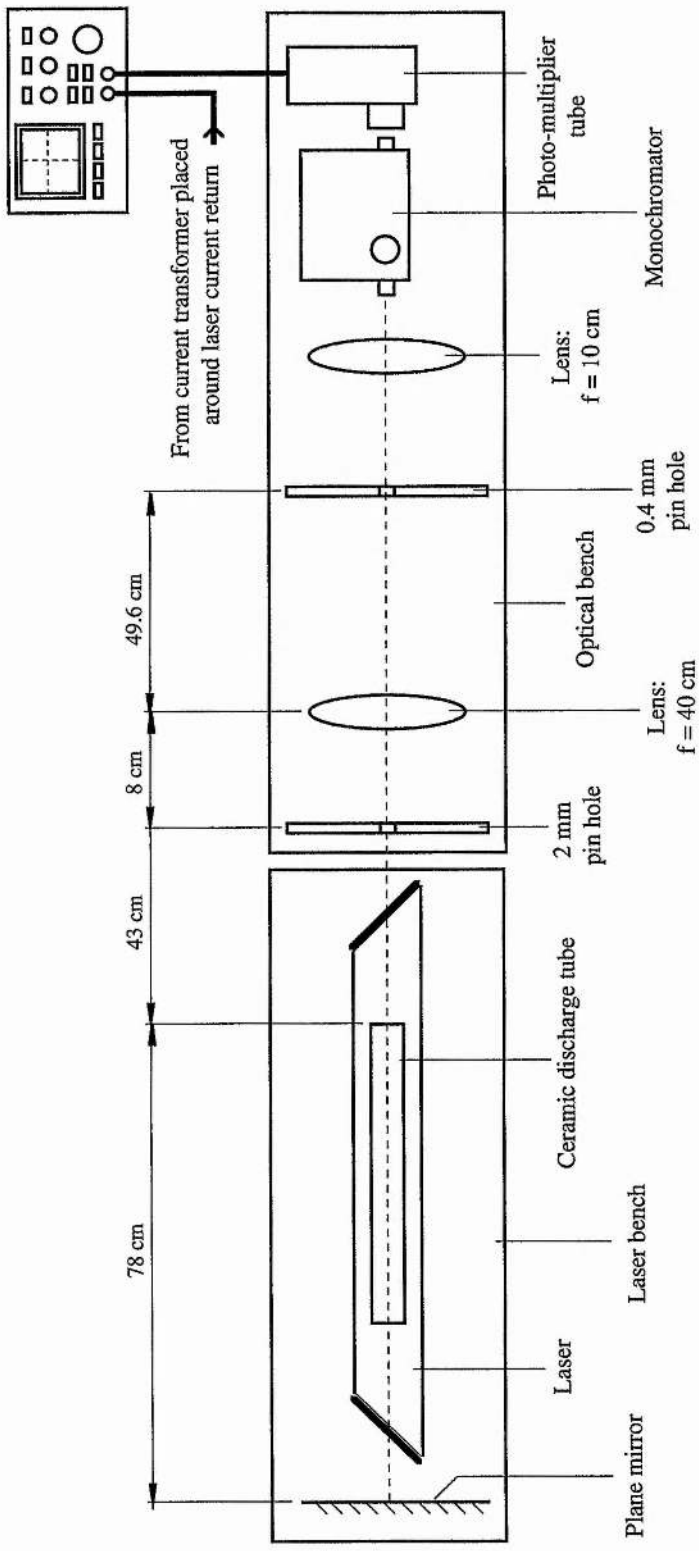

Figure 6.18 Apparatus used in order to obtain laser gain.

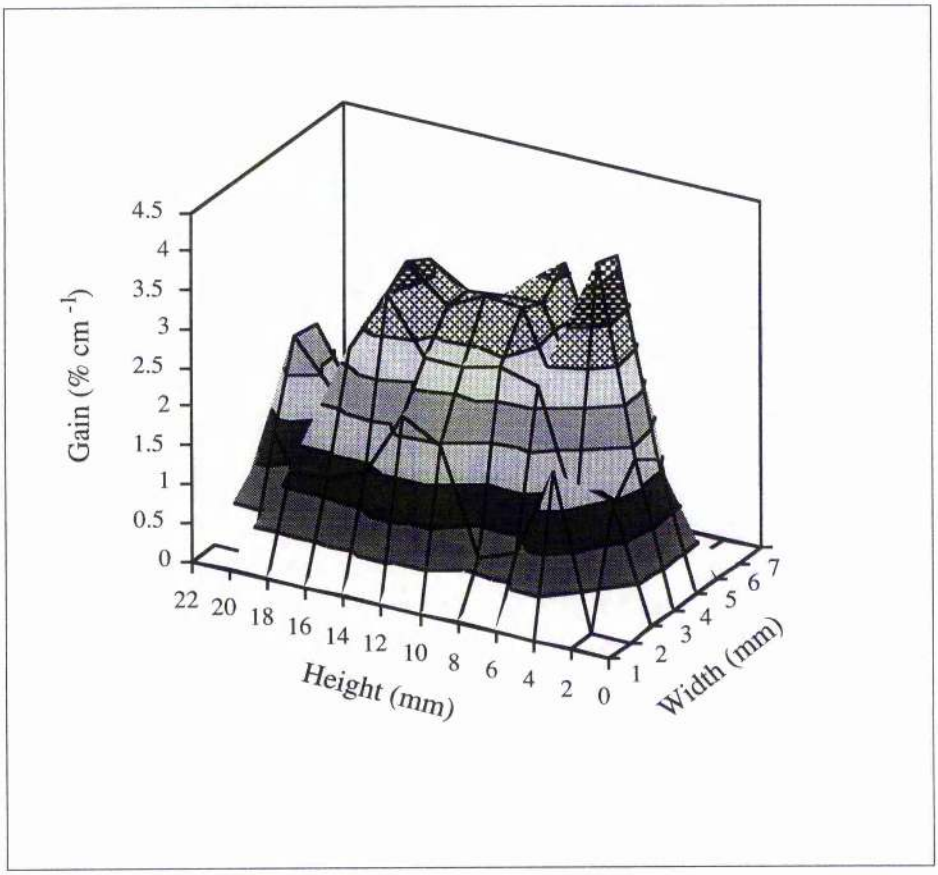

Figure 6.19 3-dimensional gain profile for ACL 5.

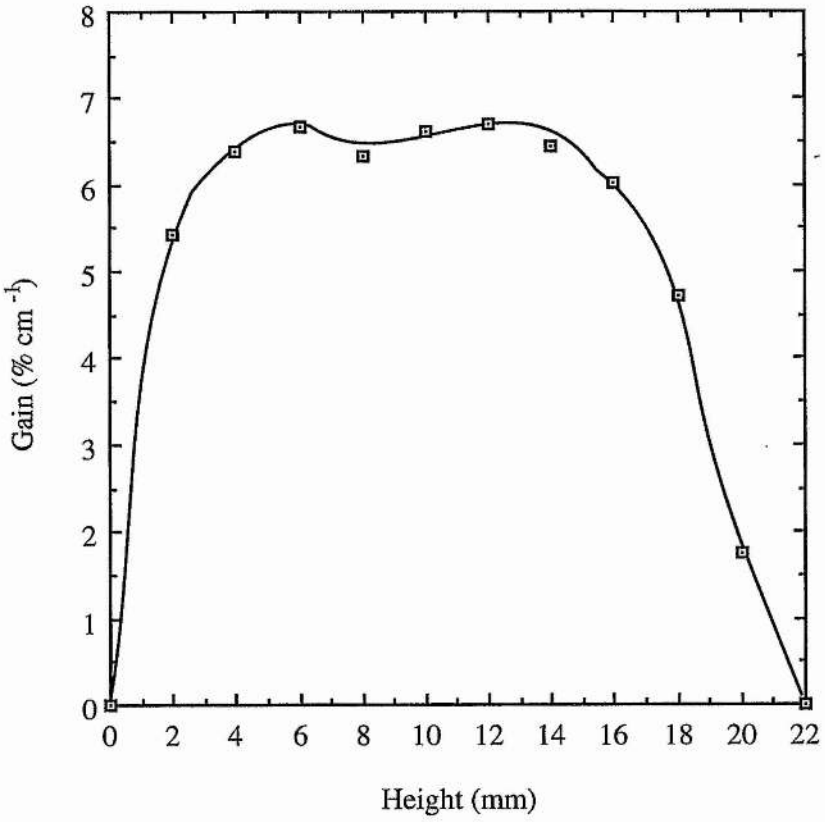

Figure 6.20 Vertical gain profile for WCL 1.

6.13 References

1. Hentschel, R. M. and Piper, J. A.,
Opt. Commun. (In press)

2. Butler, M. S. and Piper, J. A.,
IEEE J. Quant. Electron. **21**, No. 10 (1985), pp. 1563-1566

3. Webb, C. E.,
J. App Phys. **Vol. 39**, No. 12 (1968), pp. 5441-5470

4. Silfvast, W. T. and Deech, J. S.,
App Phys Lett. **Vol. 11**, No. 3 (1967), pp. 97-99

5. Little, C. E. and Piper, J. A.,
IEEE J. Quantum Electron. **QE-26**, No. 5 (1990), pp. 903-910

6. Butler, M. S.,
Ph. D. Thesis, Macquarie University, 1986

CHAPTER 7:

Summary, conclusions and suggestions for further work

7.1 Summary and conclusions

The strontium recombination laser's output power is very sensitive to the laser's input power. If the input power is raised above the optimum value for a given laser, it will overheat (due to the production of too much strontium vapour) and the laser output power will fall. If the linear input power density to a laser is made too high, gas temperatures will become excessive, leading to poor population inversion and poor laser output power.

In order to achieve high output powers from the SRL system, high input powers must be deposited while maintaining the optimum discharge channel wall temperature (~600°C) and low gas temperatures (< 2300 K [1]).

In the case of a free-convection air-cooled laser, the optimum input power is set by the dimensions of the laser tube. A significant proportion of the heat deposited in such a laser (~60%) is removed via radiation from the outer surface of the discharge tube. A model has been developed to predict the optimum input power in the case of free-convection cooling. Experiments have been performed which increase the power loading of a given alumina discharge tube by coating its outer surface with a thin layer of manganese dioxide. This increases the discharge tube's emissivity and therefore enhances radiative heat extraction. The deposition of an additional input power of ~15% has been made possible by the use of enhanced radiative heat extraction, with laser output powers being increasing by ~10%.

The need to process alumina discharge tubes in forming gas, and to load them with uncontaminated strontium, (i.e., which has not been stored under oil) has been demonstrated through an increase in laser output power of ~175% (from ~310 mW to ~ 850 mW).

Water-cooling the discharge tube, via conduction through a thin layer of helium, enables the input power to a given discharge tube to be increased, above that required were the tube air-cooled, while the optimum discharge channel operating temperature is maintained. A thermal loading model has been described and developed into a computer program, in order to predict the optimum input powers for water-cooled SRLs. The input power to a discharge tube of given dimensions can be varied by adjusting the helium layer thickness, smaller helium layer thicknesses giving rise to higher optimum input powers.

As the linear input power density to a given discharge tube is increased (i.e., through the use of water-cooling), the buffer gas temperature rises. Models have been developed which show that the average gas temperature in a rectangular bore (24 mm by 8 mm) discharge tube is theoretically lower than that in a circular bore tube of identical bore cross-sectional area, operating at the same linear input power density. Rectangular bore water-cooled SRLs have been designed and operated for the first time. Three water jackets were designed to define helium layer thicknesses of 7 mm, 3.5 mm and ~0.9 mm, when used in conjunction with our rectangular bore beryllia discharge tube of 31 mm outer diameter. Our thermal loading model was able to predict

the input powers to the water-cooled lasers to within 10% of the experimental values (based on laser tube voltage and current measurements). An average laser output power of 2.3 W has been observed from the laser tube with a 3.5 mm thick helium layer at discharge tube input power of 2.6 kW. This is substantially higher than that obtained from the same discharge tube (760 mW) by free-convection cooling.

The laser tube incorporating the 0.9 mm thick helium layer failed to produce significant output. This may be due to the gas temperature being too high, which needs to be checked in future experiments.

Our beryllia discharge tube is unsuitable for use in water-cooled lasers requiring linear input power densities of 6.5 kW m^{-1} and more, owing to the appearance of longitudinal cracks, which result in the discharge deviating from the centre of the discharge channel bore as they fill with strontium.

The performance of our lasers is believed to have been limited by the electrodes used. These often produced unstable discharges, leading to unstable laser output powers.

7.2 Suggestions for future work

During our work, many problems were encountered with the electrodes. If the electrodes give rise to an unstable discharge current,

the laser output will similarly be unstable. It is clear that better electrodes, giving reliable, stable discharge currents, must be developed before any further progress can be made with our laser tubes. This will necessitate the design of new laser heads. We were limited in the diameter of the electrodes we could use by the inner diameter of the laser heads. The stability of a electric laser discharge can often be improved by pushing the ends of the electrodes into the discharge tube [2]. This may be possible with the rectangular bore tube, but will involve some difficult machining. Welds on the electrodes are undesirable, since the discharge often tends to strike at the weld.

The rectangular bore discharge tube promises lower gas temperatures than a circular bore tube of the same bore cross-sectional area, when used at the same linear input power density. This should enable rectangular bore tubes to be operated at higher input powers than circular bore tubes, before severe (gas temperature produced) detriment to the SRL population inversion is encountered. This could be checked experimentally by measuring the Doppler broadening of the H_α (656.3 nm) line profile in atomic hydrogen [3] to estimate the gas temperature.

Since our rectangular bore tube cracked when operated at linear input power densities of 6.5 W m^{-1} and higher, it is suggested that future rectangular bore tubes have a larger wall thickness than ours (3.55 mm at its thinnest). Although this will make the discharge tube more expensive, it will permit the helium layer thickness to be increased to obtain a given optimum input power from a water-cooled tube. A larger

helium layer thickness will simplify the assembly of the laser tube as it will make the collars used to support the discharge tube stronger and easier to machine. Small (unavoidable) non-uniformities in the helium layer thickness will also be less cruical to the uniformity of the wall temperature as the helium layer thickness is increased.

Scaling the length of our most successful water-cooled laser (WCL 1) would appear to be a promising method by which ~3W output could be obtained reliably from an SRL. The additional input power could thus be delivered at a constant optimum linear density, maintaining the gas temperatures at a low value. This could be accomplished by placing two WCL 1 tubes in series, with a centre electrode and exciting the two tubes simultaneously from separate storage capacitors.

In order to obtain lower gas temperatures for a given linear input power density and therefore enable higher linear input power densities to be deposited, both the centre and outside of the discharge channel could be cooled through the use of forced-convection.

Several small bore tubes could be fitted into the same water jacket in parallel and excited separately, but simultaneously. Individual laser cavities could be arranged around each tube and the outputs of these tubes focused to form a single beam. Alternatively, a single cavity could be defined, by using mirrors to 'zig-zag' the photons through the parallel tubes.

7.3 References

1. Bukshpun, L. M. , Latush, E. L. and Sem, M. F.,
Sov. J. Quantum Electron. **18**, No. 9 (1988), pp. 1098-1100

2. Latush, E. L,
Private communication

3. Blau, P. and Smilanski, A. I.,
J. Appl. Phys. **72**, No. 3 (1992) pp. 849-854

APPENDICES

Appendix A: The code for Water-Cooled Laser Designer 1

The computer program, Water-Cooled Laser Designer 1, the code for which is listed below, was written in BBC BASIC.

```
10  PRINT "      Thermal modelling program for helium filled,"
20  PRINT "          water-cooled beryllia laser tubes"
30  PRINT
40  PRINT "                Version 11.2"
50  PRINT
60  PRINT "                T. R. Pugsley"
70  PRINT "              Copyright 1992,1994"
80  PRINT
90  LET K1=62
100 LET K3=1.4
110 PRINT " Enter tube id in mm, Tube od in mm, Quartz thickness in mm,"
120 PRINT " Tube length in metres, Tube emissivity, Twall (°C) , Tfluid (°C)"
130 PRINT
140 INPUT D1, D0, X2, L, G, T1, T2
150 R1=D1/2
160 R0=D0/2
170 PRINT
180 PRINT " To try a single helium layer thickness type S,"
190 PRINT " for an 0.25 mm incremented range of Helium thicknesses type R"
200 INPUT ANS$:IF ANS$="r" GOTO 270
210 PRINT
220 LET FLAG=0
```

```
230 PRINT " Enter desired helium thickness in mm"
240 INPUT X1
250 PRINT
260 GOTO 300
270 LET FLAG=1
280 PRINT
290 LET X1=.25
300 K2=0.0024*((T1+273)^(0.73))
310 R3=(R0+X1)
320 R4=(R3+X2)
330 LET D=0
340 LET P=10^12
350 R2=R0*(1+7.6*(10^-6)*(T1-D))
360 A=(LN(R2/R1))/K1
370 B=(LN(R3/R2))/K2
380 C=(LN(R4/R3))/K3
390 Q=2*PI*(T1-T2)/(A+B+C)
400 D=A*(Q/(2*PI))
410 E=B*(Q/(2*PI))
420 F=C*(Q/(2*PI))
430 K2=(0.0024/(1.73*E))*((((T1-D)+273)^1.73)-(((T1-D-E)+273)^1.73))
440 IF (P-Q)<1 GOTO 470
450 P=Q
460 GOTO 350
470 H=G*2*(PI)* 5.67*(10^-8)*(R2/1000)*L*((((T1-D)+273)^4)-((T2+273)^4))
480 PRINT " Q/L tot = ";INT(Q+(H/L)+0.5)" W/m,
    Q cond+conv = ";INT((Q*L)+0.5)" W, Q rad = ";INT(H+.5)" W,
    Q tot = ";INT((Q*L)+H+0.5)" W"
```

```
490 PRINT " at a nominal He thickness of ";X1 " mm,
    actual He thickness of ";(INT(((X1+R0-R2)*100)+.5))/100" mm."
500 PRINT " ΔT tube = ";(INT((D*10)+0.5))/10" °C,
    ΔT helium = ";(INT((E*10)+0.5))/10" °C,
    ΔT quartz = ";(INT((F*10)+0.5))/10" °C"
510 PRINT
520 PRINT " For a water temp gradient of < 10 °C/m, the water flow rate must
    be > ";INT(((Q+(H/L))/700)+0.5)" litres/min"
530 PRINT
540 IF FLAG=0 GOTO 600
550 PRINT " Type C to continue, S to stop"
560 INPUT ANS$ :IF ANS$ = "s" GOTO 620
570 PRINT
580 X1=X1+.25
590 GOTO 300
600 PRINT " Type D to try a different helium thickness, S to stop"
610 INPUT ANS$:IF ANS$="d" GOTO 220
620 PRINT" Would you like to design for a different discharge tube? (type Y/N)"
630 INPUT ANS$ :IF ANS$="y" GOTO 80
640 PRINT" Design session terminated"
650 END
```

Appendix B: Average gas temperature in a cylindrical bore tube

The average gas temperature $\langle T_g \rangle$ over an area A is given by:

$$\langle T_g \rangle = \frac{\int T(r) \mathrm{d}A}{A}. \qquad [B1]$$

Here the gas temperature is a function of radial position so that in order to perform the integration, dA must be written as:

$$dA = 2\pi r \mathrm{d}r, \qquad [B2]$$

and the integral then becomes:

$$\langle T_g \rangle = \frac{\int_0^R 2\pi T(r) r \mathrm{d}r}{\int_0^R 2\pi r \mathrm{d}r}, \qquad [B3]$$

which simplifies to:

$$\langle T_g \rangle = \frac{2}{R^2} \int_0^R T(r) r \mathrm{d}r. \qquad [B4]$$

The radial variation of gas temperature is given by (Equation 3.2.10):

$$T(r) = \left(T_w{}^{1.73} + \frac{1.73 q^*}{4\lambda_0} (R^2 - r^2) \right)^{\left(\frac{1}{1.73}\right)}, \qquad [B5]$$

so that the integral, written in full, is,

$$\left\langle T_g \right\rangle = \frac{2}{R^2}\int_0^R \left({T_w}^{1.73} + \frac{1.73q^*}{4\lambda_0}(R^2 - r^2) \right)^{\left(\frac{1}{1.73}\right)} r\mathrm{d}r. \qquad [B6]$$

This integral is non-linear as it stands, but it can be linearized by letting $\rho(r) = r^2$ so that $\mathrm{d}\rho = 2r\mathrm{d}r$ to give:

$$\left\langle T_g \right\rangle = \frac{1}{R^2}\int_{\rho(0)}^{\rho(R)} \left({T_w}^{1.73} + \frac{1.73q^*}{4\lambda_0}(R^2 - \rho) \right)^{\left(\frac{1}{1.73}\right)} \mathrm{d}\rho. \qquad [B7]$$

Now let,

$$u(\rho) = \left({T_w}^{1.73} + \frac{1.73q^*}{4\lambda_0}(R^2 - r^2) \right). \qquad [B8]$$

so that:

$$\frac{\mathrm{d}u}{\mathrm{d}\rho} = -\frac{1.73q^*}{4\lambda_0}. \qquad [B9]$$

Hence, we get:

$$\left\langle T_g \right\rangle = \frac{1}{R^2}\int_{u(\rho(0))}^{u(\rho(R))} -\frac{4\lambda_0}{1.73q^*} u^{\left(\frac{1}{1.73}\right)} \mathrm{d}u \qquad [B10]$$

$$\Rightarrow \qquad \langle T_g \rangle = -\frac{4\lambda_0}{1.73 q^* R^2}\left[\frac{1.73}{2.73}u^{\left(\frac{2.73}{1.73}\right)}\right]_{u(\rho(0))}^{u(\rho(R))} \qquad [B11]$$

$$\Rightarrow \quad \langle T_g \rangle = -\frac{4\lambda_0}{2.73 q^* R^2}\left[\left(T_w{}^{1.73} + \frac{1.73 q^*}{4\lambda_0}(R^2 - r^2)\right)^{\left(\frac{2.73}{1.73}\right)}\right]_0^R . \qquad [B12]$$

The average temperature of a gas contained in a cylindrical volume within which heat is uniformly deposited at a rate q^* is therefore given by the expression:

$$\langle T_g \rangle = \frac{4\lambda_0}{2.73 q^* R^2}\left[\left(T_w{}^{1.73} + \frac{1.73 q^*}{4\lambda_0}R^2\right)^{\left(\frac{2.73}{1.73}\right)} - T_w{}^{2.73}\right]. \qquad [B13]$$

The on-axis gas temperature follows from Equation B5 as:

$$T(0) = \left(T_w{}^{1.73} + \frac{1.73 q^*}{4\lambda_0}R^2\right)^{\left(\frac{1}{1.73}\right)}, \qquad [B14]$$

so that the average gas temperature can be written as:

$$\langle T_g \rangle = \frac{4\lambda_0}{2.73 q^* R^2}\left(T(0)^{2.73} - T_w{}^{2.73}\right). \qquad [B15]$$

Appendix C: The code for Gas Temperature Determinator A

The computer program, Gas Temperature Determinator A, the code for which is listed below, was written in BBC BASIC.

```
10  PRINT "  This program calculates the steady-state gas (He) temperature"
20  PRINT "        in a discharge heated cylindrical bore laser tube as a"
30  PRINT "         function of the radial distance from the tube's axis."
40  PRINT
50  PRINT "                                Version 2"
60  PRINT
70  PRINT "                        Copyright T. R. Pugsley 1992,1994"
80  PRINT
90  PRINT " Enter bore diameter (mm), bore length (mm),"
100 PRINT " tube wall temperature in °C, total input power in W"
110 PRINT " and the number of graph points desired."
120 PRINT
130 INPUT DIAM, L, TW, P, Z
140 PRINT
150 R = DIAM/2
160 VOL = ((R/1000)^2)*(L/1000)*PI
170 PRINT " Gas volume = ";(INT(VOL*10^7+0.5))/10" cm^3"
180 PD = P/VOL
190 PRINT " Power density = ";(INT(PD/10^4+0.5))/100" W/cm^3"
200 PRINT
210 A=(TW+273)^1.73
220 B=(1.73/0.0096)*PD
```

```
230 C=(R/1000)^2
240 D=(1/1.73)
250 N=(Z-1)
260 DX=(R/1000)/N
270 LET M=0
280 X=M*DX
290 TX = INT(((A+B*(C-X*X))^D)+0.5)
300 PRINT" T(± ";X*1000") = ";TX" K (";(TX-273)" °C)."
310 M=M+1
320 IF M=Z GOTO 340
330 GOTO 280
340 PRINT
350 TAV = (0.003516/(PD*(R/1000)*(R/1000)))*((((A+B*C)^D)^2.73)-
    ((TW+273)^2.73))
360 PRINT " Average gas temperature = ";INT(TAV+0.5)" K."
370 PRINT
380 PRINT " Would you like to try a different input power (y/n)?"
390 INPUT ANS$
400 IF ANS$="n" GOTO 440
410 PRINT " Enter new input power (W)"
420 INPUT P
430 GOTO 180
440 PRINT "Calculation terminated"
```

Appendix D: Computer modelling of the gas temperatures in a rectangular bore laser tube

D1: The code for Gas Temperature Determinator B

The computer program, Gas Temperature Determinator B, the code for which is listed below, was written in BBC BASIC.

```
10  PRINT "  This program calculates the steady-state gas (He) temperature"
20  PRINT "       in a discharge heated rectangular bore laser tube as a"
30  PRINT "         function of the distance from the tube's x=0 axis."
40  PRINT
50  PRINT "                              Version 2"
60  PRINT
70  PRINT "                    Copyright T. R. Pugsley 1992,1994"
80  PRINT
90  PRINT " Enter bore width (mm), bore height (mm), bore length (mm),"
100 PRINT " tube wall temperature in °C, total input power in W"
110 PRINT " and the number of graph points desired."
120 PRINT
130 INPUT W, H, L,TW, P, Z
140 PRINT
150 VOL = (W/1000)*(H/1000)*(L/1000)
160 PRINT " Gas volume = ";(INT(VOL*10^7+0.5))/10" cm^3"
170 PD = P/VOL
180 PRINT " Power density = ";(INT(PD/10^4+0.5))/100" W/cm^3"
```

```
190 PRINT
200 A=(TW+273)^1.73
210 B=(1.73/0.0048)*PD
220 C=(W/2000)^2
230 D=(1/1.73)
240 N=(Z-1)
250 DX=(W/2000)/N
260 LET M=0
270 X=M*DX
280 TX = INT(((A+B*(C-X*X))^D)+0.5)
290 PRINT" T(± ";X*1000") = ";TX" K (";(TX-273)" °C)."
300 M=M+1
310 IF M=Z GOTO 330
320 GOTO 270
330 PRINT
340 PRINT " Would you like to try a different input power (y/n)?"
350 INPUT ANS$
360 IF ANS$="n" GOTO 400
370 PRINT " Enter new input power (W)"
380 INPUT P
390 GOTO 170
400 PRINT "Calculation terminated"
```

D2: The code for Average Gas Temperature Determinator

The computer program, Gas Temperature Determinator B, the code for which is listed below, was written in BBC BASIC.

```
10  PRINT "  This program calculates the average steady-state gas (He)"
20  PRINT " temperature in a discharge heated rectangular bore laser tube."
30  PRINT
40  PRINT "                              Version 2"
50  PRINT
60  PRINT "                Copyright T. R. Pugsley 1992,1994"
70  PRINT
80  PRINT " Enter bore width (mm), bore height (mm), bore length (mm),"
90  PRINT " tube wall temperature in °C, total input power in W"
100 PRINT " and the number of integration intervals."
110 PRINT
120 INPUT W, H, L,TW, P, N
130 VOL = (W/1000)*(H/1000)*(L/1000)
140 PRINT
150 PRINT "Volume = ";(INT(VOL*10^7+0.5))/10" cm^3"
160 PD = P/VOL
170 PRINT "Power density = ";(INT(PD/10^4+0.5))/100" W/cm^3"
180 PRINT
190 A = (TW+273)^1.73
200 B = (1.73/0.0048)*PD
210 C = (W/2000)^2
220 D = (1/1.73)
```

D2: The code for Average Gas Temperature Determinator

The computer program, Gas Temperature Determinator B, the code for which is listed below, was written in BBC BASIC.

```
10  PRINT "  This program calculates the average steady-state gas (He)"
20  PRINT " temperature in a discharge heated rectangular bore laser tube."
30  PRINT
40  PRINT "                              Version 2"
50  PRINT
60  PRINT "                  Copyright T. R. Pugsley 1992,1994"
70  PRINT
80  PRINT " Enter bore width (mm), bore height (mm), bore length (mm),"
90  PRINT " tube wall temperature in °C, total input power in W"
100 PRINT " and the number of integration intervals."
110 PRINT
120 INPUT W, H, L,TW, P, N
130 VOL = (W/1000)*(H/1000)*(L/1000)
140 PRINT
150 PRINT "Volume = ";(INT(VOL*10^7+0.5))/10" cm^3"
160 PD = P/VOL
170 PRINT "Power density = ";(INT(PD/10^4+0.5))/100" W/cm^3"
180 PRINT
190 A = (TW+273)^1.73
200 B = (1.73/0.0048)*PD
210 C = (W/2000)^2
220 D = (1/1.73)
```

```
500 GOTO 160
510 PRINT "Calculation terminated"
```

D.3: The method of numerical integration used by Average Gas Temperature Determinator

Consider a function f(x), as shown graphically below, which is to be integrated between the limits [0,a].

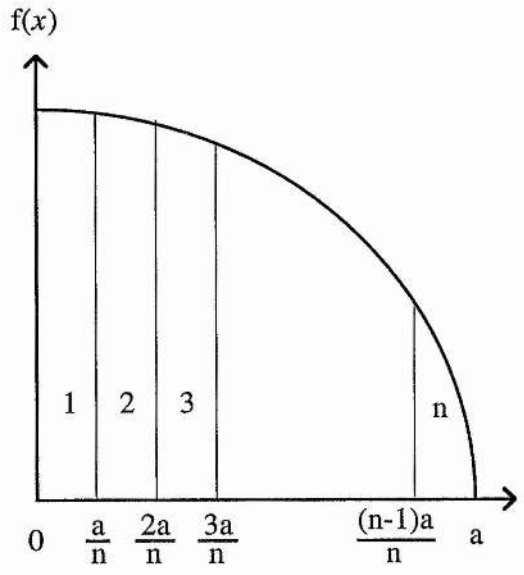

The interval [0,a] is split into n equal sub-intervals of width $\Delta x = a/n$ and the function is taken to be linear over each of the sub-intervals. The area

under the function between $x = 0$ and $x = a/n$ is then given approximately by the expression:

$$\int_0^{a/n} f(x)dx \approx \frac{a}{n} f\left(\frac{a}{n}\right) + \frac{a}{2n}\left[f(0) - f\left(\frac{a}{n}\right)\right], \qquad [D.3.1]$$

which can be simplified to obtain:

$$\int_0^{a/n} f(x)dx \approx \frac{a}{n}\left[\frac{1}{2}f(0) + \frac{1}{2}f\left(\frac{a}{n}\right)\right]. \qquad [D.3.2]$$

Similar expressions can be written down for each of the n sub-intervals so that the sum of these expressions yields the required area under the curve:

$$\int_0^{a} f(x)dx \approx \frac{a}{n}\left[\frac{1}{2}f(0) + \sum_{m=1}^{m=n-1} f\left(\frac{ma}{n}\right) + \frac{1}{2}f(a)\right]. \qquad [D.3.3]$$

The method of performing numerical integration described above leads to an approximate value for the area under a non-linearly varying function, because the function is treated as being linear between the limits of each sub-interval. However, the accuracy of the method increases with an increasing number of sub-intervals, so that if a computer is utilized to perform the necessary calculations, the number of sub-intervals need only be limited by available computing time and a good approximation can be obtained.

D4: The code for Gas Temperature Determinator C

The program listed below is written in FORTRAN. It calls upon a numerical algorithm subroutine to solve the 48 non-linear differential equations listed in the code.

```
program gas temp determinator for rectangular bore laser tube

implicit none
integer N,LWA,IFAIL,i,T(48)
parameter(N=48,LWA=4000)
real*8 X(N),FVEC(N),XTOL,WA(LWA)
real*8 Tguess
real*8 q,Tw,Ko
character*30 data_file
common /block/ q,Tw,Ko

EXTERNAL FCN

q = 3.39d-2
Tw = 873
Ko = 2.4d-6

print*,'enter value of q...'
read*,q
print*,'name of data file (file.dat)..'
read*,data_file

open(unit=8,file=data_file,status='unknown')

write(8,*)q
```

```
IFAIL=0
XTOL=1.0d-7
Tguess = Tw
do i=1,48
 X(i)=Tguess
end do
call C05NBF(FCN,N,X,FVEC,XTOL,WA,LWA,IFAIL)

do i=1,48
 print*,X(i)
 T(i) = X(i)+0.5
 write(8,*)i,T(i)
end do

close(8)

end

subroutine FCN(N,X,FVEC,IFLAG)

implicit none
integer N,IFLAG,i
real*8 X(48),FVEC(48),T(48)
real*8 K(48),q,Tw,Ko
common /block/ q,Tw,Ko


do i=1,48
  T(i) = X(i)
  K(i)=Ko*T(i)**(0.73)
end do

if (IFLAG.ge.0.0) then
FVEC(1)=K(1)*(2*Tw+T(2)+T(5)-4*T(1))+q
FVEC(2)=K(2)*(Tw+T(1)+T(3)+T(6)-4*T(2))+q
FVEC(3)=K(3)*(Tw+T(2)+T(4)+T(7)-4*T(3))+q
```

```
FVEC(4)=K(4)*(Tw+2*T(3)+T(8)-4*T(4))+q
FVEC(5)=K(5)*(Tw+T(6)+T(1)+T(9)-4*T(5))+q
FVEC(6)=K(6)*(T(5)+T(7)+T(2)+T(10)-4*T(6))+q
FVEC(7)=K(7)*(T(6)+T(8)+T(3)+T(11)-4*T(7))+q
FVEC(8)=K(8)*(2*T(7)+T(4)+T(12)-4*T(8))+q
FVEC(9)=K(9)*(Tw+T(10)+T(5)+T(13)-4*T(9))+q
FVEC(10)=K(10)*(T(9)+T(11)+T(6)+T(14)-4*T(10))+q
FVEC(11)=K(11)*(T(10)+T(12)+T(7)+T(15)-4*T(11))+q
FVEC(12)=K(12)*(2*T(11)+T(8)+T(16)-4*T(12))+q
FVEC(13)=K(13)*(Tw+T(14)+T(9)+T(17)-4*T(13))+q
FVEC(14)=K(14)*(T(13)+T(15)+T(18)+T(10)-4*T(14))+q
FVEC(15)=K(15)*(T(14)+T(16)+T(11)+T(19)-4*T(15))+q
FVEC(16)=K(16)*(2*T(15)+T(12)+T(20)-4*T(16))+q
FVEC(17)=K(17)*(Tw+T(18)+T(13)+T(21)-4*T(17))+q
FVEC(18)=K(18)*(T(17)+T(19)+T(14)+T(22)-4*T(18))+q
FVEC(19)=K(19)*(T(18)+T(20)+T(15)+T(23)-4*T(19))+q
FVEC(20)=K(20)*(2*T(19)+T(16)+T(24)-4*T(20))+q
FVEC(21)=K(21)*(Tw+T(22)+T(17)+T(25)-4*T(21))+q
FVEC(22)=K(22)*(T(21)+T(23)+T(18)+T(26)-4*T(22))+q
FVEC(23)=K(23)*(T(22)+T(24)+T(19)+T(27)-4*T(23))+q
FVEC(24)=K(24)*(2*T(23)+T(20)+T(28)-4*T(24))+q
FVEC(25)=K(25)*(Tw+T(26)+T(21)+T(29)-4*T(25))+q
FVEC(26)=K(26)*(T(25)+T(27)+T(22)+T(30)-4*T(26))+q
FVEC(27)=K(27)*(T(26)+T(28)+T(23)+T(31)-4*T(27))+q
FVEC(28)=K(28)*(2*T(27)+T(24)+T(32)-4*T(28))+q
FVEC(29)=K(29)*(Tw+T(30)+T(25)+T(33)-4*T(29))+q
FVEC(30)=K(30)*(T(29)+T(31)+T(26)+T(34)-4*T(30))+q
FVEC(31)=K(31)*(T(30)+T(32)+T(27)+T(35)-4*T(31))+q
FVEC(32)=K(32)*(2*T(31)+T(28)+T(36)-4*T(32))+q
FVEC(33)=K(33)*(Tw+T(34)+T(29)+T(37)-4*T(33))+q
FVEC(34)=K(34)*(T(33)+T(35)+T(30)+T(38)-4*T(34))+q
FVEC(35)=K(35)*(T(34)+T(36)+T(31)+T(39)-4*T(35))+q
FVEC(36)=K(36)*(2*T(35)+T(32)+T(40)-4*T(36))+q
FVEC(37)=K(37)*(Tw+T(38)+T(33)+T(41)-4*T(37))+q
FVEC(38)=K(38)*(T(37)+T(39)+T(34)+T(42)-4*T(38))+q
FVEC(39)=K(39)*(T(38)+T(40)+T(35)+T(43)-4*T(39))+q
```

```
FVEC(40)=K(40)*(2*T(39)+T(36)+T(44)-4*T(40))+q
FVEC(41)=K(41)*(Tw+T(42)+T(37)+T(45)-4*T(41))+q
FVEC(42)=K(42)*(T(41)+T(43)+T(38)+T(46)-4*T(42))+q
FVEC(43)=K(43)*(T(42)+T(44)+T(39)+T(47)-4*T(43))+q
FVEC(44)=K(44)*(2*T(43)+T(40)+T(48)-4*T(44))+q
FVEC(45)=K(45)*(Tw+T(46)+2*T(41)-4*T(45))+q
FVEC(46)=K(46)*(T(45)+T(47)+2*T(42)-4*T(46))+q
FVEC(47)=K(47)*(T(46)+T(48)+2*T(43)-4*T(47))+q
FVEC(48)=K(48)*(2*T(47)+2*T(44)-4*T(48))+q
end if

do i=1,48
 print*,i,T(i),X(i),FVEC(i)
end do
end
```

Appendix E: The code for Water-Cooled Laser Designer 2

The computer program, Water-Cooled Laser Designer 2, the code for which is listed below, was written in BBC BASIC.

```
10  PRINT "      Thermal modelling program for helium filled,"
20  PRINT "      cylindrical water-cooled beryllia laser tubes"
30  PRINT
40  PRINT "                  Version 11.4"
50  PRINT
60  PRINT "                  T. R. Pugsley"
70  PRINT "                Copyright 1992, 1994"
80  PRINT
90  LET K1=62
100 LET K3=1.4
110 PRINT " Enter tube id in mm, Tube od in mm, Quartz thickness in mm,"
120 PRINT " Tube length in metres, Tube emissivity, Twall (°C) , Tfluid (°C)"
130 PRINT
140 INPUT D1, D0, X2, L, G, T1, T2
150 R1=D1/2
160 R0=D0/2
170 PRINT
180 PRINT " To try a single helium layer thickness type S,"
190 PRINT " for an 0.25 mm incremented range of Helium thicknesses type R"
200 INPUT ANS$:IF ANS$="r" GOTO 270
210 PRINT
220 LET FLAG=0
```

```
230 PRINT " Enter desired helium thickness in mm"
240 INPUT X1
250 PRINT
260 GOTO 300
270 LET FLAG=1
280 PRINT
290 LET X1=.25
300 K2=0.0024*((T1+273)^(0.73))
310 R3=(R0+X1)
320 R4=(R3+X2)
330 LET D=0
340 LET P=10^12
350 R2=R0*(1+7.6*(10^-6)*(T1-D))
360 A=(LN(R2/R1))/K1
370 B=(LN(R3/R2))/K2
380 C=(LN(R4/R3))/K3
390 Q=2*PI*(T1-T2)/(A+B+C)
400 D=A*(Q/(2*PI))
410 E=B*(Q/(2*PI))
420 F=C*(Q/(2*PI))
430 K2=(0.0024/(1.73*E))*((((T1-D)+273)^1.73)-(((T1-D-E)+273)^1.73))
440 IF (P-Q)<1 GOTO 470
450 P=Q
460 GOTO 350
470 H=G*2*(PI)* 5.67*(10^-8)*(R2/1000)*L*((((T1-D)+273)^4)-((T2+273)^4))
480 PRINT " Q cond+conv = ";INT((Q*L)+0.5)" W, Q rad = ";INT(H+.5)" W,
    Q tot = ";INT((Q*L)+H+0.5)" W"
490 PRINT " at a nominal He thickness of ";X1 " mm,
```

```
      actual He thickness of ";(INT(((X1+R0-R2)*100)+.5))/100" mm."
500   PRINT " ΔT tube = ";(INT((D*10)+0.5))/10" °C,
      ΔT helium = ";(INT((E*10)+0.5))/10" °C,
      ΔT quartz = ";(INT((F*10)+0.5))/10" °C"
510   PRINT
520   VOL=PI*((R1/10)^2)*L*100
530   PV=(INT(((Q*L+H)*100/VOL)+0.5))/100
540   PL=Q+(H/L)
550   PRF=(INT((PV*100/5)+0.5))/100
560   PRINT " Volume = ";(INT(VOL*10+0.5)/10)" cm^3, P/V = ";PV" W/cm^3,
      P/L = ";(INT(PL+0.5))/1000" kW/m, PRF = ";PRF" kHz"
570   T0 = (((T1+273)^1.73)+(1.73*PL)/(0.0096*PI))^(1/1.73)
580   TAV = ((0.0096*PI)/(2.73*PL))*(((T0)^2.73)-((T1+273)^2.73))
590   PRINT" Axis gas temperature = ";INT(T0+0.5)" K (";INT(T0-273+0.5)" °C),
      Average gas temperature = ";INT(TAV+0.5)" K (";INT(TAV-273+0.5)" °C)."
600   PRINT
610   PRINT" For a water temp gradient of < 10 °C/m, the water flow rate must
      be > ";INT((PL+0.5)/700)" litres/min"
620   PRINT
630   IF FLAG=0 GOTO 690
640   PRINT " Type C to continue, S to stop"
650   INPUT ANS$ :IF ANS$ = "s" GOTO 710
660   X1=X1+.25
670   PRINT
680   GOTO 300
690   PRINT " Type D to try a different helium thickness, S to stop"
700   INPUT ANS$:IF ANS$="d" GOTO 220
710   PRINT" Would you like to design for a different discharge tube? (type Y/N)"
```

```
720 INPUT ANS$ :IF ANS$="y" GOTO 80
730 PRINT" Design session terminated"
740 END
```

Appendix F: Calculation of the real laser input power

F.1 Introduction

The power supplied to a laser tube can be obtained by:

1. calculating the energy stored in the capacitors prior to discharge and multiplying by the PRF or

2. multiplying the power supply voltage and average current delivered.

These methods do not, however, give an accurate value for the amount of power actually deposited in the discharge channel as they neglect the power wasted elsewhere in the circuit. Energy is dissipated in the lead resistances, the internal resistance of the capacitor, the charging inductor and diode and in the thyratron during its commutation period.

A more accurate value for the actual power deposited in the discharge tube can be obtained by integrating the product of the voltage across the laser tube and the laser current, over the time of the current pulse and multiplying this by the PRF. The measured laser tube voltage is, however, composed of two components, namely, a resistive component and a reactive component due to the laser head inductance. When the storage capacitor is discharged through the laser tube, the stored energy is dissipated as heat in the resistive component of the

plasma impedance and stored as an electromagnetic field in the reactive component. The energy stored in this inductance will ultimately be dissipated in the laser tube's resistance. Hence, if the distribution of input power over the current pulse is important, the laser head inductance must be taken into account during the calculations and only the voltage dropped across the plasma resistance used to calculate the power.

The laser head inductance can be calculated from the laser assembly's geometry, although, in practice, this often proves to be difficult. The required measurements of tube voltage and laser current can, however, be manipulated to reveal information about the laser head inductance. A procedure for calculating the average power deposited in a laser tube discharge, based on measuring the tube voltage and laser current is given below. For completeness the laser head inductance is taken into consideration (although for our purposes it need not be).

F.2 Theory

The apparent *instantaneous* power, P_{app}, delivered to a discharge is given by:

$$P_{app} = VI, \qquad [F.1]$$

where, V is the instantaneous measured potential difference between the cathode and the anode and I is the instantaneous measured discharge current. The tube voltage can be separated into two components:

$$V = IR + L\frac{\mathrm{d}I}{\mathrm{d}t}, \qquad [F.2]$$

so that,

$$P_{\mathrm{app}} = \left(IR + L\frac{\mathrm{d}I}{\mathrm{d}t}\right)I. \qquad [F.3]$$

The first term in brackets is the resistive component of the tube voltage while the second is due to the laser head inductance. Differentiating Equation F.3 with respect to time yields the equation:

$$\frac{\mathrm{d}P_{\mathrm{app}}}{\mathrm{d}t} = 2IR\frac{\mathrm{d}I}{\mathrm{d}t} + L\left(\frac{\mathrm{d}I}{\mathrm{d}t}\right)^2 + LI\frac{\mathrm{d}^2I}{\mathrm{d}t^2}. \qquad [F.4]$$

At the peak of the laser current pulse, the rate of change of current with time is zero, leading to the expression:

$$\frac{\mathrm{d}P_{\mathrm{app}}}{\mathrm{d}t} = LI\frac{\mathrm{d}^2I}{\mathrm{d}t^2}, \qquad [F.5]$$

which can be rearranged to give an expression for the laser head inductance, thus:

$$L = \left(\frac{\mathrm{d}P_{\mathrm{app}}}{\mathrm{d}t}\right) \Big/ \left(I\frac{\mathrm{d}^2I}{\mathrm{d}t^2}\right). \qquad [F.6]$$

Now, the actual instantaneous power delivered to the discharge is that which is dissipated in the laser tube's resistance,

$$P_{\text{actual}} = P_{\text{app}} - LI\frac{\mathrm{d}I}{\mathrm{d}t}. \qquad \text{[F.7]}$$

Equation F.7 can be integrated with respect to time, over the duration of the current pulse, to give the pulse energy supplied to the discharge. Multiplying this pulse energy by the PRF at which the laser is operating, f, gives the required average input power which actually heats the discharge tube's contents:

$$\langle P_{\text{actual}} \rangle = \left(\int_{\tau_1}^{\tau_2} P_{\text{actual}} \mathrm{d}t \right) f. \qquad \text{[F8]}$$

F.3 Method

1. An oscillogram displaying the laser current and tube voltage is obtained when the laser is at its optimum operating temperature. The tube voltage is obtained by subtracting the anode voltage from the cathode voltage.

2. The oscillogram of current and tube voltage is enlarged and the time axis divided up into intervals of 5 ns, say. The laser current and tube voltage are tabulated for each time.

3. The laser head inductance is calculated from the data using Equation F.6.

4. Equation F.7 is used to determine the instantaneous input power.

5. The instantaneous input power is plotted against time so that the average input power can be obtained from the area under the curve using Equation F.8.

F.4 Results obtained for WCL 2

Running through the above method for the WCL 2 tube gave the following results:

1. Laser head inductance = 375 μH
2. Peak actual instantaneous input power = 1.6 MW
3. Apparent average input power = 2.6 kW
4. Actual average input power = 2.6 kW

F5 Discussion

Figure F.1 shows the actual instantaneous input power and apparent instantaneous input power for WCL 2. The laser head inductance moves the curve later in time, and reduces the peak input power slightly. The fact that the apparent and actual input powers are approximately the same indicates that the calculated value for the laser head inductance is a reasonably accurate one.

The power supply based optimum input power for WCL 2 of 3.3 kW is 43% higher than the predicted value of 2.3 kW (see Chapter 6), while the actual average input power obtained from laser current and tube voltage data is 13% higher than the predicted value. However, neither result takes into account the power wasted in the electrodes. It is therefore believed that the actual average input power result obtained here indicates that the thermal loading model gives an accurate prediction of the laser's thermal performance.

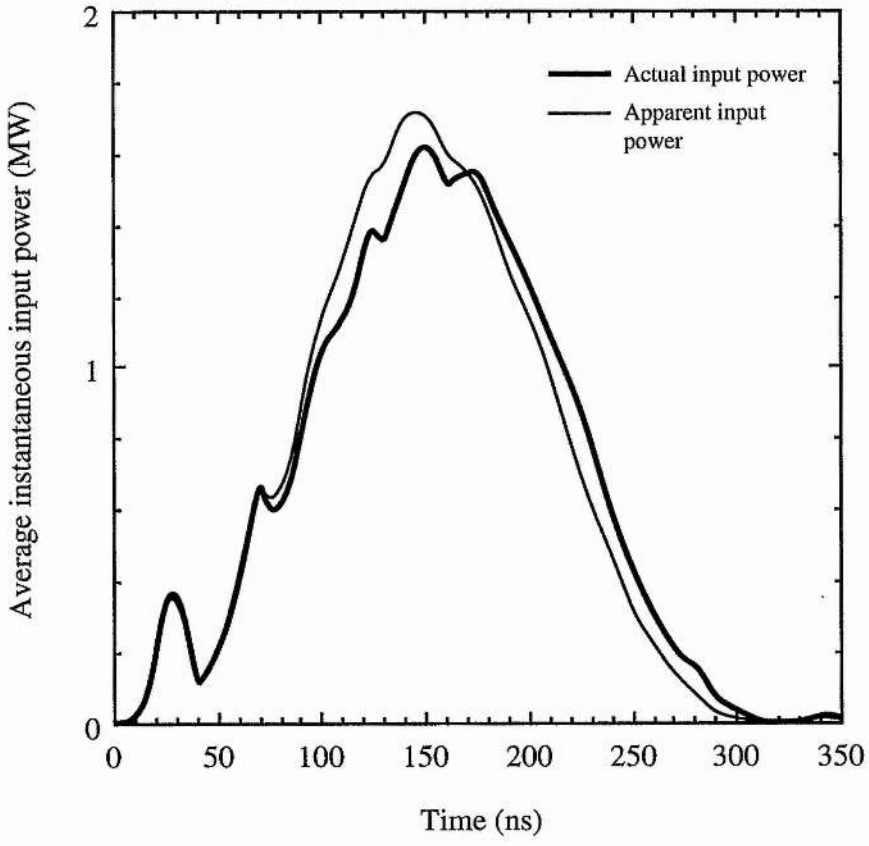

Figure F.1 Graph of actual and apparent instantaneous input power for WCL 2.

Appendix G: Acoustic standing waves in helium filled open pipes

If a laser discharge tube is treated as an open pipe of length, L, the boundary condition for acoustic standing wave formation is that the pressure change at the pipe ends must be zero. This means that pressure nodes (displacement antinodes) occur at the open ends. The fundamental mode of vibration is therefore established when:

$$\lambda_0 = 2L, \qquad [G.1]$$

where λ_0 is the wavelength associated with the lowest natural frequency, f_0. It follows from the boundary conditions that the overtones comprise of both the even and odd harmonics, the nth overtone being of frequency:

$$f_n = (n+1)f_0. \qquad [G.2]$$

Recasting Equation G.2 in terms of the pipe length yields:

$$f_n = \frac{(n+1)c}{2L} \qquad [G.3]$$

where, provided that the frequency is within the audible range, c is the adiabatic speed of sound in the discharge tube. For a tube filled with helium[†]:

$$c = \left(\frac{5kT}{3M}\right)^{1/2} = 58.84T^{1/2} \qquad [G.4]$$

where k is the Boltzmann constant, T is the absolute gas temperature and M the mass of a helium atom.

Figure G.1, below, shows the frequencies of standing wave formation (up to the 4th overtone) in a helium filled open pipe of 40 cm length as a function of the gas temperature.

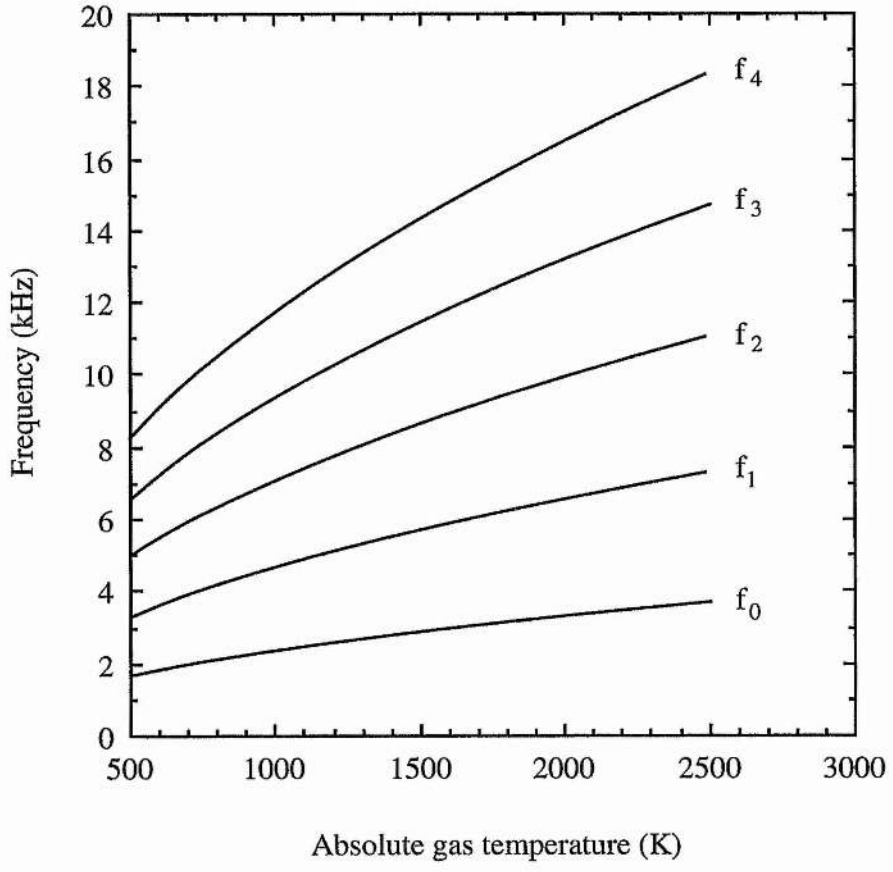

Figure G.1

Water-cooled laser 1 exhibited an output power minimum somewhere between the operating frequencies of 6 kHz and 8 kHz. The expected average helium gas temperature in WCL 1, at optimum input power was 1150 K. At this gas temperature, an acoustic resonance (the 2nd overtone) might be expected to occur at ~7.4 kHz.

† Whelan, P. M. and Hodgson, M. J.,
Essential Principles of Physics
John Murray (London) 1982